

---

---

DISSERTATION

INDEPENDENT MEASUREMENT OF THE T2K NEAR DETECTOR CONSTRAINT  
USING THE OFF-AXIS PI-ZERO DETECTOR

Submitted by

Matthew Gregory Hogan

Department of Physics

In partial fulfillment of the requirements

For the Degree of Doctor of Philosophy

Colorado State University

Fort Collins, Colorado

Fall 2019

Doctoral Committee:

Advisor: Walter Toki

Co-Advisor: Robert Wilson

Norman Buchanan

Wen Zhou

---

---

Copyright by Matthew Gregory Hogan 2019

---

All Rights Reserved

---

---

## ABSTRACT

### INDEPENDENT MEASUREMENT OF THE T2K NEAR DETECTOR CONSTRAINT USING THE OFF-AXIS PI-ZERO DETECTOR

The Tokai to Kamioka (T2K) experiment is a long baseline neutrino oscillation experiment hosted in Japan in search for electron neutrino appearance in a high purity muon neutrino beam. In order to constrain the systematic uncertainties in the oscillation analysis, a dedicated near detector (ND) complex called ND280 is located 280 meters from the neutrino production source in line of the beam. To date, the Fine Grain Detector (FGD) in ND280 has provided the ND constraint using a binned maximum likelihood estimate fit. This thesis describes the effort to validate the ND constraint using the same framework, but with an independent data set from the ND280 Pi-Zero Detector (PØD). Expanding on previously developed PØD selections, new selections have been developed to select neutrino and antineutrino events in one and multiple track topologies on water and carbon. These selections are shown to have sensitivity similar sensitivity to the T2K flux and cross section systematic uncertainties. Using the same parameterization as the official ND constraint result, the PØD data fit results demonstrate similar flux and cross section results with that of the FGD data.

---

---

## ACKNOWLEDGEMENTS

---

I would like to thank the Elliott Forney for making a publicly accessible L<sup>A</sup>T<sub>E</sub>X template

---

# Contents

ABSTRACT . . . . .	ii
ACKNOWLEDGEMENTS . . . . .	iii
Contents . . . . .	iv
List of Tables . . . . .	vii
List of Figures . . . . .	ix
Chapter 1 Introduction . . . . .	1
1.1 Introduction to Neutrinos . . . . .	1
1.1.1 Neutrinos in the Standard Model . . . . .	3
1.1.2 Neutrino Oscillations . . . . .	14
1.1.3 CP Violation: Origins of Matter . . . . .	25
1.2 Tokai to- amioka Experiment . . . . .	26
1.2.1 Neutrino Production at J-PARC . . . . .	27
1.2.2 Neutrino Near Detectors: ND280 . . . . .	35
1.2.3 Neutrino Far Detector: Super-Kamiokande . . . . .	47
1.2.4 ND Constraint . . . . .	49
1.2.5 Contributions to the T2K Experiment . . . . .	52
1.3 Summary . . . . .	52
Chapter 2 BANFF Likelihood . . . . .	54

2.0.1	Introduction to Conditional PDFs and Likelihoods . . . . .	55
2.1	BANFF Fit Test Statistic . . . . .	56
Chapter 3	The PØD Selections and Samples . . . . .	61
3.1	Global Reconstruction . . . . .	62
3.2	PØD Selection Cuts . . . . .	63
3.2.1	Precuts . . . . .	63
3.2.2	The $\nu_\mu$ CC Inclusive in FHC Cut . . . . .	66
3.2.3	The $\bar{\nu}_\mu$ CC Inclusive in RHC Cuts . . . . .	66
3.2.4	The $\nu_\mu$ Background CC Inclusive in RHC Cuts . . . . .	67
3.3	Selection Kinematics . . . . .	68
3.3.1	$\nu_\mu$ in FHC CC 1-Track . . . . .	73
3.3.2	$\nu_\mu$ in FHC CC N-Tracks . . . . .	78
3.3.3	$\bar{\nu}_\mu$ in RHC CC 1-Track . . . . .	82
3.3.4	$\bar{\nu}_\mu$ in RHC CC N-Tracks . . . . .	84
3.3.5	$\nu_\mu$ Background in RHC CC 1-Track . . . . .	86
3.3.6	$\nu_\mu$ Background in RHC CC N-Tracks . . . . .	88
3.4	Summary of Selections . . . . .	90
Chapter 4	The PØD-Only in BANFF Parameterization . . . . .	94
4.1	Fit Binning . . . . .	95
4.1.1	Fit Binning Determination . . . . .	96
4.2	Penalty Terms and Systematic Uncertainties . . . . .	97
4.2.1	Flux Model . . . . .	98
4.2.2	Detector Inefficiencies Model . . . . .	105
4.2.3	Cross Section Model . . . . .	120
4.3	BANFF Fit Parameterization Summary . . . . .	128

Chapter 5	Fitter Validation . . . . .	130
5.1	Asimov Data Fit . . . . .	130
5.1.1	Event Rate . . . . .	132
5.1.2	One Sigma Variation of Cross Section Parameters . . . . .	134
5.1.3	Log-Likelihood Scans . . . . .	134
5.1.4	Fit Results . . . . .	134
5.2	Fake Data . . . . .	141
5.2.1	High Energy $\nu_\mu$ in FHC Flux Variation . . . . .	141
5.2.2	Single Pion Event Rate Variation . . . . .	143
5.3	Validation Summary . . . . .	146
Chapter 6	Fitter Results . . . . .	148
6.1	Prefit Sample Distributions . . . . .	148
6.2	Postfit Results . . . . .	148
6.2.1	Parameter Value Comparisons . . . . .	148
6.2.2	Postfit Sample Distributions . . . . .	148
6.2.3	P-Value Between PØD and FGD Fits . . . . .	148
Bibliography	. . . . .	182
Appendix A	Toy Experiment Variations . . . . .	189
Appendix B	Cross Section Parameters Variations . . . . .	216
Appendix C	Log-Likelihood Sample Scans . . . . .	233
Appendix D	Log-Likelihood Penalty Scans . . . . .	243

---

# List of Tables

1.1	Sensitivity of Different Oscillation Experiments . . . . .	20
1.2	Table of Best Fit MNSP Parameters Split by Normal and Inverted hierarchy . . . . .	24
1.3	PØD Water Target Mass Composition . . . . .	45
3.1	The PØD WT FV and Corridor Definition . . . . .	65
3.2	POT Used in This Analysis . . . . .	68
3.3	The Expanded $\nu$ NEUT Reactions Table . . . . .	70
3.4	The Expanded $\bar{\nu}$ NEUT Reactions Table . . . . .	71
4.1	Flux Binning and Uncertainties Used in the BANFF Fit . . . . .	101
4.1	Flux Binning and Uncertainties Used in the BANFF Fit . . . . .	102
4.1	Flux Binning and Uncertainties Used in the BANFF Fit . . . . .	103
4.1	Flux Binning and Uncertainties Used in the BANFF Fit . . . . .	104
4.2	List of Detector Systematic Effects and Treatment . . . . .	106
4.3	Cross Section Model Fit Parameters in the BANFF Fit . . . . .	127
4.3	Cross Section Model Fit Parameters in the BANFF Fit . . . . .	128
5.1	Event Rate Table for Asimov Set . . . . .	133
B.1	Event rate broken by sample for one $\sigma$ variation of each parameter. . . . .	217
B.1	Event rate broken by sample for one $\sigma$ variation of each parameter. . . . .	218
B.1	Event rate broken by sample for one $\sigma$ variation of each parameter. . . . .	219

---

B.1	Event rate broken by sample for one $\sigma$ variation of each parameter.	220
B.1	Event rate broken by sample for one $\sigma$ variation of each parameter.	221
B.1	Event rate broken by sample for one $\sigma$ variation of each parameter.	222
B.1	Event rate broken by sample for one $\sigma$ variation of each parameter.	223
B.1	Event rate broken by sample for one $\sigma$ variation of each parameter.	224
B.1	Event rate broken by sample for one $\sigma$ variation of each parameter.	225
B.1	Event rate broken by sample for one $\sigma$ variation of each parameter.	226
B.1	Event rate broken by sample for one $\sigma$ variation of each parameter.	227
B.1	Event rate broken by sample for one $\sigma$ variation of each parameter.	228
B.1	Event rate broken by sample for one $\sigma$ variation of each parameter.	229
B.1	Event rate broken by sample for one $\sigma$ variation of each parameter.	230
B.1	Event rate broken by sample for one $\sigma$ variation of each parameter.	231
B.1	Event rate broken by sample for one $\sigma$ variation of each parameter.	232

---

# List of Figures

1.1	The Standard Model of particle physics . . . . .	4
1.2	CC And NC Feynman Diagrams . . . . .	6
1.3	Helicity of Neutrino Through Decay of Charged Pi Mesons . . . . .	7
1.4	$\nu_e + e^-$ Scattering . . . . .	12
1.5	A $\nu_\mu$ -Induced CCQE Interaction . . . . .	13
1.6	Depiction of Two Neutrino Flavor Change of Basis . . . . .	16
1.7	Survival and Disappearance Probability . . . . .	18
1.8	Logarithmic Plot of the Two Flavor Survival Probability . . . . .	19
1.9	Mass hierarchy Problem And MNSP Representation . . . . .	23
1.10	Display of the matter and energy content of the Universe . . . . .	26
1.11	Birds eye view of the T2K experiment on the Japanese archipelago . . . . .	27
1.12	The T2K Unoscillated $\nu_\mu$ Flux at SK . . . . .	28
1.13	Bird's eye view of the J-PARC center . . . . .	29
1.14	Schematics of the J-PARC Accelerators . . . . .	30
1.15	The neutrino beamline at J-PARC . . . . .	31
1.16	Photographs of the Target Station . . . . .	32
1.17	T2K Accumulated Protons on Target . . . . .	33
1.18	Photographs of the T2K MPPC . . . . .	36
1.19	Schematic of INGRID . . . . .	37
1.20	INGRID Beam Profile . . . . .	38

1.21	INGRID Event Rate . . . . .	39
1.22	Schematic of the Off-Axis Near Detector ND280 . . . . .	40
1.23	ND280 Magnetic Field Deviations from a Data Fit . . . . .	42
1.24	Schematic of the PØD . . . . .	44
1.25	A cross section of a PØD scintillating bar . . . . .	45
1.26	Cut-Away Drawing of a TPC Volume in ND280 . . . . .	46
1.27	Diagram of the Super-Kamiokande Detector . . . . .	48
1.28	Representative T2K Events in Super-Kamiokande . . . . .	48
1.29	Predicted and Best Fit Measurements for the SK Flux . . . . .	50
1.30	Predicted CCInc Cross Section at T2K Energies . . . . .	51
3.1	Data and MC distributions of the $\nu_\mu$ and $\bar{\nu}_\mu$ water-in CC signal selections . . . . .	62
3.2	The NEUT Interaction CCQE and non-CCQE Legend . . . . .	70
3.3	True Particle Selected Legend . . . . .	71
3.4	NEUT $\nu$ Interaction Legend . . . . .	72
3.5	NEUT $\bar{\nu}$ Interaction Legend . . . . .	72
3.6	Reconstructed Kinematics for the $\nu_\mu$ in FHC CC 1-Track Selection for CCQE and non-CCQE Interactions . . . . .	74
3.7	Reconstructed Kinematics for the $\nu_\mu$ in FHC CC 1-Track Selection for the True Selected Particle . . . . .	75
3.8	Vertex Z Position of the $\nu_\mu$ in FHC CC 1-Track Selection . . . . .	76
3.9	Efficiency and Purity of $\nu_\mu$ CCQE Interactions in the $\nu_\mu$ in FHC CC 1-Track Selection . . . . .	76
3.10	The $\nu_\mu$ in FHC CC 1-Track True Kinematics . . . . .	77
3.11	Lepton Candidate Reconstructed Kinematics for the $\nu_\mu$ in FHC CC N-Tracks Selection for CCQE and non-CCQE Interactions . . . . .	78
3.12	Lepton Candidate Reconstructed Kinematics for the $\nu_\mu$ in FHC CC N-Tracks Selection for the True Selected Particle . . . . .	79

3.13	Vertex position of the $\nu_\mu$ in FHC CC N-Tracks Selection . . . . .	79
3.14	Efficiency and Purity of $\nu_\mu$ CCQE Interactions in the $\nu_\mu$ in FHC CC N-Tracks Selection . . . . .	80
3.15	The $\nu_\mu$ in FHC CC N-Tracks True Kinematics . . . . .	81
3.16	Reconstructed Kinematics for the $\bar{\nu}_\mu$ in RHC CC 1-Track Selection for CCQE and non-CCQE Interactions . . . . .	82
3.17	Reconstructed Kinematics for the $\bar{\nu}_\mu$ in RHC CC 1-Track Selection for the True Selected Particle . . . . .	83
3.18	Efficiency and Purity of $\bar{\nu}_\mu$ CCQE Interactions in the $\bar{\nu}_\mu$ in RHC CC 1-Track Selection . . . . .	83
3.19	The $\bar{\nu}_\mu$ in RHC CC 1-Track True Kinematics . . . . .	84
3.20	Lepton Candidate Reconstructed Kinematics for the $\bar{\nu}_\mu$ in RHC CC N-Tracks Selection for CCQE and non-CCQE Interactions . . . . .	85
3.21	Lepton Candidate Reconstructed Kinematics for the $\bar{\nu}_\mu$ in RHC CC N-Tracks Selections for the True Selected Particle . . . . .	85
3.22	Efficiency and Purity of $\bar{\nu}_\mu$ CC non-QE Interactions in the $\bar{\nu}_\mu$ in RHC CC N-Tracks Selection . . . . .	86
3.23	The $\bar{\nu}_\mu$ in RHC CC N-Tracks True Kinematics . . . . .	87
3.24	Reconstructed Kinematics for the $\nu_\mu$ in RHC CC 1-Track Selection for CCQE and non-CCQE Interactions . . . . .	88
3.25	Reconstructed Kinematics for the $\nu_\mu$ in RHC CC 1-Track Selection for the True Selected Particle . . . . .	89
3.26	Efficiency and Purity of $\nu_\mu$ CCQE Interactions in the $\nu_\mu$ in RHC CC 1-Track Selection . . . . .	89
3.27	The $\nu_\mu$ in RHC CC 1-Track True Kinematics . . . . .	90
3.28	Reconstructed Kinematics for the $\nu_\mu$ in RHC CC N-Tracks Selection for CCQE and non-CCQE Interactions . . . . .	91

3.29	Reconstructed Kinematics for the $\nu_\mu$ in RHC CC N-Tracks Selection for the True Selected Particle . . . . .	91
3.30	Efficiency and Purity of $\nu_\mu$ CC non-QE Interactions in the $\nu_\mu$ in RHC CC N-Tracks Selection . . . . .	92
3.31	The $\nu_\mu$ in RHC CC N-Tracks True Kinematics . . . . .	93
4.1	The PØD Momenta Resolutions Used for Fit Binning . . . . .	97
4.2	The PØD Angular Residuals Used for Fit Binning . . . . .	98
4.3	BANFF Pre-fit Flux Covariance Matrix . . . . .	99
4.4	The T2K Unoscillated Neutrino Flux Prediction at SK . . . . .	100
4.5	Bin Normalization Edges for the $\nu_\mu$ in FHC Selections . . . . .	111
4.6	Bin Normalization Edges for the $\bar{\nu}_\mu$ in RHC Selections . . . . .	112
4.7	Bin Normalization Edges for the $\nu_\mu$ in RHC Selections . . . . .	114
4.8	Event Variations in Observable Normalization Bins . . . . .	116
4.9	Detector Covariance Matrix . . . . .	119
4.10	Cross Section Parameters Prefit Covariance Matrix . . . . .	126
5.1	Complete Prefit Correlation Matrix for the BANFF Fit. . . . .	131
5.2	Test Statistic Scans for Variations of Fit Parameters in the Asimov Set . . . . .	135
5.3	Asimov Fit Results for the Flux at ND280 . . . . .	136
5.4	Asimov Fit Results for the Flux at Super-K . . . . .	137
5.5	Asimov Fit Results for the Bin Normalization Parameters . . . . .	138
5.6	Asimov Fit Results for the Cross Section and FSI Parameters . . . . .	139
5.7	Complete Postfit Correlation Matrix for the Asimov Data Fit . . . . .	140
5.8	Flux and Cross Section Postfit Correlation Matrix for the Asimov Data Fit . . . . .	140
5.9	Neutrino Flux in the High Energy Neutrino Flux Variation Fake Data Set . . . . .	142
5.10	Postfit Parameters for the High Energy $\nu_\mu$ in FHC Flux Fake Data fit . . . . .	144

5.11	Lepton Candidate Momentum in the Single Pion Event Rate Variation Fake Data Set	145
5.12	Postfit Parameters for the $C_A^5$ Fake Data Fit	147
6.1	PØD Water-In $\nu_\mu$ in FHC CC 1-Track	149
6.2	PØD Water-In $\nu_\mu$ in FHC CC N-Tracks	150
6.3	PØD Water-In $\bar{\nu}_\mu$ in RHC CC 1-Track	151
6.4	PØD Water-In $\bar{\nu}_\mu$ in RHC CC N-Tracks	152
6.5	PØD Water-In $\nu_\mu$ in RHC CC 1-Track	153
6.6	PØD Water-In $\nu_\mu$ in RHC CC N-Tracks	154
6.7	PØD Water-Out $\nu_\mu$ in FHC CC 1-Track	155
6.8	PØD Water-Out $\nu_\mu$ in FHC CC N-Tracks	156
6.9	PØD Water-Out $\bar{\nu}_\mu$ in RHC CC 1-Track	157
6.10	PØD Water-Out $\bar{\nu}_\mu$ in RHC CC N-Tracks	158
6.11	PØD Water-Out $\nu_\mu$ in RHC CC 1-Track	159
6.12	PØD Water-Out $\nu_\mu$ in RHC CC N-Tracks	160
6.13	Prefit and postfit ND280 flux parameters for the PØD-only and FGD-only results	161
6.14	Prefit and postfit Super-K flux parameters for the PØD-only and FGD-only results	162
6.15	Prefit and postfit cross-section parameters with their uncertainties.	163
6.16	Prefit and postfit PØD bin normalization parameters	164
6.17		165
6.18	Prefit and post flux and cross section correlations	166
6.19	PØD Water-In $\nu_\mu$ in FHC CC 1-Track	167
6.20	PØD Water-In $\nu_\mu$ in FHC CC N-Tracks	168
6.21	PØD Water-In $\bar{\nu}_\mu$ in RHC CC 1-Track	169
6.22	PØD Water-In $\bar{\nu}_\mu$ in RHC CC N-Tracks	170
6.23	PØD Water-In $\nu_\mu$ in RHC CC 1-Track	171
6.24	PØD Water-In $\nu_\mu$ in RHC CC N-Tracks	172

6.25 PØD Water-Out $\nu_\mu$ in FHC CC 1-Track . . . . .	173
6.26 PØD Water-Out $\nu_\mu$ in FHC CC N-Tracks . . . . .	174
6.27 PØD Water-Out $\bar{\nu}_\mu$ in RHC CC 1-Track . . . . .	175
6.28 PØD Water-Out $\bar{\nu}_\mu$ in RHC CC N-Tracks . . . . .	176
6.29 PØD Water-Out $\nu_\mu$ in RHC CC 1-Track . . . . .	177
6.30 PØD Water-Out $\nu_\mu$ in RHC CC N-Tracks . . . . .	178
6.31 r=125 and p-value=0.7163 . . . . .	180
6.32 r=75 and p-value=0.1673 . . . . .	181
C.1 Corrected 2p2h Shape Location Scans . . . . .	242

---

# Chapter 1

## Introduction

*Chose trop vue n'est chère tenue*

A thing too much seen is little prized

French proverb

### 1.1 Introduction to Neutrinos

The history of the neutrino can be traced back to electron energy spectrum observed in neutron  $\beta$ -decay. While measurements of  $\alpha$ - and  $\gamma$ -decay of atomic nuclei showed discrete spectral lines, the electron ( $\beta$  particle) exhibited a continuous energy spectrum. Experimentally, there were two observed particles in each decay process and classical physics dictated that the outgoing daughter particles should have discrete energies. The fact that the  $\beta$ -decay spectrum was not this way posed a fundamental problem for physicists in the mid-1910s that energy was not conserved. Two solutions were postulated: either the “energy conservation law is only valid statistically in such a process [...] or an additional undetectable new particle [...] carrying away the additional energy and spin [...] is emitted [68].” The latter solution was proposed by Wolfgang Pauli in a letter dated 4 December 1930 to a group of physicists

---

meeting in Tübingen, modern Germany, where he first proposed the neutrino<sup>1</sup>. Pauli's solution also predicted that the undetected neutrino would have half-integer spin, a quantum mechanical property of matter, since the observed particles in  $\beta$ -decay did not conserve angular momentum. The existence of the neutrino and validation of Pauli's predictions would not be experimentally verified for another 20 years.

The neutrino was first observed in 1953 by Clyde Cowan and Frederick Reines using a nuclear reactor in South Carolina, U.S.A.. Since then three types or "flavors" of neutrinos and antineutrinos have been observed from accelerators and also from unique sources like the Sun and a supernova. Neutrino physics continues to be an active area of physics since neutrinos are unique probes to processes otherwise inaccessible in laboratories. For instance in the depths of the Sun's core where fusion occurs and neutrinos are created, neutrinos are able to travel through the ultra dense and hot medium of the core (over  $10^7$  degrees Kelvin) and outer layers of the Sun and reach us on Earth.

Neutrinos rarely interact with normal matter, meaning that they travel essentially unimpeded towards one's particle detector. The rarity of such interactions can be illustrated with the fact that given nearly  $7.0 \times 10^{10}$  neutrinos/cm<sup>2</sup>/sec are incident on the Earth from the Sun<sup>2</sup>, statistically one solar neutrino can harmlessly interact with an individual in their lifetime. So this begs the question: how does one detect a neutrino? The short answer is one requires a large enough flux of neutrinos passing through a large dense volume of matter just to detect one given today's technology.

Scientists continue to be interested in neutrinos due to the unusual properties they exhibit. One of the more recent and surprising aspects about neutrinos is their ability to

---

<sup>1</sup>In W Pauli's December 1930 letter, he referred to his proposed particle as the "neutron", which is not the same neutron known of today. At that point in time, the neutral particles inside the atomic nucleus, also called "neutrons", had not been discovered, let alone understood. The neutron, which was discovered in 1932 by James Chadwick, has been formally associated as the neutral, cousin particle to the proton. It would be Enrico Fermi who would coin the particle in W Pauli's letter and solution to the  $\beta$ -decay spectrum as a "neutrino" meaning in Italian *little neutral one*.

<sup>2</sup>To give some perspective to this number, this means 70 billion neutrinos are traveling every second through an area similar to one's own thumb nail.

---

undergo “flavor oscillations” where a neutrino of definite flavor (type) is created and later observed as a different flavor. The impact of differences between neutrino and antineutrino oscillations could help explain the observed matter and anti-matter asymmetry in the Universe which one of the most profound mysteries in physics today.

### 1.1.1 Neutrinos in the Standard Model

The Standard Model (SM) of particle physics is the theory of elementary or fundamental particle constituents and the forces between them. These standard model forces are the electromagnetic, weak and strong. String theory, which is not yet tested, attempts to incorporate the gravitational force. The SM forces and the gravitational force constitute the four *known* fundamental forces of the Universe. Each force in the SM has at least one “force carrier” particle that mediates the interactions between particles. The force carriers are formally called “gauge bosons” which indicates they are particles with integer  $(0, 1, 2, \dots)$  spin that mediate the interaction. The weak nuclear bosons, the charged  $W^\pm$  and neutral Z, couple to neutrinos as well as the other fermions, particles with half-integer  $(\frac{1}{2}, \frac{3}{2}, \frac{5}{2}, \dots)$  spin, in the SM. All the elementary particles of the SM are shown in Figure 1.1 on page 4.

Neutrinos in the SM are electrically neutral, massless particles categorized into three generations based on their charged, more massive Lepton cousins. In the SM, the three neutrinos and the three antineutrinos are the only spin  $1/2$  particles, among quarks and leptons, that have only weak interactions. The neutrino and charged lepton pair into a “weak isospin doublet” in the SM. These doublets are locally gauge invariant under a  $SU(2) \times U(1)$  symmetry which leads to the postulated existence of the photon, the  $W^\pm$  and  $Z$  bosons. They are necessary to enable local gauge invariance<sup>3</sup>.

---

<sup>3</sup>A gauge theory describes ways to measure physical forces or fields through interactions between elementary particles. The electric or magnetic fields for example can only be probed by charged particles. In the realm of quantum field theories, fields are postulated to permeate everywhere and it is excitations of these fields which produce experimental observables. Fields are constructed using the Lagrangian formalism and altered using gauge transformations. If altering the Lagrangian in some way does not affect the observables, this is referred to as a gauge invariance. Local gauge invariance means that under the constraints of the experiment, certain gauge transformations do not affect the observables. The allowed locally gauge invariant

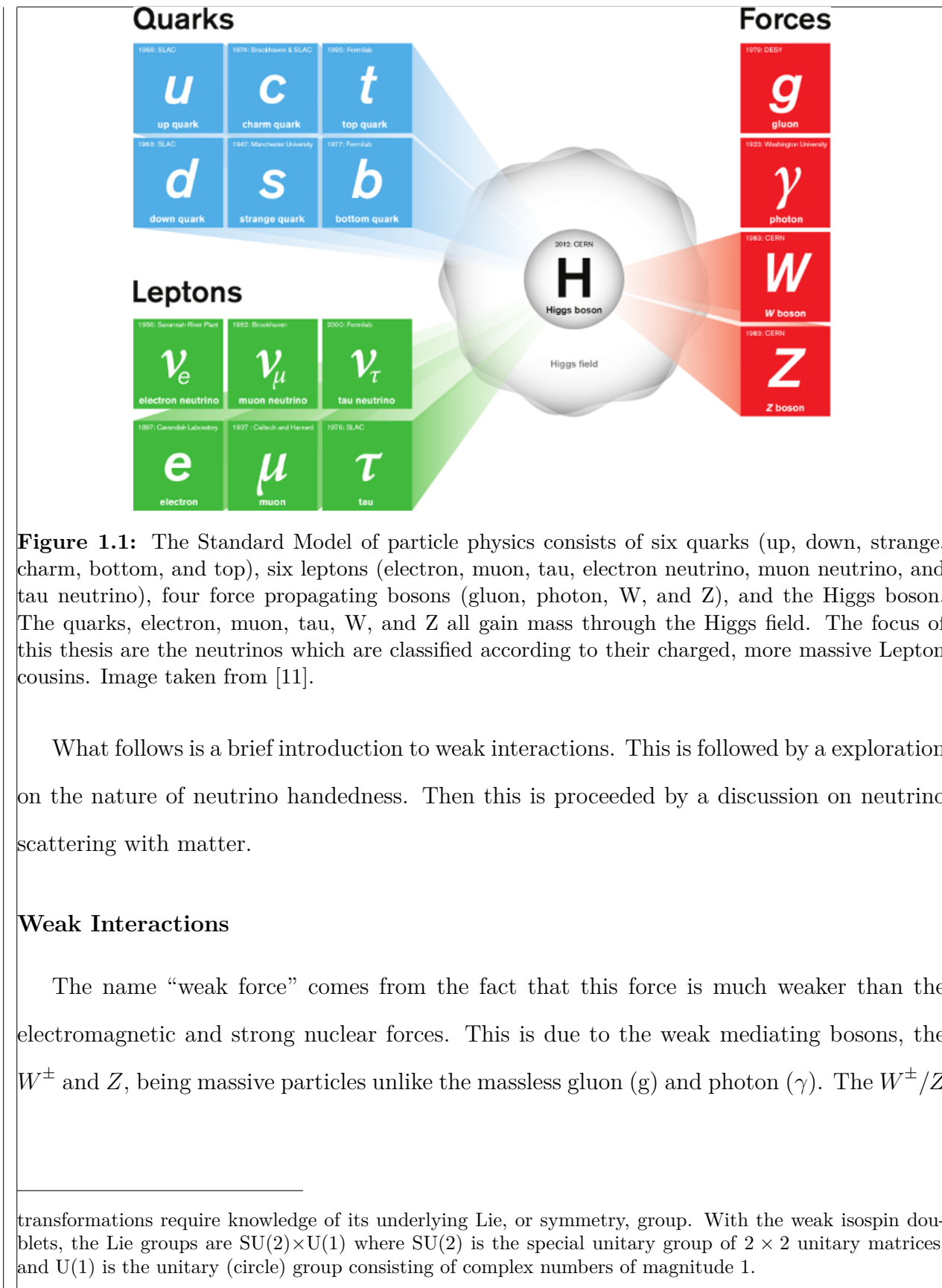


**Figure 1.1:** The Standard Model of particle physics consists of six quarks (up, down, strange, charm, bottom, and top), six leptons (electron, muon, tau, electron neutrino, muon neutrino, and tau neutrino), four force propagating bosons (gluon, photon, W, and Z), and the Higgs boson. The quarks, electron, muon, tau, W, and Z all gain mass through the Higgs field. The focus of this thesis are the neutrinos which are classified according to their charged, more massive Lepton cousins. Image taken from [11].

What follows is a brief introduction to weak interactions. This is followed by a exploration on the nature of neutrino handedness. Then this is proceeded by a discussion on neutrino scattering with matter.

## Weak Interactions

The name “weak force” comes from the fact that this force is much weaker than the electromagnetic and strong nuclear forces. This is due to the weak mediating bosons, the  $W^\pm$  and  $Z$ , being massive particles unlike the massless gluon ( $g$ ) and photon ( $\gamma$ ). The  $W^\pm/Z$

---

transformations require knowledge of its underlying Lie, or symmetry, group. With the weak isospin doublets, the Lie groups are  $SU(2) \times U(1)$  where  $SU(2)$  is the special unitary group of  $2 \times 2$  unitary matrices, and  $U(1)$  is the unitary (circle) group consisting of complex numbers of magnitude 1.

---

have masses of  $80/90 \text{ GeV}/c^2$ , which is more massive than all the elementary particles except for the top quark.

For weak interactions to occur at energies far below the masses (also called “off-shell”) of the  $W^\pm$  and  $Z$ , the interaction time must be infinitesimally small as dictated by the Heisenberg Uncertainty Principle

$$\Delta E \Delta t \gtrsim \hbar \quad (1.1)$$

where  $\Delta E$  is the energy of the particle and  $\Delta t$  is the time which the particle exists. As an example, consider a neutrino of energy of 1 GeV emitting a Z-boson of off-shell energy,  $\Delta E = 1 \text{ GeV}$  like shown in Figure 1.2 on page 6. The lifetime of that boson is about  $10^{-25} \text{ seconds}$  according to (1.1). In general, the probability that a massive particle of mass  $M$  will be created from the collision of two particles is given by a relativistic Breit–Wigner distribution

$$f(M) \propto \frac{1}{(M^2 - M_0^2)^2 c^4 + M_0^2 \Gamma^2}, \quad (1.2)$$

where  $M_0$  is the rest mass and  $\Gamma$  is the decay width of the particle. For  $M \ll M_0$ , the probability of creating that particle will be infinitesimally small. Therefore to observe a single weak interaction requires a large amount of weakly interacting particles.

Weak interactions are classified into two classes of interactions: charged current (CC) and neutral current (NC). The CC interactions involve a charged W boson and change the scattering neutrino into a electrically charged lepton of flavor  $l$  where the flavor of the neutrino  $\nu_l$  is inferred from the charged lepton. The same cannot be said of NC interactions which exchange a neutral Z boson. The NC interactions are flavor agnostic since they do not produce a charged lepton. An example of each interaction type is shown in Figure 1.2 on page 6.

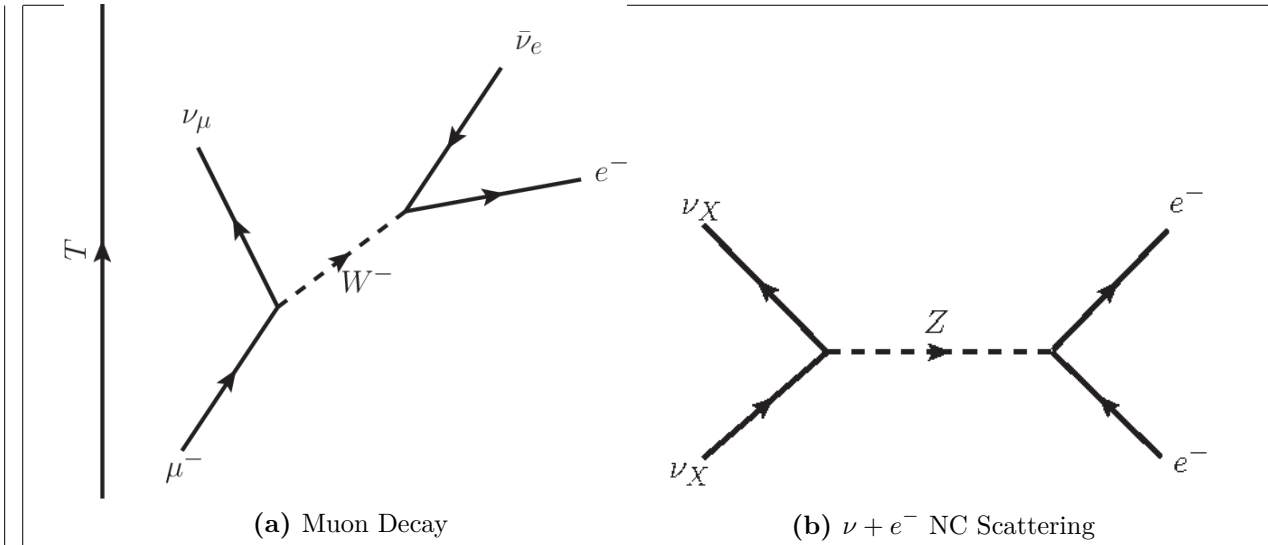


**Figure 1.2:** (a) Muon decay ( $\mu^- \rightarrow \nu_\mu \bar{\nu}_e e^-$ ) Feynman diagram with time increasing from bottom to top. This is a charged current process that converts a muon into a muon neutrino via the emission of a W boson. Due to a conserved quantum number called lepton number, the W must emit an electron and electron neutrino pair. (b) Neutral current interaction Feynman diagram where time increases from left to right. This is a neutral current interaction where a neutrino of arbitrary flavor  $X$  scatters off an electron via the emission of a Z boson.

### Chirality: How Neutrinos are Left Handed

Neutrinos are observed to have their spin direction vectors  $\sigma$  opposite to their momentum  $\mathbf{P}$  and this is reversed for anti-neutrinos. This property is called helicity and is given by (1.3)

$$\mathcal{H} = \frac{\sigma \cdot \mathbf{P}}{|\mathbf{P}|}. \quad (1.3)$$

Although neutrino detection is difficult, the neutrino helicity is readily inferred from the decay of the daughter muon in the pion decay,  $\pi^+ \rightarrow \mu^+ + \nu_\mu$ . Since a pion has net zero (0) spin, the spin vectors of the daughters must also sum to zero. The muon from a  $\pi^+$  decay has negative helicity (-1) hence the neutrino also has negative helicity. To confirm the anti-neutrino's helicity is positive (+1), the interaction requires both a charge (C) conjugation and parity (P) transformation as shown in Figure 1.3 on page 7. A C conjugation is a linear transformation that transforms all particles into their corresponding antiparticles while the P transformation inverts all spatial coordinates. Thus neutrinos are referred to *left-handed*

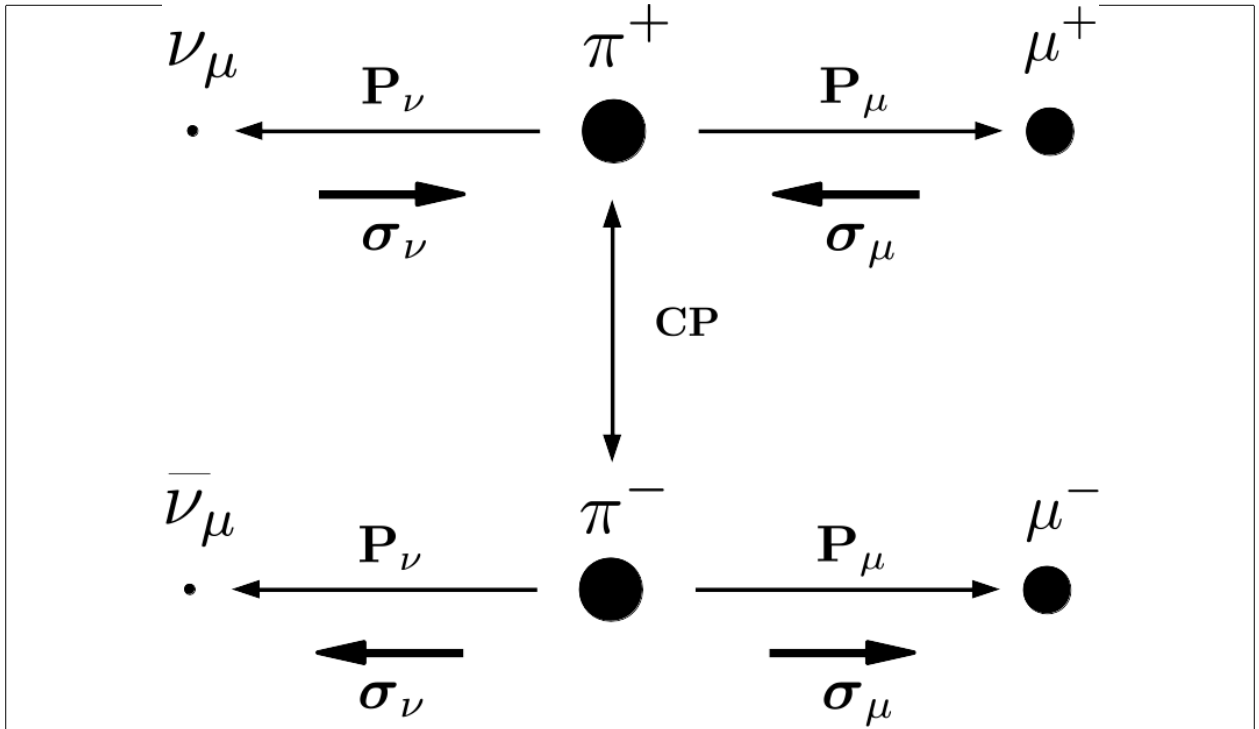


**Figure 1.3:** Decay of a charged pi meson into a muon and neutrino show the direction of the momentum  $\mathbf{P}$  and spin  $\boldsymbol{\sigma}$  of the outgoing particles. Since a pion at rest has zero (0) angular momentum, the system of daughter particles must have net zero angular momentum as well. A neutrino (antineutrino) is a right- (left-) handed helicity particle since its spin is (anti-)parallel to its momentum. Application of charge and parity (CP) converts all the particles into their respective antiparticles.

(LH) particles while anti-neutrinos are *right-handed* (RH) particles. It turns out helicity is a useful quantum number to describe neutrinos and coincides with a property called chirality. To understand chirality and its relationship to helicity requires an analysis of the Dirac Lagrangian and Dirac equation.

The Dirac Lagrangian for a free particle field  $\psi(x)$  with half-integer spin can be written as

$$\mathcal{L} = \bar{\psi}(x) \left[ \frac{i\hbar}{2} \sum_{\mu=0}^3 \gamma^\mu (\overrightarrow{\partial}_\mu - \overleftarrow{\partial}_\mu) - mc \right] \psi(x) \quad (1.4)$$

where  $\psi(x)$  is a four-component vector (spinor) describing a particle field and  $\gamma^\mu$  are a set of four 4x4 matrices. The adjoint field  $\bar{\psi}(x)$  is defined as

$$\bar{\psi}(x) \equiv \psi^\dagger(x) \gamma^0 \quad (1.5)$$

where  $\dagger$  denotes the conjugate and transpose operations. The  $\overrightarrow{\partial}_\mu$  operator is a four-vector defined as

$$\partial_0 = \frac{1}{c} \frac{\partial}{\partial t}, \partial_1 = \frac{\partial}{\partial x}, \partial_2 = \frac{\partial}{\partial y}, \partial_3 = \frac{\partial}{\partial z} \quad (1.6)$$

that acts only on the right of it while  $\overleftarrow{\partial}_\mu$  only acts on its left (i.e.  $\overline{\psi} \overleftarrow{\partial}_\mu = \partial_\mu \overline{\psi}$ ). The  $\gamma^\mu$  matrices are not unique and different representations dictate different kinematic regimes. The field equations are extracted from the Lagrangian using the Euler-Lagrange procedure. In general for a set of  $M$  fields, the field equation are given by

$$\partial_\mu \frac{\partial \mathcal{L}}{\partial (\partial_\mu \psi_r)} - \frac{\partial \mathcal{L}}{\partial \psi_r} = 0 \quad (r = 0, 1, 2, \dots, M-1, M). \quad (1.7)$$

For the Dirac Lagrangian, the field equation for  $\psi$  is given by

$$\partial_\mu \frac{\partial \mathcal{L}}{\partial (\partial_\mu \overline{\psi})} - \frac{\partial \mathcal{L}}{\partial \overline{\psi}} = 0 \quad (1.8)$$

which yields the Dirac equation

$$\left[ i\hbar \sum_{\mu=0}^3 \gamma^\mu \partial_\mu - mc \right] \psi(x) = 0. \quad (1.9)$$

The representation of the  $\gamma^\mu$  matrices that is useful to describe neutrinos is the *Chiral representation* (also called the *Weyl representation*) where

$$\gamma^0 = \begin{bmatrix} 0 & I_2 \\ I_2 & 0 \end{bmatrix}, \gamma^1 = \begin{bmatrix} 0 & \sigma_x \\ -\sigma_x & 0 \end{bmatrix}, \gamma^2 = \begin{bmatrix} 0 & \sigma_y \\ -\sigma_y & 0 \end{bmatrix}, \gamma^3 = \begin{bmatrix} 0 & \sigma_z \\ -\sigma_z & 0 \end{bmatrix}, \quad (1.10)$$

$I_2$  is the  $2 \times 2$  identity matrix,  $\sigma_{x,y,z}$  are the Pauli Spin matrices given by

$$\sigma_x = \sigma_1 = \begin{pmatrix} 0 & 1 \\ 1 & 0 \end{pmatrix}, \quad \sigma_y = \sigma_2 = \begin{pmatrix} 0 & -i \\ i & 0 \end{pmatrix}, \quad \sigma_z = \sigma_3 = \begin{pmatrix} 1 & 0 \\ 0 & -1 \end{pmatrix}.$$

---

Using the Chiral representation, the chirality matrix,  $\gamma^5$  (the fifth gamma matrix), is defined as

$$\gamma^5 = i\gamma^0\gamma^1\gamma^2\gamma^3 = \begin{bmatrix} -I_2 & 0 \\ 0 & I_2 \end{bmatrix}, \quad (1.11)$$

which is diagonal as well as Hermitian meaning that its eigenvalues are real and observable. Let eigenfunctions of the chirality matrix be denoted with subscripts  $P$  and  $M$  such that the eigenvalue equations are

$$\begin{aligned} \gamma^5\psi_P &= +1\psi_P, \\ \gamma^5\psi_M &= -1\psi_M. \end{aligned} \quad (1.12)$$

The field equation solutions to (1.9) can be decomposed into  $\psi_P$  and  $\psi_M$  projections using two chiral projection operators  $\hat{O}_{P,M}$  where

$$\psi = (\hat{O}_P + \hat{O}_M)\psi = \psi_P + \psi_M. \quad (1.13)$$

The chiral operators are explicitly given by

$$\begin{aligned} \hat{O}_M &= \frac{1}{2}(I_4 - \gamma^5) = \begin{pmatrix} 0 & 0 \\ 0 & I_2 \end{pmatrix}, \\ \hat{O}_P &= \frac{1}{2}(I_4 + \gamma^5) = \begin{pmatrix} I_2 & 0 \\ 0 & 0 \end{pmatrix}, \end{aligned} \quad (1.14)$$

where  $I_4$  is the  $4 \times 4$  identity matrix. Taken together (1.13) and (1.14) indicate the free neutrino field is a vector  $\psi$  minus axial vector  $\gamma^5\psi$ , also referred to as V-A, under P transformations. This feature is what allows for the weak force to violate P-symmetry and CP-symmetry. Referring back to (1.4) and (1.7), the Dirac equation becomes a set of coupled equations

---

$$\begin{aligned} i\hbar \sum_{\mu=0}^3 \gamma^\mu \partial_\mu \psi_P &= mc\psi_M, \\ i\hbar \sum_{\mu=0}^3 \gamma^\mu \partial_\mu \psi_M &= mc\psi_P \end{aligned} \tag{1.15}$$

where dynamics are set by the mass.

Since the chiral projection operators are decompositions of the identity matrix, the simplest nontrivial solution to  $\psi$  is

$$\psi = \begin{pmatrix} \chi_P \\ \chi_M \end{pmatrix} \tag{1.16}$$

where  $\chi$  represent two-component spinors. Using 1.16 the Dirac equation in (1.15) can again be rewritten as

$$\begin{aligned} i\hbar \left[ \frac{1}{c} \frac{\partial}{\partial t} + \boldsymbol{\sigma} \cdot \boldsymbol{\nabla} \right] \chi_P &= -mc\chi_M, \\ i\hbar \left[ \frac{1}{c} \frac{\partial}{\partial t} - \boldsymbol{\sigma} \cdot \boldsymbol{\nabla} \right] \chi_M &= -mc\chi_P, \end{aligned} \tag{1.17}$$

where

$$\boldsymbol{\sigma} \cdot \boldsymbol{\nabla} = \sigma_x \frac{\partial}{\partial x} + \sigma_y \frac{\partial}{\partial y} + \sigma_z \frac{\partial}{\partial z}. \tag{1.18}$$

In the limiting case of vanishing mass ( $m \rightarrow 0$ ), as is in the SM, the free particle field equations in (1.17) decouple into

$$\begin{aligned} \left( \frac{E}{c} + \boldsymbol{\sigma} \cdot \boldsymbol{P} \right) \chi_P &= 0, \\ \left( \frac{E}{c} - \boldsymbol{\sigma} \cdot \boldsymbol{P} \right) \chi_M &= 0, \end{aligned} \tag{1.19}$$

where the differential operators have been evaluated as the particle's energy  $E$  and momentum three-vector  $\boldsymbol{P}$ . For massless neutrinos,  $\chi_P$  and hence  $\psi_P$ , describe particles of negative energy  $E = -|\boldsymbol{P}|c$  which in the context of quantum field theory are interpreted as antiparticles traveling backwards in time. Conversely,  $\psi_M$  have positive energy  $E = |\boldsymbol{P}|c$  and which means they are particles traveling forward in time.

If one also multiplies (1.15) by  $\gamma^5 \gamma^0$  and using the fact that the spin operator  $\boldsymbol{\sigma}$  is

---


$$\boldsymbol{\sigma} = i(\gamma^2\gamma^3, \gamma^3\gamma^1, \gamma^1\gamma^2) = \gamma^0\gamma^k\gamma^5 \quad (k = 1, 2, 3) \quad (1.20)$$

each decoupled equation becomes

$$\frac{\boldsymbol{\sigma} \cdot \mathbf{P}}{|\mathbf{P}|}\psi_{P,M} = \gamma^5\psi_{P,M} = \pm\psi_{P,M}, \quad (1.21)$$

where one recognizes that helicity and chiral states are the same for  $m \rightarrow 0$  only. Thus the labels  $M$  and  $P$  actually are identical to the LH and RH helicity labels, respectively. Using the results on helicity from before, a neutrino is always observed as a LH particle while the anti-neutrino is always observed as a RH antiparticle.

The observation of only LH neutrinos and RH anti-neutrinos is an important feature in the SM. However, since neutrinos are known to have mass from oscillations, it is theoretically possible to observe a RH neutrino and LH anti-neutrino. That would require boosting to a highly relativistic reference frame with respect to the laboratory.

## Neutrino Scattering with Matter

Charged current (CC) neutrino interactions on nuclear particles are the interactions used in this thesis. These interactions produce an outgoing charged lepton and a variety of hadronic states. While interactions with valence electrons is possible, they are far less common in large, subatomic particle detectors. However, the physics of neutrino-electron scattering is very similar to neutrino-nucleus scattering.

Consider neutrino-electron scattering, the cross section for  $\nu_e + e^-$  is given by

$$\frac{d\sigma}{d\Omega} = \left(\frac{G\hbar c}{2\pi}\right)^2 s, \quad (1.22)$$

where  $G$  is the Fermi constant and  $s$  is the center of mass energy squared. Due to the V-A nature of the Weak force, neutrinos couple to LH particles and RH antiparticles. The outgoing particles are isotropically distributed in the center-of-mass frame since the initial

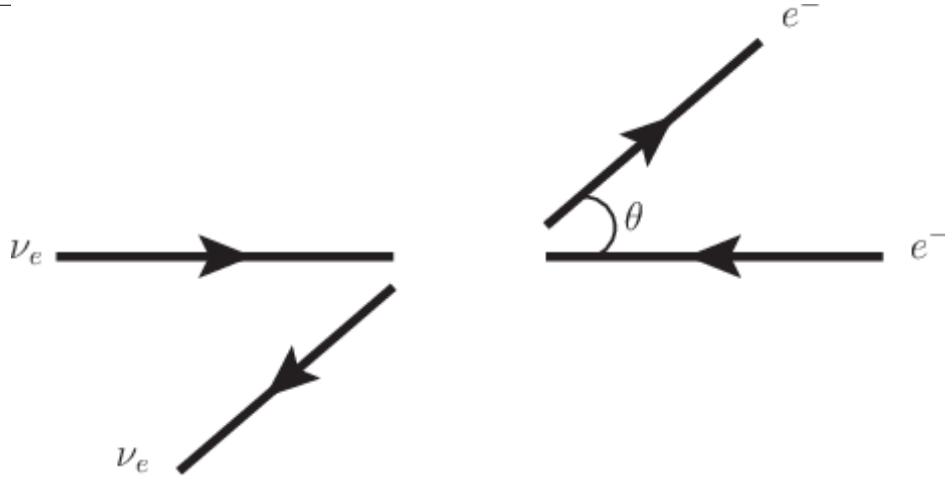


**Figure 1.4:** The definition of  $\theta$  in  $\nu_e + e^-$  (shown) and  $\bar{\nu}_e + e^-$  (not shown) scattering.

and final spin state of the system is  $J = 0$ . Compare (1.22) with the cross section for  $\bar{\nu}_e + e^-$

$$\frac{d\sigma}{d\Omega} = \left( \frac{G\hbar c}{4\pi} \right)^2 (1 - \cos \theta)^2 s, \quad (1.23)$$

where  $\theta$  is the observed scattering angle of the electron as shown in Figure 1.4 on page 12. Since the total spin of the  $\bar{\nu}_e + e^-$  system is  $J = 1$  with z-projection  $J_z = 1$ , the antineutrino is preferentially forward scattered. Integrating over all angles, the cross sections are related to each other as

$$\sigma(\bar{\nu}_e + e^-) = \frac{1}{3} \sigma(\nu_e + e^-).$$

The factor  $1/3$  arises from the fact that angular momentum conservation forbids the  $J_z = -1$  and  $0$  states for  $\bar{\nu}_e + e^-$  scattering. The same  $1/3$  factor arises between  $\nu_\mu + d \rightarrow \mu^- + u$  and  $\bar{\nu}_\mu + u \rightarrow \mu^+ + d$  scattering.

In neutrino-nuclear scattering, the simple picture of free quarks must be replaced with the reality of the nuclear medium. Interactions with a single quark are still possible, but nuclear effects can alter the products of the interactions. The kinematics of the particles involved can be altered as well as the existence of a particle can be changed depending on the point of interaction. Distinctions must be made in neutrino physics between point-like

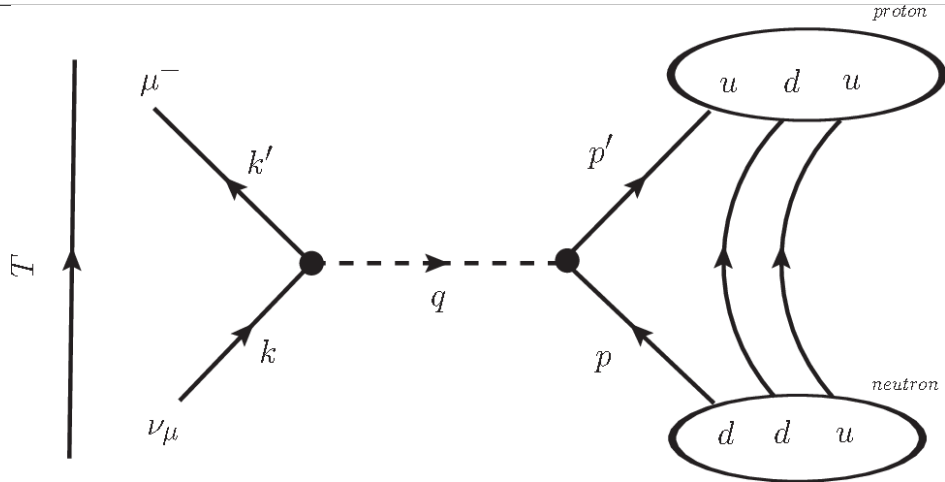


**Figure 1.5:** A  $\nu_\mu$ -induced CCQE interaction.

interactions ( $\nu_e + e^-$ ) and post “final state interactions” (FSI) are what is actually observable in an experiment.

Neutrino-nuclear scattering presented in this thesis come in three primary CC varieties: quasi-elastic (CCQE), deep inelastic scattering (CC-DIS), and single pion production (CC- $1\pi$ ). The  $\nu_\mu$  CCQE interaction refers to the process where an incoming neutrino and neutron (udd) scatter to produce a charged lepton and proton (uud) as shown in Figure 1.5 on page 13. For  $\bar{\nu}_\mu$  CCQE, the proton is converted to a neutron instead. The CCQE interaction is the lowest energy CC interaction with a nucleon and is thought of classically to have approximate mass conservation between the proton-neutron states ( $\Delta m = 1.29 \text{ MeV}/c^2$ ). While CCQE models work well to predict the neutrino energy for low-Z atoms like hydrogen, they do not extend well into many nucleon atoms due to similar observable final state nucleons. The CC-DIS interaction, also called CC Other, is a high energy transfer process that shatters the nucleus apart which has the observation of many post-FSI hadrons. Modeling CCDIS can be challenging due to FSI and the uncertainty of the possible initial states of the nucleus. Finally, CC- $1\pi$  interactions refer to processes where a post-FSI charged pion is experimentally observed presumably from the decay of resonance state like the  $\Delta(1232)$  baryon. These interactions are not well understood currently since they occur in the transition between CCQE and CCDIS interaction modes.

---

### 1.1.2 Neutrino Oscillations

Neutrino oscillations are the observation of a neutrino produced with a particular, definite flavor and later observed as a different flavor. This phenomenon was first observed as a deficit of neutrinos for a number of atmospheric and solar neutrino experiments. The deficit also seemed more pronounced for atmospheric neutrinos as the distance from their source increased. For neutrino oscillations to occur, at least one neutrino must be massive. This observation firmly established that the SM is wrong with its assumption of massless neutrinos.

The first indication of neutrino oscillations was from the Ray Davis Homestake Mine experiment [24] which began in the 1960s. Ray Davis was an expert chemist and designed a radiochemical experiment to measure the flux of neutrinos from Sun. The purpose of this experiment was to test John Bahcall's prediction of the fusion rate in the Sun and neutrino flux from it as well. Davis' experiment would need to operate for many years to collect enough statistics due to expected low capture rate. Measurements continued into the 1980s and showed that the flux of neutrinos as measured at Homestake and this was about  $\frac{1}{3}$  the expected rate and this became known as the "Solar Neutrino Problem." The primary solutions were either the solar model was incorrect or the neutrino capture cross section was incorrect. The Sudbury Neutrino Observatory (SNO) was able to resolve this problem by making a model-independent measurement of the solar neutrino flux. SNO observed a  $\nu_e$  CC-to-NC ratio of  $0.301 \pm 0.033$ , which confirmed that only about 30% of neutrinos arrive as  $\nu_e$  flavors on Earth. In other words, the majority of neutrinos arrive as the wrong flavor [68].

Another outstanding problem emerged with measurements of atmospheric neutrinos, in particular muon and electron types. Atmospheric neutrinos are produced when high energy cosmic rays strike atmospheric particles. These cosmic ray collisions generate mostly pions and kaons that decay into neutrinos. When trying to measure the  $\nu_\mu/\nu_e$  ratio and comparing that with expected ratio, there was another significant deficit. This was particularly a problem as a function of the zenith angle for the Super-Kamiokande (SK) experiment. SK is

---

a 50kt tank of pure water lined with thousands of photomultiplier tubes designed to observe solar and atmospheric neutrinos. It was the first experiment to perform a neutrino oscillation analysis that successfully explained the deficit.

The observation of neutrino oscillations is relatively new, or about three decades old. Bruno Pontecorvo [50] first proposed such a mechanism in 1957 between neutrinos and antineutrinos much like known neutral K-mesons oscillations. However, oscillations between flavored neutrinos was not expected since it requires the neutrino to have mass. The reasons why are explained in the next subsection.

## Two Flavor Derivation

The phenomenon of neutrino oscillations can be described with elementary, non-relativistic Quantum Mechanics. Beginning with the Schrödinger Equation in (1.24)

$$-\frac{\hbar}{i} \frac{d}{dt} |\nu(\mathbf{r}, t)\rangle = \hat{H} |\nu(\mathbf{r}, t)\rangle, \quad (1.24)$$

where  $\hat{H}$  is the Hamiltonian for the physical system, one considers a massive neutrino of mass  $m_j$  in its rest frame (free particle). The Hamiltonian is diagonal in this case, which acting on  $|\nu_j\rangle$  results in the eigenvalue equation

$$\hat{H} |\nu_j(\mathbf{r}, t)\rangle = E_j |\nu_j(\mathbf{r}, t)\rangle, \quad (1.25)$$

where  $E_j$  is the energy of the neutrino  $|\nu_j\rangle$ . Substituting (1.25) into (1.24) and solving for  $|\nu(\mathbf{r}, t)\rangle$ , one obtains the following

$$|\nu_j(\mathbf{r}, t)\rangle = e^{-iE_j t/\hbar} |\nu_j(\mathbf{r}, t=0)\rangle, \quad (1.26)$$

where  $|\nu_j(\mathbf{r}, t=0)\rangle$  is created with momentum  $\mathbf{p}$  at the origin  $\mathbf{r} = 0$ . The time-independent solution to (1.24) is a plane-wave given by

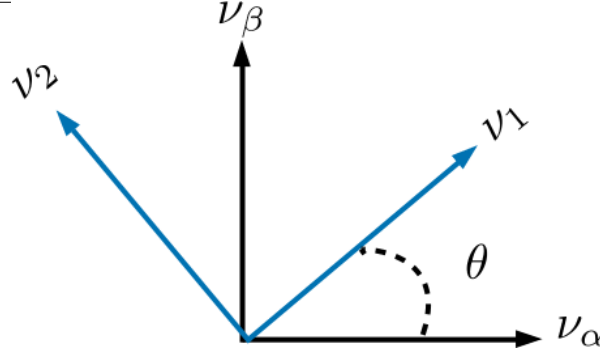


**Figure 1.6:** The depiction of two neutrino flavor change of basis using a rotation matrix. Compare this with (1.29).

$$|\nu_j(\mathbf{r}, t = 0)\rangle = e^{i\mathbf{p} \cdot \mathbf{r}/\hbar} |\nu_j\rangle. \quad (1.27)$$

Before being able to describe neutrino oscillations, the basis states must be defined. For this example, consider that there are only two eigenstates, labeled  $\nu_1$  and  $\nu_2$ , in the “mass” basis with definite mass  $m_1$  and  $m_2$ , respectively. However, experiments can produce neutrinos, as well as probe them, only in a definite flavor state, denoted by a Greek letter subscript  $\lambda$ . Let the generated neutrino, which is a linear superposition of mass states 1 and 2, have momentum  $\mathbf{p}$  and flavor  $\alpha$ . Since both mass eigenstates share the same momentum  $\mathbf{p}$  (but not energy!), the exponential term in (1.27) is an overall phase that will cancel out later. One can postulate a linear transformation,  $U$ , between the basis states given by (1.28).

$$\begin{bmatrix} \nu_\alpha \\ \nu_\beta \end{bmatrix} = \begin{bmatrix} U_{11} & U_{12} \\ U_{21} & U_{22} \end{bmatrix} \begin{bmatrix} \nu_1 \\ \nu_2 \end{bmatrix} \quad (1.28)$$

This linear transformation must be a unitary matrix ( $U^{-1} = U^\dagger$ ,  $\dagger$  = transpose conjugate) since the states  $\nu_{1,2}$  constitute a complete orthonormal basis in the mass basis. With this unitary property,  $U$  can be written as a rotation matrix

---


$$\begin{bmatrix} \nu_\alpha \\ \nu_\beta \end{bmatrix} = \begin{bmatrix} \cos(\theta) & \sin(\theta) \\ -\sin(\theta) & \cos(\theta) \end{bmatrix} \begin{bmatrix} \nu_1 \\ \nu_2 \end{bmatrix}, \quad (1.29)$$

where  $\theta$  is the angle between the two bases. One can imagine this transformation between bases as shown in Figure 1.6 on page 16. Creating a neutrino of flavor  $\alpha$  and observing it after a time  $t = T > 0$ , the probability of observing it as flavor  $\beta \neq \alpha$  is given by

$$\begin{aligned} \mathcal{P}(\nu_\alpha \rightarrow \nu_\beta) &= |\langle \nu_\alpha(t=0) | \nu_\beta(t=T) \rangle|^2 \\ &= |\{\cos(\theta) \langle \nu_1(t=0) | + \sin(\theta) \langle \nu_2(t=0) |\} \\ &\quad \times \{-\sin(\theta) |\nu_1(t=T)\rangle + \cos(\theta) |\nu_2(t=T)\rangle\}|^2. \end{aligned} \quad (1.30)$$

Evaluating all inner products and simplifying terms in (1.30) results in (1.31) below.

$$\mathcal{P}(\nu_\alpha \rightarrow \nu_\beta) = \sin^2(2\theta) \sin^2\left(\frac{E_1 - E_2}{2\hbar}T\right) \quad (1.31)$$

The terminology of “neutrino oscillations” should be more apparent now since (1.31) demonstrates that the probability changes sinusoidally as a function of time  $T$ . This equation is not, however, terribly useful in the laboratory frame since it is hard to design an experiment where the travel time an individual neutrino is actually measured. Instead, one can make useful approximations that are accessible in the laboratory frame. Since neutrinos are nearly massless, they travel very close to the speed of light. Therefore time  $T$  is replaced with  $L/c$  where  $L$  is the distance between the neutrino origin and detection and  $c$  is now the speed of light in vacuum. One can also approximate the energy of the mass eigenstate as

$$\begin{aligned} E_j &= (m_j^2 c^4 + p_j^2 c^2)^{\frac{1}{2}} = p_j c \left(1 + \frac{m_j^2 c^2}{p_j^2}\right)^{\frac{1}{2}} \\ &\approx p_j c \left(1 + \frac{m_j^2 c^2}{2p_j^2} + \mathcal{O}\left(\frac{m_j c}{p_j}\right)^4\right) \\ &\approx E_\nu + \frac{m_j^2 c^4}{2E_\nu}, \end{aligned} \quad (1.32)$$

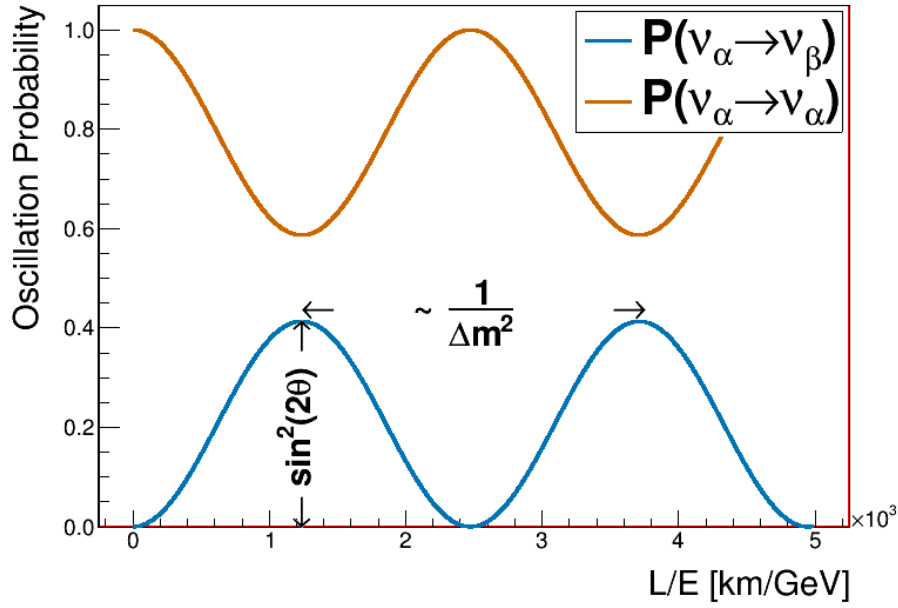


**Figure 1.7:** Two flavor oscillation probability as a function  $L/E$  is shown using  $\theta = 20^\circ$  and  $\Delta m^2 = 10^{-3} \text{ eV}^2/c^4$ . The spacing between adjacent peaks/troughs is proportional to the inverse of  $\Delta m^2$ . Note that  $\mathcal{P}(\nu_\alpha \rightarrow \nu_\alpha) = 1 - \mathcal{P}(\nu_\alpha \rightarrow \nu_\beta)$  since the oscillation probability must always sum to 1.

where for oscillation experiments  $p_j \gg m_j c$  and  $p_j c \approx E_\nu$  where  $E_\nu$  is the neutrino energy as measured in the laboratory. Substituting these assumptions in (1.31), the oscillation probability is given by

$$\mathcal{P}(\nu_\alpha \rightarrow \nu_\beta) = \sin^2(2\theta) \sin^2 \left( \frac{\Delta m^2 c^3}{4\hbar} \frac{L}{E_\nu} \right), \quad (1.33)$$

where  $\Delta m^2 = m_2^2 - m_1^2$  is the mass-squared difference between the mass states. For a momentum consider evaluating all the physical constants in natural units ( $c = \hbar = 1$ ). An appropriate choice of units for  $\Delta m^2$ ,  $L$ , and  $E_\nu$  results in

$$\mathcal{P}(\nu_\alpha \rightarrow \nu_\beta) = \sin^2(2\theta) \sin^2 \left( 1.27 \frac{\Delta m^2}{[\text{eV}^2]} \frac{L/E_\nu}{[\text{km}/\text{GeV}]} \right) \text{ [natural units]} \quad (1.34)$$

which more clearly demonstrates the Physics in neutrino oscillations. The oscillation probability has an amplitude of  $\sin^2(2\theta)$  and varies with frequency inversely proportional to  $\Delta m^2$

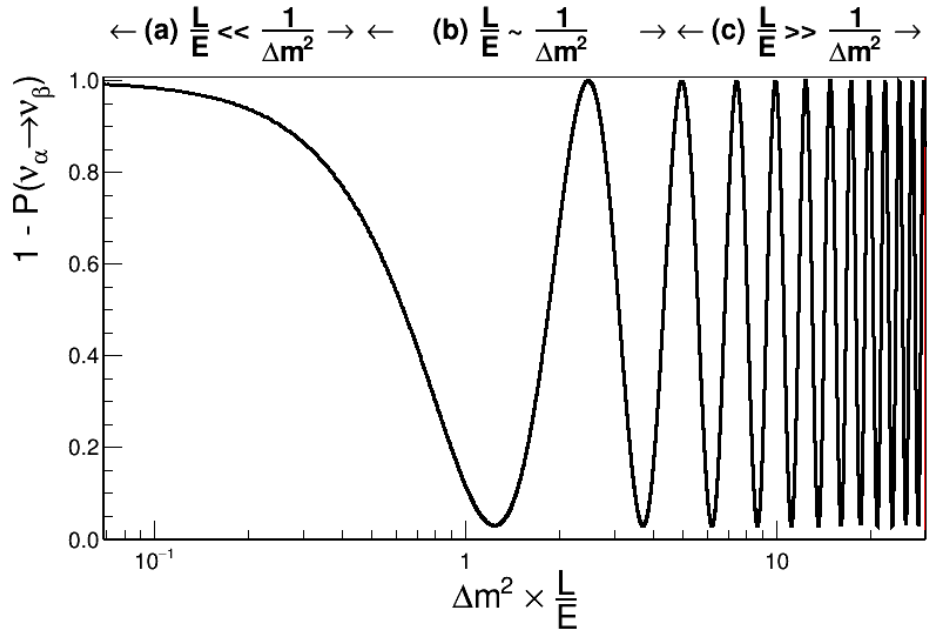


**Figure 1.8:** Logarithmic plot of the survival probability of flavor  $\alpha$  ( $1 - \mathcal{P}(\nu_\alpha \rightarrow \nu_\beta) = \mathcal{P}(\nu_\alpha \rightarrow \nu_\alpha)$ ) over a wide range of  $L/E$  values for  $\theta = 40^\circ$ . The arrows above the plot very roughly denote three possible cases: (a) no oscillations ( $L/E \ll 1/\Delta m^2$ ); (b) sensitivity to oscillations ( $L/E \sim 1/\Delta m^2$ ); (c) only average measurement ( $L/E \gg 1/\Delta m^2$ ). Image originally inspired by [59].

as illustrated in Figure 1.7 on page 18. Since  $L$  and  $E_\nu$  are the only controllable parameters for an oscillation experiment, probing  $\theta$  or  $\Delta m^2$  can be difficult unless the experiment can probe a large range of  $L/E_\nu$  as shown in Figure 1.8 on page 19.

### Three Flavor Oscillations

In the general case of oscillations using a  $n \times n$  mixing matrix, the unitary transformation can be written as a rotation matrix with  $\frac{n}{2}(n-1)$  weak mixing angles with  $\frac{1}{2}(n-2)(n-1)$  Charge-Parity (CP) violating phases. In addition, oscillations are dictated by a total of  $n-1$  mass-squared splittings [68]. This all assumes that neutrinos obey the Dirac Equation, or that they are not their own antiparticles. The favored mixing model is the  $3 \times 3$  matrix since there are three known neutrino flavors,  $\nu_e$ ,  $\nu_\mu$ , and  $\nu_\tau$ . This means that there are three (3) mixing angles, one (1) CP violating phase, and three (3) mass-squared splittings.

Source	Species	Baseline [km]	Mean Energy [GeV]	$\min(\Delta m^2)$ [eV <sup>2</sup> ]
Reactor	$\bar{\nu}_e$	1	$\sim 10^{-3}$	$\sim 10^{-3}$
Reactor	$\bar{\nu}_e$	100	$\sim 10^{-3}$	$\sim 10^{-5}$
Accelerator	$\nu_\mu, \bar{\nu}_\mu$	1	$\sim 1$	$\sim 1$
Accelerator	$\nu_\mu, \bar{\nu}_\mu$	$10^3$	$\sim 1$	$\sim 10^{-3}$
Atmospheric $\nu$ 's	$\nu_{e,\mu}, \bar{\nu}_{\mu,e}$	$10^4$	$\sim 1$	$\sim 10^{-4}$
Sun	$\nu_e$	$1.5 \times 10^8$	$\sim 10^{-3}$	$\sim 10^{-11}$

**Table 1.1:** Sensitivity of different oscillation experiments originally published in [62].

The most frequently used matrix parameterization is the MNSP (MNSP: Maki-Nakagawa-Sakata-Pontecorvo) matrix. Pontecorvo is accredited for first conceiving of neutrino oscillations, albeit between neutrino and anti-neutrinos [49]. It was Maki, Nakagawa, and Sakata who conceived of the parameterization based off the ideas of Pontecorvo [45]. The MNSP matrix is decomposed into separate rotation matrices as given by (1.35)

$$U_{\text{MNSP}} = \underbrace{\begin{bmatrix} 1 & 0 & 0 \\ 0 & c_{32} & s_{32} \\ 0 & -s_{32} & c_{32} \end{bmatrix}}_{U_{32}=U_{\text{atm}}} \times \underbrace{\begin{bmatrix} c_{31} & 0 & s_{31}e^{i\delta_{\text{CP}}} \\ 0 & 1 & 0 \\ -s_{31}e^{-i\delta_{\text{CP}}} & 0 & c_{31} \end{bmatrix}}_{U_{31}=U_{\text{rea}}} \times \underbrace{\begin{bmatrix} c_{21} & s_{21} & 0 \\ -s_{21} & c_{21} & 0 \\ 0 & 0 & 1 \end{bmatrix}}_{U_{21}=U_{\text{sol}}}, \quad (1.35)$$

where

$$c_{ij} = \cos \theta_{ij}, \quad s_{ij} = \sin \theta_{ij}, \quad (1.36)$$

and  $\delta_{\text{CP}}$  represents the CP violating phase. Each rotation matrix  $U_{ij}$  represents the different sources for neutrino oscillations experiments with “atm”, “rea”, and “sol” representing atmospheric  $\nu$ 's, nuclear reactor  $\nu$ 's, and Solar  $\nu$ 's, respectively. The sensitivity of neutrino oscillations for different sources is given in Table 1.1 on page 20.

If neutrinos are their own antiparticles, like the photon, they do not follow the Dirac Equation but do follow the Majorana Equation. This adds two (in general  $n - 1$ ) more CP violating Majorana phases,  $\alpha$  and  $\beta$ , to the MNSP matrix

$$U_{\text{MNSP}} \rightarrow U_{\text{MNSP}} \times \overbrace{\begin{bmatrix} 1 & 0 & 0 \\ 0 & e^{i\alpha} & 0 \\ 0 & 0 & e^{i\beta} \end{bmatrix}}^{\text{U}_{\text{Majorana}}}. \quad (1.37)$$

Unfortunately, neutrino oscillations are not able to probe the Majorana phases since the Majorana matrix is diagonal. The question of if neutrinos are Majorana ( $\nu = \bar{\nu}$ ) or Dirac ( $\nu \neq \bar{\nu}$ ) particles is an open question and is being explored by neutrinoless double beta decay experiments [58].

The full three flavor oscillation probability is given by

$$\begin{aligned} \mathcal{P}(\nu_\alpha \rightarrow \nu_\beta) = & \delta_{\alpha\beta} - 4 \sum_{j=1}^3 \left[ \sum_{i>j}^3 \text{Re}(K_{\alpha\beta,ij}) \sin^2(\phi_{ij}) \right] \\ & + 4 \sum_{j=1}^3 \left[ \sum_{i>j}^3 \text{Im}(K_{\alpha\beta,ij}) \sin(\phi_{ij}) \cos(\phi_{ij}) \right] \end{aligned} \quad (1.38)$$

where

$$K_{\alpha\beta,ij} = U_{\alpha i} U_{\beta i}^* U_{\alpha j}^* U_{\beta j} \quad (1.39)$$

encapsulates the MNSP matrix elements and

$$\phi_{ij} = \frac{\Delta m_{ij}^2 c^3}{4\hbar} \frac{L}{E_\nu}. \quad (1.40)$$

Since CP violation means that  $\mathcal{P}(\nu_\alpha \rightarrow \nu_{\beta \neq \alpha}) \neq \mathcal{P}(\bar{\nu}_\alpha \rightarrow \bar{\nu}_{\beta \neq \alpha})$ , CP violating terms must be an odd function of  $\delta_{\text{CP}}$ . Consider the following examples, muon neutrino survival and muon neutrino to electron neutrino appearance.

**Muon Neutrino Survival** The probability of a muon type neutrinos surviving is given by

$$\begin{aligned}\mathcal{P} \left( {}^{(-)}\bar{\nu}_\mu \rightarrow {}^{(-)}\nu_\mu \right) = & 1 - 4s_{23}^2 c_{13}^2 \left( V_{\cos \delta_{\text{CP}}} \right) \sin^2 \phi_{31} \\ & - 4s_{23}^2 c_{13}^2 \left( Z_{\cos \delta_{\text{CP}}} \right) \sin^2 \phi_{32} \\ & - 4 \left( V_{\cos \delta_{\text{CP}}} \right) \left( Z_{\cos \delta_{\text{CP}}} \right) \sin^2 \phi_{21}\end{aligned}\quad (1.41)$$

where

$$V_{\cos \delta_{\text{CP}}} = s_{12}^2 c_{23}^2 + s_{13}^2 s_{23}^2 c_{12}^2 + 2s_{12}s_{13}s_{23}c_{12}c_{23} \cos \delta_{\text{CP}} \quad (1.42)$$

$$Z_{\cos \delta_{\text{CP}}} = c_{12}^2 c_{23}^2 + s_{13}^2 s_{23}^2 s_{12}^2 - 2s_{12}s_{13}s_{23}c_{12}c_{23} \cos \delta_{\text{CP}} \quad (1.43)$$

and  ${}^{(-)}\nu_\mu$  represents either  $\nu_\mu$  or  $\bar{\nu}_\mu$ . If a definitive measurement of  $\mathcal{P} \left( \nu_\mu \rightarrow \nu_\mu \right) \neq \mathcal{P} \left( \bar{\nu}_\mu \rightarrow \bar{\nu}_\mu \right)$  in vacuum occurs, this implies that the combined C, P and time (CPT) symmetry is violated<sup>4</sup>.

**Electron Neutrino Appearance** The previous subsection briefly explored the muon disappearance probability, which is not tested as a channel for CP violation. Electron neutrino appearance, however, does provide insight into CP violation in the lepton sector. The appearance probability of electron neutrinos types from muon types is given by

$$\begin{aligned}\mathcal{P} \left( {}^{(-)}\bar{\nu}_\mu \rightarrow {}^{(-)}\nu_e \right) = & 4c_{13}^2 s_{13}^2 s_{23}^2 \sin^2 \phi_{31} \\ & + 8 \left( X_{\cos \delta_{\text{CP}}} \right) \cos \phi_{23} \sin \phi_{31} \sin \phi_{21} \\ & - 8 \underbrace{\left( Y_{\sin \delta_{\text{CP}}} \right)}_{\text{CP violating}}^{(+)} \sin \phi_{32} \sin \phi_{31} \sin \phi_{21} \\ & + 4 \left( Z_{\cos \delta_{\text{CP}}} \right) s_{12}^2 c_{13}^2 \sin^2 \phi_{21}\end{aligned}\quad (1.44)$$

where

$$X_{\cos \delta_{\text{CP}}} = c_{13}^2 s_{12} s_{13} s_{23} (c_{12} c_{23} \cos \delta_{\text{CP}} - s_{12} s_{13}) \quad (1.45)$$

$$Y_{\sin \delta_{\text{CP}}} = \frac{1}{8} \sin(2\theta_{12}) \sin(2\theta_{13}) \sin(2\theta_{23}) c_{13} \sin \delta_{\text{CP}} \quad (1.46)$$

---

<sup>4</sup>When going to through matter however, the oscillation probability is affected. This is explained more in Section 1.1.2.

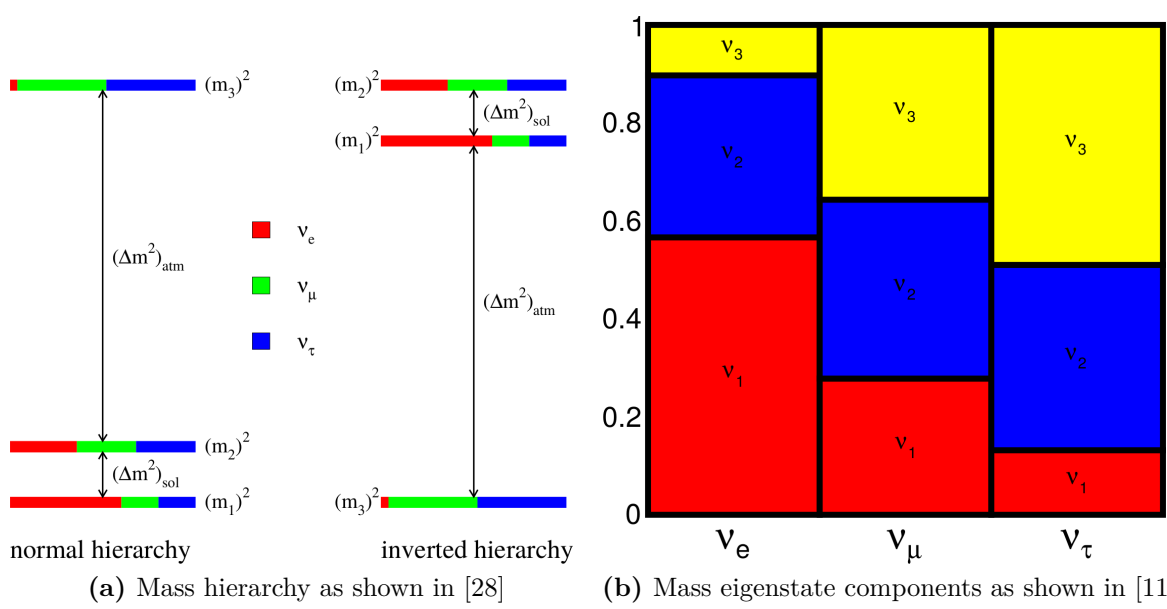


**Figure 1.9:** Left: the mass hierarchy problem is such that while the solar and atmospheric mixing mass-squared differences are clearly defined, the absolute mass scale is unknown. Since  $m_2 > m_1$  by definition, it is currently unknown if  $m_3$  is more or less massive than  $m_2$ , or even massless! Notice the colored bars for each mass eigenstate which corresponded to the approximate flavor content of the neutrino. For example, state “2” has about equal three portions of all three flavors. Right: the mass eigenstate components of each flavor eigenstate. This is a complementary demonstration of the MNSP matrix.

and (+) represents the sign change from neutrinos to anti-neutrinos. The CP violating term (1.46) is also known as the Jarlskog Invariant and is a measure of CP violation independent of the mixing parameterization [41]. This oscillation channel are of primary importance in current and future proposed accelerator and atmospheric neutrino oscillation experiments.

Current and next generation experiments aim to improve knowledge of the mixing parameters. There are a couple of degeneracies to unravel as well as precise measurement of  $\delta_{\text{CP}}$ . While the two defined mass-squared splittings  $\Delta m_{21}^2 = \Delta m_{\text{sol}}^2$  and  $\Delta m_{32}^2 = \Delta m_{\text{atm}}^2$  are known, it is unknown which eigenstates are more massive. This problem is known as the mass hierarchy problem and is illustrated in Figure 1.9a on page 23. Normal hierarchy refers to the case where  $m_3 > m_2 > m_1$  whereas the inverted hierarchy has  $m_2 > m_1 > m_3$ . Also knowledge if  $\theta_{23}$  is in the first octant  $\theta \in (0, \pi/2)$  or second octant  $\theta \in (\pi/2, \pi/4)$  requires large statistics. Finally the value of  $\delta_{\text{CP}}$  is quite uncertain with values in the 3rd and 4th

Parameter	Normal Hierarchy value	Inverted Hierarchy value	Units
$\Delta m_{32}^2 = \Delta m_{\text{atm}}^2$	$2.51 \pm 0.05$	$-2.56 \pm 0.04$	$10^{-3}$ eV <sup>2</sup>
$\Delta m_{21}^2 = \Delta m_{\text{sol}}^2$	$7.53 \pm 0.18$		$10^{-5}$ eV <sup>2</sup>
$\sin^2(\theta_{21}) = \sin^2(\theta_{\text{sol}})$	$0.307^{+0.013}_{-0.012}$		1
$\sin^2(\theta_{32}) = \sin^2(\theta_{\text{atm}})$	O1: $0.417^{+0.025}_{-0.028}$ O2: $0.597^{+0.024}_{-0.030}$	O1: $0.421^{+0.033}_{-0.025}$ O2: $0.592^{+0.023}_{-0.030}$	1
$\sin^2(\theta_{31})$	$2.12 \pm 0.08$		$10^{-2}$
$\delta_{\text{CP}}$	$217^{+40}_{-28}$	$280^{+25}_{-28}$	degrees

**Table 1.2:** Table of best fit MNSP parameters split by normal and inverted hierarchy. O1 and O2 correspond to the first octant ( $\theta \in (0, \pi/2)$ ) or second octant ( $\theta \in (\pi/2, \pi/4)$ ). All values except for  $\delta_{\text{CP}}$  are combined values from the Particle Data Group and  $\delta_{\text{CP}}$  is from the 2018 NuFit analysis [29, 62].

quadrants. Best fit measurements of the oscillations parameters is given in Table 1.2 on page 24.

### Matter Effects

Traveling through matter has the potential to increase the sensitivity of oscillation measurements if the baseline is long enough. Known as the Mikheyev-Smirnov-Wolfenstein (MSW) effect [65], all oscillations are affected by coherent forward scattering of neutrinos with electrons in the media. Taking the example of  $(\bar{\nu}_\mu \rightarrow \bar{\nu}_e)$  from (1.41), the MSW effect to first order is

$$\begin{aligned} \mathcal{P}((\bar{\nu}_\mu \rightarrow \bar{\nu}_e)) \rightarrow & \mathcal{P}((\bar{\nu}_\mu \rightarrow \bar{\nu}_e)) + \frac{8\alpha}{\Delta m_{31}^2} (c_{13}^2 s_{13}^2 s_{23}^2) (1 - 2s_{13}^2) \\ & \times \left( \sin^2 \phi_{31} \underbrace{- \left( \frac{\Delta m_{31}^2 c^3}{4\hbar} \frac{L}{E_\nu} \right)}_{\phi_{31}} \cos \phi_{32} \sin \phi_{31} \right), \end{aligned} \quad (1.47)$$

---

where

$$\alpha = 2\sqrt{2}G_F n_e E_\nu \quad (1.48)$$

and  $G_F$  is the Fermi constant and  $n_e$  is the average electron density of the Earth which the neutrinos travel [13]. Carefully studying (1.47) reveals that the MSW effect alters the oscillation probability as a function of the electron density and increases in magnitude with baseline.

### 1.1.3 CP Violation: Origins of Matter

To conclude the introduction on neutrinos, it is important to examine the implications of CP violation. The observation of CP violation in the lepton sector might provide critical insight into the origins of the matter. CP violation dictates that certain interactions behave differently between matter or antimatter like  $\mathcal{P}(\nu_\mu \rightarrow \nu_e) \neq \mathcal{P}(\bar{\nu}_\mu \rightarrow \bar{\nu}_e)$ . The Big Bang Theory suggests that in the first fractions of a second of the Universe, equal amounts of matter and antimatter were created. However, observational evidence shows the Universe consists of only 4.5% baryonic matter (i.e. protons and neutrons) from cosmological models as shown in Figure 1.10 on page 26. The anti-baryonic fraction of the baryonic matter is infinitesimally low from external constraints on data from gamma-ray telescopes like Fermi-GLAST [63]. This problem is known as the Baryon Asymmetry of the Universe (BAU).

The process of Baryogenesis<sup>5</sup> is a favored model to explain the BAU and lacks a necessary precursor mechanism. One of the necessary conditions for Baryogenesis [56] is C symmetry violation and CP violation. Evidence of CP violation has been experimentally confirmed in the quarks, but not to the level which resolves the BAU. Baryogenesis can be achieved by having Leptogenesis<sup>6</sup> occur first through the decay of very heavy, right handed Majorana

---

<sup>5</sup>Baryogenesis is the mechanism by which matter and antimatter baryons are created in the early Universe.

<sup>6</sup>Leptogenesis is the mechanism by which leptons and anti-leptons are created in the early Universe.

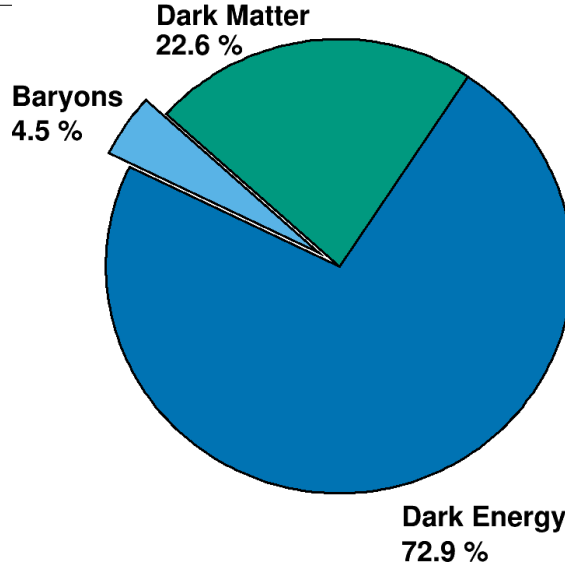


**Figure 1.10:** Display of the matter and energy content of the Universe. The observed content is 4.5% of baryonic matter. The rest of the Universe consists of non-baryonic matter called Dark Matter and a form of energy called Dark Energy. These inferred parameters are taken from the  $\Lambda$ CDM model, the simplest model that describes the cosmos [43].

neutrino ( $\nu = \bar{\nu}$ ) through the *see-saw* mechanism. Detailed discussions on Leptogenesis and the *see-saw* mechanism can be found in [11].

## 1.2 Tokai to- amioka Experiment

The Tokai to Kamioka (T2K) experiment is a long baseline, neutrino oscillation experiment hosted in Japan [1] as shown in Figure 1.11 on page 27. It is the successor experiment to the KEK-to-Kamioka neutrino oscillation experiment also hosted in Japan. T2K produces its high intensity, relatively pure muon neutrino beam at the Japan Proton Accelerator Complex (J-PARC), a world class particle accelerator facility. The beam is directed at the Super-Kamiokande (SK) [33] detector which is 295 km away from the source. Along the beamline at 280m from the beam source are a series of near detectors called ND280 [31] to observe and characterize the unoscillated beam. This thesis uses data from ND280 detector to test for increased sensitivity to beam characterization. The beam is designed to maximize the  $\nu_\mu \rightarrow \nu_e$  probability at the  $L = 295$  km baseline using a neutrino energy spectrum sharply



**Figure 1.11:** Birds eye view of the T2K experiment on the Japanese archipelago. An intense beam of neutrinos are produced at the J-PARC site (bottom right red box) using high energy protons. The beam is directed towards the Super-Kamiokande detector (top left blue box) at a distance of 295 km away from J-PARC.

peaked at  $E_\nu = 0.6$  GeV as shown in Figure 1.12 on page 28. This spectrum is achieved by directing the center of the beam axis 2.5 degrees off center from SK.

T2K was primarily designed to measure the last unknown MNSP mixing angle  $\theta_{13}$ , which was thought to be nearly zero. In addition it set out to measure to high precision the atmospheric mixing parameters,  $\theta_{23}$  and  $\Delta m_{23}^2$ . One of its early successes was a landmark  $7.3\sigma$  measurement of a non-zero  $\theta_{13}$  using the electron-neutrino appearance measurement [3]. It continues to be a world leader in oscillation physics and as of 2018 rejects CP conserving values ( $\delta_{\text{CP}} = 0, \pi$ ) at the  $2\sigma$  level [8].

The following topics will be discussed in the following order. First a look how neutrinos are produced at J-PARC. Next a detailed look at the T2K near detectors which are used in this thesis. This is followed by a discussion on Super-Kamiokande, the T2K far detector.

### 1.2.1 Neutrino Production at J-PARC

To facilitate the high intensity neutrino beam requirements for T2K, the J-PARC site generates a high intensity proton beam through a series of particle accelerators. A bird's

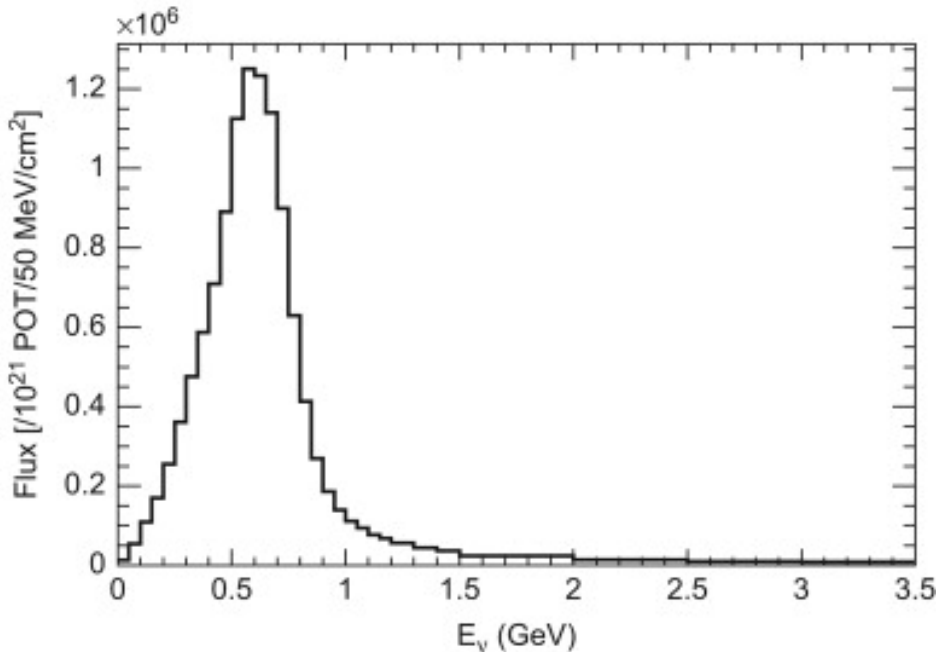


**Figure 1.12:** The T2K unoscillated  $\nu_\mu$  flux at SK at the off-axis angle of  $2.5^\circ$ .

eye view of J-PARC can be seen in Figure 1.13 on page 29 which highlights its different accelerators and facilities. For this section, note that all beam energies are kinetic energies.

Protons for the T2K beamline are first accelerated in the J-PARC linear accelerator<sup>7</sup> (linac) and then the rapid cycle synchrotron<sup>8</sup> (RCS). Hydrogen ions ( ${}_1^1\text{H}^-$ ) are extracted from plasma in a electrical discharge chamber and feed through a series of linac elements as shown in Figure 1.14a on page 30. Each linac element except for the initial quadrupole magnet apparatus accelerates the ions using carefully coordinated oscillating electric fields generated by radio frequency pulses. After traveling 240m along the linac, the ions have been boosted to 181 MeV of kinetic energy and transported into the RCS. In transit to the RCS, the ions are stripped of their electrons via charge stripping foils. The 348m circumference RCS then further boosts the protons to 3 GeV at an operating frequency of 25 Hz. While being

<sup>7</sup>A linear accelerator accelerates particles using time varying electric fields along a one direction, terminal beamline. Not only used in particle physics, they are also used in the medical field to generate X-rays.

<sup>8</sup>A synchrotron is cyclic particle accelerator that relies on time varying magnetic fields to accelerate particles. Since they require many magnets and large spaces to operate, they are usually operated at national laboratories for others uses as well like material and life sciences.

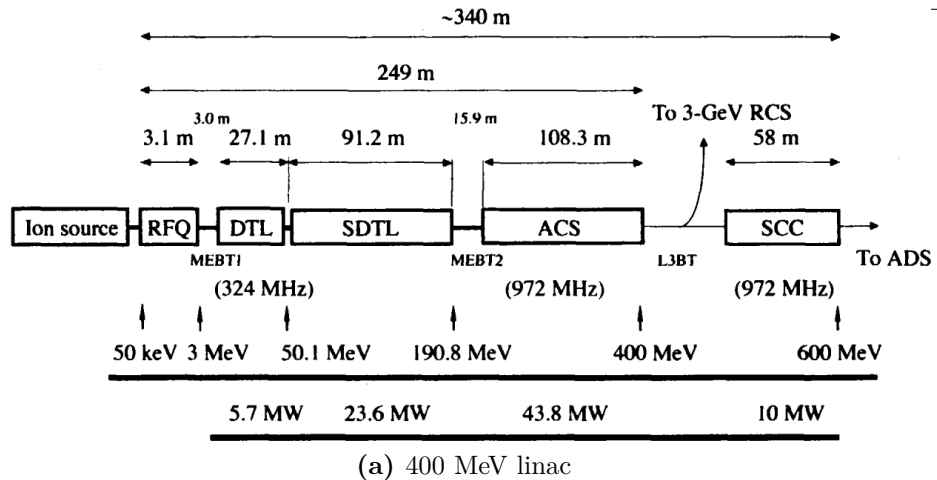


**Figure 1.13:** Bird's eye view of the J-PARC center showing the primary components of its accelerator programs. To generate the high intensity neutrino beam, first the linear accelerator (Linac, red) accelerates hydrogen ions (protons) into the 3 GeV Synchrotron (also red) called the rapid-cycle synchrotron (RCS). The RCS then injects some of its protons into the 50 GeV Synchrotron (yellow) called the main ring (MR) which currently runs at 30 GeV. Finally the MR protons are directed into a target material along the neutrino beamline (teal) [21].

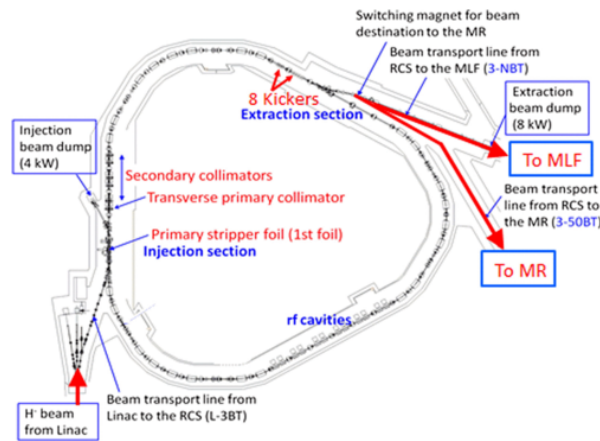
accelerated, protons are aggregated into two bunches and focused using particle collimators as shown in Figure 1.14b on page 30.

The next stage for the protons intended for the neutrino beamline is the much larger main ring (MR) synchrotron as shown in Figure 1.14c on page 30 which has a circumference of 1567m. While nominally designed to boost protons to 50 GeV, it currently operates at 30 GeV. Protons are injected into the MR to form eight proton bunches (spill), initially six when T2K first ran, before entering the neutrino beamline. The total temporal width of the spill is approximately  $0.5\mu\text{s}$  [1]. At a spill cycle frequency of 0.5Hz, the bunches are extracted from the MR into the neutrino beamline.

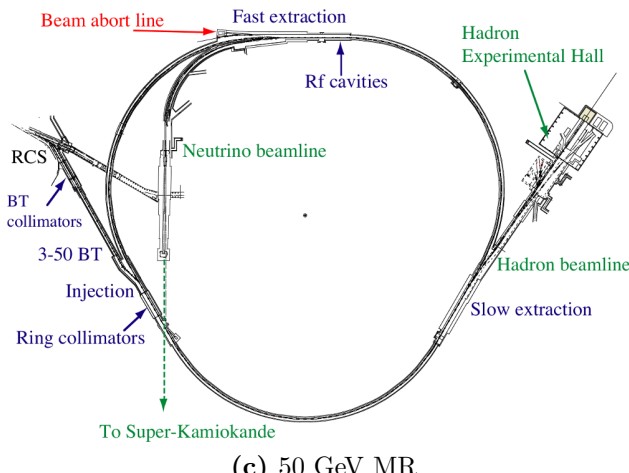
The neutrino beamline is designed to direct the protons toward SK and generate neutrinos by striking them on a cylindrical target. Figure 1.15a on page 31 shows the process of proton



(a) 400 MeV linac



(b) 3 GeV RCS



(c) 50 GeV MR

**Figure 1.14:** Schematics of the J-PARC accelerators. (a) The linac accelerates hydrogen ions to 181 MeV of kinetic energy, designed for 400 MeV, from the ion source [67]. (b) Protons from the linac are collected into the RCS and accelerated to 3 GeV [55]. (c) Protons from the RCS are injected into the MR synchrotron. While the MR is designed for 50 GeV, it currently operates at 30 GeV.

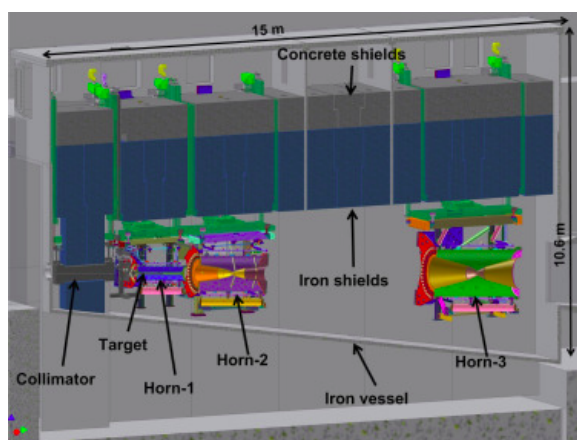
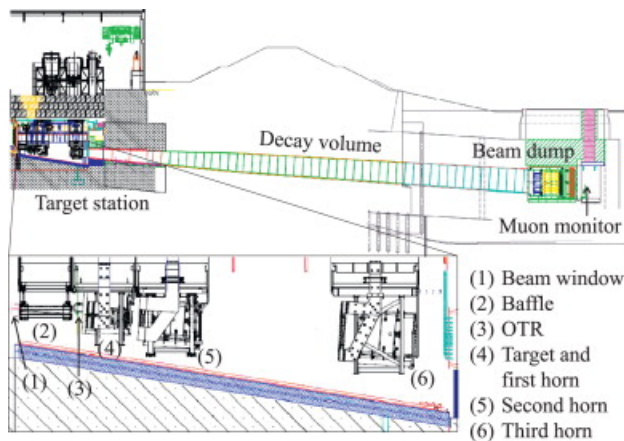
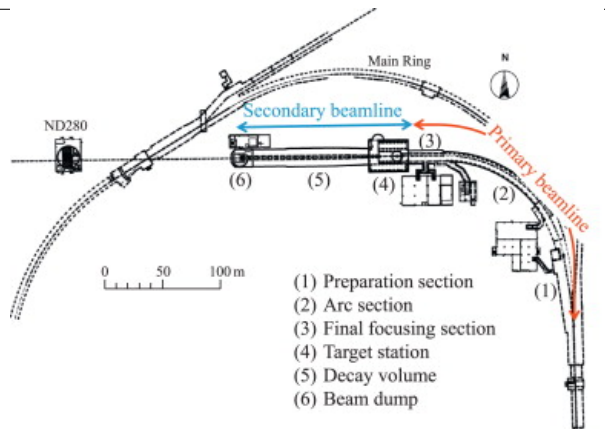


**Figure 1.15:** The neutrino beamline at J-PARC consists of a primary and secondary beamline. (a) The primary beamline redirects the protons towards the secondary beamline [1]. (b) In the secondary beamline, the protons are impinged on a cylindrical target producing mostly pions. The pions are focused using in sequence horns and decay in a long decay volume. Any non-decayed particles are stopped at the beam dump. (c) A further zoomed in cross section of the target station showing the target and focusing horns [60].



(a) A graphite target at the target station



(b) A magnetic focusing horn

**Figure 1.16:** Shown are photos of work performed on the target station. (a) The graphite rod being extracted from the target station is shown in the black-dashed box. (b) One focusing horn in T2K.

extraction from the MR for both primary and secondary neutrino beamlines. In the primary beamline, a series of normal and superconducting magnets steer the proton beam away from the MR first along a 54m preparation section and then a 147m arc section to bend the beam towards SK. A final focusing section in the primary beamline focuses the protons into the secondary beam while directing it downwards  $3.637^\circ$  with respect to the local horizontal. Since a well tuned and stable proton beam is necessary for neutrino production, numerous beam monitors are installed along the primary beamline to measure any losses.

The secondary beamline marks the end of the proton beam and production of a neutrino beam. In the secondary beamline, as shown in Figure 1.15b on page 31, it consists of a target station, a decay volume for the outgoing particles from the target station, and a beam dump for any remaining particles. The target station houses a 91.4cm long, 2.6cm diameter, and  $1.8\text{g}/\text{cm}^3$  graphite rod which corresponds to 1.9 radiation lengths. When the protons strike the target, strong (nuclear) interactions produce  $\pi(\pi)$ -mesons (pions) and K-mesons (kaons). like those produced from cosmic ray collisions in the upper atmosphere. To enhance the flux of neutrinos, a series of three current pulsed, focusing magnets called

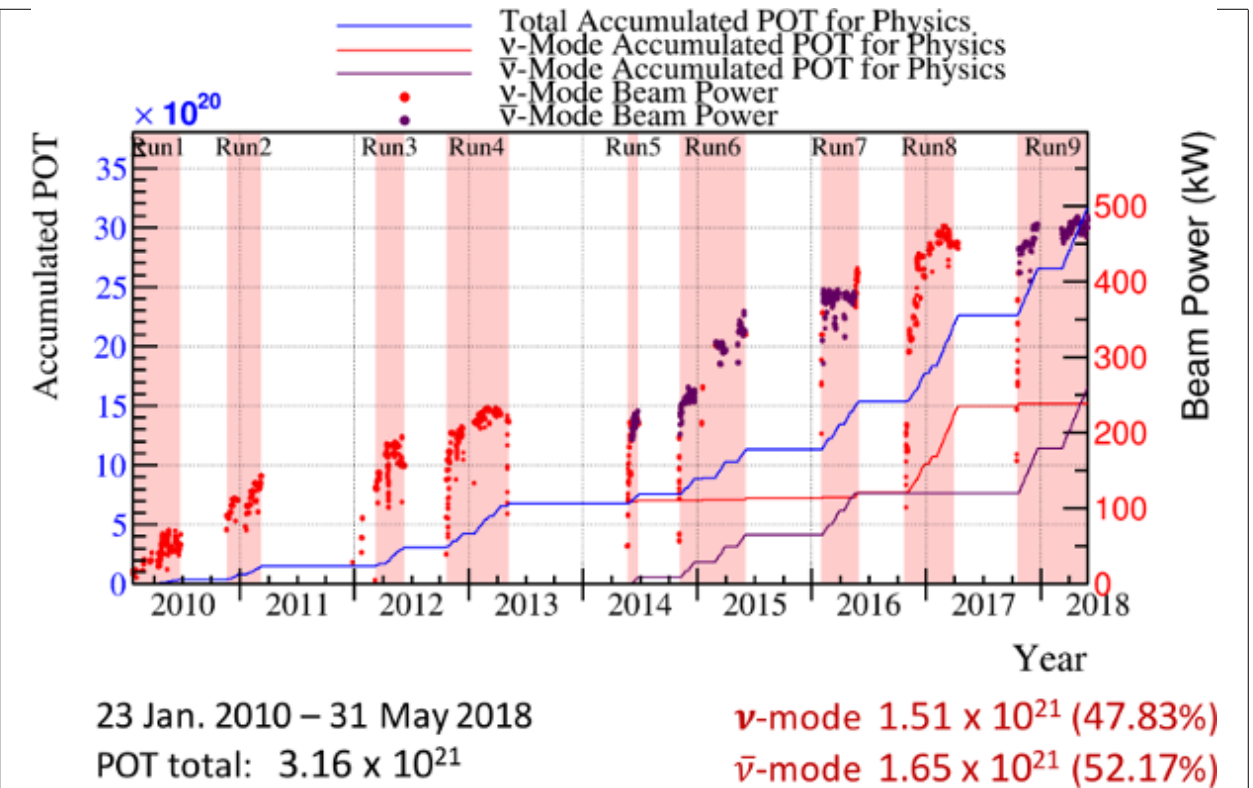


**Figure 1.17:** T2K accumulated protons on target since 2010 shows a steady increase in beam power over time. The gap between Run2 and Run3 is due to the damage suffered at J-PARC after the 2011 Tōhoku earthquake.

horns<sup>9</sup> as shown in Figure 1.15c on page 31 are used to focus the mesons of the correct charge towards SK. Photographs of a graphite target and focusing horn are shown in Figure 1.16 on page 32. The horns are pulsed at +250kA (-250kA) to select positively (negatively) charged pions. The focused pions are allowed to decay along the 96m long decay volume as to boost the daughter neutrinos along the secondary beamline direction. For safety reasons, the decay volume is filled with gaseous helium at 1 atm of pressure which has a low pion absorption rate. The daughter particles in the decay volume should be mostly muons and muon-neutrinos traveling towards SK. A beam dump is placed at the end of the decay volume to stop particles that have not yet decayed to prevent uncontrolled decay products from contaminating the beam.

<sup>9</sup>The name horn derives from the fact that the focusing magnets are shaped like brass horns in a music ensemble or marching band. One can think of these horns like a focusing lens for charged particles.

---

---

Along both beamlines are numerous monitors and timing systems to observe the proton beam to ensure stable production of neutrinos. Proton beam monitors are placed along the primary beamline to ensure the proton beam is properly steered into the secondary beamline. An optical transition radiation monitor is situated around the target to observe any protons not intersecting with the target region itself. The last monitor along the secondary beamline is the a muon monitor (MUMON), which is placed downstream of the beam dump to observe the daughter muons of  $> 5$  GeV/c momentum [1].

In order to provide timing information for the neutrino beam at SK, a global positioning system (GPS) is used to synchronize clocks at SK and J-PARC. Any event outside the beam timing window are rejected in the T2K oscillation analysis, and so having precise timing information for the neutrino beam is critical for the experiment. The GPS has an internal accuracy of 50ns, or about  $\sim 150$ m assuming the neutrinos are traveling near the speed of light. This is well within the time it takes for any neutrino to travel the 295 km between J-PARC and SK.

J-PARC continues to improve the proton delivery and neutrino modes since T2K began in 2010. T2K has run in two horn current modes:  $\nu$ -mode and  $\bar{\nu}_\mu$ -mode. Focusing positively charged pions with  $+250$  kA horn current is called forward horn current (FHC) mode. Similarly, using  $-250$  kA horn current is called reverse horn current (RHC) mode. The aggregate running of T2K for both FHC and RHC modes are shown in Figure 1.17 on page 33 in units of protons on target (POT).

In addition the proton beam intensity, as measured in kW (energy/proton/second), has been increased over time which increases the number of neutrino interactions observed at SK. Note that while  $\pm 250$  kA is the preferred horn current in both FHC and RHC modes, the horns were run briefly at  $+205$ kA when operations resumed after 2011 Tōhoku earthquake.

---

### 1.2.2 Neutrino Near Detectors: ND280

T2K has a near detector (ND) site at J-PARC that is designed specifically observe the neutrinos in flight aimed at Super-K. The purpose of a ND site is to *constrain the neutrino flux and interaction rate* at SK in order to reduce the impact of their systematic uncertainties in the oscillation analysis. The analysis in this thesis uses the data provided by the off-axis ND. The site is called ND280 and is located 280m away from the production target. The primary detector is an off-axis, magnetized tracking detector consisting of different subdetectors. A separate detector array called the Interactive Neutrino Grid (INGRID) measures the neutrino beam profile. Both on-axis and off-axis detectors extensively utilize a commercial light sensor called a multi-pixel photon counter (MPPC) for the light collection in the scintillator-based detectors.

The following subsections begin with a description of the MPPC technology used in T2K. Next is a description of INGRID and its purpose at ND280. This is followed by a general description primary off-axis, magnetized detector. The last two subsections are descriptions of two primary subdetectors in the off axis detector. The first and second being the pi-zero detector (PØD) and time projection chamber (TPC), respectively.

From here on unless specified, INGRID will refer only to the on-axis ND and ND280 will refer only to off-axis ND.

#### Multi-pixel photon counter (MPPC)

While the reliable photo-multiplier tube (PMT) technology was used in previous scintillator-based detectors, T2K needed a different technology to work in the strong magnetic field environment. T2K selected a commercially available silicon photomultiplier sensor developed by the Hamamatsu corporation called a MPPC. A MPPC is a compact device containing many sensitive avalanche photodiode pixels that act as Geiger micro-counters. They are well matched with the spectral emission of wavelength-shifting (WLS) fibers used to collect the scintillator light in ND280 and operate in a strong magnetic field environment. T2K utilizes

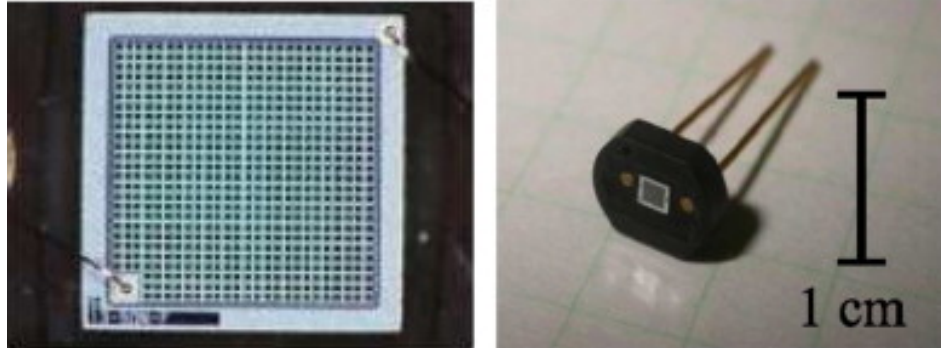


**Figure 1.18:** Photographs of the specially designed MPPC used in T2K. A magnified face view is shown on the left with an entire unit shown on the right [1].

specialized 667-pixel MPPCs with an effective area of  $1.3 \text{ mm} \times 1.3 \text{ mm}$  as shown in Figure 1.18 on page 36.

### On-Axis Detector

The on-axis near detector called the Interactive Neutrino Grid (INGRID) is a tracking scintillator detector designed to directly measure the neutrino beam profile. As shown in Figure 1.19 on page 37, it is a cross grid of tracking modules centered at the designed neutrino beam center ( $\theta = 0$ ). Each module consists of alternating layers of iron plates and scintillator bars except for the two most downstream scintillating layers which lack iron plates. To monitor any beam asymmetry, two separate modules are placed off the grid axis.

Each scintillating bar consists of scintillator-doped polystyrene which emits light when a charged particle deposits energy in the media. Each bar contains a single wavelength-shifting (WLS) fiber to collect and shift the light to a different energy. The light is collected at a single MPPC device and converted into an electrical signal. In order to enhance the collection efficiency, a reflective  $\text{TiO}_2$  doped polystyrene shell surrounds each bar. Bars are assembled into planes to provide tracking capabilities. Veto planes also surround each module to prevent false signals to trigger.

INGRID is continuously operated to check that the neutrino beam center was properly aligned at its designed center. Diagnostic plots such as Figure 1.20 on page 38 are collected

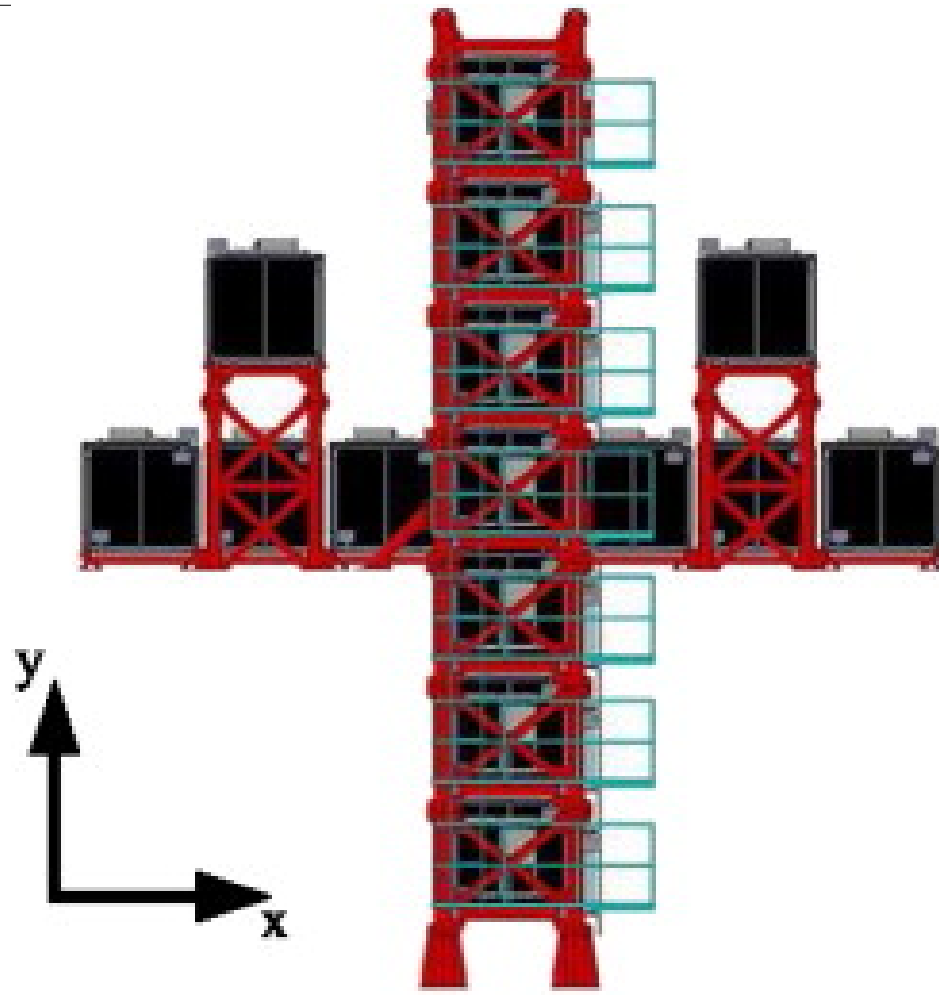


**Figure 1.19:** A schematic of INGRID shows the arrangement of the tracking scintillating modules. There are 16 identical modules total with seven in the vertical row, seven in the horizontal row, and two at off-axis positions. INGRID is capable of measuring the neutrino beam in a transverse area of  $10\text{m} \times 10\text{ m}$ . With the vertical row upstream of the horizontal row, the designed beam center intersects each row's center module [2].

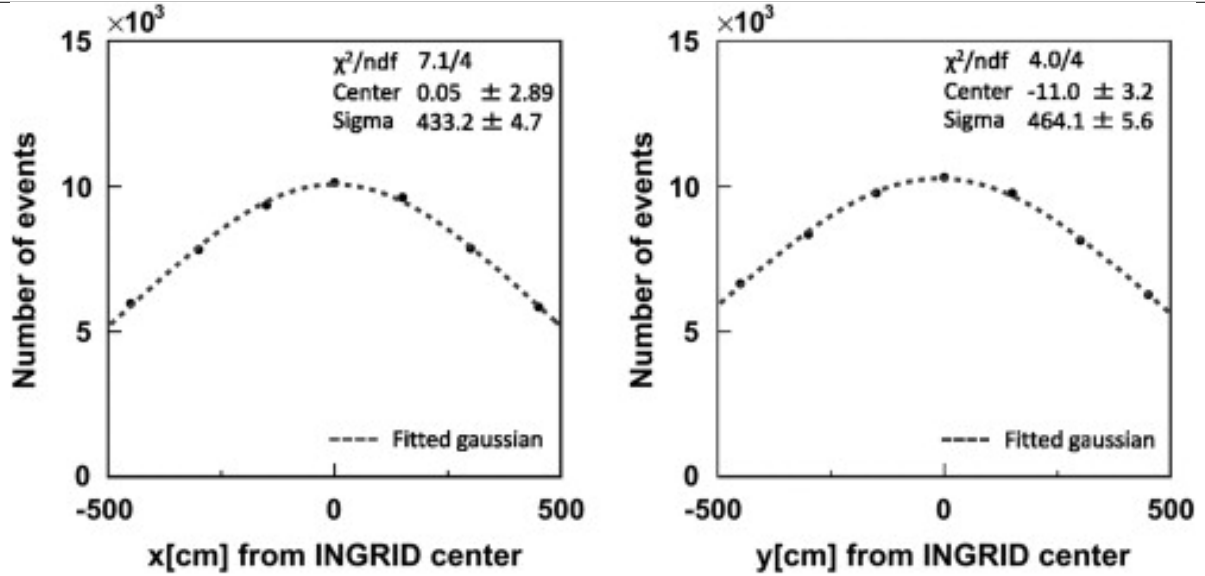


**Figure 1.20:** A beam profile taken with INGRID in April 2010 shows the Gaussian nature of the beam. The errors on the data points are about 1%. [2]

on a monthly basis to ensure that the neutrino flux at Super-Kamiokande (SK) is consistent with T2K’s design. A history of the beam profile and event rate on INGRID between January 2010 and October 2016 is shown in Figure 1.21 on page 39.

### Off-Axis Detector Summary

The near detector in T2K is ND280, which is an off-axis, magnetized tracking detector. It is a collection of different detector technologies designed to facilitate three primary measurements:

1.  $\nu_\mu$  flux at SK,
2. Irreducible  $\nu_e$  background flux at SK, and
3.  $\nu_\mu$  interaction backgrounds and cross sections for the  $\nu_\mu \rightarrow \nu_e$  search.

ND280 consists of the pi-zero detector (PØD), the tracker region consisting of a fine grain detector (FGD) and time projection chamber (TPC), an electromagnetic calorimeter (ECal), and side muon range detector (SMRD). The ND280 subdetectors are instrumented inside

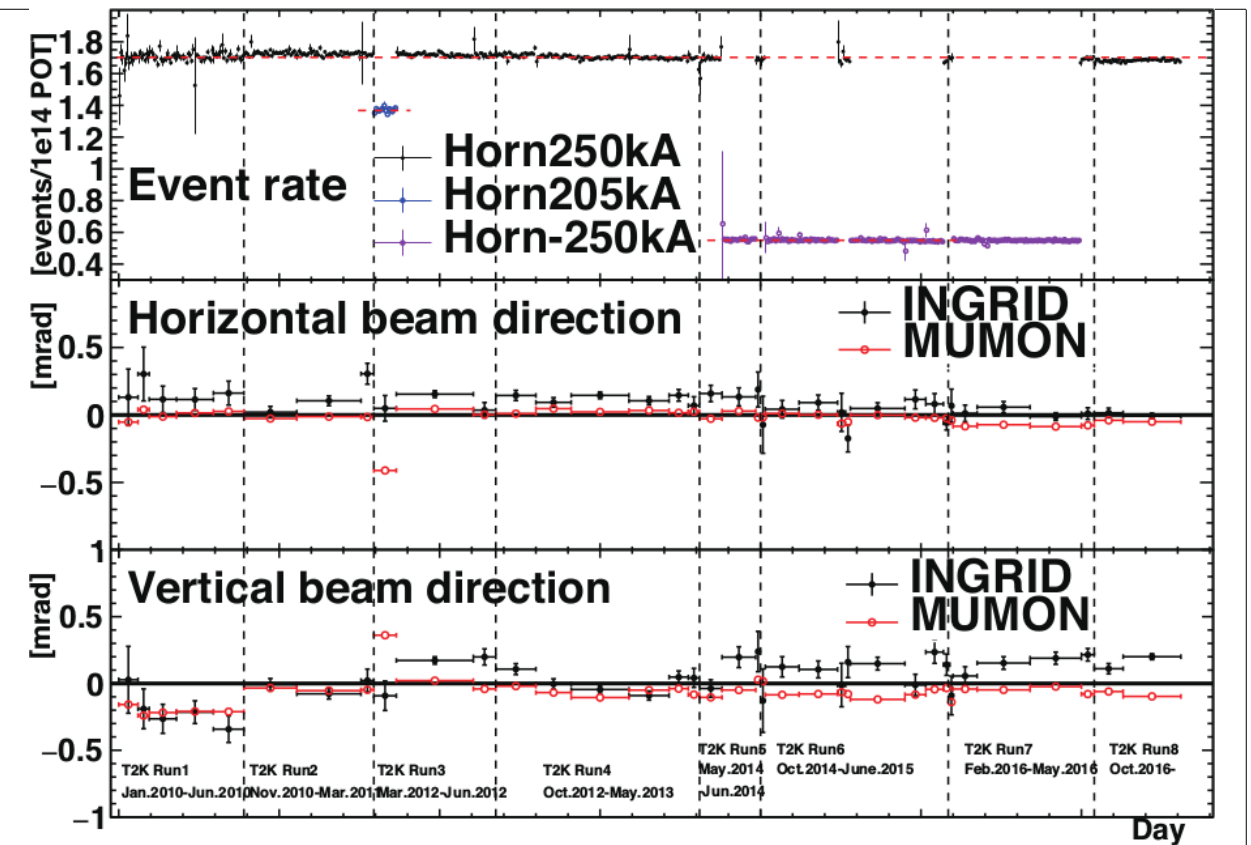


**Figure 1.21:** INGRID interaction event rate and beam profiles are shown. The top panel shows the event rate for the three different horn currents. The middle and bottom panels show the horizontal and vertical beam directions with respect to the beam center, respectively. A deviation of 1 mrad corresponds to a little under 30 cm. The error bars shown are the statistical errors on the mean.

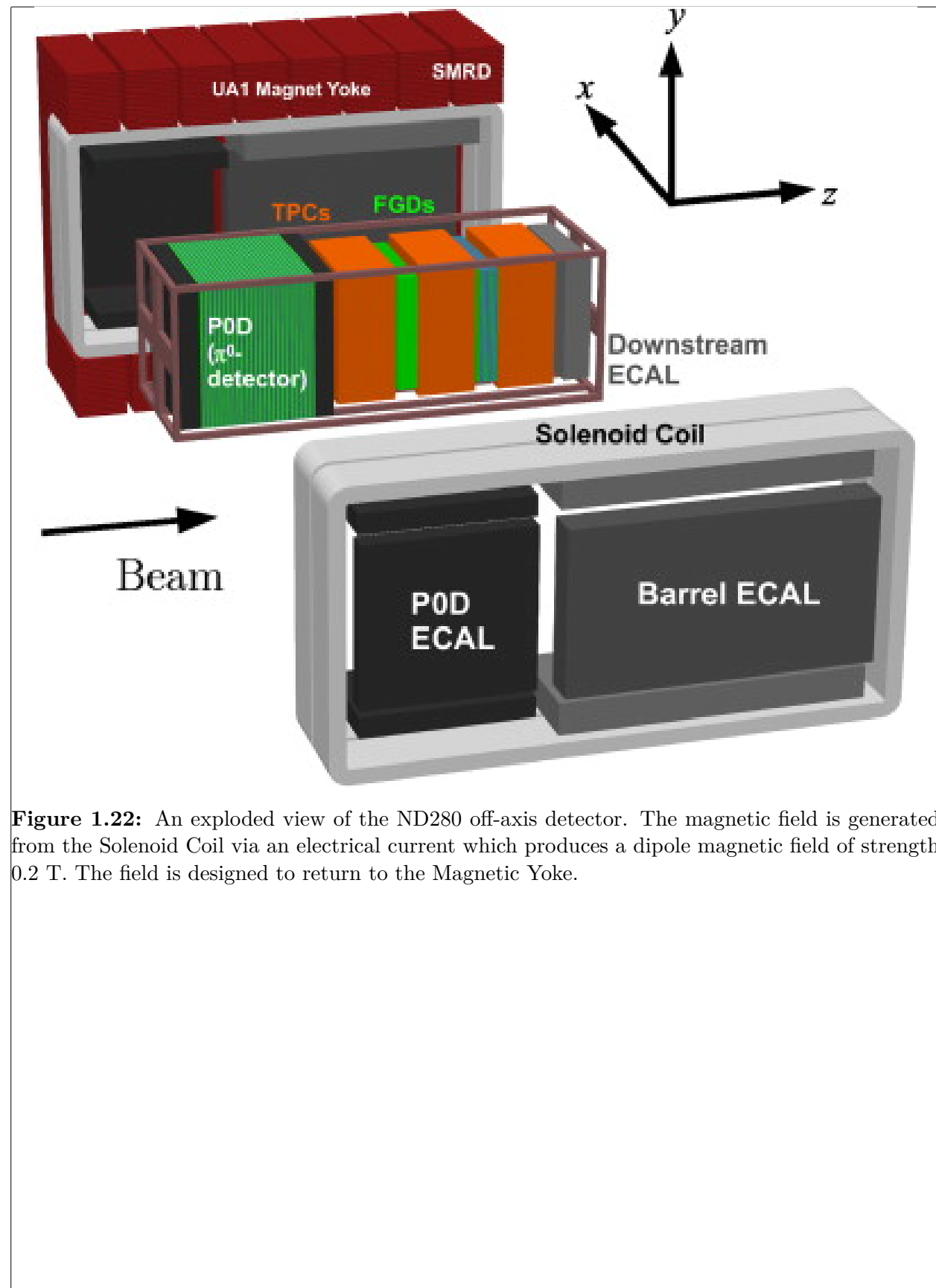


**Figure 1.22:** An exploded view of the ND280 off-axis detector. The magnetic field is generated from the Solenoid Coil via an electrical current which produces a dipole magnetic field of strength 0.2 T. The field is designed to return to the Magnetic Yoke.

the recycled UA1/NOMAD magnet with the SMRD in the magnetic field return yoke itself. All but the FGD is instrumented with the same scintillating-bar bar technology collected by MPPCs. A schematic of the different detector components of ND280 is shown in Figure 1.22 on page 40.

The analysis in this thesis use measurements from the primary subdetectors, the PØD and the TPC. The PØD serves as a massive target for the incident neutrino beam and the TPC serves to measure the charge and momentum of the outgoing particles.

The ND280 magnetic field is generated using electrical current fed through solenoid coils to generate a dipole field of strength  $0.2\text{ T}^{10}$  in the x direction. The field is highly uniform near the center of the detector which is where the majority of the TPC system is located. However, it has significant deviations from 0.2 T near the solenoid edges. In order to fully understand the field inside ND280, a precise 3D model was generated using a machine controlled Hall probe. The operating field strength during the mapping process was 0.07 T due to power restrictions at the time. The model was then compared with measurements in the TPC region as shown in Figure 1.23 on page 42. After scaling the model to the nominal operating strength of 0.2 T, a fractional uncertainty of  $10^{-3}$  or uncertainty of 2 Gauss in each direction was obtained.

The ND280 magnetic field permits the measurements of particle charge and momentum. A particle of charge  $q$ , rest mass  $m_0$ , and velocity  $\mathbf{v}$  under the influence of an external electric and magnetic fields,  $\mathbf{E}$  and  $\mathbf{B}$ , respectively, experiences a force  $\mathbf{F}$  given by the Lorentz force equation

$$\mathbf{F} = q(\mathbf{E} + \mathbf{v} \times \mathbf{B}). \quad (1.49)$$

Assuming for now that there is no external electric field, the force on the particle is

$$\mathbf{F} = q\mathbf{v} \times \mathbf{B}, \quad (1.50)$$

---

<sup>10</sup>This is a powerful magnetic field. According to the The US/UK World Magnetic Model for 2015-2020, the magnetic field strength on the surface of the Earth is about 0.294385 Gauss or  $2.94385 \times 10^{-5}\text{ T}$ . So the field inside ND280 is about 6800 times more forceful than the Earth's influence [23].

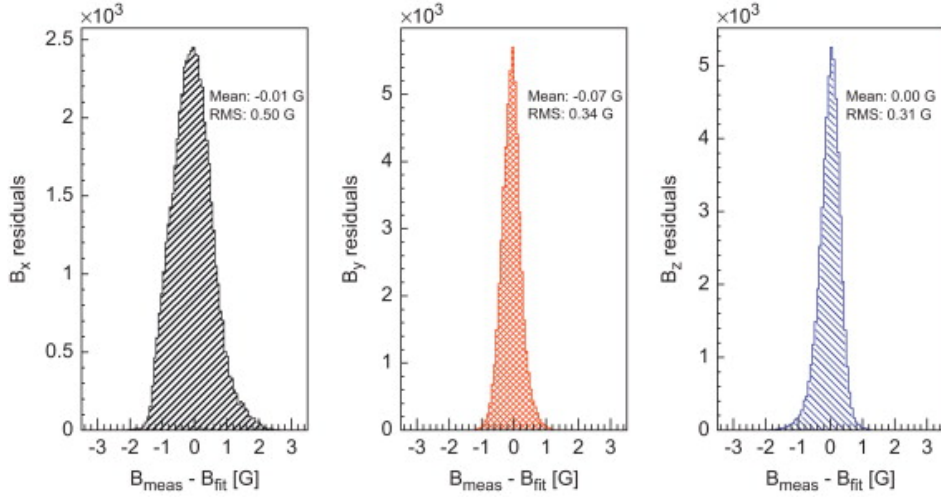


**Figure 1.23:** Each of the magnetic field components (x, y and z, respectively) are compared between a fit of the data and the actual measurements near the center of ND280. The systematic uncertainty on the field is extracted from the RMS of the mapping [1].

which is both orthogonal to  $\mathbf{v}$  and  $\mathbf{B}$ . Since the mechanical work on a particle in a magnetic field is zero, the particle's energy is unchanged ( $|\mathbf{v}| = v = \text{constant}$ ). Newton's Second Law allows us to rewrite the force as an change in momentum  $\mathbf{P}$

$$\begin{aligned}
\mathbf{F} &= \frac{d\mathbf{P}}{dt} \\
&= \frac{d}{dt} (\gamma(v)m_0\mathbf{v}) \\
&= m_0\mathbf{v} \left( \frac{d\gamma(v)}{dt} \right) + \gamma(v)m_0 \left( \frac{d\mathbf{v}}{dt} \right) \\
&= m_0\mathbf{v} \left( \frac{d\gamma(v)}{dv} \right) \cancel{\left( \frac{dv}{dt} \right)}^0 + \gamma(v)m_0\mathbf{a} \\
&= \gamma(v)m_0\mathbf{a},
\end{aligned} \tag{1.51}$$

where  $\mathbf{P} = \gamma(v)m_0\mathbf{v}$  is the relativistic momentum and  $\gamma(v) = (1 - (v/c)^2)^{-1/2}$  is the Lorentz factor for relativistic particles. For uniform circular motion, the magnitude of the acceleration is given by

$$|\mathbf{a}| = v^2/R, \tag{1.52}$$

where  $R$  is the radius of curvature for the circle. Combining (1.52) and (1.51) with some algebra yields

$$R = \frac{\gamma(v)m_0v}{q|\mathbf{B}|\sin\theta_{\mathbf{vB}}}, \quad (1.53)$$

where  $\theta_{\mathbf{vB}}$  is the angle between  $\mathbf{v}$  and  $\mathbf{B}$ . The numerator of (1.53) is recognized as the magnitude of the momentum  $|\mathbf{P}|$ . Some further rearrangement yields

$$|\mathbf{P}| = q|\mathbf{B}|R\sin\theta_{\mathbf{vB}}, \quad (1.54)$$

and thus measuring the direction and radius of curvature inside the field provides the charge and momentum, respectively, as desired.

### Off Axis pi-zero detector (PØD)

The PØD is the primary detector used as the neutrino target in this thesis. It is a plastic scintillator based tracking calorimeter inside the ND280 magnet region. It was designed to measure the neutral current (NC) process  $\nu_\mu + N \rightarrow \nu_\mu + N + \pi^0 + X$  on water where  $N$  is a nucleus and  $X$  is any set of final state particles. The NC  $\pi^0$  process was expected to be a significant background in the  $\nu_e$  appearance search in the likelihood that  $\theta_{13} \approx 0$ . The PØD is a modifiable detector which can be filled or drained of water during data taking, enabling the determination of water target (WT) cross sections by comparing water-in data with water-out data.

A representation of the PØD is shown in Figure 1.24 on page 44. The active detector components are very similar to INGRID's design where scintillation light is captured by a WSF and counted by a MPPC. Each bar is triangular in shape as shown in Figure 1.25 on page 45. A plane of 134 horizontal and 129 vertical bars together to form a PØD module (PØDule) as shown in 1.24b. The PØD dimensions are  $2.298 \times 2.468 \times 2.350\text{m}^3$ , in XYZ respectively, with a total mass of  $\sim 1900$  kg of water and 3570 kg of other material. The total mass of the PØD is approximately 15,800 kg when the bags are full of water. PØDules are

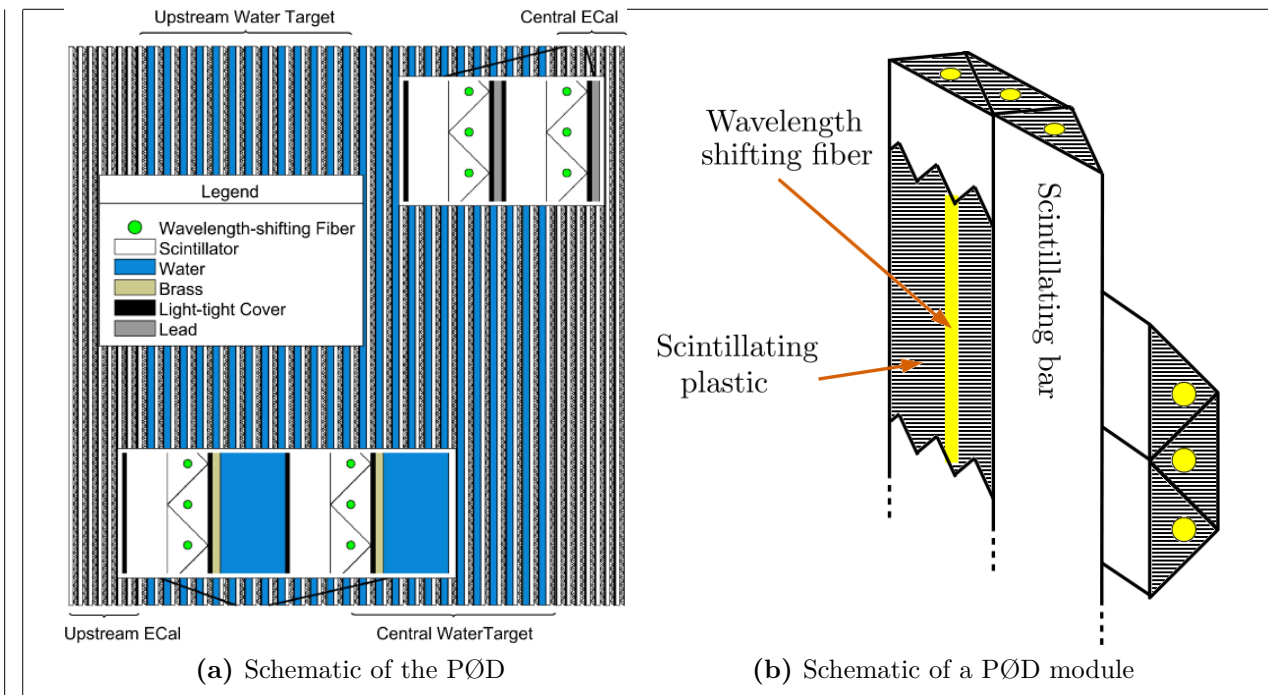


**Figure 1.24:** Schematics of the PØD. Left: insets detail the Water Target and ECal layers. Right: A view of a PØD module illustrating the orthogonal layout of the scintillating planes. Both: the neutrino beam is coming from the left.

arranged into three primary regions. The water target (WT) region contains 26 PØDules interleaved between bags of water 2.8 cm thick when filled and 1.3 mm thick brass sheets designed to help contain  $\pi^0$  decay photons. The last two regions are the upstream ECal (USECal) central ECal (CECal). Each ECal region contains 7 PØDules with steel sheets clad with lead between them [6]. An elemental composition of the WT is shown in Table 1.3 on page 45.

The readout electronics for the PØD is based on the Trip-T application specific integrated circuit (ASIC) shared among the SMRD, ECals, and INGRID. Signals from 64 MPPCs are routed to Trip-T front end boards (TFB) that each house 4 Trip-T ASICs. Each Trip-T collects the MPPC charge in 23 programmable integration cycles.

The TFB are readout to back-end electronics which control the TFBs and synchronize clocks. A total of six readout merger module (RMM) electronics receive TFB the data and control each TFB ASIC. RMM timing are synchronized with a cosmic trigger module and

Element	Symbol	Fraction [%]
Carbon	C	45.0
Oxygen	O	29.9
Copper	Cu	14.3
Hydrogen	H	8.0
Zinc	Zn	1.6
Chlorine	Cl	1.1
Titanium	Ti	0.1

**Table 1.3:** Elemental composition of PØD water target region. The table is sorted from top to bottom by fraction of mass. This table was originally produced in Reference [6]

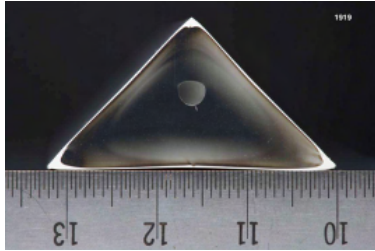


**Figure 1.25:** A cross section of a PØD scintillating bar. The base and height is 33 mm long and 17 mm high. The wavelength shifting fiber is inserted in the bored hole which is half-way between the base and tip.

a slave clock module (SCM), of which both are synchronized with a master clock module from the beamline. Synchronizing the RMMs with the SCM allows for the Trip-T ASIC integration windows to match with the beam. The RMMs are responsible for distributing the TFB data to the data acquisition (DAQ) system for storage.

The ND280 DAQ consists of a MIDAS framework to monitor and control data collection. The primary client of the DAQ is to merge data and package it for long term storage. In parallel to it is the Global Slow Control (GSC) system which measures temperatures, voltages, and other physical quantities. Together the DAQ and GSC help scientists consistently produce high quality data and maintain the overall stability of the detector.

### Off Axis Time Projection Chamber (TPC)

The ND280 TPC is designed to provide momenta measurements of charged particle tracks as discussed above, high resolution particle counting capabilities, and particle identification

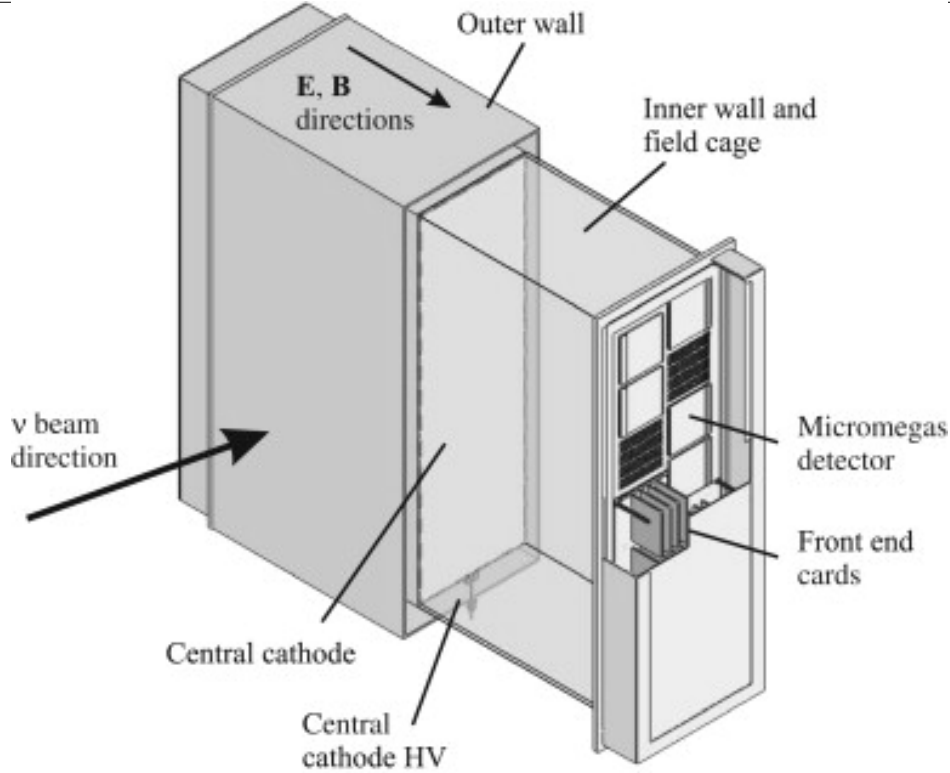


**Figure 1.26:** Cut-away drawing of a TPC volume in ND280 [1].

based on energy deposition. The latter most aspect is not utilized in this thesis. The TPC is divided into three volumes separated by the two FGD volumes. Each TPC volume ( $2.3 \times 2.4 \times 1.0 \text{ m}^3$ ) consists of an inner box that holds an argon-based gas and an outer box that holds an insulating  $\text{CO}_2$  gas. The inner gas mixture is 3000 L of  $\text{Ar:CF}_4:\text{iC}_4\text{H}_{10}$  (95:3:2) gas. It was selected for its high speed, low diffusion, and good performance with the micromegas [1]. A simplified schematic of the TPC is shown in Figure 1.26 on page 46.

As charged particles traverse the inner TPC volume, they create ionization electrons in the gas which drift towards readout planes away from a central cathode. The electron drift acceleration is rapid due to the strong 5 kV/cm electric field present. Drift electrons are multiplied and sampled by micromega detectors that line the sides of the TPC, providing nearly  $3 \text{ m}^2$  of active surface coverage. Arrival times of the electrons provide timing information to give a full three dimensional portrait of the events.

---

## Track Reconstruction in ND280

The goal of track reconstruction software is to capture the shape and history of energy deposited in the detector. Since ND280 is collection of different technologies, highly specific algorithms and models are used to identify track-like patterns. Since this analysis uses neutrino events incident in the PØD and cross into the TPC, an unified and coherent reconstruction model is needed. A reconstruction package called “Global” is designed to combine all ND280 information for this purpose. The Global reconstruction will be revisited in Chapter 3.

### 1.2.3 Neutrino Far Detector: Super-Kamiokande

The Super-Kamioka neutrino detection experiment (Super-Kamiokande) is the dedicated far detector for the T2K experiment. Positioned at 295 km away from the neutrino source with a 1 km overburden, it is well designed to detect the elusive neutrino. Containing about 50 kt of pure water, is it lined with PMTs in both an inner and veto outer detector as shown in Figure 1.27 on page 48.

When charged particles travel through the water, a Cherenkov radiation cone is produced. The sharpness of the cone edge is an unique ID for the particle species that produced it. An electron produces a fuzzy edge since it experiences many large multiple scatterings off the water molecules. A muon on the other hand produces a sharp edge since it is much more massive and thus less perturbed by the water molecules. Both types of events are shown in Figure 1.28 on page 48. By determining the particle that produced it and isolating the event during the T2K beam, the neutrino flavor is deduced.

While events from SK are not used in this analysis, the goal is to try to improve T2K’s parameters which depend on comparing the Near Detector neutrino measurements to the Far Detector neutrino measurements. Therefore having some background on the oscillation analysis will illustrate ND280’s utility and discussed in the next section.

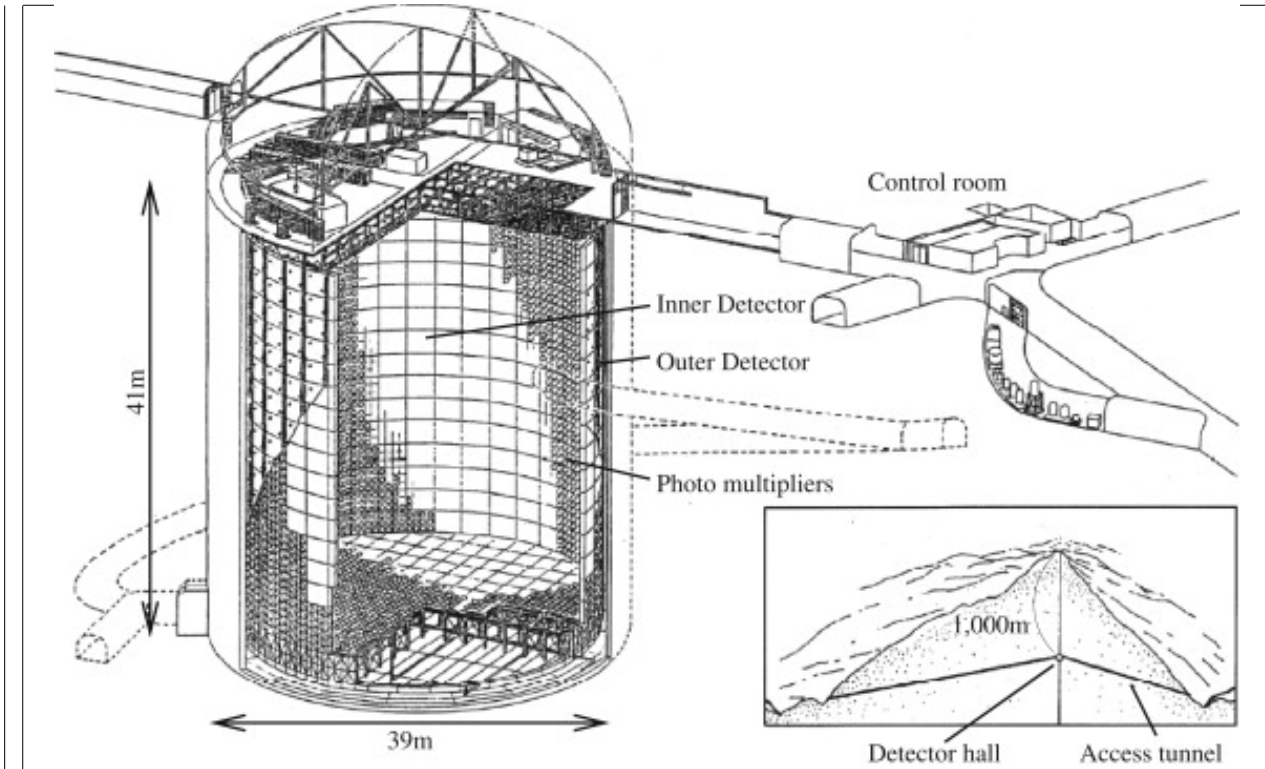


**Figure 1.27:** Diagram of the Super-Kamiokande detector consisting mainly of the inner and outer detector segments. The boundary between the two segments is cylindrical scaffolding used to mount photomultiplier tubes and optically isolate the segments.

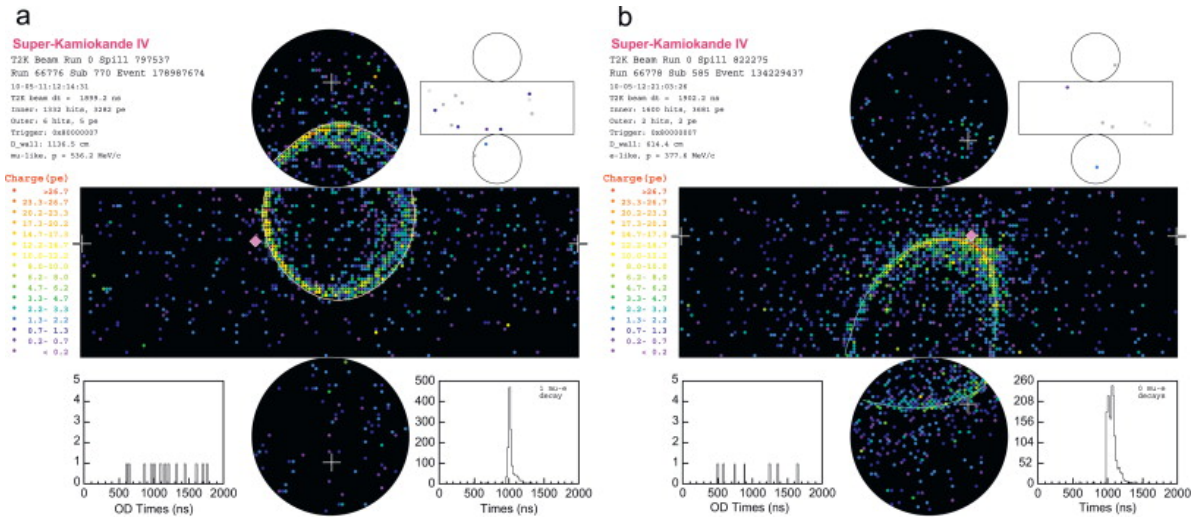


**Figure 1.28:** Representative T2K events in Super-Kamiokande for (a) a muon-like ring and (b) an electron-like ring. Both figures show Super-Kamiokande unrolled onto a plane with each colored point representing a PMT. The color of each PMT corresponds to the amount of charge collected. In upper right corner shows the same unrolled hit map for the veto outer detector. White crosses indicate the location of the reconstructed vertex. A solid diamond marks the location where a ray parallel to the beam would intersect from the vertex.

### 1.2.4 ND Constraint

As started before, the primary goals of T2K are measure to measure the oscillation parameters  $\theta_{13}$ ,  $\theta_{23}$ , and  $\Delta m_{23}^2$ . This is performed by fitting the oscillation parameters to the number of observed flavored neutrinos at SK. The number of reconstructed neutrino events of flavor  $\alpha$ ,  $N_{\nu_\alpha}$ , observed is

$$N_{\nu_\alpha} = B + S_{\nu_\alpha} \quad (1.55)$$

where  $B$  are all misidentified  $\nu_\alpha$  events and  $S_{\nu_\alpha}$  is the number of true events. The expected reconstructed neutrino appearance rate is given by

$$\begin{aligned} S_{\nu_\alpha} &= \sum_{\lambda=e,\mu} \left[ \mathcal{P}_{\nu_\lambda \rightarrow \nu_\alpha} (E_\nu; \vec{o}) \right] \times \sum_t \left[ \sigma_{\nu_\alpha}^t (E_\nu) \cdot t_N \right] \\ &\quad \times \Phi_{\nu_\alpha} (E_\nu) \times \epsilon(p_\alpha, \theta_\alpha), \end{aligned} \quad (1.56)$$

where  $\vec{o}$  is a vector of the oscillation parameters from (1.38),  $\sigma_{\nu_\alpha}^t$  is the cross section for  $\nu_\alpha$  on target  $t$ ,  $t_N$  is the number of targets of type  $t$ ,  $\Phi_{\nu_\alpha}$  is the flux of neutrinos, and  $\epsilon(p_\alpha, \cos \theta_\alpha)$  is the efficiency of reconstructing and correctly categorizing the event as a function of momentum  $p$  and angle  $\theta$ .

*Having a large, sensitive off-axis ND like ND280 provides critical constraints to the neutrino flux in the oscillation analysis.* This includes the oscillation channel  $\nu_\mu \rightarrow \nu_e$ , but also the intrinsic  $(\bar{\nu}_e)$  background in the T2K beam. These neutrinos interact the same way an oscillated neutrino would at SK. Without ND280, the fractional uncertainty on the flux rate is about  $\sim 10\%$  per energy bin. These constraints are obtained from MUMON discussed above and the NA61/SHINE experiment [10]. Adding the ND constraint reduces the uncertainty to about  $\sim 5\%$  as seen in fig. 1.29 on the following page.

T2K uses the NEUT<sup>11</sup> [40] program library to simulate neutrino interactions with nucleons and the nucleus. It was originally designed to simulate atmospheric neutrinos for the Kamioka Nucleon Decay Experiment (Kamiokande). Included in NEUT are numerous

---

<sup>11</sup>NEUT is neither an initialism nor acronym

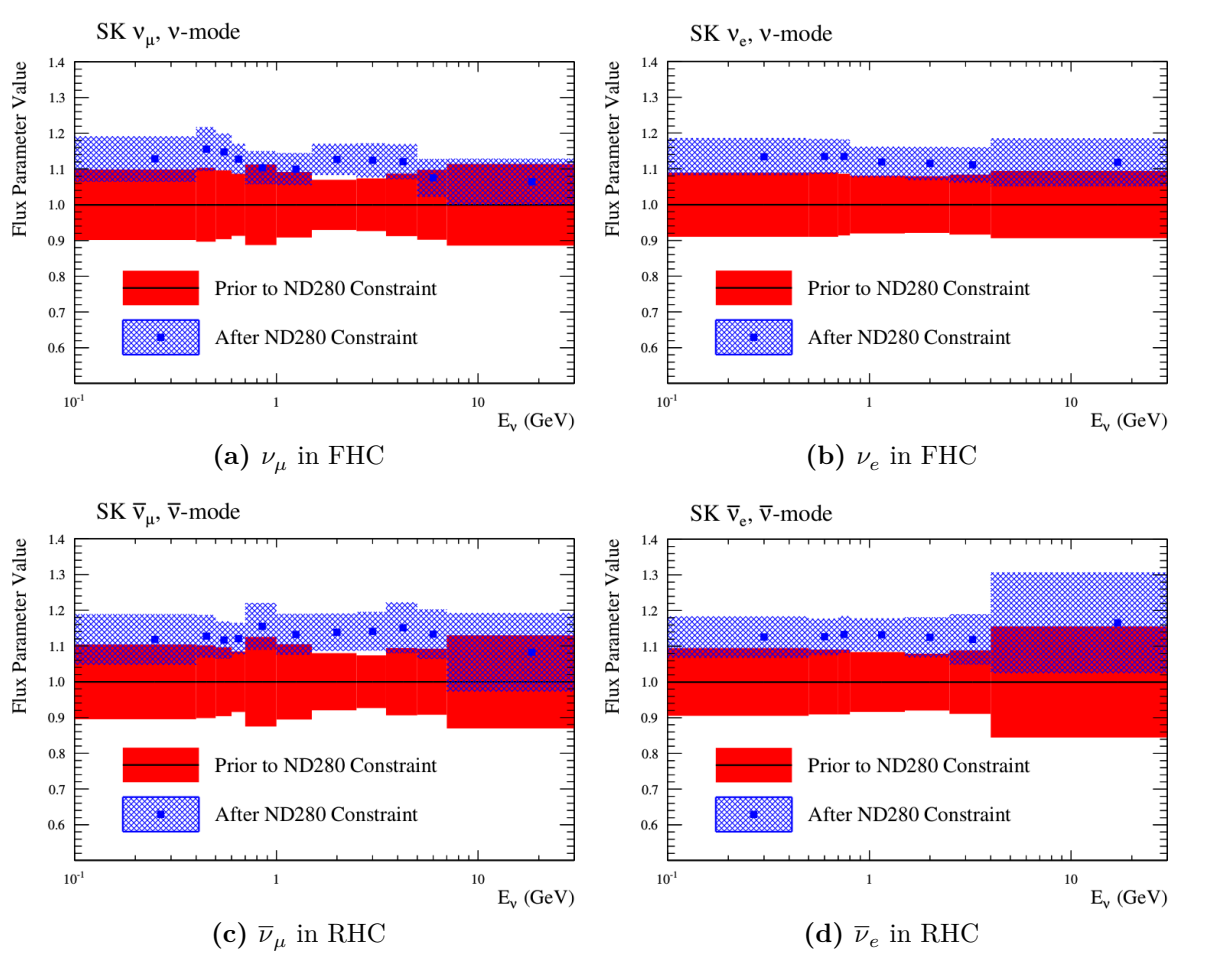


**Figure 1.29:** Predicted and best fit measurements for the SK flux. The horizontal axes are the neutrino energy and the vertical axes are the fractional change in the flux normalization. These figures were taken from the 2017 T2K oscillation analysis [4]. A value 1.1 corresponds to a 10% increase in the number of predicted events.

models for neutrino interactions on matter and intra-medium hadron transport within the nucleus.

Using the ND280 constraint can tune the NEUT cross section model to best match the T2K data. The canonical T2K cross section model in NEUT is problematic due to depending on older neutrino-nuclear scattering models developed for low-Z nuclear targets like deuterium. The models implemented in NEUT, while being well studied in previous neutrino-nuclear Physics experiments, are known as effective models in T2K. In particular, large disparities exist in recent, high statistics CCQE measurements [32] which is forcing T2K to explore other and new Nuclear Physics models in this analysis.

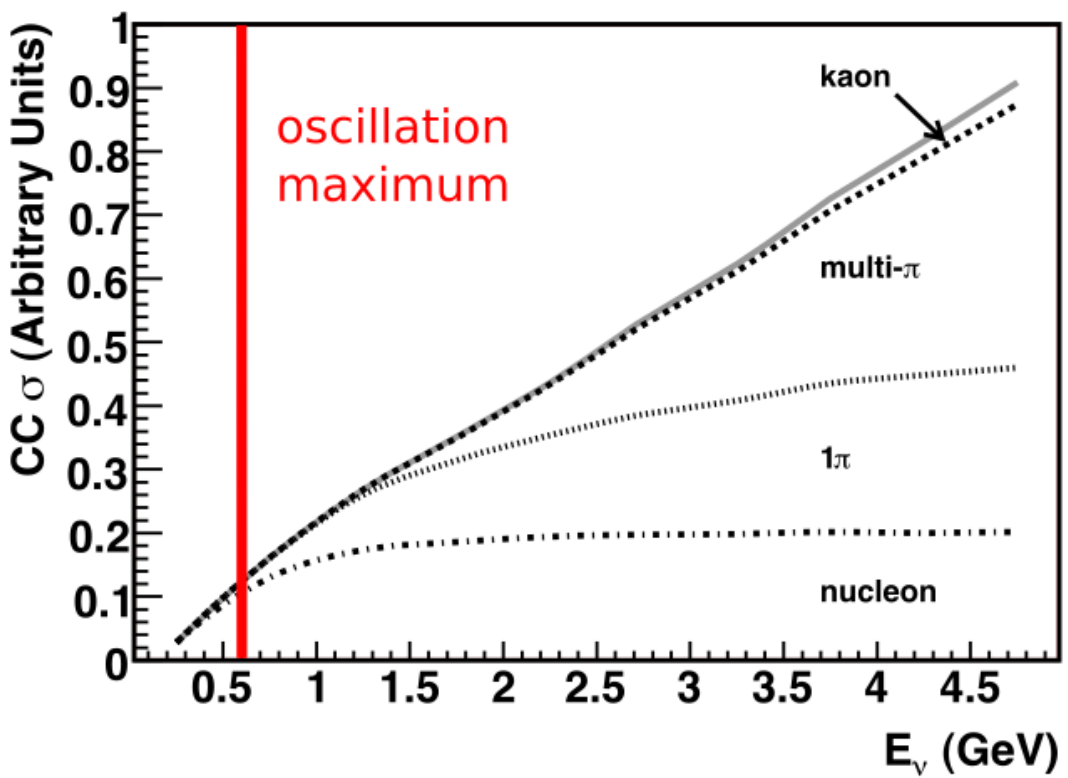


**Figure 1.30:** Predicted CC inclusive scattering cross section at T2K relevant energies. Only the most common final state modes are shown. A thick, red line indicates the T2K  $\nu_e$  appearance probability maximum. For CCQE-like interactions, they usually include the emission of one or more nucleons. Resonance states and DIS interactions produce  $1\pi$ ,  $N\pi$  (multi- $\pi$ ) and kaon final states as well. Combined, the inclusive cross section increases linearly with energy. This image was edited and originally produced by Formaggio and Zeller [32].

---

### 1.2.5 Contributions to the T2K Experiment

Since joining the T2K experiment five years ago, I have played a critical role in analysis that is currently in preparation for publication. This analysis was a second generation measurement of the  $\nu_\mu$  CC single pion production cross section on water in the PØD. I am a co-author of that paper and its internal T2K technical document that outlines the analysis procedure and studies. In particular, I have contributed to data management, reconstructed kinematic validation and characterization, observable feature engineering to describe events in the PØD, and cross validation of complex event selections using boosted random forest classifiers.

Outside of analysis work, the majority of my contributions to the experiment include on-site PØD and ND280 expertise. I was involved in the 2015 work to replace two PØD water bags when they showed evidence of leaking. Additionally, I helped measure the PØD water mass and its “bulging” due to the water. During data taking periods, I signed up at least once a year to perform shifts. I am certified as a TTD expert, PØD water system and calibration expert, and experienced DAQ shifter. As TTD and PØD expert, this included daily reporting and point of contact for the SMRD, ECals, and PØD along with the PØD water target system whenever problems arose. My most recent contribution was participating in the 2018 Super-K open tank work at the Kamioka Observatory. That work included removing any found oxidation, diesel fumes from the initial construction, and glass shards remaining after a significant multi-PMT implosion in 2001. When not cleaning, the other important task was to install light-tight Tyvek sheets to insulate the inner detector.

## 1.3 Summary

The neutrino is an elusive particle to detect. The relatively new neutrino oscillation phenomenon has opened up the possibility of exploring fundamental questions of the Universe like CP violation. In the T2K experiment, some of the uncertainties associated with

---

---

neutrino oscillations are being explored. To facilitate these goals, constraining all forms of uncertainty in neutrino-nuclear interactions and flux help improve its sensitivity to the oscillation predictions.

The next chapters in this thesis are presented in the following order. First is the ND280 constraint on the flux and cross section models using the BANFF maximum likelihood fit. Next is the description of the analysis samples that are used in the BANFF fit. With the samples defined, the parameterization of the fit bins and penalty terms are defined for this analysis. This is followed by the validation of the BANFF fit in a few scenarios. Then the BANFF postfit results will be analyzed in relation to previous analyses. The final chapter is a discussion of the results and prospects for the future.

---

# Chapter 2

## BANFF Likelihood

The BANFF likelihood maximization procedure is a binned likelihood maximization fitting of the ND280 data. This fit is done separately from the fitting the Super-Kamiokande (SK) data for the oscillation analysis. In a joint fit, the measurements from both detectors are considered along with their respective nuisance parameters. This joint-fit approach is more computationally expensive since the time to perform a fit increases non-linearly with increasing the number of fit parameters. However it is developed in an alternate method called the Markov Chain Monte Carlo analysis (MaCh3) and this will not be explained here. The BANFF likelihood maximization, hitherto referred to as the “BANFF-fit”, includes nuisance parameters that affect the measurement of the oscillation parameters, but are not physics goals of the T2K experiment. The BANFF-fit parameters and their respective covariances are then used as inputs in the oscillation analysis. This “divide-and-conquer” approach allows for more rapidly completed studies on the effects of model parameters and biases present. Also this approach should provide the same result with a joint ND280 and SK analysis as is performed in MaCh3. However, information encoded in the ND280 measurements for shared nuisance parameters like the neutrino flux is inevitably lost in the BANFF-fit.

The modern BANFF-fit likelihood is described in detail in detail in [Insert PRD instead](#) TN-220 [39]. It uses a frequentist approach to find the best nuisance parameter set to maximize a

---

binned likelihood. Subsequent updates to the BANFF-fit have increased the sample sizes and systematic parameterizations.

### 2.0.1 Introduction to Conditional PDFs and Likelihoods

Curve fitting is commonly found in the particle physics community literature due to the need to compare two models or constrain unknown model parameters using one or more histograms. For the first case, this involves two competing hypotheses or models,  $H_0$  and  $H_1$ , in order to establish if the data supports new Physics ( $H_1$ ) not predicted in the Standard Model ( $H_0$ ). The second case finds the “best” set of the model predictions,  $\theta$ , that match the data as is the case for the BANFF-fit. In both cases, chi-squared tests are performed to provide goodness of fit, parameter estimation (also referred to as “best fit parameters”), and error/confidence estimation.

Consider the problem of extracting physics parameters  $\vec{y}$  given some data vector  $\vec{N}$ . The conditional probability density function (PDF)  $\mathcal{P}$  to measure these parameters is given as

$$\mathcal{P}(\vec{y}|\vec{N}) = \frac{\mathcal{L}(\vec{N}|\vec{y})\mathcal{P}(\vec{y})}{\int \mathcal{L}(\vec{N}|\vec{x})\mathcal{P}(\vec{x})d\vec{x}}, \quad (2.1)$$

where anything right of a vertical line represents a condition on the probability.  $\mathcal{L}(\vec{N}|\vec{y})$  is the likelihood of the model with parameters  $\vec{y}$ ,  $\mathcal{P}(\vec{y})$  is the probability for the model, and the denominator is the normalization over all possible constraints on the observations. A frequentist interpretation of a PDF is a proportion of outcomes of repeated trials or experiments. A likelihood function is an expression of the probability of observing data as a function of the model parameters in their appropriate ranges.

One arrives at (2.1) by using the definition of compound probabilities

$$\mathcal{P}(A, B) = \mathcal{P}(B|A)\mathcal{P}(A) \quad (2.2)$$

to evaluate  $\mathcal{P}(\vec{y}|\vec{N})$  as

$$\mathcal{P}\left(\underbrace{\vec{y}}_B \middle| \underbrace{\vec{N}}_A\right) = \frac{\mathcal{P}(\vec{N}, \vec{y})}{\mathcal{P}(\vec{N})} \quad (2.3)$$

with the denominator here is recognized as the normalization of the PDF. The compound PDF  $\mathcal{P}(\vec{N}, \vec{y})$  can expanded using Bayes' theorem which states

$$\mathcal{P}(A|B)\mathcal{P}(B) = \mathcal{P}(B|A)\mathcal{P}(A), \quad (2.4)$$

and combined with (2.2) yielding

$$\mathcal{P}\left(\underbrace{\vec{N}}_A, \underbrace{\vec{y}}_B\right) = \mathcal{P}(\vec{N}|\vec{y}) \times \mathcal{P}(\vec{y}), \quad (2.5)$$

where the PDFs to the left and right of the  $\times$  operator are recognized as the likelihoods and priors, respectively. Combining resulting in (2.3) and (2.5) reproduces the original expression of (2.1).

## 2.1 BANFF Fit Test Statistic

For the BANFF fit, one considers the problem of trying to maximize the agreement between measured and predicted data histograms. This is equivalent to maximizing a binned likelihood function  $\mathcal{L}$  of the data given a set of parameters in the likelihood function  $\mathcal{L}$  that predict the measured rate. The use of likelihood functions in fits to histogram is explained further in reference [14] and the PDG review on Statistics. By invoking Wilks' theorem, also known as the likelihood ratio theorem, the likelihood maximization procedure is converted into a minimization problem involving a test statistic denoted as a chi-squared. Below is an explanation of the BANFF test statistic,  $\Delta\chi^2$ , and its systematic model terms.

Consider many binned samples that select different charged current topologies. A convenient choice of observables for all the samples are the outgoing charged lepton  $l$  momentum

---

$P_l$  and angle  $\cos \theta_l$  as measured in ND280. Much of this is also documented in TN-220 [39] where additional details can be found. For each  $(P_l, \cos \theta_l)$  analysis bin  $i = 1, 2, \dots, M-1, M$ , the likelihood is given by

$$\mathcal{L}(\vec{N}^d | \vec{N}^p) = \left( \prod_{i=1}^M \left( \vec{N}_i^p \right)^{\vec{N}_i^d} \frac{e^{-\vec{N}_i^p}}{\vec{N}_i^p!} \right) \quad (2.6)$$

where  $\vec{N}_i^d$  is the number of observed data events in the  $i$ th bin and  $\vec{N}_i^p$  is the number of predicted events as a function of nuisance parameters in the  $i$ th bin. One recognizes the likelihood function in (2.6) as a product of Poisson distributions, since this is counting data measured in  $M$  analysis bins. The sets of dependent nuisance parameters, also sometimes called systematics, that affect the predicted event rate are

- cross section physics models, labeled as “xsec”,
- neutrino flux,
- detector biases and inefficiencies.

Given these three sets of systematics, the number of predicted CC events from any neutrino flavor  $\nu_l$  at ND280 is calculated using the general formula

$$N_{\nu_l} = \underbrace{\Phi_{\nu_l}}_{\text{Flux per area}} \left[ \sum_t \underbrace{\left( \sigma_{\nu_l}^t M_t \right)}_{\text{Effective area}} \right] \underbrace{\epsilon_{\nu_l}}_{\text{Efficiency}} , \quad (2.7)$$

where  $\Phi_{\nu_l}$  is the flux of  $l$  flavor neutrinos,  $\sigma_{\nu_l}^t$  is the cross section of the interaction for neutrino flavor  $l$  on target  $t$ ,  $M_t$  is the number of  $t$  targets, and  $\epsilon_{\nu_l}$  is the total efficiency to reconstruct and properly identify the event as  $\nu_l$ CC interactions. Since the cross section is a measure of interaction probability in units of area, multiplication of  $M_t$  represents the effective cross sectional area of material  $t$  in the detector. Each term in (2.7) is modeled carefully and the efficiency term is estimated using Monte Carlo (MC) simulations and control samples. The number of events in a given analysis bin is varied in the BANFF using flux, cross section,

detector efficiency weight functions. In the  $i$ th analysis bin, the number of events in that bin,  $N_i$ , is given by

$$N_i(\vec{b}, \vec{x}, \vec{d}) = w_i^{\text{POT}} (\vec{d})_i^{\text{Det}} \sum_{j=1}^{N_i^{\text{MC}}} \left[ \sum_{k=1}^{N^{\text{Flux}}} \left( \delta_{j,k}^{\text{Flux}} (\vec{b})_k^{\text{Flux}} \right) \prod_{l=1}^{N^{\text{xSyst}}} w_{j,l}((\vec{x})_l^{\text{xsec}}) \right]. \quad (2.8)$$

Here  $w_i^{\text{POT}}$  is the protons on target (POT) weight for analysis bin  $i$  which normalizes the MC statistics to expected data statistics. To account for the detector inefficiencies, the  $(\vec{d})_i^{\text{Det}}$  parameters are normalization parameters that vary the total number of predicted events in the  $i$ th bin. Each  $(\vec{d})_i^{\text{Det}}$  is determined prior to the fit by surveying over a large number of toy experiments with the detector systematics varied in each. The sum over  $j = 1, 2, \dots, N_i^{\text{MC}} - 1, N_i^{\text{MC}}$  considers the contribution of all MC events in the  $i$ th analysis bin. The  $(\vec{b})_k^{\text{Flux}}$  parameters, out of a total of  $N^{\text{Flux}}$ , are flux normalization systematics for each flux bin. Since the flux bins are categorized not only by neutrino energy, but also by flavor and horn current, the  $\delta_{j,k}^{\text{Flux}}$  term in the sum over  $k$  selects the correct flux bin. The parameters  $w_{j,l}$  are pre-calculated weights as a function for the  $l$ th cross section model,  $(\vec{x})_l^{\text{xsec}}$ , with a total of  $N^{\text{xSyst}}$  cross section model terms. Different  $t$  target materials have separate cross section parameters. Also the number of targets  $M_t$  can vary via detector systematics.

Using the likelihood ratio test theorem, a test statistic is defined as taking -2 times the natural logarithm of the ratio of predicted to observed likelihoods

$$\Delta\chi_{\text{LLR}}^2 = -2 \log \frac{\mathcal{L}(\vec{N}^d | \vec{N}^p)}{\mathcal{L}(\vec{N}^d | \vec{N}^d)}, \quad (2.9)$$

where this test statistic  $\Delta\chi_{\text{LLR}}^2$  obeys a true chi-squared distribution for asymptotically large statistics and the likelihood functions are of the form (2.6). The denominator in (2.9) is the MC predicted probability which assumes the best maximum likelihood estimate is the number of observed events. Penalty terms from the cross section, flux, and detector systematics are

included in order to force the results to be consistent with systematic uncertainties. The new test statistic for all of ND280,  $\Delta\chi^2_{\text{ND280}}$ , is given by

$$\begin{aligned}\Delta\chi^2_{\text{ND280}} &= \Delta\chi^2_{\text{LLR}} + \Delta\chi^2_{\text{xsec}} + \Delta\chi^2_{\text{Flux}} + \Delta\chi^2_{\text{Det}} \\ &\quad - 2 \left( \log \frac{\mathcal{L}(\vec{N}^d | \vec{N}^p)}{\mathcal{L}(\vec{N}^d | \vec{N}^d)} + \underbrace{\log \pi(\vec{x})}_{\text{xsec}} + \underbrace{\log \pi(\vec{b})}_{\text{Flux}} + \underbrace{\log \pi(\vec{d})}_{\text{Det}} \right),\end{aligned}\quad (2.10)$$

where each of the PDFs  $\pi(\vec{y} = \vec{x}, \vec{b}, \vec{d})$  are assumed multivariate normal distributions

$$\pi(\vec{y}) = C_y e^{(-\frac{1}{2}\Delta\vec{y} \cdot V_y^{-1} \cdot \Delta\vec{y}^T)}, \quad (2.11)$$

$\Delta\vec{y}$  is a vector with the difference between the current/explored and nominal set of vector parameters  $\vec{y}$ ,  $T$  corresponds to the transpose operator, and the normalization is given by

$$C_y = ((2\pi)^{k_y} \det(V_y))^{-\frac{1}{2}} \quad (2.12)$$

with  $V_y$  being the covariance matrix for a vector  $\vec{y}$  with  $k_y$  rows. The expanded form of the test statistic  $\Delta\chi^2_{\text{ND280}}$  is given by

$$\begin{aligned}\Delta\chi^2_{\text{ND280}} &= 2 \sum_{i=1}^M \left[ \vec{N}_i^p - \vec{N}_i^d + \vec{N}_i^d \log \left( \frac{\vec{N}_i^d}{\vec{N}_i^p} \right) \right] \\ &\quad + \Delta\vec{x} \cdot (V_x^{-1}) \cdot \Delta\vec{x}^T + \Delta\vec{b} \cdot (V_b^{-1}) \cdot \Delta\vec{b}^T + \Delta\vec{d} \cdot (V_d^{-1}) \cdot \Delta\vec{d}^T\end{aligned}\quad (2.13)$$

where the “ $\cdot$ ” is the matrix multiplication operator. It must be stated that the test statistic (2.13) purposefully *excludes normalization terms*. The specific parameterization of the penalty terms in (2.13) will be further discussed in Chapter 4. Once the global minimum of the test statistic is found, the postfit covariance matrix  $V$  is calculated as the inverse of the Hessian matrix  $H$

$$V_{i,j}^{-1}(\hat{\vec{y}}) = H_{i,j} = \left. \frac{\partial^2}{\partial y_i \partial y_j} (\Delta\chi^2_{\text{ND280}}) \right|_{\vec{y}=\hat{\vec{y}}} \quad (2.14)$$

---

---

where  $y_i, y_j \in \vec{y}$  and  $\hat{\vec{y}}$  is the maximum likelihood estimate for the parameters  $\vec{y}$ .

---

# Chapter 3

## The PØD Selections and Samples

This chapter describes the development of  $\nu_\mu$  and  $\bar{\nu}_\mu$  CC inclusive selections in both FHC and RHC beam configuration for PØD-based analyses. These selections are the continuation of previous works that developed  $\nu_\mu$  CC inclusive selections between the PØD and the TPC. The first such analysis was the  $\nu_\mu$  CC inclusive cross-section using the previous ND280 simulation and reconstruction software called Production 5 [27]. That analysis relied on each sub-detector's reconstruction software and developed a track matching algorithm since the ND280 “Global” reconstruction matching was not available in that software production. Another cross section analysis measuring the cross section ratio of  $\bar{\nu}_\mu/\nu_\mu$  also used this “pre-Global” technique with the modern T2K Production 6 software [6]. As the inter-detector matching reconstruction became available in Global, two cross section analyzes,  $\nu_\mu$  CC  $0\pi$  [7] and  $\bar{\nu}_\mu$  CC  $0\pi$  [9, 18], were developed that also used the CC inclusive selection as pre-selection cuts. These pre-selection cuts are well validated and have published results as shown in Figure 3.1 on page 62. The selections described in this thesis also employ the same pre-selection cuts with the latest stable Global reconstruction software, Production 6.

This paragraph is a layout of the topics in the chapter. The first topic is the event reconstruction using the “Global” reconstruction software. Next is the pre-selection cut flow. With the pre-selection cuts established, each of the three CC inclusive selection’s cut

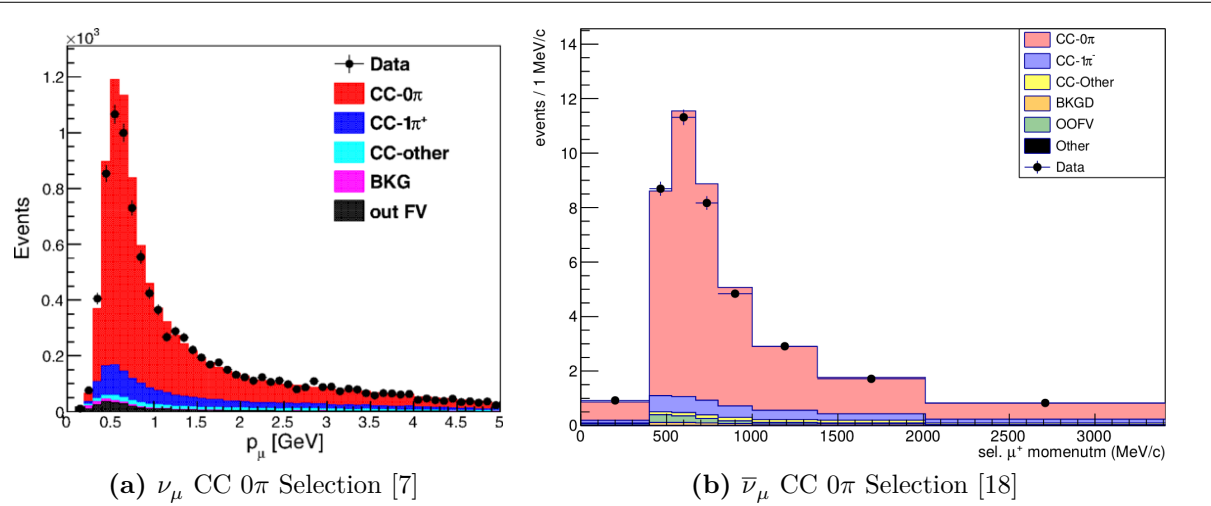


**Figure 3.1:** Data and MC distributions of the PØD water-in  $\nu_\mu$  and  $\bar{\nu}_\mu$  CC  $0\pi$  signal selections. They importantly share the same pre-selection cuts as this analysis. The plots have been normalized to data POT and are sorted into various truth topologies.

flow is described. Concluding this section is a discussion of the three samples in the following order:  $\nu_\mu$  in FHC mode,  $\bar{\nu}_\mu$  in RHC, and  $\nu_\mu$  background in RHC.

### 3.1 Global Reconstruction

The task of the Global reconstruction is to combine all the ND280 information into a combined reconstructed object. It was originally designed to analyze “CCQE-like” events in the Tracker, FGD+TPC, region and has been extended to operate with all of ND280. A brief description of the Global reconstruction is described below.

The Global reconstruction is a software package that attempts to recognize patterns in data events to form tracks and find their common origin, or vertices, for those tracks. Particle shower reconstruction in Global will not be discussed in this thesis since no shower objects are considered. Each sub-detector reconstruction is run separately as the seed to Global’s track matching algorithms. This includes the PØD’s track-finding algorithms, which defines a PØD track as a sequence of nodes each at a single bar layer. To facilitate inter-detector matching, Global attempts to re-fit the PØD track using a Kalman filter [64]. The re-fit procedure also corrects for particle energy loss as a function of length ( $dT/dx$ ) and multiple

---

scattering processes. A PØD vertex, which is the reconstructed location of the neutrino interaction, is then associated with the re-fit track using another Kalman filter algorithm. Matching tracks between the PØD and the TPC is done automatically in the ND280 Global fit.

## 3.2 PØD Selection Cuts

The selection of CC inclusive events use a series of cuts to select the primary lepton. Prior to any cuts and after the reconstruction, corrections are applied first to both data and MC events to correct for well known residual differences between them. This includes the correcting the particle  $dT/dx$  in the TPC. The pre-selection cuts (“precuts”) are then applied to extract events that start in the PØD fiducial volume (FV). A minimum ionizing particle (MIP) is more likely to reach TPC1 from the PØD FV since the PØD is constructed out of heavy materials especially in the CECal. So the main track each selection is designed to select a muon.

This following sections will describe the precuts common to all CC inclusive selections and the branching of different cuts, after the precuts, to select the main track.

### 3.2.1 Precuts

The precuts were initially developed to select  $\nu_\mu$  CC inclusive to select events using the PØD and TPC sub-detector reconstruction softwares separately [6, 27]. They were then used with the Global reconstruction software for the  $\nu_\mu$  CC- $0\pi$  selection in the FHC beam configuration [7]. The description and sequence of the precuts is described below.

The following precuts are checked on the collected data from each Trip-T integration cycle as follows:

1. The event has a “good” data quality flag.

- An event is rejected if any sub-detector or electronics in ND280 reported as “bad” during that bunch.
2. There is at least one (1) track reconstructed in TPC1.
    - There are no restrictions on the number of tracks fully contained in the PØD or exiting into other sub-detectors.
  3. The track in the TPC must have more than 18 nodes.
    - The TPC reconstruction gathers vertical and horizontal hits into clusters of hits. The charge distribution of the cluster is used to get a vertical (horizontal) position that is more accurate than the individual readout pads. A node is constructed out of each cluster with associated track state information. The set of nodes are used to fit a helix shaped track.
  4. The reconstructed vertex is within the PØD water target (WT) FV.
    - The PØD FV is defined to include as much as the WT regions as possible. Its X and Y borders are 25 cm away from the PØDule edges while its Z borders intersect the last and first half downstream PØDule in the USECal and CECal, respectively. The enumerated volume edges are shown in Table 3.1 on page 65. This volume, while used for track-based analyzes in the past, was optimized for  $\pi^0$  and  $\nu_e$  analyses.
  5. All tracks that enter the TPC pass the veto cut
    - An event is rejected if any PØD track enters the TPC from outside the “corridor” volume. This cut was designed to eliminate broken tracks between the PØD and TPC1 the pre-Global separate sub-detector reconstruction was used [19]. In practice, this cut ensures that Global tracks entering the TPC are away from its X and Y edges. The corridor definition is the same as defined in the pre-published  $\bar{\nu}_\mu/\nu_\mu$  cross section ratio analysis [20] and shown in Table 3.1 on page 65.

PØD WT FV			Corridor Volume		
-836	< X <	764	-988	< X <	910
-871	< Y <	869	-1020	< Y <	1010
-2969	< Z <	-1264	-3139	< Z <	-900

**Table 3.1:** The PØD WT FV (left) and veto corridor volume (right) in the ND280 coordinate system. The corridor spans from the 5th (8th) to 40th (80th) PØDule (scintillator layer). All the units are given in millimeters.

After passing all the precuts, a single, global track, which is observed in TPC1, is assigned as the lepton candidate or “main track” of a selection.

The momentum of the main track,  $P$ , is sum of its momentum in the TPC,  $P_{\text{TPC}}$ , with the estimate momentum lost in the PØD,  $\Delta P_{\text{PØD}}$

$$P = P_{\text{TPC}} + \Delta P_{\text{PØD}}. \quad (3.1)$$

Momentum lost in the PØD is estimated by first summing the total energy loss,  $\Delta T$ , along the track path  $\mathcal{C}$

$$\Delta T = \int_{\mathcal{C}} \left( \frac{dT}{dx} \right) dx. \quad (3.2)$$

Using the chain rule, we can convert the energy loss function,  $dT/dx$ , into momentum loss

$$\begin{aligned} \frac{dT}{dx} &= \left( \frac{dT}{dP} \right) \left( \frac{dP}{dx} \right) \\ &= \left( \frac{Pc^2}{E} \right) \left( \frac{dP}{dx} \right) \\ &= \beta c \left( \frac{dP}{dx} \right), \end{aligned} \quad (3.3)$$

where  $\beta$  is the changing particle velocity as a ratio of the speed of light  $c$ . The fundamental theorem of Calculus permits us to write the energy loss as a momentum loss along the track’s

path  $\mathcal{C}$  as

$$\Delta P_{\text{P}\bar{\text{O}}\text{D}} = \int_{\mathcal{C}} \left( \frac{dP}{dx} \right) dx = \frac{1}{c} \int_{\mathcal{C}} \left[ \left( \frac{dT}{dx} \right) \frac{1}{\beta(x)} \right] dx. \quad (3.4)$$

Since the reconstructed track's path  $\mathcal{C}$  is not infinitesimally precise due to inherent detector resolution, we must replace the integral with a sum and differential  $dx \rightarrow \Delta x$ . We then arrive at the expression of the momentum loss estimate in the P $\bar{\text{O}}$ D as

$$P = P_{\text{TPC}} + \frac{1}{c} \sum_t \left[ \left( \frac{dT}{dx} \right) \left( \frac{\Delta x}{\beta(x)} \right) \right]_t. \quad (3.5)$$

For most tracks entering the TPC, they will be highly relativistic in the P $\bar{\text{O}}$ D ( $\beta \approx 1$ ), and (3.5) simplifies to

$$P = P_{\text{TPC}} + \frac{1}{c} \sum_t \left[ \left( \frac{dT}{dx} \right) \Delta x \right]_t \quad (3.6)$$

The next sections describe the selection cuts, first in FHC mode and then RHC mode.

### 3.2.2 The $\nu_\mu$ CC Inclusive in FHC Cut

- The highest momentum negatively charged track (HMNT) is the lepton candidate

As discussed in Section section 3.2.1 on page 63, this selection is the basis for the P $\bar{\text{O}}$ D  $\nu_\mu$  CC-0 $\pi$  analysis [7]. In FHC mode, the vast majority of neutrino interactions are  $\nu_\mu$ CC events producing an outgoing, negatively charged muon. So if there is no negatively charged track in the TPC, the event is rejected.

### 3.2.3 The $\bar{\nu}_\mu$ CC Inclusive in RHC Cuts

- The highest momentum positively charged track (HMPT) is the lepton candidate
- The HMPT must be the highest momentum track (HMT)

In RHC, the majority of neutrinos in the beam is  $\bar{\nu}_\mu$  since the horn focuses negatively charged pions. To select  $\bar{\nu}_\mu$  CC interaction events, the lepton candidate is the HMPT in the TPC.

---

The event is rejected if there is no positively charged track. However, since the RHC mode beam is not as  $\bar{\nu}_\mu$  pure as the FHC beam is for  $\nu_\mu$ , another cut was added to reduce this effect.

Since RHC neutrino beam can be described as a  $\bar{\nu}_\mu$ -enhanced beam, the HMPT must also be the HMT due to the significant “wrong-sign”  $\nu_\mu$  background. This effect is two fold due to the nature of the neutrino source and the cross section between neutrinos and antineutrinos. Firstly the neutrino flux is larger in RHC mode due to neutrino production at the target. The source of neutrinos are from mainly positively charged pions and kaons decays produced proton collisions on a graphite target. This method is more likely to produce positively charged pions in the target than negatively charged one. While the horns are designed to select the negatively charged pions in RHC mode, the excess amount of positively charged pions will penetrate this filter. Therefore there are many more  $\pi^+ \rightarrow \mu^+ + \nu_\mu$  decays in RHC compared to FHC mode. Secondly, antineutrino interactions on matter are suppressed by  $\sim 1/3$  compared to neutrinos due to helicity considerations as explained in Section 1.1.1.

### 3.2.4 The $\nu_\mu$ Background CC Inclusive in RHC Cuts

- The highest momentum negative track (HMNT) is the lepton candidate
- The HMNT must be the highest momentum track (HMT)

As discussed in section 3.2.3 on the facing page, the RHC neutrino beam has a significant wrong-sign  $\nu_\mu$  background. The selection of the HMNT is designed to select the negatively charged muons. To prevent selecting the antineutrino events, the HMNT must also be the HMT. The event is rejected if there is no negatively charged track. If there are both positively and negatively charged tracks, the HMT cut discriminates if the event originates from a  $\nu_\mu$  or  $\bar{\nu}_\mu$ .

Run period	Horn current [kA]	PØD status	Data POT ( $\times 10^{20}$ )	MC POT ( $\times 10^{20}$ )
2	+250	Water	0.4339	12.03
		Air	0.3591	9.239
3b	+205		0.2172	4.478
3c	+250		1.364	26.32
4			1.782	34.99
		Water	1.642	34.97
5c	-250		0.4346	22.77
6b		Air	1.288	14.17
6c			0.5058	5.275
6d			0.7753	6.884
6e			0.8479	8.594
7b		Water	2.436	33.70
8	+250		1.580	26.46
		Air	4.148	36.06
Sand	+250		-	11.19
Sand	-250		-	12.92
2, 3b, 3c, 4, 8	FHC	Air	7.872	79.18
2, 4, 8		Water	3.657	73.47
6b, 6c, 6d, 6e	RHC	Air	3.417	34.92
5c, 7b		Water	2.871	56.48

**Table 3.2:** T2K MC and data POT divided by run periods. The bottom four rows are the aggregated periods grouped by horn current and PØD status which is how the data analysis is performed.

### 3.3 Selection Kinematics

This section examines the kinematics for each of selections while differentiating between water-in and water-out mode. The selection cuts were implemented in Psyche which is the software interface that BANFF uses to select events. The data sets used in this analysis are runs 2-8 in both PØD water-in and water-out (air) modes as shown in Table 3.2 on page 68. There will be no data events shown to prevent any potential biases that exist between the data and MC. Simulated events will be broken down into various true categories to understand selection kinematics, efficiencies, and purities.

True interactions for these selections are generally divided into four interactions classes:

- neutrino-induced CCQE ( $\nu$  CCQE):
  - Only NEUT generated neutrino-induced CCQE event at the interaction vertex
- neutrino-induced non-CCQE ( $\nu$  non-CCQE),
  - Any NEUT generated neutrino-induced CC and NC event *except* neutrino-induced CCQE at the interaction vertex
- antineutrino-induced CCQE ( $\bar{\nu}$  CCQE)
  - Only NEUT generated antineutrino-induced CCQE event at the interaction vertex
- antineutrino-induced non-CCQE ( $\bar{\nu}$  non-CCQE)
  - Any NEUT generated antineutrino-induced CC and NC event *except* antineutrino-induced CCQE at the interaction vertex

An enlarged legend of these four interaction classes used in this analysis is shown in Figure 3.2 on page 70. Out of fiducial volume (OOFV) events refer to neutrino and antineutrino interactions occurring in ND280, but not in the PØD water target (WT) fiducial volume (FV). Sand muons, similar to OOFV events, are any neutrino/antineutrino-induced interaction truly occurring in the sand surrounding the ND280 pit.

The non-CCQE category can be further divided among the dominant T2K CC and all NC interactions modes as enumerated in Table 3.3 on page 70 and Table 3.4 on page 71. For neutrino-based selections, the legend shown in Figure 3.4 on page 72 is also used to describe the neutrino-induced interaction purity of the selection. Similarly for antineutrino-based selections, the legend shown in Figure 3.5 on page 72 is used for the same purpose.

The true particle matched with the main track is also analyzed here as shown in Figure 3.3 on page 71. The ND280 MC uses the GEANT4 software toolkit [12] to simulate the passage of particles through matter. A GEANT4 particle is assigned to a reconstructed track if it contributed the most to the track's reconstructed hits. True particles include protons (p)

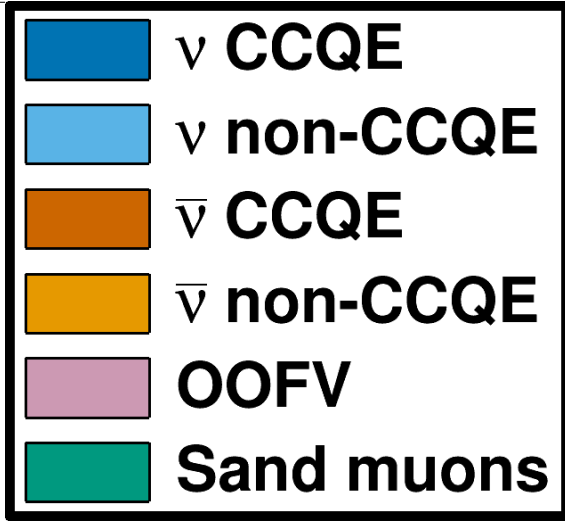


**Figure 3.2:** NEUT CCQE and non-CCQE interactions legend. The enumerated NEUT codes are given in Figure 3.4 on page 72 and Figure 3.5 on page 72.

Category	NEUT Codes
$\nu$ CCQE	1
$\nu$ 2p2h	2
$\nu$ CC-1 $\pi$	11 → 16
$\nu$ non-CCQE	$\nu$ CC-N $\pi$
	21
$\nu$ CC-DIS	26
$\nu$ CC-Other	17, 22, 23
$\nu$ NC	31 → 100
$\bar{\nu}$	−1 → −100
OOFV	−100 → 100
Sand muons	−100 → 100

**Table 3.3:** The expanded  $\nu$  NEUT reactions table as shown in Figure 3.4 on page 72. An arrow indicates a sequence of integer steps from left to right of the arrow.

Category	NEUT Codes
$\bar{\nu}$ CCQE	-1
$\bar{\nu}$ 2p2h	-2
$\bar{\nu}$ CC-1 $\pi$	-11 → -16
$\bar{\nu}$ non-CCQE	$\bar{\nu}$ CC-N $\pi$ $\bar{\nu}$ CC-DIS $\bar{\nu}$ CC-Other $\bar{\nu}$ NC
$\bar{\nu}$ CC-N $\pi$	-21
$\bar{\nu}$ CC-DIS	-26
$\bar{\nu}$ CC-Other	-17, -22, -23
$\bar{\nu}$ NC	-31 → -100
$\nu$	1 → 100
OOFV	-100 → 100
Sand muons	-100 → 100

**Table 3.4:** The expanded  $\bar{\nu}$  NEUT reactions table as shown in Figure 3.5 on page 72.

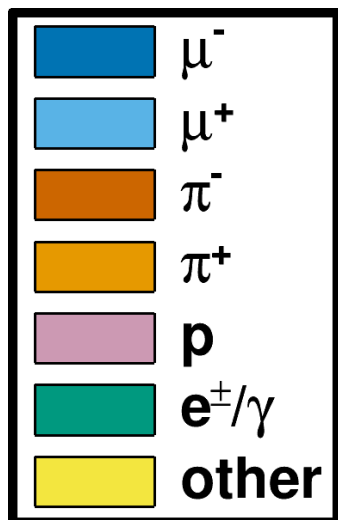


**Figure 3.3:** True particle selected legend

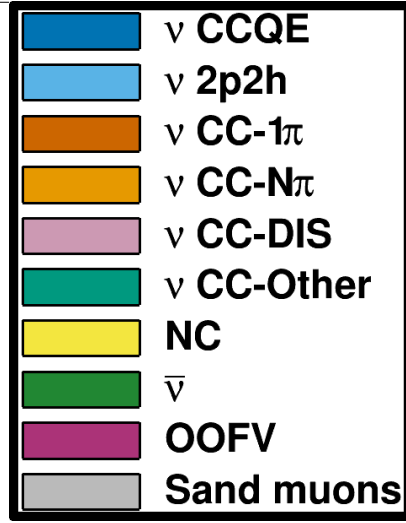


**Figure 3.4:** The NEUT neutrino interaction legend used in this analysis. The labels are enumerated in Table 3.3 on page 70.

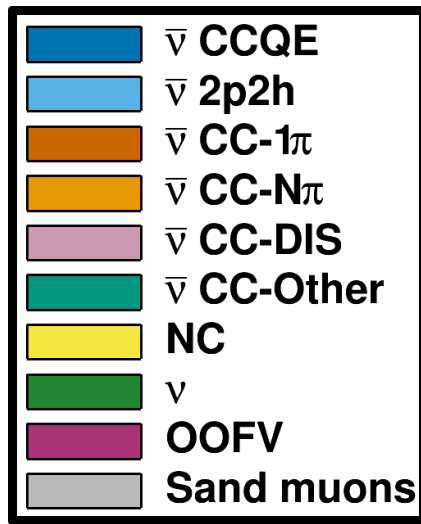


**Figure 3.5:** NEUT antineutrino interaction legend used in this analysis. The labels are enumerated in Table 3.4 on page 71.

---

and both negatively and positively charged muons ( $\mu^\pm$ ), pions ( $\pi^\pm$ ), and electrons/positrons ( $e^\pm$ ). In addition, any electron and positron generated from pair production are grouped together as “ $e^\pm/\gamma$ ”. Particles that do not match any of these categories is labeled as “other”.

### 3.3.1 $\nu_\mu$ in FHC CC 1-Track

This selection provides the CCQE-like samples in FHC mode. Figure 3.6 on page 74 and Figure 3.7 on page 75 displays the momentum and angular distributions that are inputs to BANFF. Comparing between water-in and water-out modes, we see the reconstructed kinematics are nearly identical. In the majority of cases, the lepton candidate is the true muon, making this a very pure  $\nu_\mu$  sample. We also see that there are non-CCQE events which will be better understood in the coming paragraphs. Following this paragraph and the following sections, only the PØD water-in mode kinematics, i.e.  $p$  and  $\cos\theta$ , will be shown.

The target nuclei between water-in and water-out modes is slightly different as seen in Figure 3.8 on page 76. This is expected given that there is atmosphere instead of water in the bags and the simulated neutrino-nucleus scattering target is either an oxygen or hydrogen nucleus. After carbon and oxygen as the most likely targets, copper in the brass layers contribute a significant fraction of events. The events on lead are true OOFV and primarily occur in the last PØDule. Due to a software bug in the MC, coherent events on hydrogen were incorrectly categorized and have their own category.

The underlying true kinematics of the interactions are shown in Figure 3.10 on page 77 which are of theoretical importance in the cross section and flux models. Using Figure 1.5 on page 13 as reference, the true neutrino energy  $E_\nu = k_0$  and 4-momentum transfer  $Q^2 = -q^2$ . An interesting CCQE-like topology in this selection are 2p2h events. Interaction model uncertainties for 2p2h are quite large in T2K and are included the BANFF fit. Therefore these events could help reduce the 2p2h model uncertainties.

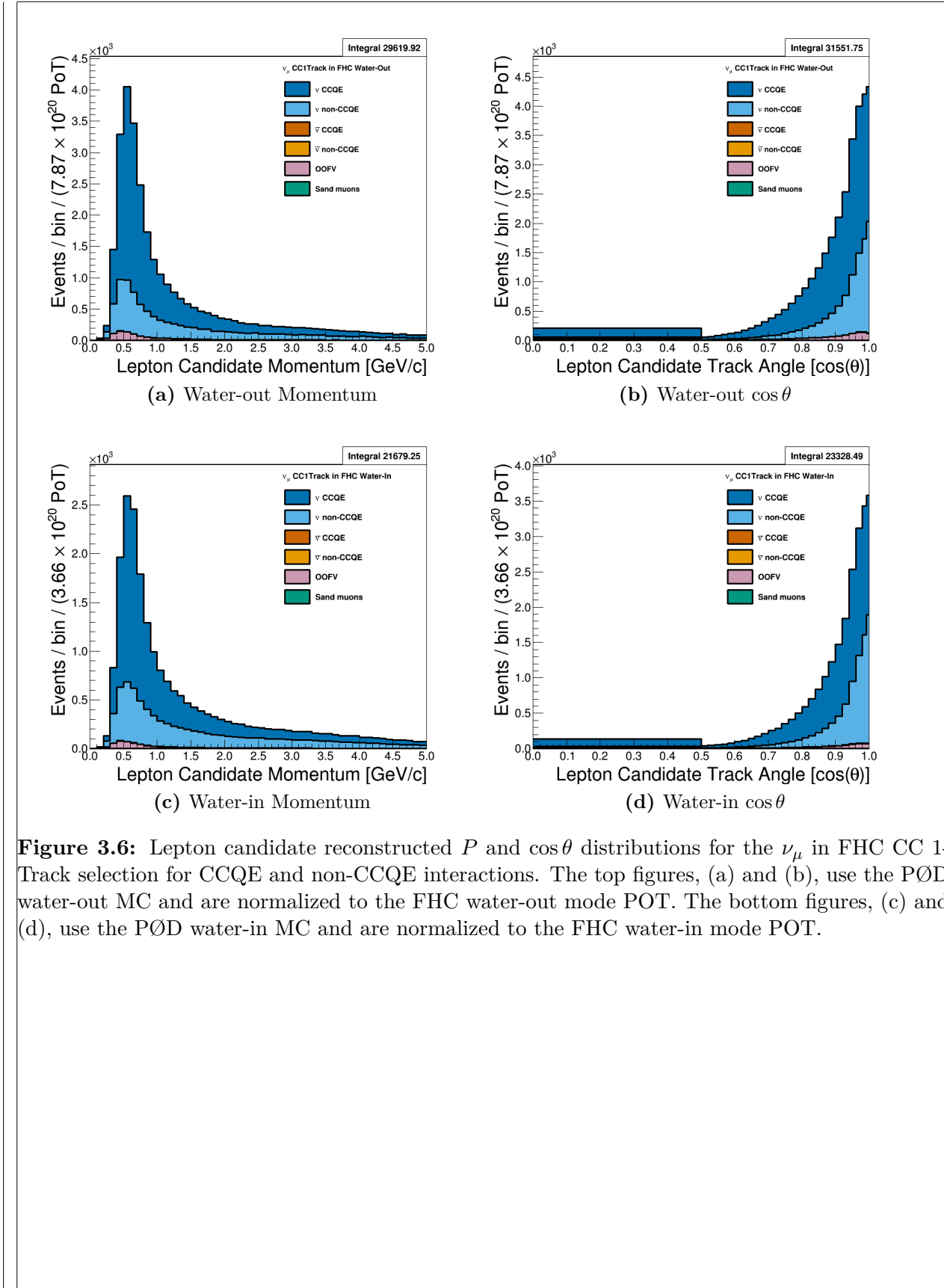


**Figure 3.6:** Lepton candidate reconstructed  $P$  and  $\cos\theta$  distributions for the  $\nu_\mu$  in FHC CC 1-Track selection for CCQE and non-CCQE interactions. The top figures, (a) and (b), use the PØD water-out MC and are normalized to the FHC water-out mode POT. The bottom figures, (c) and (d), use the PØD water-in MC and are normalized to the FHC water-in mode POT.

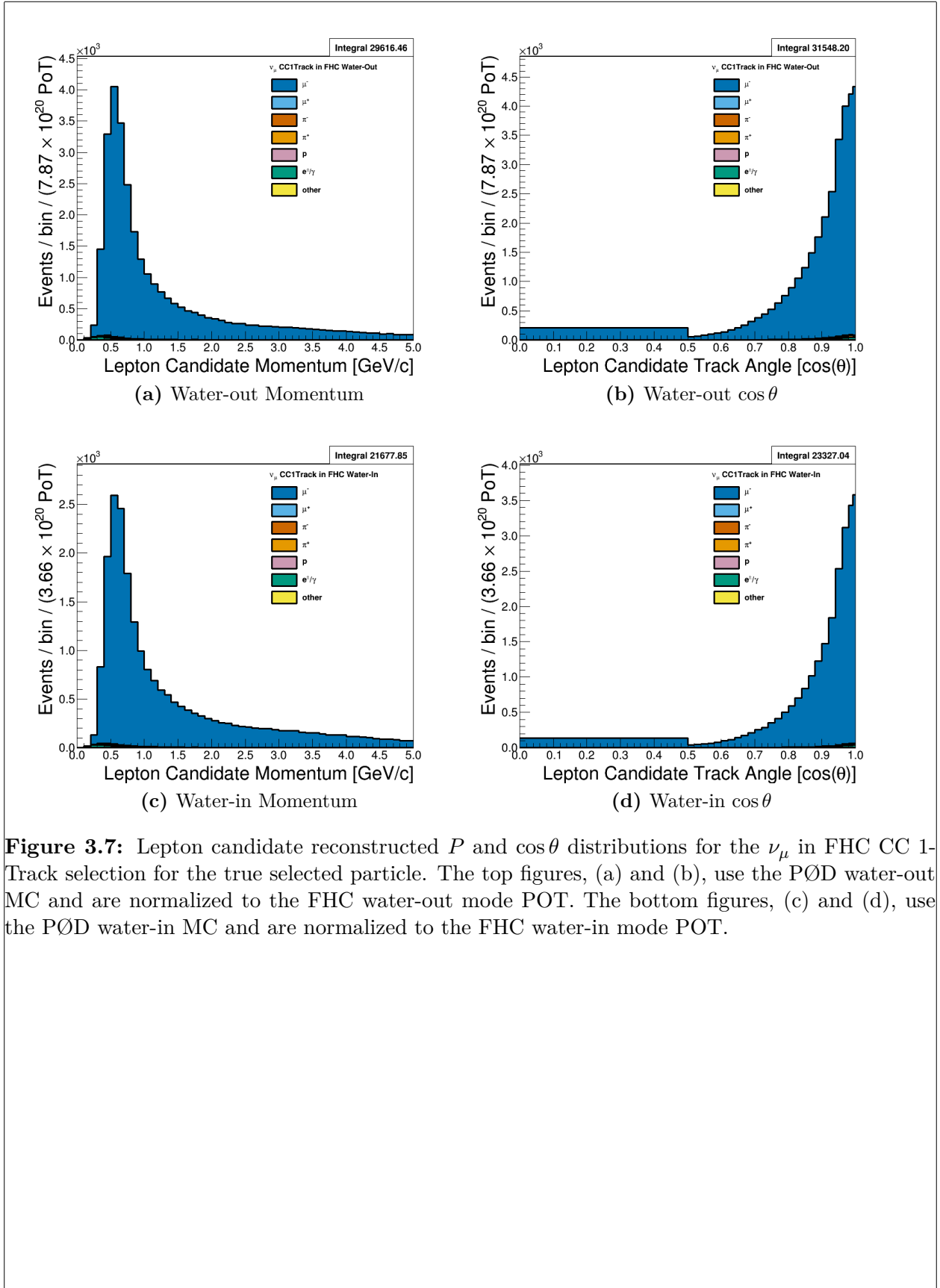
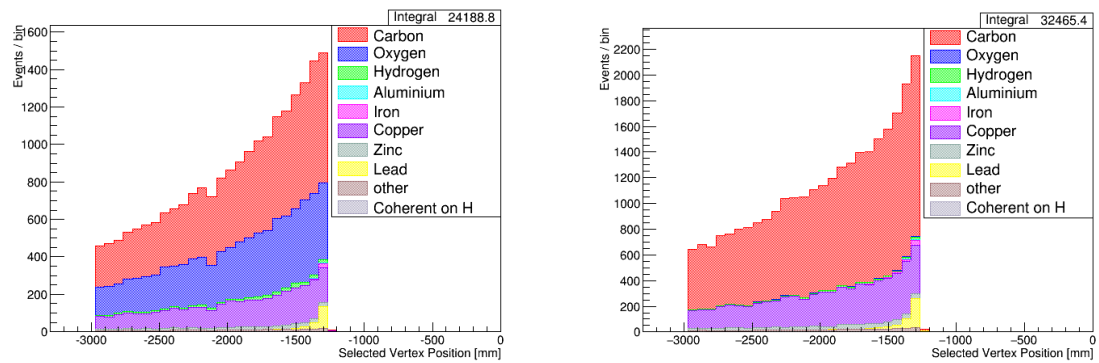


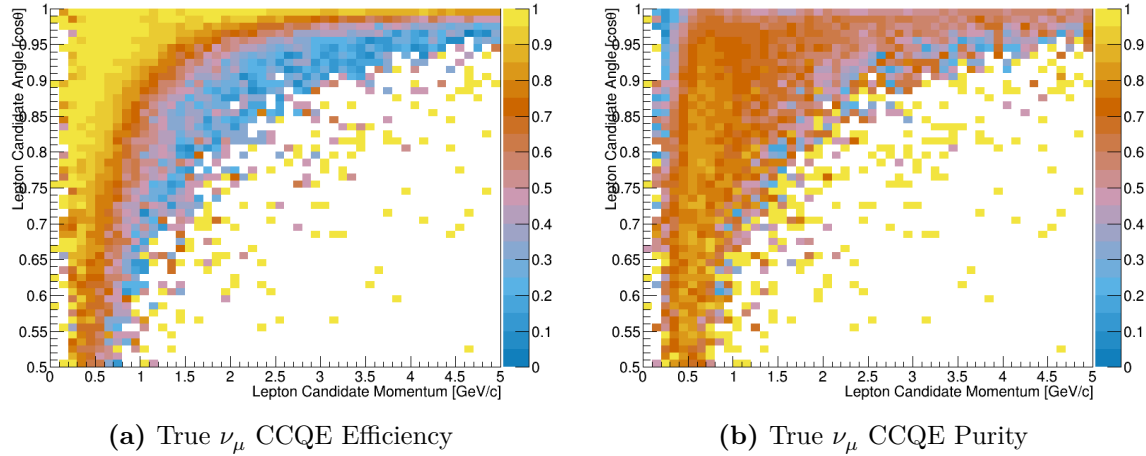
**Figure 3.7:** Lepton candidate reconstructed  $P$  and  $\cos\theta$  distributions for the  $\nu_\mu$  in FHC CC 1-Track selection for the true selected particle. The top figures, (a) and (b), use the PØD water-out MC and are normalized to the FHC water-out mode POT. The bottom figures, (c) and (d), use the PØD water-in MC and are normalized to the FHC water-in mode POT.



(a) Water-in

(b) Water-out

**Figure 3.8:** Vertex Z position of the  $\nu_\mu$  in FHC CC 1-Track selection broken down by true target nucleus. The number of events increases with increasing Z since the probability of an interaction increases as the neutrino crosses more media in the PØD.

(a) True  $\nu_\mu$  CCQE Efficiency(b) True  $\nu_\mu$  CCQE Purity

**Figure 3.9:** The efficiency and purity in reconstructed kinematics of  $\nu_\mu$  CCQE interactions in the  $\nu_\mu$  in FHC CC 1-Track selection. True events are defined as correctly matched  $\mu^-$  tracks from  $\nu_\mu$ -induced CCQE interactions at the vertex .

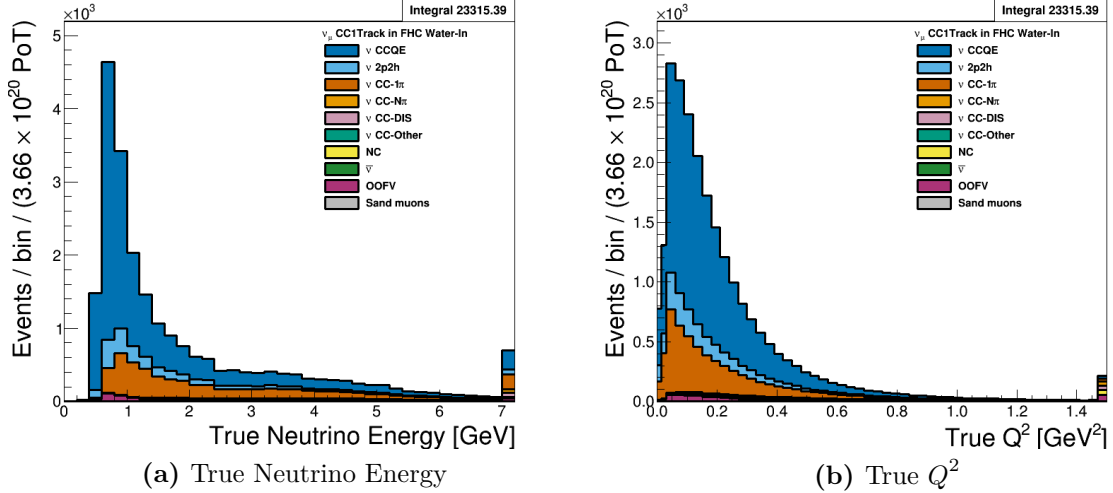


**Figure 3.10:** The  $\nu_\mu$  in FHC CC 1-Track true kinematics broken down by true NEUT interaction modes. Water-in mode is displayed here only with the last bin shown is used as overflow. The figures use the PØD water-in MC and are normalized to the FHC water-in mode POT.

This selection contains a modest fraction of non-CCQE interactions. The largest contamination is  $1\pi$  interactions, which can happen primarily for a couple of reasons. Firstly, when the final state pion is produced, it is subject to final state interactions (FSI) where a pion can be absorbed or scattered in the nucleus. Secondly, and more importantly, a pion might not be reconstructed as a track in the PØD if its energy is below reconstruction threshold. Together, the large  $1\pi$  background affects the CC- $0\pi$  and CC- $1\pi$  model parameters in the BANFF fit.

We can examine the efficiencies and purities differentially for true  $\nu_\mu$  CCQE interactions in Figure 3.9 on page 76. The efficiency,  $\epsilon$ , and purity,  $\rho$ , are defined as

$$\epsilon = \frac{N_{\text{Selected}}^{\text{True}}}{N^{\text{True}}} \quad \rho = \frac{N_{\text{Selected}}^{\text{True}}}{N_{\text{Selected}}}, \quad (3.7)$$

where  $N_{\text{Selected}}^{\text{True}}$  is the number of true, selected events,  $N^{\text{True}}$  is the number of true events, and  $N_{\text{Selected}}$  is the number of selected events. They demonstrate that the purity is highest near 0.5 GeV/c with the efficiency highly dependent on the track angle.

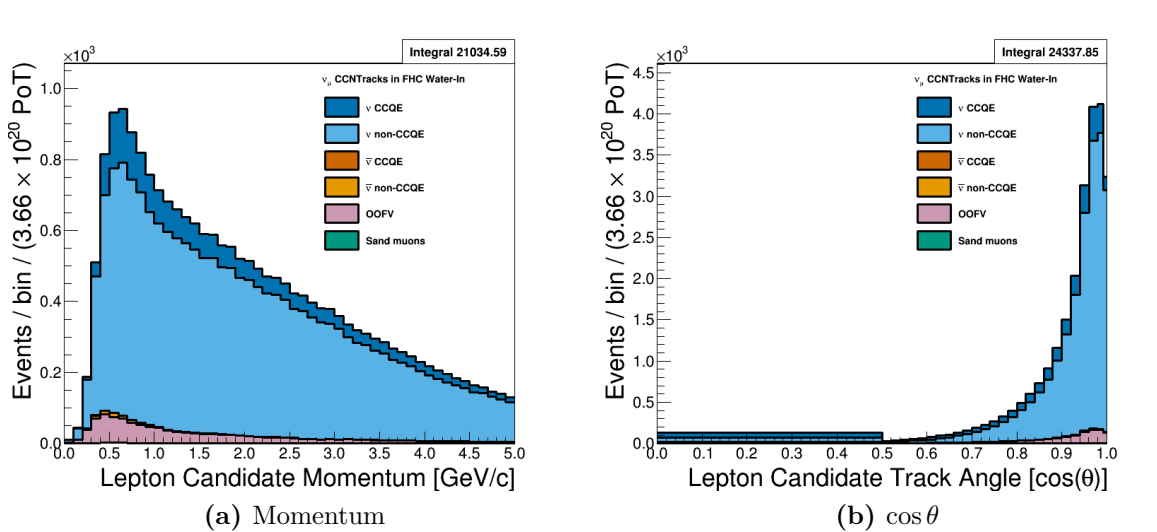


**Figure 3.11:** Lepton candidate reconstructed  $P$  and  $\cos\theta$  distributions for the  $\nu_\mu$  in FHC CC N-Tracks selection for CCQE and non-CCQE interactions. The figures use the PØD water-in MC and are normalized to the FHC water-in mode POT.

### 3.3.2 $\nu_\mu$ in FHC CC N-Tracks

This selection provides non-CCQE-like samples in FHC mode inputs to BANFF. The reconstructed momentum and angular distributions are shown in Figure 3.11 on page 78 and Figure 3.12 on page 79. Since this selection is not optimized for any particular CC topology, there are a variety of interactions modes present including  $1\pi$ , multiple pion ( $N\pi$ ) and deep inelastic scattering (DIS). There are a number of mis-identified lepton candidates in the form of electrons and pions. There is a relatively larger OOFV contamination compared with the 1-Track selection with some events originating in the USECal as seen in Figure 3.13 on page 79. Otherwise, the vertex position and target materials are quite similar between the 1-Track and N-Tracks selections.

We can examine the efficiencies and purities differentially for the selection in Figure 3.14 on page 80. The true signal here is any  $\nu_\mu$  CC interaction except  $\nu_\mu$  CCQE (CC non-QE) which the CC 1-Track selection is designed to select. The efficiency is high for the higher momenta and higher angle tracks suggesting this is a high  $Q^2$  selection. In addition, the purity is around ~70% in this region.

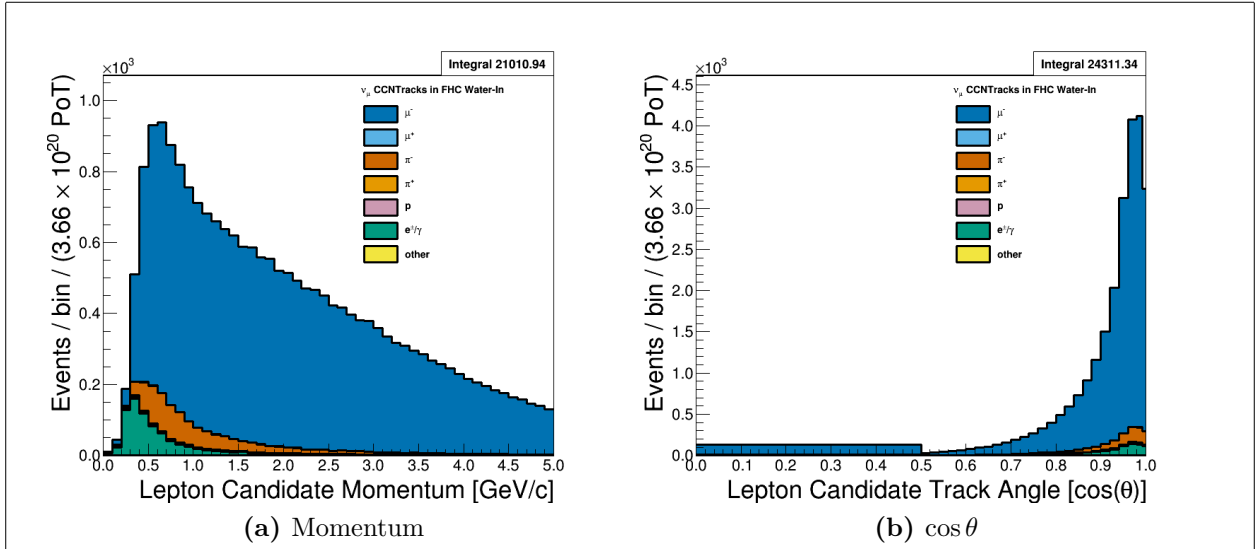


**Figure 3.12:** Lepton candidate reconstructed  $P$  and  $\cos\theta$  distributions for the  $\nu_\mu$  in FHC CC N-Tracks selection for the true selected particle. The figures use the PØD water-in MC and are normalized to the FHC water-in mode POT.

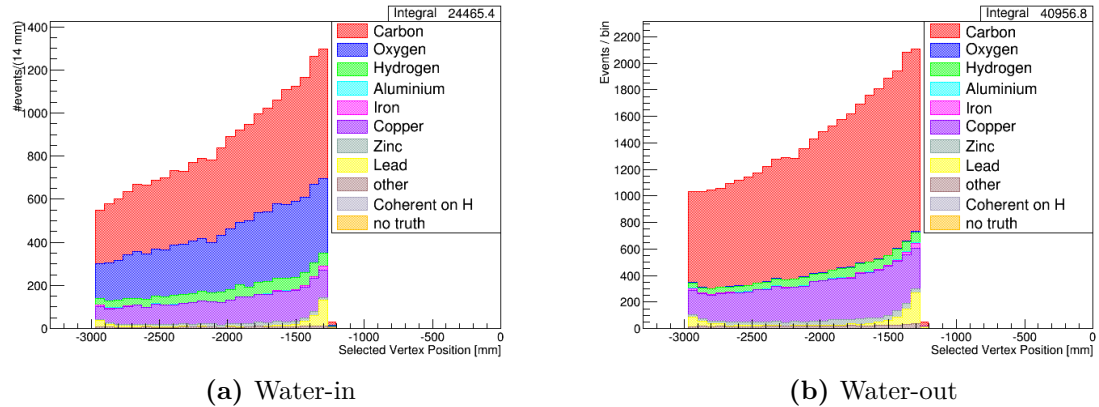


**Figure 3.13:** Vertex position of the  $\nu_\mu$  in FHC CC N-Tracks selection broken down by true target nucleus. The number of events increases with increasing  $Z$  since the probability of an interaction increases as the neutrino crosses more media in the PØD.

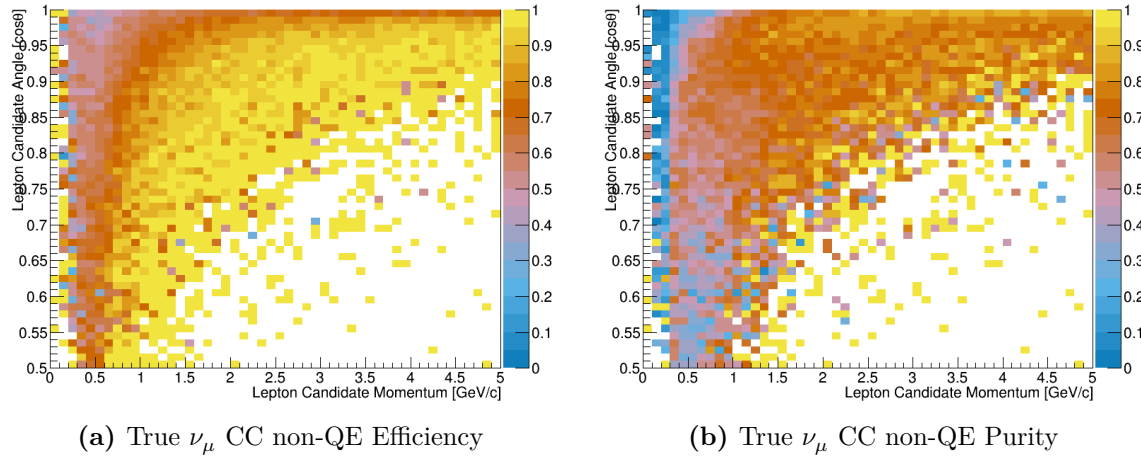


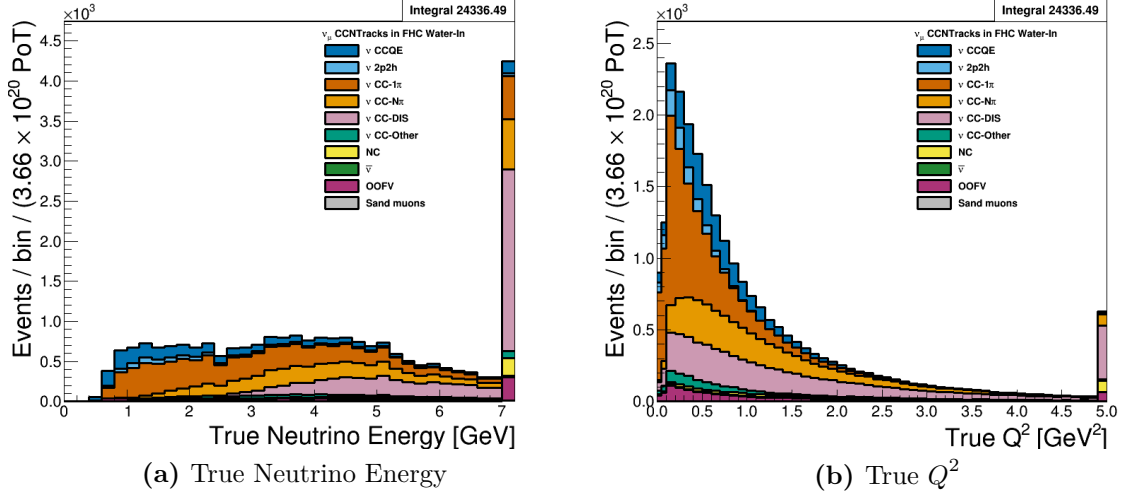
**Figure 3.14:** The efficiency and purity in reconstructed kinematics of  $\nu_\mu$  CC non-QE interactions in the  $\nu_\mu$  in FHC CC N-Tracks selection. True events are defined as correctly matched  $\mu^-$  tracks from  $\nu_\mu$ -induced CC non-QE interactions at the vertex.

The fundamental kinematics of the selection are shown in Figure 3.15 on page 81. The selection is relatively  $\nu_\mu$ -pure and captures the high energy tail of the neutrino flux. True kinematics that describe the  $1\pi$ ,  $N\pi$ , and DIS models are parameterized in  $Q^2$  and the hadronic system mass  $W$ . Using Figure 1.5 on page 13, we can define the invariant mass of hadronic system as

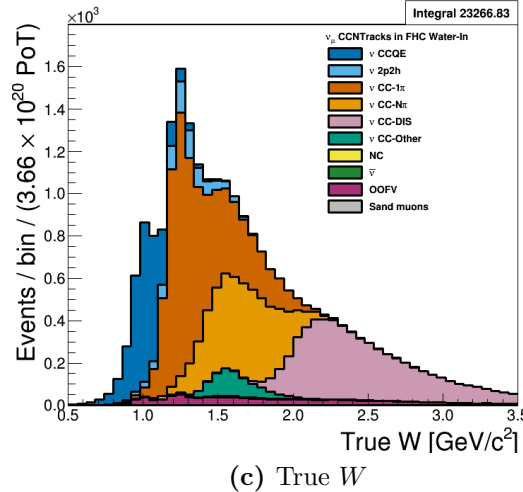
$$\begin{aligned} (Wc^2)^2 &= (p+q)^2 = p^2 + 2p \cdot q + q^2 \\ &= (M_N c^2)^2 + 2(M_N c^2)(k_0 - k'_0) - Q^2, \end{aligned} \tag{3.8}$$

where  $M_N$  is the mass of the struck nucleon and  $k_0/k'_0$  is the energy of the neutrino/outgoing lepton. A dominant mode in the selection are  $1\pi$  events from a  $\Delta$  resonance. A resonance is clearly seen in the  $W$  distribution in Figure 3.15 on page 81 which is the  $\Delta$  baryon which has a rest mass of  $1.232 \text{ GeV}/c^2$ . Higher order resonance states are present as well since there are no cuts to distinguish muons and pions from protons.

The origin of the mis-identified particles, in particular the pions, becomes more clear since this is a high  $Q^2$  selection. Multiple pion and DIS events can produce a negatively charged pion. For high  $Q^2$  interactions topologies, the energy transfer to the final hadronic



(a) True Neutrino Energy

(b) True  $Q^2$ (c) True  $W$ 

**Figure 3.15:** The  $\nu_\mu$  in FHC CC N-Tracks true kinematics broken down by true NEUT interaction modes. The last bin shown in (a) and (b) is used as overflow. The figures use the PØD water-in MC and are normalized to the FHC water-in mode POT.

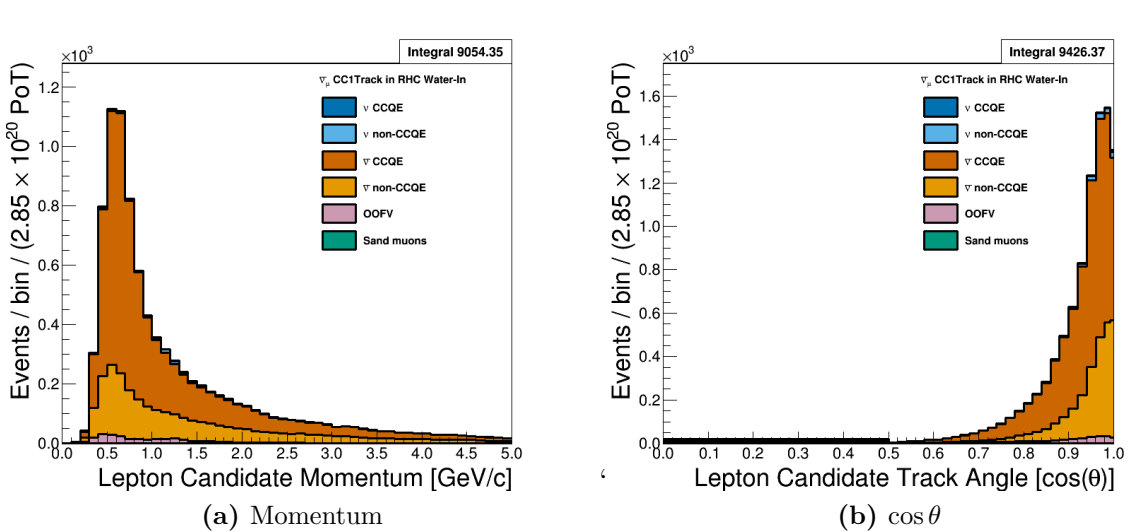


**Figure 3.16:** Lepton candidate reconstructed  $P$  and  $\cos\theta$  distributions for the  $\bar{\nu}_\mu$  in RHC CC 1-Track selection for CCQE and non-CCQE interactions. The figures use the PØD water-in MC and are normalized to the RHC water-in mode POT.

state can produce a higher energy pion than the true muon or the muon does not enter the TPC.

### 3.3.3 $\bar{\nu}_\mu$ in RHC CC 1-Track

This selection provides the  $\bar{\nu}_\mu$  CCQE-like samples in RHC mode that are inputs to BANFF. In Figure 3.16 on page 82 and Figure 3.17 on page 83 display the momentum and angular distributions for this selection. The selection is  $\bar{\nu}_\mu$ -pure with the selected lepton candidate being positively charged muons. There is a large OOFV background from proton tracks. They are high momentum ( $> 1$  GeV/c) tracks which, at these energies, are become minimum ionizing and can reach into the TPC.

We can examine the efficiencies and purities differentially for the selection in Figure 3.18 on page 83. The two distributions are very similar to the  $\nu_\mu$  in FHC CC 1-Track efficiencies and purities, with the efficiency being relatively high (90%) for high statistics regions.

The underlying true kinematics,  $E_\nu$  and  $Q^2$ , of the interactions are shown in Figure 3.19 on page 84. We see a similar true reaction composition to the  $\nu_\mu$  in FHC selection in Section

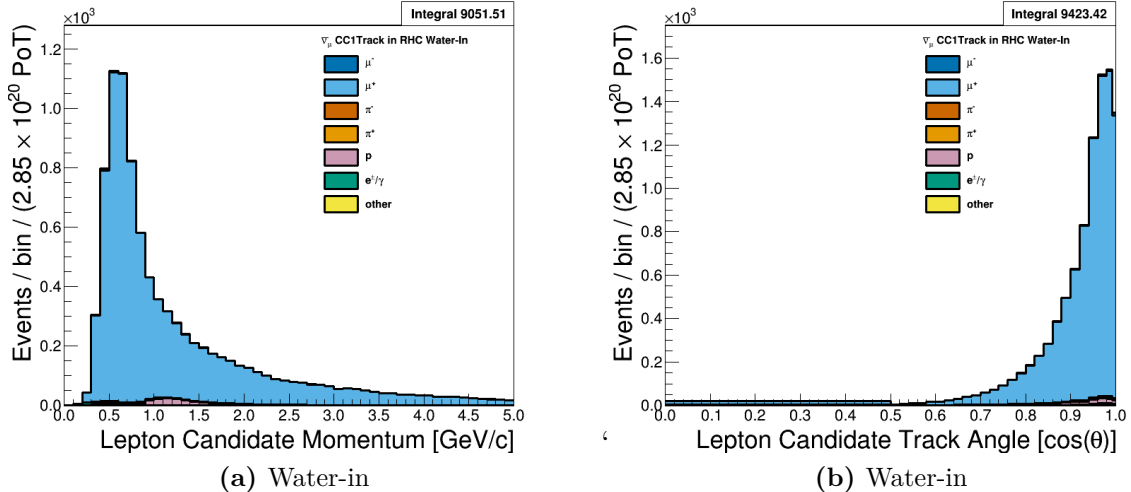


**Figure 3.17:** Lepton candidate reconstructed  $P$  and  $\cos\theta$  distributions for the  $\bar{\nu}_\mu$  in RHC CC 1-Track selection for the true selected particle. The figures use the PØD water-in MC and are normalized to the RHC water-in mode POT.

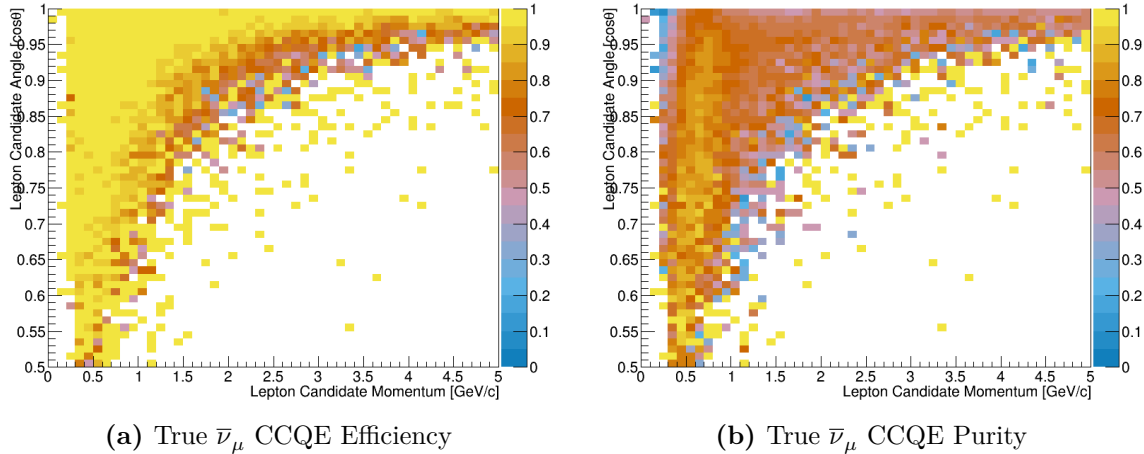


**Figure 3.18:** The efficiency and purity in reconstructed kinematics of  $\bar{\nu}_\mu$  CCQE interactions in the  $\bar{\nu}_\mu$  in RHC CC 1-Track selection. The true events are  $\bar{\nu}_\mu$  CCQE at the vertex and the selected lepton candidate is the true  $\mu^+$ .

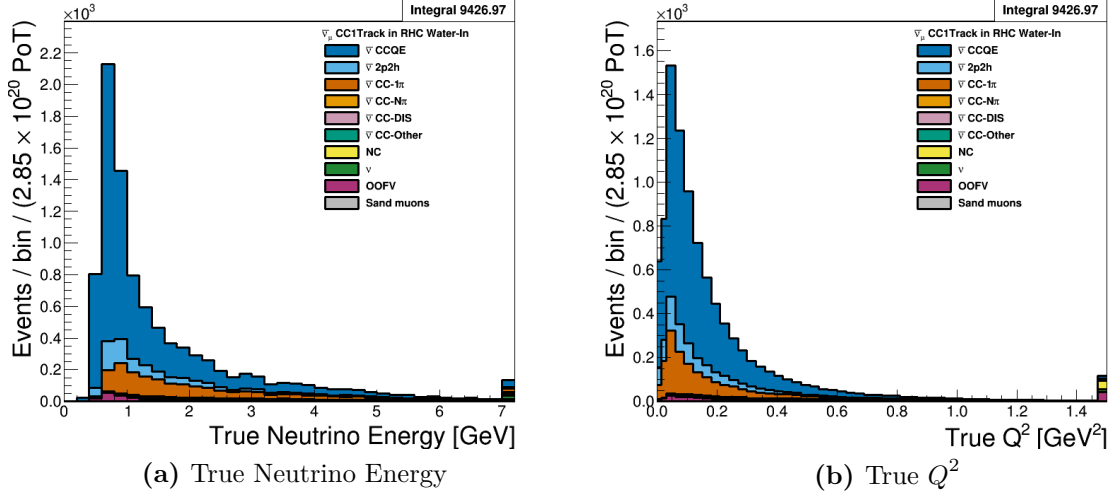


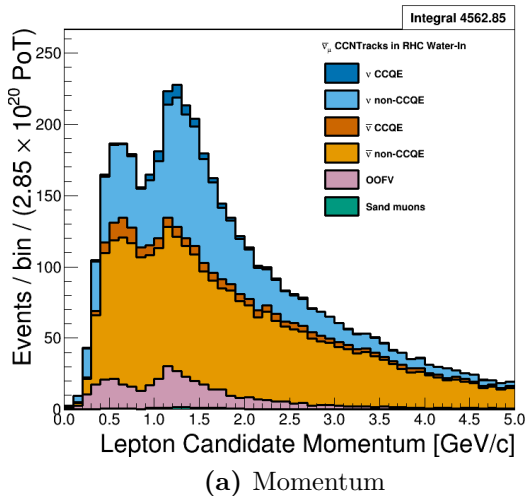
**Figure 3.19:** The  $\bar{\nu}_\mu$  in RHC CC 1-Track true kinematics broken down by true NEUT interaction modes. Water-in mode is displayed here only with the last bin shown is used as overflow. The figures use the PØD water-in MC and are normalized to the RHC water-in mode POT.

3.3.1. Most reactions are true CCQE with a mixture of 2p2h and 1 $\pi$  events. As previously seen in Section 3.3.1, the significant 1 $\pi$  contamination may reduce the sensitivity both CC-0 $\pi$  and CC-1 $\pi$  model parameters in the BANFF fit.

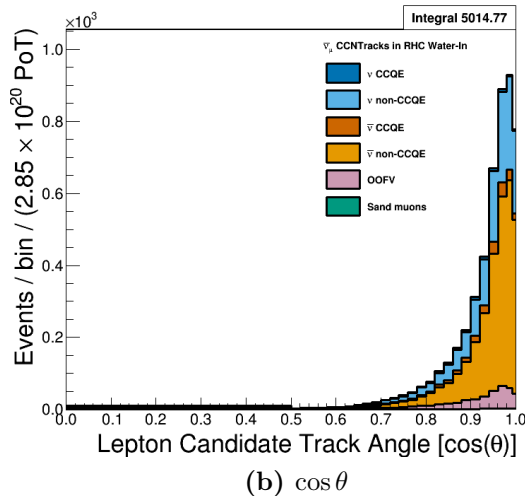
### 3.3.4 $\bar{\nu}_\mu$ in RHC CC N-Tracks

This selection provides the  $\bar{\nu}_\mu$  non-CCQE-like samples in RHC mode. Figure 3.20 on page 85 and Figure 3.21 on page 85 display the momentum and angular distributions that are inputs to BANFF. The most striking feature of this selection is the the number of mis-identified events. In particular protons are selected as the HMPT when they become minimum ionizing particles, which is about 1.3 GeV/c. At these energies protons can escape the PØD into the TPC since it deposits less energy per unit length. In addition, the intrinsic  $\nu_\mu$  background contribution is comparable to the desired  $\bar{\nu}_\mu$  flavor. These two features should be addressed to increase the utility of the selection for the next iteration of the analysis.

We can examine the efficiencies and purities differentially for the selection in Figure 3.14 on page 80. The true signal here is any  $\bar{\nu}_\mu$  CC interaction except  $\bar{\nu}_\mu$  CCQE which the CC

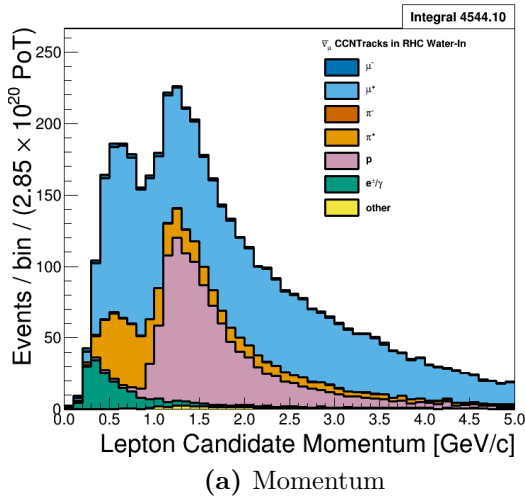


(a) Momentum

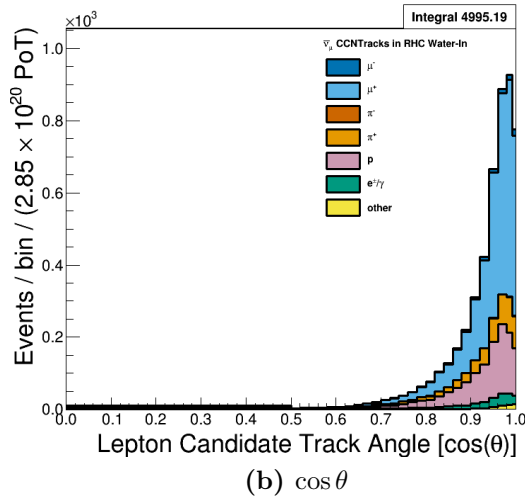


(b)  $\cos \theta$

**Figure 3.20:** Lepton candidate reconstructed  $P$  and  $\cos\theta$  distributions for the  $\bar{\nu}_\mu$  in RHC CC N-Tracks selection for CCQE and non-CCQE interactions. The figures use the PØD water-in MC and are normalized to the RHC water-in mode POT.



(a) Momentum



(b)  $\cos \theta$

**Figure 3.21:** Lepton candidate reconstructed  $P$  and  $\cos\theta$  distributions for the  $\bar{\nu}_\mu$  in RHC CC N-Tracks selection for the true selected particle. The figures use the PØD water-in MC and are normalized to the RHC water-in mode POT.

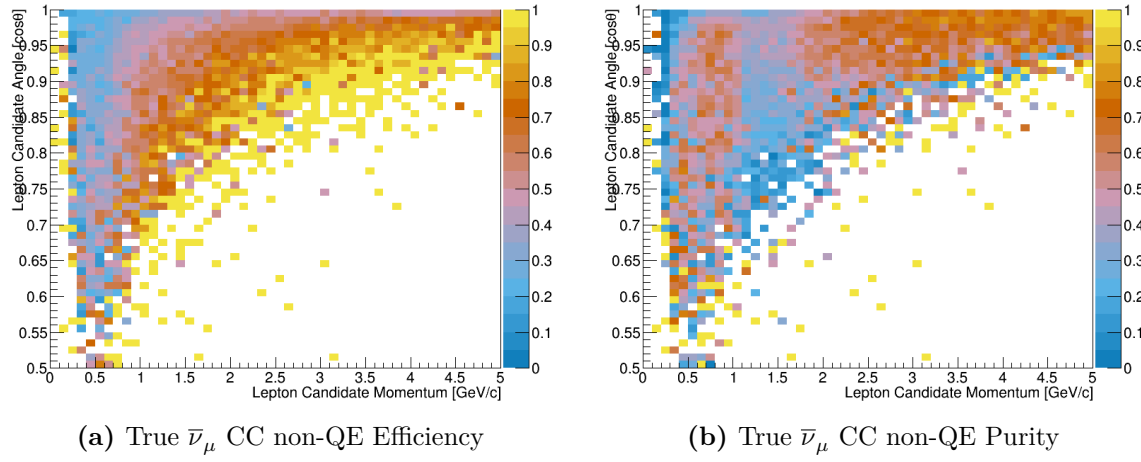


**Figure 3.22:** The efficiency and purity in reconstructed kinematics of  $\bar{\nu}_\mu$  CC non-QE interactions in the  $\bar{\nu}_\mu$  in RHC CC N-Track selections. The true events are any  $\bar{\nu}_\mu$  CC interaction except  $\bar{\nu}_\mu$  CCQE at the vertex and the selected lepton candidate is the true  $\mu^+$ .

1-Track is designed to select. As seen before, both the efficiency and purity are low where statistics are high.

The underlying true kinematics,  $E_\nu$ ,  $Q^2$ , and  $W$ , of the interactions are shown in Figure 3.23 on page 87. Here we see in better detail the origin of the  $\nu_\mu$  contamination. As a function of increasing energy, the  $\bar{\nu}_\mu$  content is decreasing while the relative  $\nu_\mu$  contribution is increasing. The  $\nu_\mu$  events also have a high  $Q^2$  content which explains the significant number of misidentified proton main track events. For the hadronic final states, the shape of the  $\bar{\nu}_\mu$ -induced resonances is similar to what we saw in Figure 3.15 on page 81. Interestingly, the  $\nu_\mu$  background hadronic mass distribution does not peak in any one region.

### 3.3.5 $\nu_\mu$ Background in RHC CC 1-Track

This selection provides the  $\nu_\mu$  in RHC, also called wrong-sign background, CCQE-like samples. Figure 3.24 on page 88 and Figure 3.25 on page 89 display the momentum and angular distributions that are inputs to BANFF. We can see this is a relatively low-angle, forward going selection compared to previous selections. Importantly the selection is  $\nu_\mu$ -pure

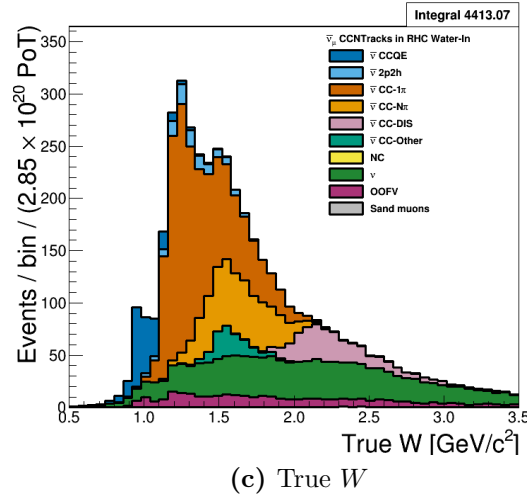
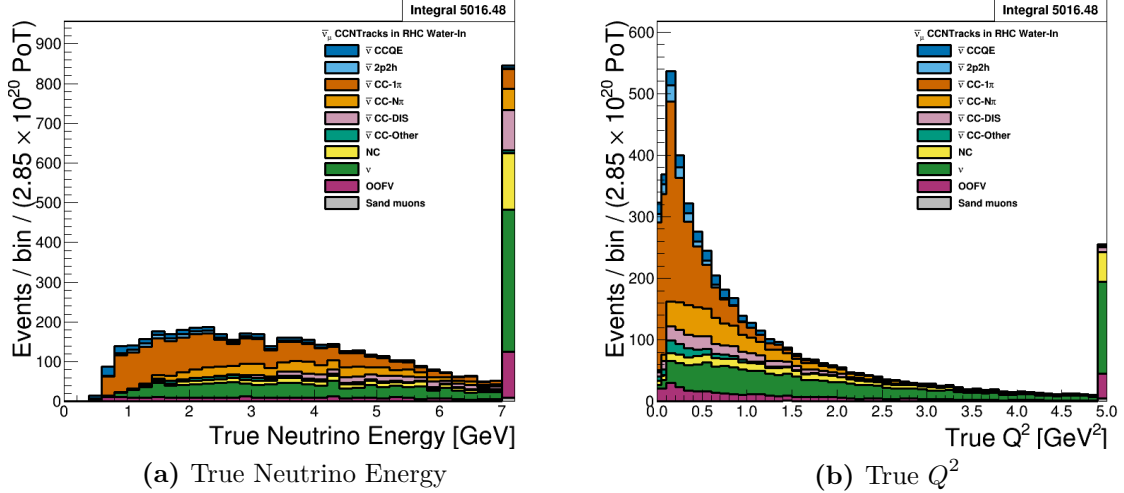


**Figure 3.23:** The  $\bar{\nu}_\mu$  in RHC CC N-Tracks true kinematics broken down by true NEUT interaction modes. The last bin shown in (a) and (b) is used as overflow. The figures use the PØD water-in MC and are normalized to the RHC water-in mode POT.

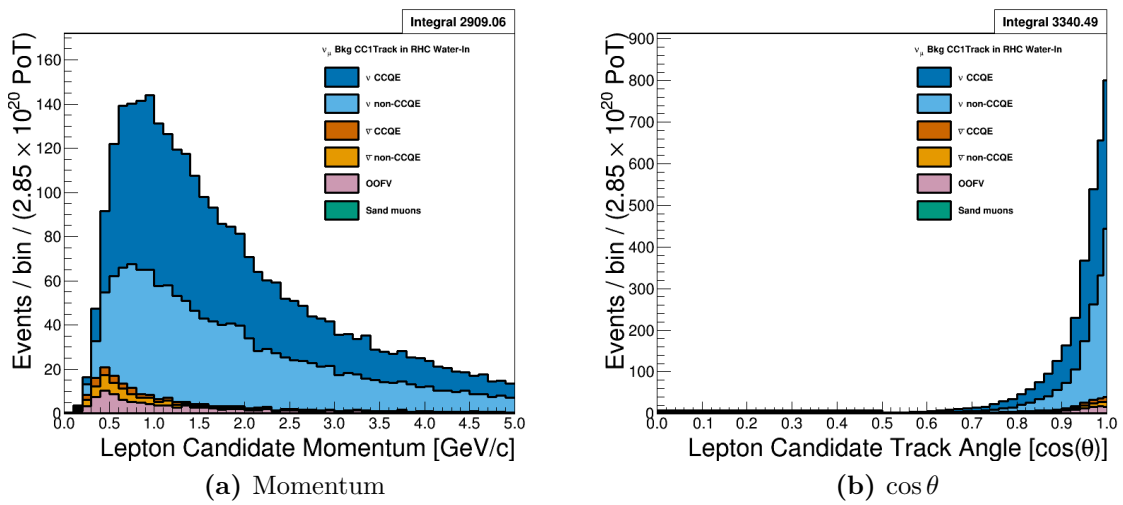


**Figure 3.24:** Lepton candidate reconstructed  $P$  and  $\cos\theta$  distributions for the  $\nu_\mu$  in RHC CC 1-Track selection for CCQE and non-CCQE interactions. The figures use the PØD water-in MC and are normalized to the RHC water-in mode POT.

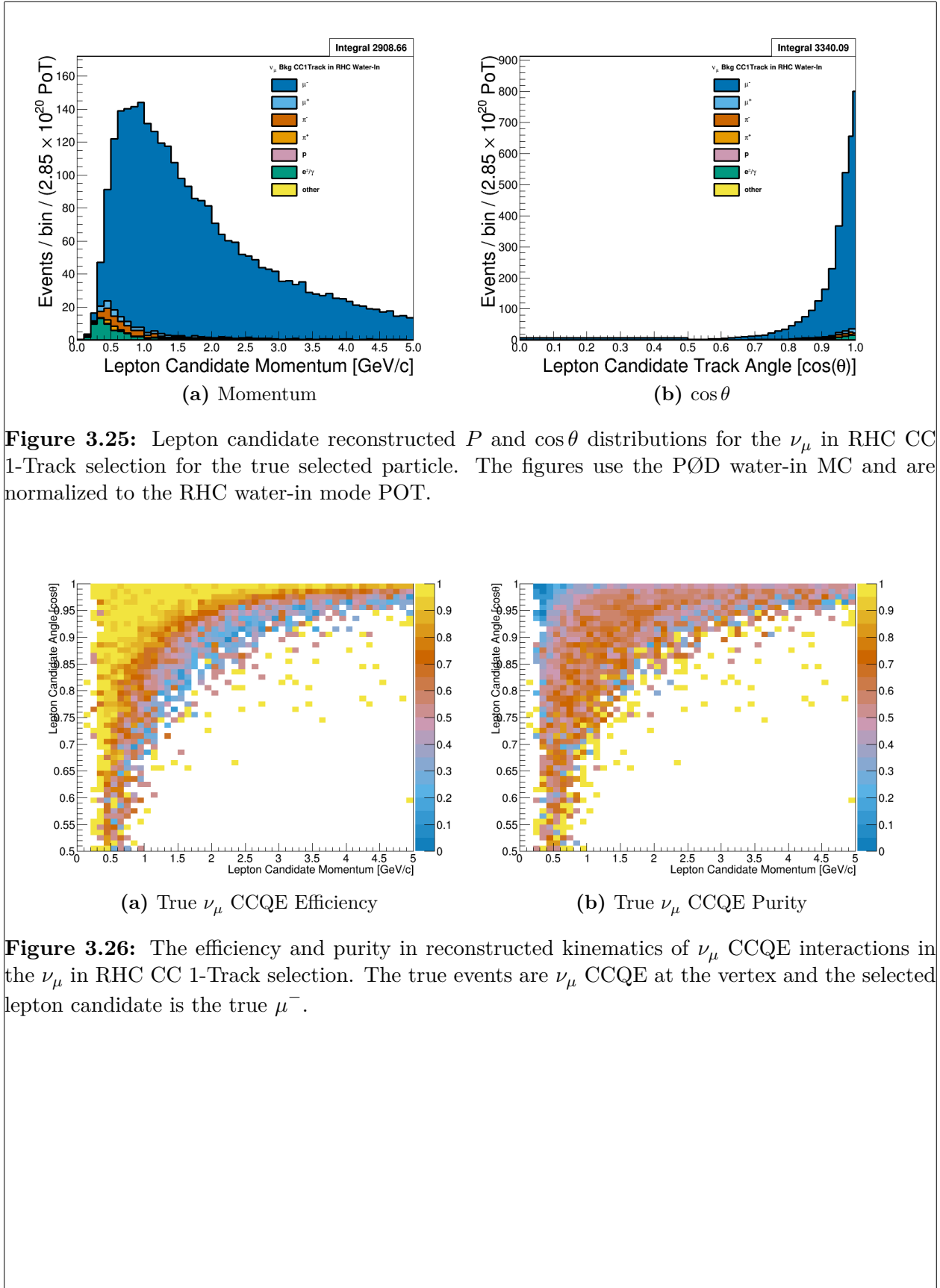
which should help constrain the wrong-sign background in BANFF. However, the CCQE purity is modest given number of correctly identified lepton candidates.

We can examine the efficiencies and purities differentially for the selection in Figure 3.26 on page 89. The efficiency is similar to the  $\nu_\mu$  in FHC CC 1-Track efficiency. As for the purity, it is roughly 70% in a banded region between low momenta, low angle and high momenta, high angle tracks.

The underlying true kinematics,  $E_\nu$  and  $Q^2$ , of the selection are shown in Figure 3.27 on page 90. Due to the flux of the wrong-sign background, the neutrino energy is not sharply peaked at 0.6 GeV. This explains the significant non-CCQE event contamination in the form of 2p2h and 1π interactions.

### 3.3.6 $\nu_\mu$ Background in RHC CC N-Tracks

This selection provides the  $\nu_\mu$  background non-CCQE-like samples in RHC mode. Figure 3.28 on page 91 and Figure 3.29 on page 91 show the momentum and angular distributions that are inputs to BANFF. We can see the selection is relatively  $\nu_\mu$ -pure with a signifi-



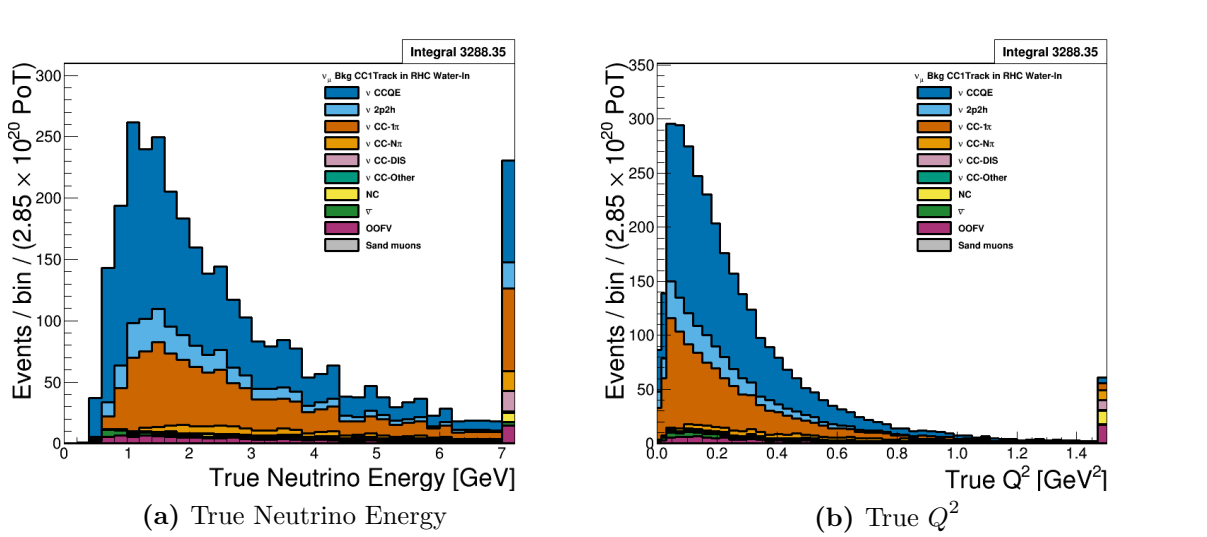


**Figure 3.27:** The  $\nu_\mu$  in RHC CC 1-Track true kinematics broken down by true NEUT interaction modes. Water-in mode is displayed here only with the last bin shown is used as overflow. The figures use the PØD water-in MC and are normalized to the RHC water-in mode POT.

cant mis-identified track rate. Interestingly, the misidentified pion main tracks have a high momentum tail.

We can examine the  $\nu_\mu$  CC non-QE efficiency and purity of the selection in Figure 3.30 on page 92. There is a reduction in the purity below 1.5 GeV/c due to the the  $\bar{\nu}_\mu$  selections occupying the same phase space. Fortunately, the efficiency and purity are relatively high above 1.5 GeV/c.

The underlying true kinematics,  $E_\nu$ ,  $Q^2$ , and  $W$ , of the interactions are shown in Figure 3.31 on page 93. As we have seen before with the CC N-Tracks samples, these are high  $E_\nu$  events with large  $Q^2$  exchanges. The invariant hadronic system displays the previously seen resonances, with the largest still being from the  $\Delta$  baryon.

## 3.4 Summary of Selections

We have examined that the selection procedures described above produces some reasonably pure CCQE samples using the 1-Track cut. By inverting that cut, we obtain some handles on other topologies like CC 1 $\pi$  and high  $Q^2$  CCDIS events. Importantly is the abil-

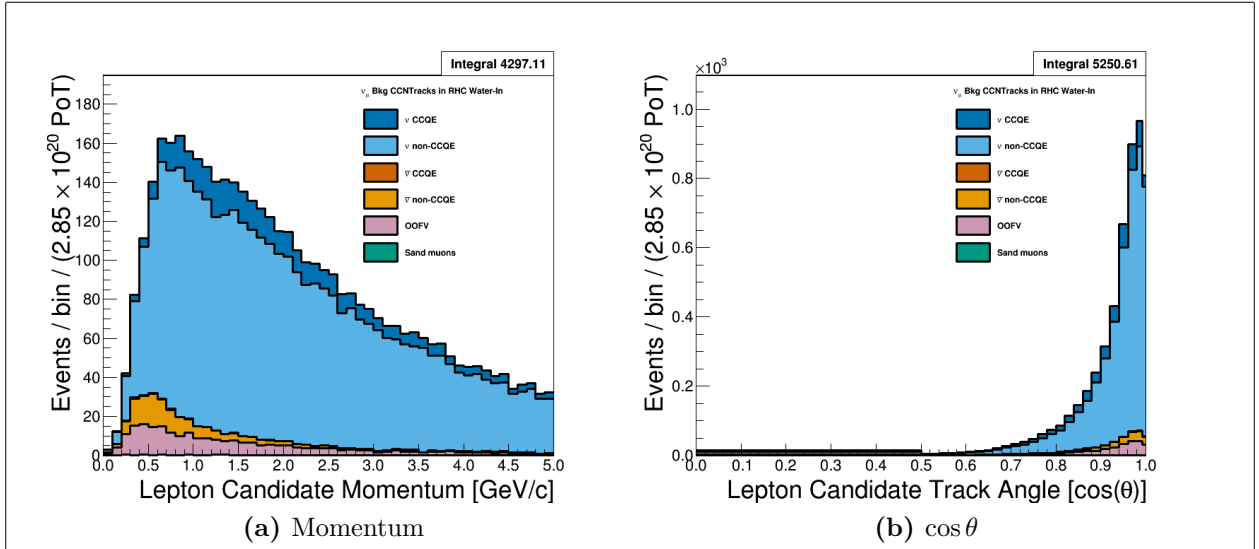


**Figure 3.28:** Lepton candidate reconstructed  $P$  and  $\cos\theta$  distributions for the  $\nu_\mu$  in RHC CC N-Tracks selection for CCQE and non-CCQE interactions. The figures use the PØD water-in MC and are normalized to the RHC water-in mode POT.

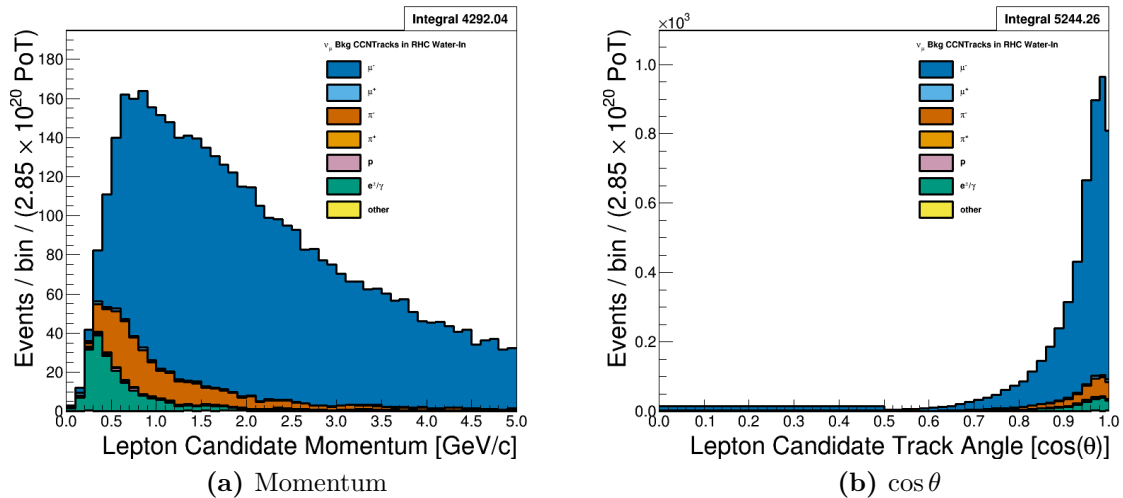
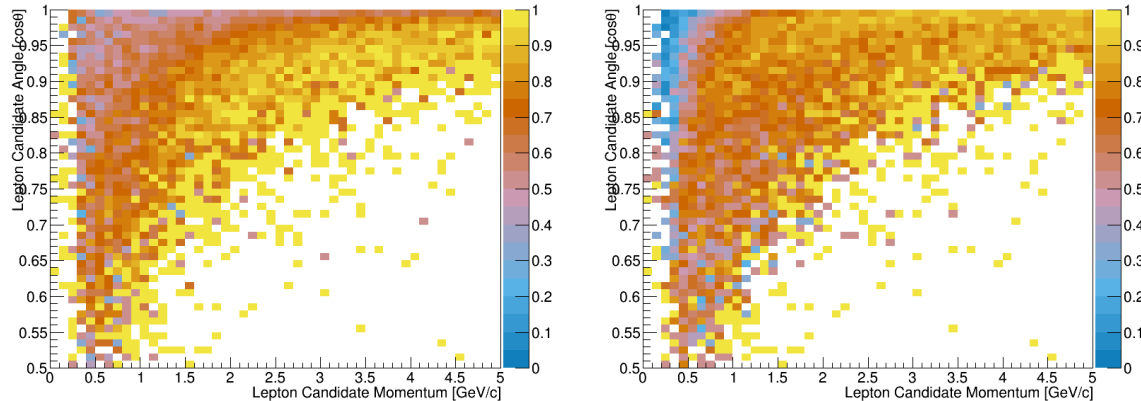


**Figure 3.29:** Lepton candidate reconstructed  $P$  and  $\cos\theta$  distributions for the  $\nu_\mu$  in RHC CC N-Tracks selection for the true selected particle. The figures use the PØD water-in MC and are normalized to the RHC water-in mode POT.

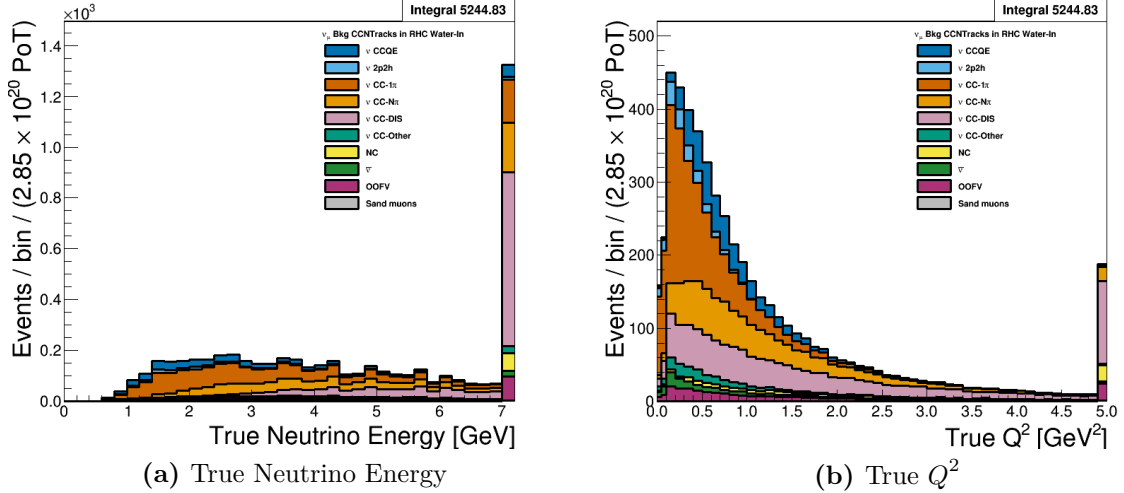


(a) True  $\bar{\nu}_\mu$  CC non-QE Efficiency

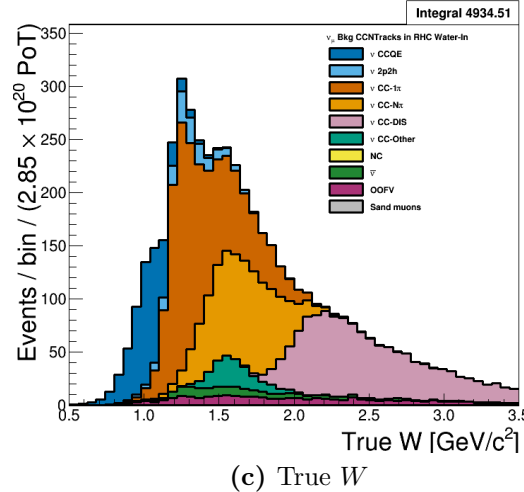
(b) True  $\bar{\nu}_\mu$  CC non-QE Purity

**Figure 3.30:** The efficiency and purity in reconstructed kinematics of  $\bar{\nu}_\mu$  CC non-QE interactions in the  $\nu_\mu$  in RHC CC N-Tracks selection. The true events are any  $\nu_\mu$  CC interaction except  $\nu_\mu$  CCQE at the vertex and the selected lepton candidate is the true  $\mu^-$ .

ity to constrain the correct sign  $\nu_\mu$  and wrong sign backgrounds in RHC. We can now move forward to the next chapter to examine the systematic uncertainties present in the analysis.



(a) True Neutrino Energy

(b) True  $Q^2$ (c) True  $W$ 

**Figure 3.31:** The  $\nu_\mu$  in RHC CC N-Tracks true kinematics broken down by true NEUT interaction modes. The last bin shown in (a) and (b) is used as overflow. The figures use the PØD water-in MC and are normalized to the RHC water-in mode POT.

---

# Chapter 4

## The PØD-Only in BANFF Parameterization

In addition to the likelihood ratio maximization, the BANFF fit includes three sources of systematic uncertainties: neutrino flux, cross section model, and detector inefficiencies. This chapter explores the fit binning and penalty terms in the test statistic in this analysis. The sources of systematic uncertainties, also referred to just as systematics, will be defined in order to understand their effect on any analysis.

This chapter is presented in the following order. The first section explores the method to define fit bins in the likelihood ratio. The second section is divided into three subsections to define the parameterization of each penalty term in the test statistic. The penalty terms discussed in order are the neutrino flux model, the detector inefficiencies, and lastly the cross section model. These three terms directly affect the flux of neutrinos, efficiency of reconstruction, and the cross section for  $\nu_\alpha$  terms, respectively, in the expected rate equation given in (1.56).

---

## 4.1 Fit Binning

The PØD ND280 BANFF fit uses the samples described in Chapter 3. The bin edges used in the BANFF fit to evaluate the log-likelihood ratio term,  $\Delta\chi^2_{\text{LLR}}$ , are tabulated below. There are a total 988 fit bins with water-in and water-out modes sharing the same bin edges. The determination of the fit binning is discussed in the next subsection.

- $\nu_\mu$  in CC 1-Track fit bin edges:
  - $p$  [GeV/c]: 0, 0.3, 0.4, 0.5, 0.6, 0.7, 0.8, 1, 1.25, 1.5, 2, 3, 4, 5.5, 30
  - $\cos\theta$ : -1, 0.7, 0.8, 0.88, 0.94, 0.96, 0.975, 0.99, 1
- $\nu_\mu$  in FHC CC N-Tracks fit bin edges:
  - $p$  [GeV/c]: 0, 0.4, 0.5, 0.6, 0.7, 0.8, 1, 1.2, 1.5, 1.8, 2.2, 2.7, 3.5, 5, 10, 30
  - $\cos\theta$ : -1, 0.65, 0.77, 0.85, 0.9, 0.94, 0.97, 0.99, 1
- $\bar{\nu}_\mu$  in RHC CC 1-Track fit bin edges:
  - $p$  [GeV/c]: 0, 0.4, 0.5, 0.6, 0.7, 0.8, 1, 1.25, 1.5, 2, 3, 30
  - $\cos\theta$ : -1, 0.82, 0.87, 0.9, 0.93, 0.95, 0.97, 0.99, 1
- $\bar{\nu}_\mu$  in RHC CC N-Tracks fit bin edges:
  - $p$  [GeV/c]: 0, 0.5, 0.9, 1.25, 1.6, 2, 3, 8, 30
  - $\cos\theta$ : -1, 0.8, 0.89, 0.95, 0.97, 0.99, 1
- $\nu_\mu$  in RHC CC 1-Track fit bin edges:
  - $p$  [GeV/c]: 0, 0.4, 0.6, 0.8, 1.1, 2, 10
  - $\cos\theta$ : -1, 0.78, 0.84, 0.89, 0.92, 0.95, 0.97, 0.98, 0.99, 1
- $\nu_\mu$  in RHC CC N-Tracks bin edges:

- $p$  [GeV/c]: 0, 0.4, 0.6, 0.8, 1, 1.5, 2, 3, 10
- $\cos \theta$  : -1, 0.7, 0.8, 0.85, 0.9, 0.94, 0.965, 0.98, 0.99, 1

### 4.1.1 Fit Binning Determination

The fit binning is optimized to ensure at least 1 predicted Monte Carlo (MC) event in each bin when scaled to the collected data POT. The fit bins must also account for detector smearing effects. In order to mitigate smearing and event migration, the reconstructed kinematics were examined to their MC truth value using only correctly identified leptons in one-dimensional kinematic slices. Since the MC provides about  $10\times$  the data statistics, the statistical uncertainty for each bin should be negligible in high statistics regions. The kinematics are scanned across their full relevant spaces in order to understand the required width for a fit bin. The first fit bin is always defined starting from the kinematic maximum.

For the momentum bins, the momentum resolution is compared to MC truth. The momentum resolution is defined as

$$R(r, t) = \frac{r - t}{t},$$

where  $r$  is the reconstructed momentum and  $t$  is the true momentum. The momentum was scanned in finite bin widths with the mean and standard deviation of the resolution  $R$  extracted. The mean and standard deviation are used as a proxy for the true bias and resolution, respectively. In addition, a bootstrapping algorithm was employed to understand the accuracy of the sample estimates. Bootstrapping in this context is sampling over all relevant values of true momentum and randomly replacing the values. For each scanned bin, at least 1000 bootstrapping sampling with replacement was performed. In the case of large variances in the bootstrapping samples, additional 10000 sampling with replacement were performed. The results for analyzing the  $\nu_\mu$  in FHC CC 1-Track selection is shown in Figure 4.1 on page 97.

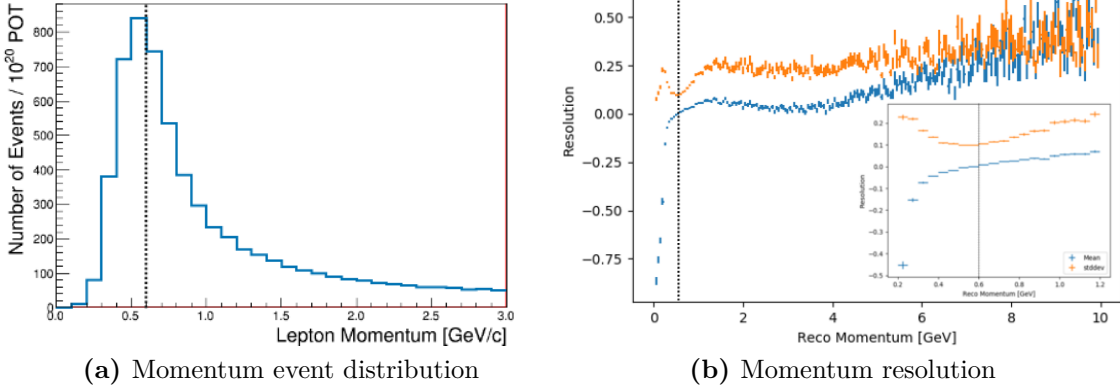


**Figure 4.1:** The momentum event distribution and uncertainty for  $\nu_\mu$  in FHC CC 1-Track events is shown above. Only correctly identified muons are shown. (a) The number of events is scaled to  $10^{20}$  POT which is the approximate scale for all the samples in this analysis. A dashed line indicates the maximum of the peak. (b) The resolution of the momentum measurement is shown for a wide region of momenta. In the inset is the resolution zoomed near the momentum distribution maximum. Like in (a), a dashed line shows the momentum maximum.

The angle fit bins are treated in an almost identical manner. While the fit bins and Physics are dictated in  $\cos\theta$  space, the detector smearing is a function  $\theta$ . In addition, since the angle can be nearly zero for the most forward-going tracks, the resolution was not used to characterize the angular uncertainties. Instead, the difference between the true and reconstructed angle were analyzed as shown in Figure 4.2 on page 98. The mean and standard deviation were studied as before to set the fit  $\cos\theta$  bin edges. Bootstrapping was again used to quantify the accuracy of the mean and standard deviation.

## 4.2 Penalty Terms and Systematic Uncertainties

This section expands on the definition of the penalty terms in the BANFF fit. The cross section and flux penalty terms in this analysis are identical to previous BANFF studies since the T2K experiment utilizes a set of canonical flux and cross section systematics that are shared between ND280 and SK. Also, those systematics are not altered in this analysis for the purpose of comparability between PØD-only and FGD-only best fit results. For the ND280

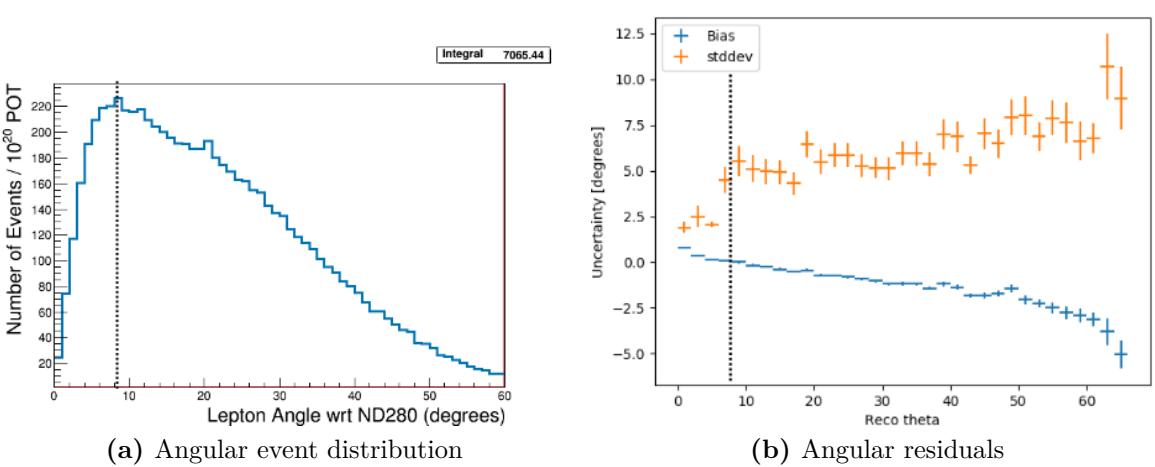


**Figure 4.2:** The angular event distribution and uncertainty for  $\nu_\mu$  in FHC CC 1-Track events is shown above. Only correctly identified muons are shown. (a) The number of events is scaled to  $10^{20}$  POT which is the approximate scale for all the samples in this analysis. A dashed line indicates the track angle distribution maximum of the peak. (b) The residual of the angular measurement is shown up to where there are sufficient statistics. Like in (a), a dashed line shows the distribution maximum.

detector systematics, many are shared between the PØD and TPC subdetectors. However, due to the different detector technologies, additional detector inefficiency systematics will be incorporated.

### 4.2.1 Flux Model

The T2K neutrino flux model is a description of the neutrino beam spectrum by run period and flavor. This model includes simulations of the beam interactions and subsequent hadron production at the target. The predicted hadron production rate, including inside and outside the target, is tuned to the results from the NA61/SHINE [10] replica target experiment and other hadron production experiments. The uncertainties in the unoscillated flux tuning are dominated on hadron production. Smaller effects on the unoscillated flux uncertainty include the proton beam profile, off-axis angle, horn current, and horn alignment. Further details about the flux model and uncertainties can be found in the following reference [4].

The flux penalty term in the BANFF fit is defined, as previously seen in Chapter 2, as

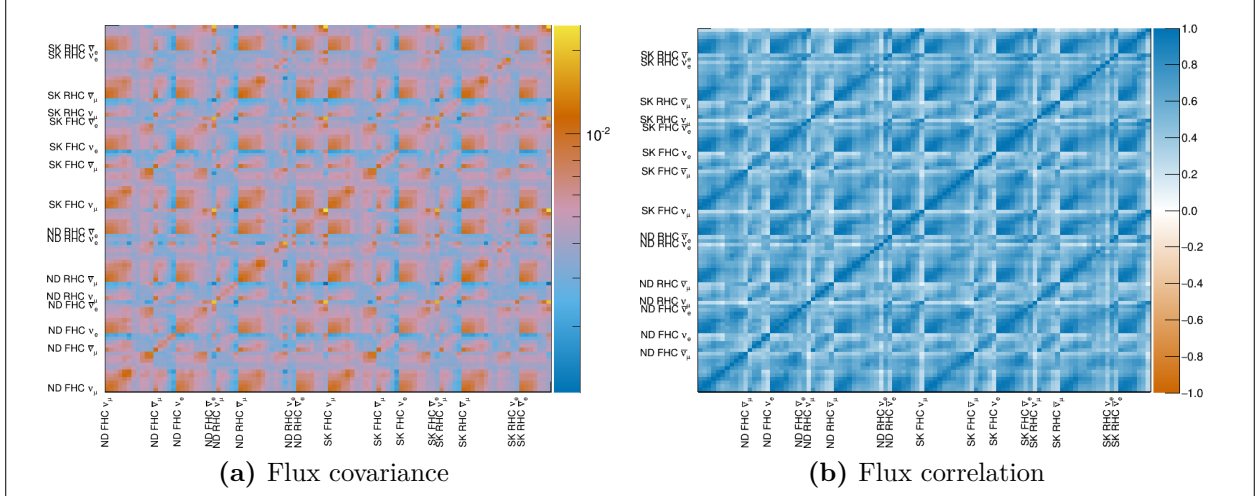


**Figure 4.3:** BANFF prefit flux covariance matrix shown with respective detector, horn current, and neutrino flavor.

$$\Delta\chi^2_{\text{Flux}} = \Delta\vec{b} \cdot \left(V_b^{-1}\right) \cdot \Delta\vec{b}^T. \quad (4.1)$$

As a remainder, all penalty terms,  $\Delta\chi^2$ , in this analysis follow this format. Each flux  $b_i$  parameter is a neutrino energy bin normalization starting at one (1). Each parameter is defined as

$$b_i = \frac{N'_{\nu,i}}{N_{\nu,i}}, \quad (4.2)$$

where  $N_{\nu,i}$  and  $N'_{\nu,i}$  are the predicted and ND constrained neutrino event rates, respectively, in the  $i$ th energy bin. In other words, *each flux term is a ratio of rates. Further, all penalty parameters and covariance terms are dimensionless.* The flux bins are differentiated by neutrino energy, horn current/polarity (FHC and RHC), neutrino flavor ( $\nu_\mu$ ,  $\bar{\nu}_\mu$ ,  $\nu_e$ , and  $\bar{\nu}_e$ ), and detector (ND280 and SK). The flux binning and covariance matrix, shown in Figure 4.3 on page 99, is provided by the T2K flux group. Shown also in Figure 4.3 is the (Pearson) correlation coefficient matrix which is defined as

$$\rho_{i,j} = \frac{V_{i,j}}{\sqrt{V_{i,i}V_{j,j}}}, \quad (4.3)$$

where  $V$  is the covariance matrix and  $i$  and  $j$  are bins in  $V$ .

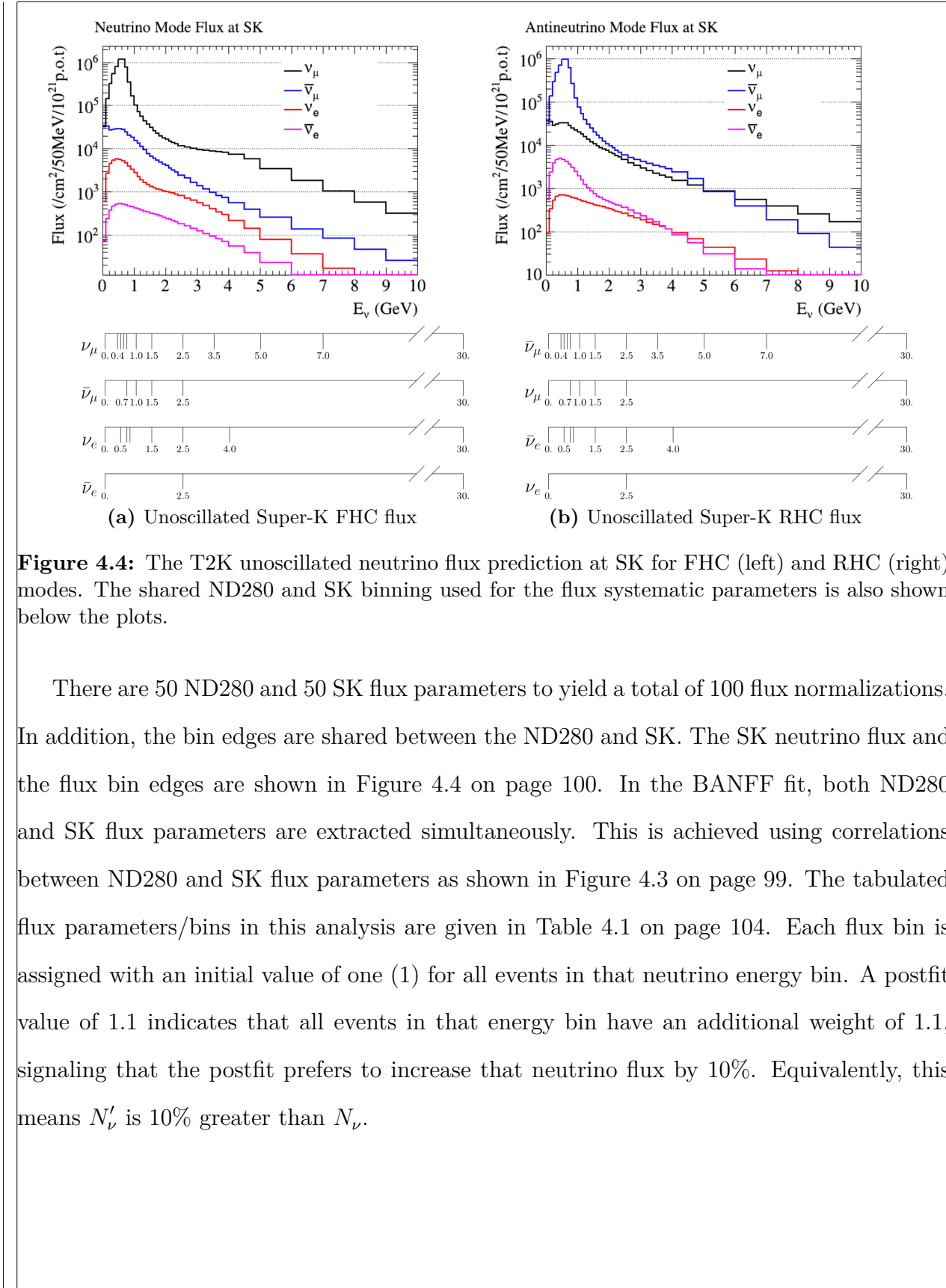


**Table 4.1:** Flux binning and uncertainties used in the BANFF fit.

Fit index	Beam mode	Bin edges [GeV]	Prefit
0	ND280 $\nu_\mu$ FHC	0.0 - 0.4	$1 \pm 0.100909$
1		0.4 - 0.5	$1 \pm 0.099431$
2		0.5 - 0.6	$1 \pm 0.092025$
3		0.6 - 0.7	$1 \pm 0.085239$
4		0.7 - 1.0	$1 \pm 0.105356$
5		1.0 - 1.5	$1 \pm 0.104375$
6		1.5 - 2.5	$1 \pm 0.073612$
7		2.5 - 3.5	$1 \pm 0.068993$
8		3.5 - 5.0	$1 \pm 0.082334$
9		5.0 - 7.0	$1 \pm 0.097308$
10		7.0 - 30	$1 \pm 0.114706$
11	ND280 $\bar{\nu}_\mu$ FHC	0.0 - 0.7	$1 \pm 0.103804$
12		0.7 - 1.0	$1 \pm 0.084158$
13		1.0 - 1.5	$1 \pm 0.081349$
14		1.5 - 2.5	$1 \pm 0.085208$
15		2.5 - 30	$1 \pm 0.087735$
16	ND280 $\nu_e$ FHC	0.0 - 0.5	$1 \pm 0.091336$
17		0.5 - 0.7	$1 \pm 0.089699$
18		0.7 - 0.8	$1 \pm 0.084648$
19		0.8 - 1.5	$1 \pm 0.079722$
20		1.5 - 2.5	$1 \pm 0.079766$
21		2.5 - 4.0	$1 \pm 0.081399$
22		4.0 - 30	$1 \pm 0.095795$
23	ND280 $\bar{\nu}_e$ FHC	0.0 - 2.5	$1 \pm 0.072069$
24		2.5 - 30	$1 \pm 0.142921$

**Table 4.1:** Flux binning and uncertainties used in the BANFF fit.

Fit index	Beam mode	Bin edges [GeV]	Prefit
25	ND280 $\nu_\mu$ RHC	0.0 - 0.7	$1 \pm 0.094066$
26		0.7 - 1.0	$1 \pm 0.079866$
27		1.0 - 1.5	$1 \pm 0.080948$
28		1.5 - 2.5	$1 \pm 0.083251$
29		2.5 - 30	$1 \pm 0.082653$
30	ND280 $\bar{\nu}_\mu$ RHC	0.0 - 0.4	$1 \pm 0.107277$
31		0.4 - 0.5	$1 \pm 0.098851$
32		0.5 - 0.6	$1 \pm 0.089710$
33		0.6 - 0.7	$1 \pm 0.084692$
34		0.7 - 1.0	$1 \pm 0.106871$
35		1.0 - 1.5	$1 \pm 0.098711$
36		1.5 - 2.5	$1 \pm 0.073350$
37		2.5 - 3.5	$1 \pm 0.070520$
38		3.5 - 5.0	$1 \pm 0.092905$
39		5.0 - 7.0	$1 \pm 0.089083$
40		7.0 - 30	$1 \pm 0.134911$
41	ND280 $\nu_e$ RHC	0.0 - 2.5	$1 \pm 0.066214$
42		2.5 - 30	$1 \pm 0.086977$
43	ND280 $\bar{\nu}_e$ RHC	0.0 - 0.5	$1 \pm 0.095575$
44		0.5 - 0.7	$1 \pm 0.089033$
45		0.7 - 0.8	$1 \pm 0.088406$
46		0.8 - 1.5	$1 \pm 0.081472$
47		1.5 - 2.5	$1 \pm 0.078353$
48		2.5 - 4.0	$1 \pm 0.089427$
49		4.0 - 30	$1 \pm 0.156972$

**Table 4.1:** Flux binning and uncertainties used in the BANFF fit.

Fit index	Beam mode	Bin edges [GeV]	Prefit
50	Super-K $\nu_\mu$ FHC	0.0 - 0.4	$1 \pm 0.102555$
51		0.4 - 0.5	$1 \pm 0.101771$
52		0.5 - 0.6	$1 \pm 0.092573$
53		0.6 - 0.7	$1 \pm 0.084265$
54		0.7 - 1.0	$1 \pm 0.102271$
55		1.0 - 1.5	$1 \pm 0.084528$
56		1.5 - 2.5	$1 \pm 0.066909$
57		2.5 - 3.5	$1 \pm 0.072355$
58		3.5 - 5.0	$1 \pm 0.085299$
59		5.0 - 7.0	$1 \pm 0.096725$
60		7.0 - 30	$1 \pm 0.114112$
61	Super-K $\bar{\nu}_\mu$ FHC	0.0 - 0.7	$1 \pm 0.103129$
62		0.7 - 1.0	$1 \pm 0.078327$
63		1.0 - 1.5	$1 \pm 0.082367$
64		1.5 - 2.5	$1 \pm 0.082121$
65		2.5 - 30	$1 \pm 0.085123$
66	Super-K $\nu_e$ FHC	0.0 - 0.5	$1 \pm 0.090918$
67		0.5 - 0.7	$1 \pm 0.087065$
68		0.7 - 0.8	$1 \pm 0.082527$
69		0.8 - 1.5	$1 \pm 0.076514$
70		1.5 - 2.5	$1 \pm 0.075773$
71		2.5 - 4.0	$1 \pm 0.082078$
72		4.0 - 30	$1 \pm 0.092882$
73	Super-K $\bar{\nu}_e$ FHC	0.0 - 2.5	$1 \pm 0.071921$
74		2.5 - 30	$1 \pm 0.128982$

**Table 4.1:** Flux binning and uncertainties used in the BANFF fit.

Fit index	Beam mode	Bin edges [GeV]	Prefit
75	Super-K $\nu_\mu$ RHC	0.0 - 0.7	$1 \pm 0.093954$
76		0.7 - 1.0	$1 \pm 0.076369$
77		1.0 - 1.5	$1 \pm 0.074900$
78		1.5 - 2.5	$1 \pm 0.078108$
79		2.5 - 30	$1 \pm 0.077505$
80	Super-K $\bar{\nu}_\mu$ RHC	0.0 - 0.4	$1 \pm 0.108593$
81		0.4 - 0.5	$1 \pm 0.101912$
82		0.5 - 0.6	$1 \pm 0.092787$
83		0.6 - 0.7	$1 \pm 0.082669$
84		0.7 - 1.0	$1 \pm 0.102090$
85		1.0 - 1.5	$1 \pm 0.087732$
86		1.5 - 2.5	$1 \pm 0.068117$
87		2.5 - 3.5	$1 \pm 0.069902$
88		3.5 - 5.0	$1 \pm 0.091711$
89		5.0 - 7.0	$1 \pm 0.084736$
90		7.0 - 30	$1 \pm 0.115488$
91	Super-K $\nu_e$ RHC	0.0 - 2.5	$1 \pm 0.066204$
92		2.5 - 30	$1 \pm 0.082645$
93	Super-K $\bar{\nu}_e$ RHC	0.0 - 0.5	$1 \pm 0.095453$
94		0.5 - 0.7	$1 \pm 0.088889$
95		0.7 - 0.8	$1 \pm 0.085644$
96		0.8 - 1.5	$1 \pm 0.078536$
97		1.5 - 2.5	$1 \pm 0.075246$
98		2.5 - 4.0	$1 \pm 0.086384$
99		4.0 - 30	$1 \pm 0.152507$

### 4.2.2 Detector Inefficiencies Model

In the BANFF fit, bin normalization parameters are used to evaluate the detector inefficiency penalty term,  $\Delta\chi^2_{\text{Det}}$ . Varying fit bins without constraint is nonphysical due to known detector inefficiencies and their systematic uncertainties. Since improperly modeled inefficiencies can cause events to migrate from bin-to-bin, numerous fake “toy experiments” are performed to evaluate the systematic uncertainties in detector inefficiencies. When all toy experiments are analyzed together, correlated variations among fit bins become apparent. These correlations provide the constraints on freely changing bin normalizations. We will see the result of running such toy experiment variations in the coming pages. Hitherto in this thesis, detector inefficiency uncertainties will be referred to as detector systematics.

All the detector systematics are evaluated either as observable variations or weights as given in given in Table 4.2 on page 106. An observable variation affects the physical observables of selected events like the calculated energy loss of a track in the PØD. A weight is a multiplicative factor that alters the normalization of a single event in a bin. There are detector systematics that affect the PØD-only, TPC-only, or both. So a description of the systematic treatments is discussed in the next section. The new PØD-only systematics in BANFF will then be explained later. Details on the TPC-only systematics implementations are discussed in the following reference [4].

## Systematic Treatments

There are two types of systematic treatments in the BANFF analysis: observable variations and weights. Each rely on the method of throwing a random number,  $x$ , to evaluate the systematic.

Efficiency-like systematics are treated as weights to the MC predictions in order to evaluate the uncertainty the systematic has on an analysis. They are based on studies comparing

Systematic effect	Affected Detector	Treatment
TPC cluster eff.	TPC	efficiency
TPC tracking eff.	TPC	efficiency
TPC charge misassignment	TPC	efficiency
TPC momentum resol.	TPC	observable variation
TPC momentum scale	TPC	observable variation
B field distortion	TPC	observable variation
Pion secondary interactions	All	efficiency
Proton secondary interactions	All	efficiency
TPC Particle ID	TPC	observable variation
TPC track quality eff.	TPC	efficiency
<hr/>		
PØD energy loss scale	PØD	observable variation
PØD energy loss resol.	PØD	observable variation
PØD mass	PØD	(see text)
PØD-TPC matching eff.	PØD+TPC	(see text)

**Table 4.2:** List of detector systematic effects and the way each one is treated within the simulated samples to propagate the uncertainty. The systematics listed above the horizontal line are discussed in the following reference [4]. The PØD mass and track matching systematics were not available in the BANFF framework and treated as uncorrelated additions to the total covariance matrix.

data and MC predictions in control samples (CS). A CS is designed to provide a reliable measurement with minimal influence from other dependent and independent factors. An example of a well established CS is a collection of single, isolated cosmic ray (muon) tracks to measure the energy loss in a detector. In general, a CS may have different properties than the analysis sample like event topology. In particular the cosmic ray CS cannot account for efficiency effects if other tracks present. Therefore a model extrapolation is needed to map the CS to the analysis sample. The model used in BANFF is that the efficiency of the data and MC is the same in both analysis sample and CS

$$\epsilon_{\text{Data}}(o) = \left( \frac{\epsilon_{\text{Data}}(o)}{\epsilon_{\text{MC}}(o)} \right)_{\text{CS}} \epsilon_{\text{MC}}(o), \quad (4.4)$$

where  $\epsilon_{\text{MC}}/\epsilon_{\text{Data}}$  denotes the mean efficiency of the MC/data as a function of some observable  $o$ . We need to update this model to account for statistical uncertainties in the CS. The updated model, with  $o$  dependence assumed, is now

---


$$\epsilon'_{\text{Data}} = \left( \frac{\epsilon_{\text{Data}} + x_{\text{Data}} \cdot \sigma_{\epsilon_{\text{Data}}}}{\epsilon_{\text{MC}} + x_{\text{MC}} \cdot \sigma_{\epsilon_{\text{MC}}}} \right)_{\text{CS}} \epsilon_{\text{MC}} \quad (4.5)$$

where  $\sigma_{\epsilon_{\text{MC}}} / \sigma_{\epsilon_{\text{Data}}}$  is the standard deviation of the efficiency of the MC/Data and  $x_{\text{Data}}$  and  $x_{\text{MC}}$  are different, random normally distributed numbers from  $\mathcal{N}(\mu = 0, \sigma^2 = 1)$ . The selection is rerun on the event and a weight is derived depending if the event is selected,  $w_{\text{eff}}$ , or not selected,  $w_{\text{ineff}}$ . These weights are given below

$$w_{\text{eff}} = \frac{\epsilon'_{\text{Data}}}{\epsilon_{\text{MC}}} \quad (4.6)$$

$$w_{\text{ineff}} = \frac{1 - \epsilon'_{\text{Data}}}{1 - \epsilon_{\text{MC}}}.$$

Observable variation systematics are evaluated as alterations to physically measured quantities like momentum and energy. The systematic can be evaluated in two different ways:

- If the reconstructed observable,  $o_{\text{reco}}$ , has a known true value,  $o_{\text{true}}$ , then the difference between those two is used as scaling. The varied observable is given by

$$o' = o_{\text{true}} + (o_{\text{reco}} - o_{\text{true}})(s + x\sigma_s), \quad (4.7)$$

where  $s$  is the mean scaling parameter to match the true value,  $\sigma_s$  is the uncertainty on  $s$ , and  $x$  is a random number from  $\mathcal{N}(\mu = 0, \sigma^2 = 1)$ . The mean scaling parameter and its uncertainty are determined from the standard deviations observed in the data and MC by

$$s = \frac{\delta^{\text{data}}}{\delta^{\text{MC}}} \quad \sigma_s = s \left| \frac{\sigma_{\delta^{\text{data}}}}{\delta^{\text{data}}} - \frac{\sigma_{\delta^{\text{MC}}}}{\delta^{\text{MC}}} \right|. \quad (4.8)$$

- If the MC reconstructed observable is corrected to match the mean from some CS reconstructed observable. The varied observable in this case is given by

$$o' = o_{\text{Nom}} + \Delta o + x\sigma_{\Delta o}, \quad (4.9)$$

---

where  $o'$  is the varied observable value,  $o_{\text{Nom}}$  is the nominal MC value,  $\Delta o$  is the average correction to the observable,  $\sigma_{\Delta o}$  is the uncertainty on the correction, and  $x$  is a random, normal number from  $\mathcal{N}(\mu = 0, \sigma^2 = 1)$ . Special cases exist for this treatment and are further discussed in the following thesis [66].

In both cases, the selection cuts are rerun on the event determining if it has changed samples.

Now that we understand how the systematics affect our observables and by using toy experiments to evaluate the systematics, we can now begin to understand how the detector systematic penalty term  $\Delta\chi^2_{\text{Det}}$  is modeled in the BANFF fit.

### Bin Normalizations And Covariance

As stated before, the bin normalization penalty parameters are restrictions on freely varying fit bins. To determine how correlated different fit bins are, many toy experiments are performed which vary the observables  $(p, \cos \theta)$ . The bin normalization parameter for the  $i$ th bin, or  $d_i$ , is defined as

$$d_i = \frac{\langle N_i \rangle_{\text{toys}}}{N_i}, \quad (4.10)$$

where  $N_i$  predicted number of events in fit bin  $i$  and  $\langle N_i \rangle_{\text{toys}}$  is the average number of events in fit bin  $i$  evaluated over all toy experiments (toys). The predicted event rate for bin  $i$  is given by

$$N_i = \sum_k^{N_{\text{MC}}} \delta_{i,k}^{\text{bin}} w_k, \quad (4.11)$$

where  $N_{\text{MC}}$  being the number of unweighted MC events,  $\delta_{i,k}^{\text{bin}}$  determines if the  $k$ th event goes into analysis bin  $i$  as a function of  $(p, \cos \theta)$ , and  $w_k$  being the product of all the weights applied to the  $k$ th event. The weights used in (4.11) are

$$w_k = w_k^{\text{POT}} \times w_k^{\text{Flux}} \times w_k^{\text{xsec}} \times w_k^{\text{Det}}, \quad (4.12)$$

(see (2.8) for all possible weights). The average number of events in fit bin  $i$  over all toys is given by

$$\begin{aligned}\langle N_i \rangle_{\text{toys}} &= \frac{1}{N_{\text{toys}}} \sum_{t=1}^{N_{\text{toys}}} (N_i)_t \\ &= \frac{1}{N_{\text{toys}}} \sum_{t=1}^{N_{\text{toys}}} \left( \sum_k^{N_{\text{MC}}} [\delta_{i,k}^{\text{bin}} w_k] \right)_t,\end{aligned}\quad (4.13)$$

where now each MC event has a toy variation out of  $N_{\text{toys}}$  total toys. For every single event in a toy experiment  $t$ , the selection cuts must be reapplied to determine if the event has changed analysis bins since the toy alters the event observables like the number of tracks or

$$(p, \cos \theta) \xrightarrow{\text{toy}} (p', \cos \theta'),$$

where  $p \neq p'$  and  $\theta \neq \theta'$  and if the event is reconstructed at all. We therefore average the results of the toys to smooth out variations among all toy experiments.

As stated before, all the penalty parameters are dimensionless and the detector systematics covariance matrix must be constructed carefully. The bin-to-bin event rate covariance,  $V_{i,j}^{\text{Cov}}$ , between bins  $i$  and  $j$  is

$$V_{i,j}^{\text{Cov}} = \frac{1}{N_{\text{toys}}} \sum_{t=1}^{N_{\text{toys}}} ((N_i)_t - \langle N_i \rangle_{\text{toys}}) \left( (N_j)_t - \langle N_j \rangle_{\text{toys}} \right), \quad (4.14)$$

where  $(N_i)_t$  is defined in (4.13). We also need to account for statistical uncertainties in the fit bins, and so let us define  $V_{i,j}^{\text{Stat}}$  as

$$V_{i,j}^{\text{Stat}} = \delta_{i,j} \sum_k^{N_{\text{MC}}} \delta_{i,k}^{\text{bin}} w_k^2, \quad (4.15)$$

where  $\delta_{i,j}$  is the Kronecker delta function. In order to use both  $V_{i,j}^{\text{Cov}}$  and  $V_{i,j}^{\text{Stat}}$  uncertainties, the total detector covariance matrix,  $V_{i,j}^{\text{Det}}$ , in the BANFF fit is defined as

$$V_{i,j}^{\text{Det}} = \left[ \frac{1}{N_i} \right] \left[ \frac{1}{N_j} \right] (V_{i,j}^{\text{Cov}} + V_{i,j}^{\text{Stat}}), \quad (4.16)$$

---

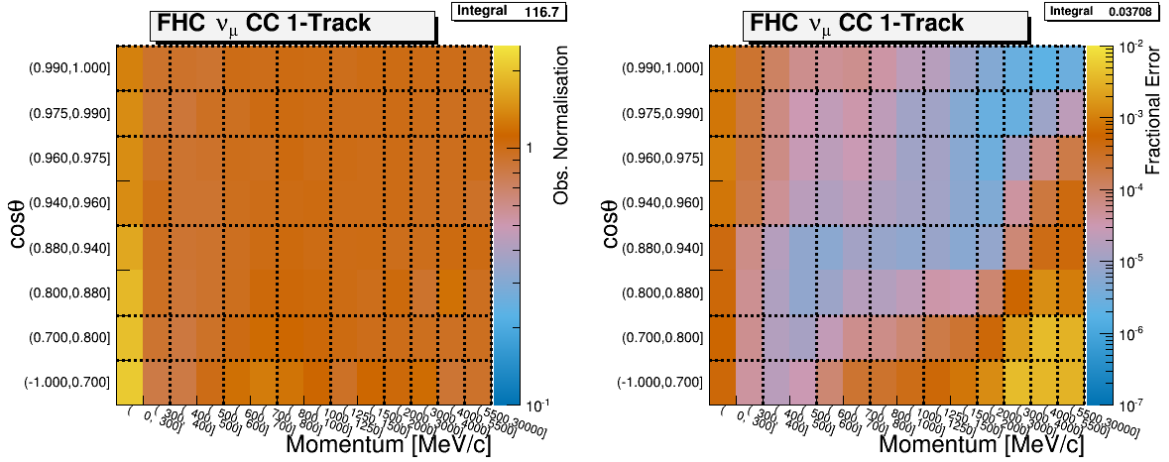
which is indeed dimensionless since we divided out the predicted event rate in bins  $i$  and  $j$ .

### Bin Normalization Edges

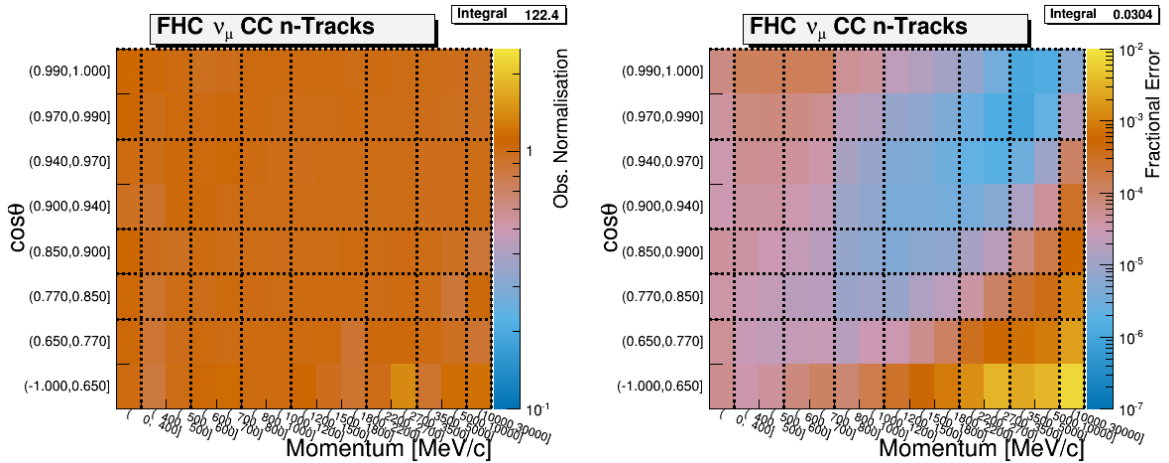
While there could be one observable normalization for each analysis bin, a single normalization can be assigned to multiple analysis bins. The purpose is to reduce the number of fit parameters since the time to fit increases non-linearly with the number of fit parameters and events. Previously, the observable normalization edges were determined by combining fit bins with “similar” covariance. This method proved problematic since the fit bins with relatively higher statistics were shared with the same observable normalization parameter. This left the remaining low statistics regions of  $(p, \cos \theta)$  phase space more susceptible to systematic variations in the toy experiments.

A new procedure was developed to improve the shortcomings of old procedure which requires careful consideration of the statistical uncertainties and variations between observable normalization prefit values. This procedure can be imagined as lowering the number of contours in a topographic map while considering external constraints from other sensing data. To start, initialize all the observable normalization bin edges to be the same as the fit bin edges. All steps after this are performed iteratively. Starting from the observable normalization bin with the highest statistics, consider merging it with all immediate adjacent bins. If the individual fractional errors differ significantly before the merge, do not merge them. In this analysis, a factor of 10 in fractional uncertainty was chosen to describe the similarity between bins. Additionally if the two unmerged bin normalizations differ by more than 10%, perform the bin merging. This step serves to smooth out the observable normalization prefit space.

While the problem of a few observable normalization parameters having the majority of statistics is still present, fluctuations between adjacent observable normalization parameters is iteratively minimized. The detector systematic that had the largest effect on the observable normalization prediction was the PØD energy loss resolution. With it, the event rate in each



(a)  $\nu_\mu$  in FHC CC 1-Track



(b)  $\nu_\mu$  in FHC CC N-Tracks

**Figure 4.5:** Bin normalization edges for the  $\nu_\mu$  in FHC selections. There are two plots shown for each sub-figure. The left and right plots show the bin normalization and the bin statistical fractional error, respectively, if each fit bin had a single bin normalization. The dashed lines indicate the edges of the bin normalization parameters finalized for this analysis.

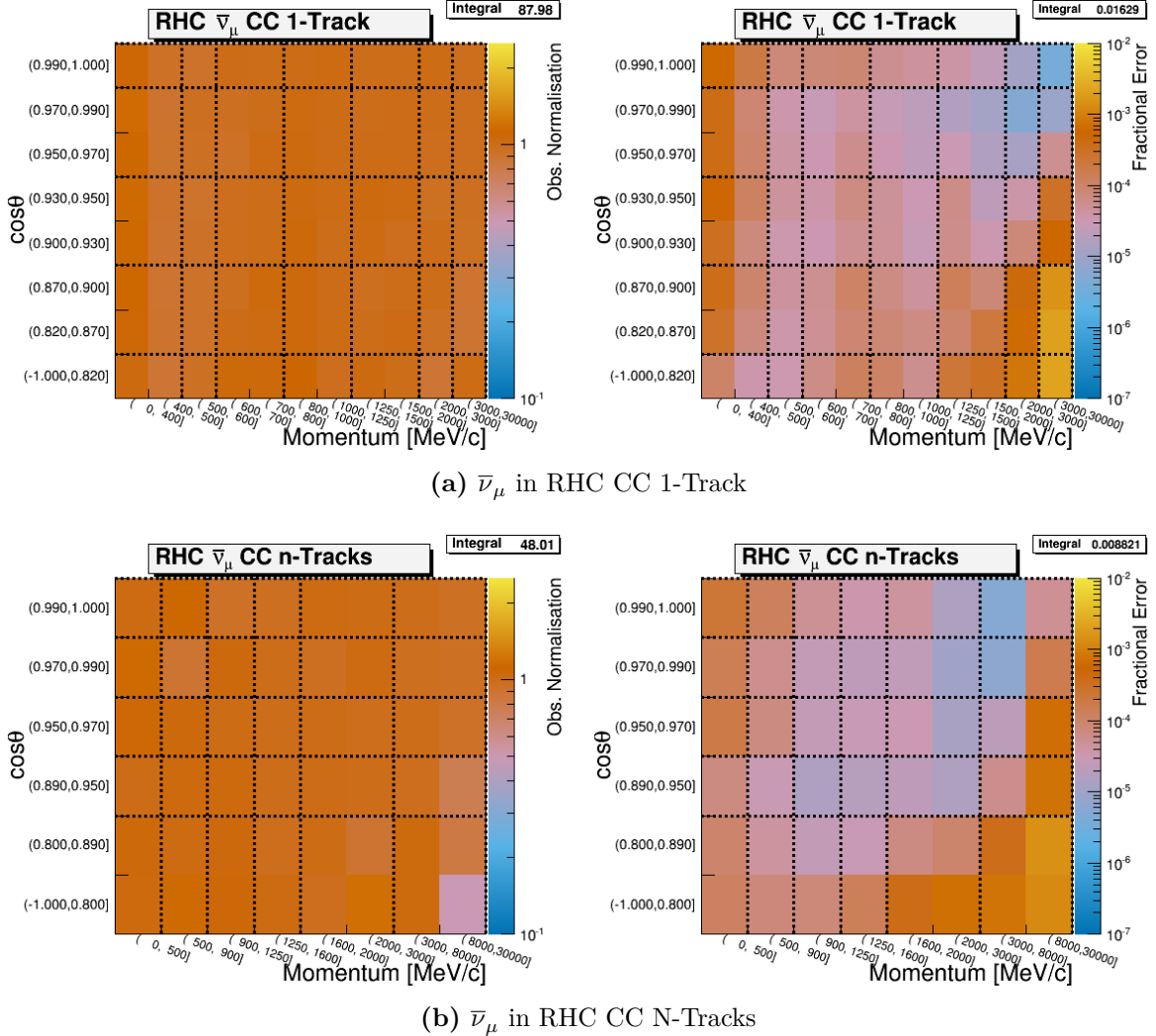


**Figure 4.6:** Bin normalization edges for the  $\bar{\nu}_\mu$  in RHC selections. There are two plots shown for each sub-figure. The left and right plots show the bin normalization and the bin statistical fractional error, respectively, if each fit bin had a single bin normalization. The dashed lines indicate the edges of the bin normalization parameters finalized for this analysis.

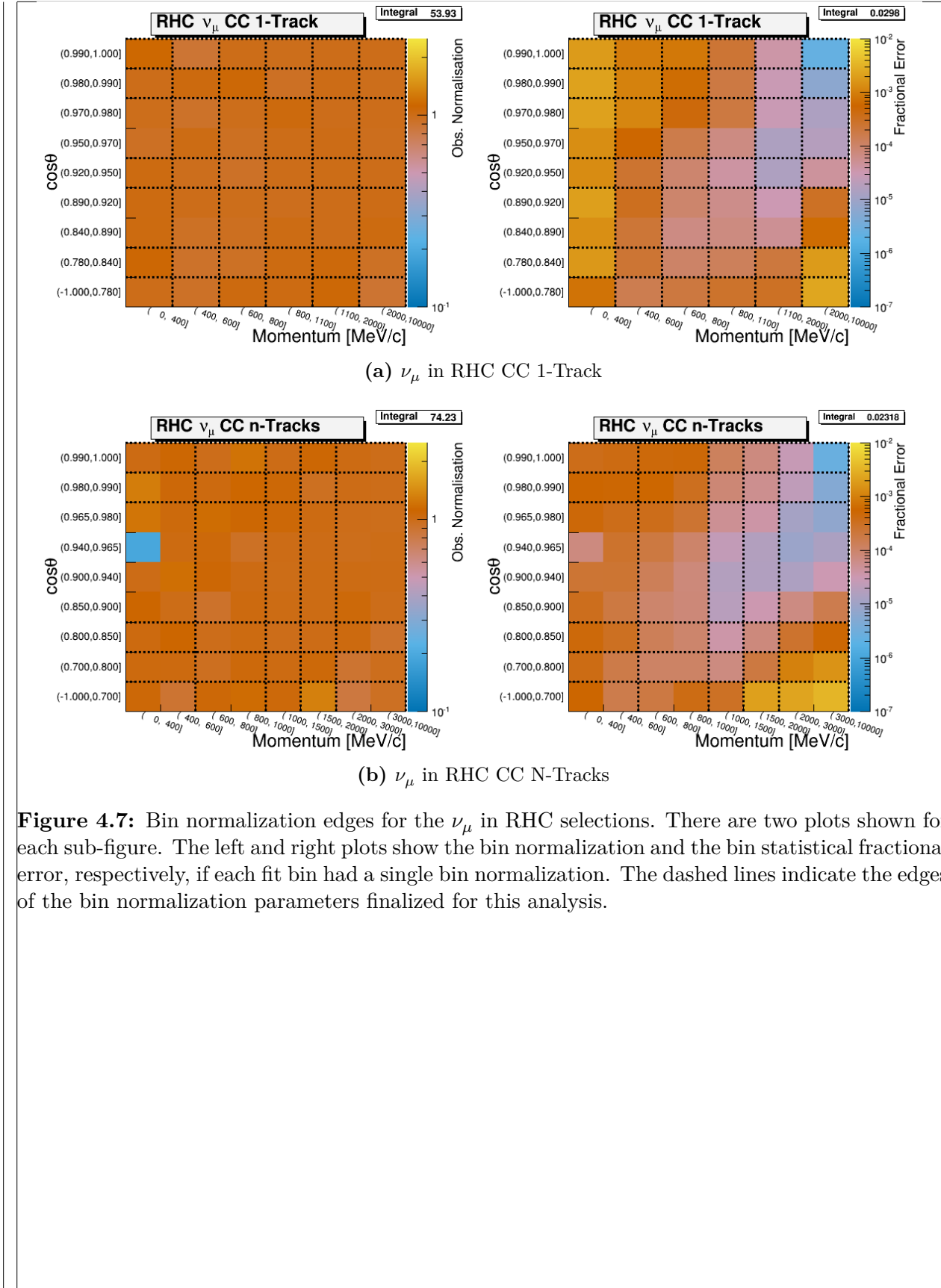
---

observable normalization bin varied non-normally. This effect can be seen in Figure 4.8 on page 116.

A considerable drawback to designing normalizations in this way of varying detector systematics in toy experiments is that not all detector systematics affect the observables ( $p, \cos \theta$ ) in the same way. There are non-symmetric systematics and are especially non-normal in their effects. Therefore, the covariance matrix from (4.16) is not an exact representation of the detector systematics. To demonstrate this, results of varied number of events are shown in Figure 4.8 on page 116 with all the varied toy experiment results are provided in B.

We can also understand the effects the PØD energy loss resolution (ELossRes) correction and systematic on the bin normalizations, which was identified in the  $\nu_\mu$  CC-0 $\pi$  analysis as the leading uncertainty in the detector systematics. In Figure 4.8 on page 116, an additional red curve is shown in each sub-figure to represent disabling the PØD ELossRes correction and systematic variation in the toy experiments. We see this systematic broadens the number of possible events in a normalization bin and its correction shifts the bin mean. This is expected since one or more particles originating from a neutrino interaction in the water could remove reconstructed tracks from the event when varying the systematic.

Observed in most observable normalization bins is that the disabled ELossRes variation distribution is below the nominal MC expectation. However, there are in the 1-Track samples, as shown in Figure 4.8 on page 116, that the shape location is above the expectation. This behavior was unexpected prior to running the toy experiment variations. A relationship between the shape location and selection purity as a function of ( $p, \cos \theta$ ) was discovered. In high purity ( $p, \cos \theta$ )-regions of the 1-Track samples, the shape location of the disabled ELossRes variations was below the nominal MC expectation. When the purity was lower, however, the shape location was above it. This effect is likely due to events migrating into the N-Tracks samples. With the ELossRes variation disabled, events in the 1-Track samples



---

with low purity, which are also more likely to have multiple reconstructed tracks, are not being migrated into the N-Track samples.

The finalized observable normalization bins are listed below and shown visually in Figures 4.5 to 4.7. Their respective fit index and prefit values are tabulated in Appendix ??.

- $\nu_\mu$  in FHC CC 1-Track bin normalization edges:
  - $p$  [GeV/c]: 0, 0.4, 0.6, 0.8, 1.25, 2, 3, 4, 5.5, 30
  - $\cos \theta$ : -1, 0.7, 0.8, 0.94, 0.975, 0.99, 1
- $\nu_\mu$  in FHC CC N-Tracks bin normalization edges:
  - $p$  [GeV/c]: 0, 0.4, 0.6, 0.8, 1.2, 2.2, 3.5, 10, 30
  - $\cos \theta$  : -1, 0.77, 0.85, 0.9, 0.97, 1
- $\bar{\nu}_\mu$  in RHC CC 1-Track bin normalization edges:
  - $p$  [GeV/c]: 0, 0.5, 0.6, 0.8, 1.25, 2, 3, 30
  - $\cos \theta$  : -1, 0.82, 0.9, 0.95, 0.99, 1
- $\bar{\nu}_\mu$  in RHC CC N-Tracks bin normalization edges:
  - $p$  [GeV/c]: 0, 0.5, 0.9, 1.25, 1.6, 3, 30
  - $\cos \theta$  : -1, 0.89, 0.95, 0.97, 0.99, 1
- $\nu_\mu$  in RHC CC T-track bin normalization edges:
  - $p$  [GeV/c]: 0, 0.4, 0.6, 0.8, 1.1, 2, 10
  - $\cos \theta$  : -1, 0.78, 0.84, 0.92, 0.95, 0.98, 0.99, 1
- $\nu_\mu$  in RHC CC N-Tracks bin normalization edges:
  - $p$  [GeV/c]: 0, 0.6, 1, 1.5, 2, 10
  - $\cos \theta$  : -1, 0.7, 0.8, 0.85, 0.98, 0.99, 1

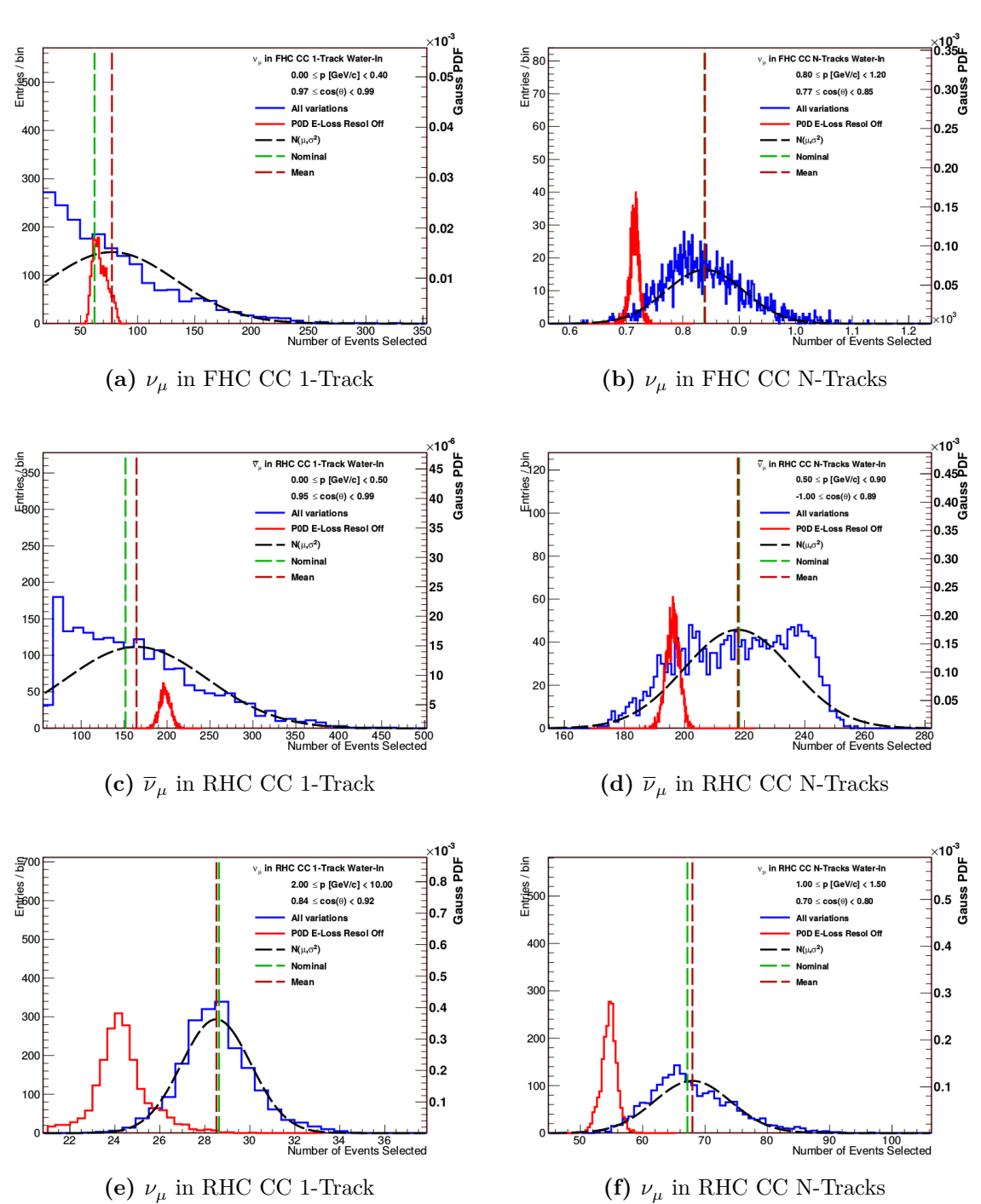


**Figure 4.8:** Event variations in representative observable normalization bins. Shown in each sub-figure the varied event rate from all toy experiments in a particular observable normalization bin as shown in blue. Vertical dashed lines show the unvaried, weighted MC prediction and varied mean of all toy experiments. The ratio of the horizontal positions of each vertical line is the prefit normalization value for that bin. A gaussian whose variance was extracted from covariance matrix is shown to illustrate the bin's estimate on the normalization uncertainty. The result of disabling the PØD energy loss resolution systematic is shown in red to illustrate its effect on the mean and spread on the toy experiments.

---

## The PØD-Only Systematics

There are four new PØD-only systematics that are considered for this BANFF fit analysis as listed in Table 4.2 on page 106. All the new sources were initially analyzed in the PØD  $\nu_\mu$  CC-0 $\pi$  cross section analysis [7].

The energy loss scale and resolution affect the measured momentum in the PØD and are very significant sources of uncertainty. In the  $\nu_\mu$  CC-0 $\pi$  cross section analysis, the same selection as the  $\nu_\mu$  in FHC CC 1-Track selection, the scale and resolution contributed 1.3% and 6.7%, respectively, to the cross section uncertainty. Those large uncertainties are due to the inherent design of the PØD as a low resolution tracking detector. Slight variations in the track reconstruction can significantly alter the energy loss as measured in (3.5).

The remaining systematics, the PØD mass and the PØD-TPC matching efficiency, were not available to analyze in toy experiments variations. They were not implemented in the BANFF framework and unavailable to implement due to time constraints on the author. Instead, they were treated as additional uncorrelated systematics on each bin normalization uncertainty with the normalization value remaining fixed. The treatment of these two systematics will be discussed shortly.

The PØD mass uncertainty is a normalization systematic which affects the event rate. This is a challenging systematic for analyses of recent T2K data due to increasingly faulty sensors to measure the water content. The procedure to fill the water bags required filling them in unison to prevent uneven bulging. However, faulty sensors would provide poor quality data, hence bags were under and overfilled. Prior PØD analyses have estimated the mass uncertainty using similar toy experiment techniques, but did not integrate them into the BANFF framework. In particular in the  $\nu_\mu$  in CC-0 $\pi$  analysis [7], the PØD mass had an 1.5% systematic effect on the cross section. Since the PØD mass uncertainty estimate was determined using the same toy experiment variation method, *a conservative estimate of 2% on the mass uncertainty included in this analysis*. So for the PØD mass systematic, let  $\tilde{\sigma}_{\text{Mass}} = 2\%$ , where the tilde ( $\sim$ ) refers to a fractional uncertainty. This will be used later.

The PØD and TPC matching efficiency is estimated to have a small systematic effect on the analysis. It was analyzed to have over a 99.8% data and MC efficiency in the single track  $\nu_\mu$  CC-0 $\pi$  analysis and thus neglected. However, since this analysis includes multiple track selections, that matching efficiency is unknown. Also, it is hard to imagine a CS that could constrain it. The best handle is from the private T2K technical note on the  $\bar{\nu}_\mu/\nu_\mu$  cross section analysis [20] which estimated the uncertainty at less than 0.14% using its in-house matching algorithm. Since that is a single bin measurement employing different matching algorithm, the uncertainty is not guaranteed to remain constant across  $(p, \cos \theta)$  bins. *A conservative estimate of 1% for the TPC matching efficiency was chosen in order to account for the inherent uncertainty in this systematic.* So for the matching efficiency systematic, let  $\tilde{\sigma}_{\text{Match}} = 1\%$ .

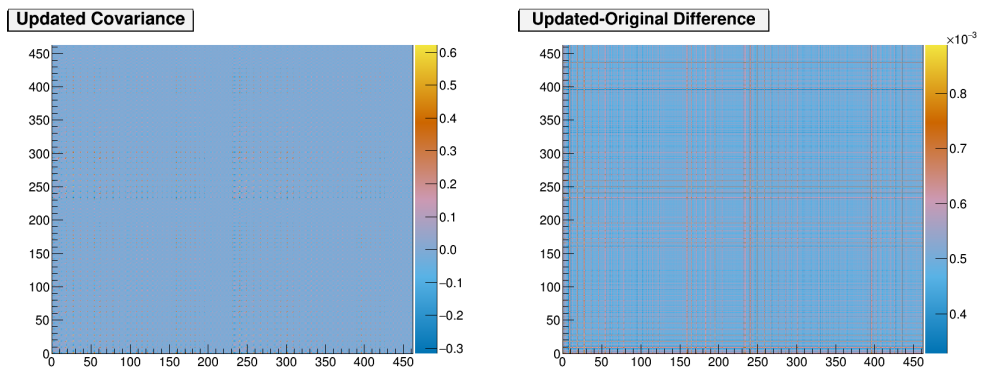
In order to propagate these two uncorrelated uncertainties, the detector covariance matrix given in (4.16) was converted into a fractional covariance matrix first. Let  $\tilde{V}_{i,j}^{\text{Det}}$  refer to the fractional covariance matrix, given explicitly as

$$\tilde{V}_{i,j}^{\text{Det}} = \frac{V_{i,j}^{\text{Det}}}{d_i d_j}, \quad (4.17)$$

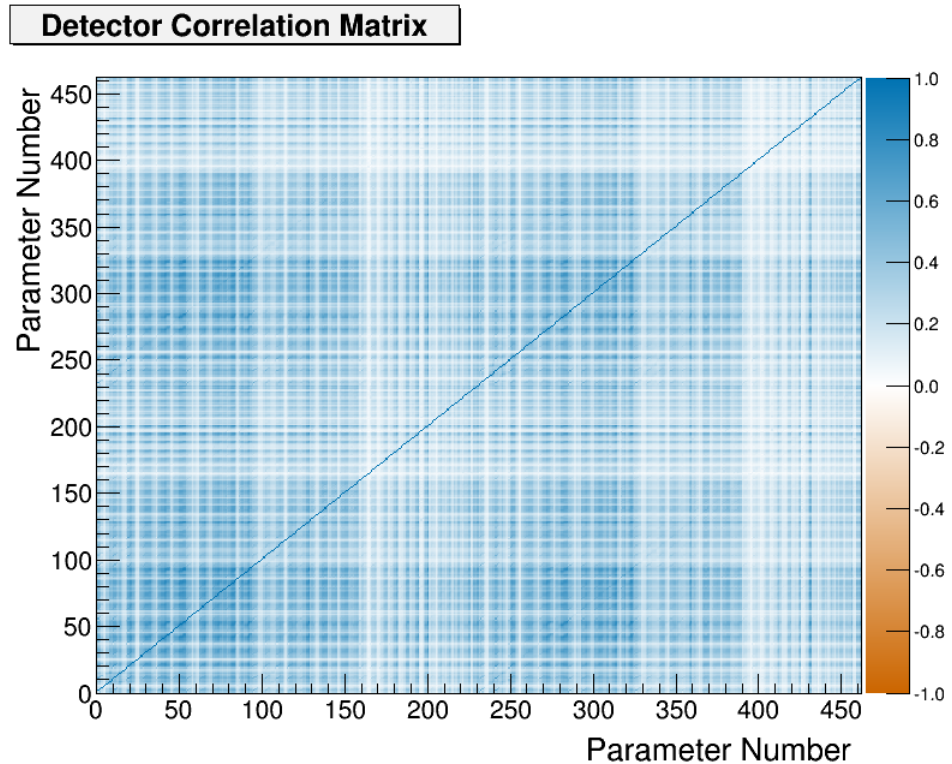
where we recognize  $\sqrt{\tilde{V}_{i,i}^{\text{Det}}}$  as the fractional uncertainty in the  $i$ th observable normalization parameter. The updated detector covariance matrix,  $\acute{V}_{i,j}^{\text{Det}}$ , which accounts for the PØD mass and TPC matching inefficiency systematics, is given by

$$\acute{V}_{i,j}^{\text{Det}} = \left( \tilde{V}_{i,j}^{\text{Det}} + \tilde{\sigma}_{\text{Mass}}^2 + \tilde{\sigma}_{\text{Match}}^2 \right) d_i d_j. \quad (4.18)$$

Together, the two additional sources of uncertainty increase each term in the covariance matrix by  $0.0005 d_i d_j$ , which increases each bin normalization error by about 2.23%. The updated covariance matrix used in this analysis is shown in Figure 4.9 on page 119.



(a) Updated detector covariance matrix    (b) Difference from original detector covariance matrix



(c) Updated detector correlation matrix

**Figure 4.9:** Updated detector covariance matrix (a), the difference from the original matrix (b), and updated correlation matrix (c). Note that the parameter numbers here are offset from their fit index value by 99.

### 4.2.3 Cross Section Model

There are a number of neutrino-nucleus model and other related systematics implemented in BANFF to account for the uncertainties in cross section measurements. They are frequently updated to account for new models and constraints from external data. The cross section models used in this analysis use the T2K 2017 parameterization, which is a canonical set of parameters shared among all analyses in T2K. A gross description of the cross section model is provided here with a full technical description of the parameterization is given in the following reference [8].

There are three types of cross section parameters: shape, normalization, and functional. A cross section shape parameter is defined as a fractional shift in the location of a certain feature in some parameter space. As a design choice, the shape location parameters all start with a prefit value of zero (0). A cross section normalization parameter,  $x_i^{\text{Norm}}$ , is defined as

$$x_i^{\text{Norm}} = \frac{p'}{p}, \quad (4.19)$$

where  $p$  and  $p'$  are NEUT nominal and ND constrained parameters, respectively. The prefit values for the normalization parameters are set to (1) unless the prefit is different from the nominal NEUT model. And finally functional parameters are normalization factors for basis functions in a particular parameter space. For example the parameters  $A$  and  $B$  are normalizations for the slope and intercept for a linear curve  $f(x) = Ax + B$ .

The next sections deal with the model parameterizations and systematic uncertainties in the NEUT version 5.3.3 [66] interaction library which is used in T2K MC and oscillation analysis.

#### CCQE and CC- $0\pi$

The cross section models with the largest impact on T2K's oscillation sensitivity are CCQE and CCQE-like interactions, collectively called CC- $0\pi$ . At energies near the  $\nu_e$  ap-

---

pearance maximum,  $E_\nu = 0.6$  GeV, the CCQE interaction is the largest contributor to the neutrino cross section as shown in Figure 1.30 on page 51. The nominal CCQE model in NEUT is a Spectral Function from Benhar and others [?]. An alternative CCQE model uses the Llewellyn-Smith model [44] with a dipole [22] axial form factor<sup>12</sup>, BBBA05 vector form factors [17] coupled to a Smith-Miniz Relativistic Fermi Gas [48, 61] (RFG). A CCQE-like excitation mode involves correlated nucleon pair scattering called “2 particle, 2 hole” [46] (2p2h)<sup>13</sup>. An additional nuclear model called “Random Phase Approximation” (RPA) [25] is used to modify single nucleon scattering by accounting for nucleon correlations inside the nucleus [47]. The default CC-0 $\pi$  model for T2K analyses is the combination of the Llewellyn-Smith+RFG model, 2p2h excitation, and RPA nuclear model. This combination was selected due to tension using the SF model to match with external data [66].

The selected CCQE model has three free parameters: the dipole axial form factor mass  $M_A^{\text{QE}}$  from the Llewellyn-Smith model, and two Fermi momentum parameters  $p_F$ , one for  $^{12}\text{C}$  and  $^{16}\text{O}$  that describe the momentum of nucleons on the surface of a RFG. In the past, these parameters have been shown to work as effective models in T2K when unconstrained. In this analysis, these three parameter are unconstrained. In other words, a flat prior is used for  $M_A^{\text{QE}}$ ,  $p_F^C$ , and  $p_F^O$ .

For the 2p2h excitation, there are a total of 5 parameters to describe the uncertainty in the model. Three are three normalization terms:  $\nu$  interaction on  $^{12}\text{C}$ ,  $\bar{\nu}$  interaction on  $^{12}\text{C}$ , and scaling for  $^{12}\text{C} \rightarrow ^{16}\text{O}$ . The remaining two systematic parameters in the 2p2h model are shape parameters, one for  $^{12}\text{C}$  and  $^{16}\text{O}$ , to describe the uncertainties in the contributing modes in 2p2h. These modes are called Meson Exchange Current (MEC) which involve a virtual meson exchange between the nucleons, nucleon-nucleon correlations (NN) which involves

---

<sup>12</sup>A form factor is a measure of scattering amplitude in the form of the Fourier transform of some charge distribution.

<sup>13</sup>The name 2p2h originates from Condensed Matter Physics which motivated the model. In solid state matter, a “hole” refers to the absence of an electron in a valence band. In the High Energy Physics context, 2p2h considers neighboring and interacting nucleon pairs (2p) scattering from an incoming  $\nu$ . The imparted energy on the pair excites them to higher energy states leaving two “hole” states (2h) behind.

virtual particle exchange, and the MEC-NN interference. A shape value of -1 determines 2p2h is completely due to MEC, 0 is the nominal MC 2p2h model, and +1 determines 2p2h is completely due to NN. Any value in between  $\pm 1$  include uses the interference term to absorb differences in the event rate. However, since no T2K nor external neutrino data can constrain the neutrino-induced 2p2h interaction, a flat prior is set for all 2p2h parameters.

The other nuclear interaction in the CC-0 $\pi$  model uses the Nieves RPA model [47] to describe nucleon correlations. The RPA model primarily alters the single nucleon cross section and has dependence on both  $E_\nu$  and  $Q^2$ . A functional weighting scheme only in  $Q^2$  was found to work well to mimic the inherent uncertainties in the Nieves RPA model. Using a third order polynomial in the Bernstein polynomial basis  $B_i^n$  [30]

$$B_i^n(x) = \binom{n}{i} x^i (1-x)^{n-i} \quad x \in [0, 1] \quad (4.20)$$

where

$$\binom{n}{i} = \frac{n!}{(n-i)! \times i!}. \quad (4.21)$$

with a high- $Q^2$  exponential tail, the “BeRPA” model functional weight is parameterized as

$$w_{\text{BeRPA}}(Q^2) = \begin{cases} A(1-x)^3 + 3B(1-x)^2x + 3p_1(1-x)x^2 + Dx^3 & Q^2 \leq U \\ 1 + p_2 \exp(-E[Q^2 - U]), & Q^2 > U \end{cases} \quad (4.22)$$

where  $x = Q^2/U$ ,  $A$ ,  $B$ ,  $D$ , and  $E$  are scale/normalization factors for the basis functions, and  $U$  signifies when the two functions intersect with  $p_1$  and  $p_2$  absorbing the continuity conditions

$$p_1 = D + \frac{UE(D-1)}{3}, \quad p_2 = D - 1. \quad (4.23)$$

The parameters  $A$ ,  $B$ ,  $D$ , and  $E$  are allowed to vary while  $U$  is fixed to prevent unwieldy correlations from appearing.

---

## CC- $1\pi$

Another important exclusive channel in NEUT are resonance states that produce a single pion or CC- $1\pi$ . The CC- $1\pi$  model is based on the Rein-Seghal model [52] with lepton mass corrections [15, 38] of neutrino-induced  $\Delta$  resonance decay [35–37]. There are three tunable parameters that describe the systematics in the CC- $1\pi$  model. They are resonant axial mass  $M_A^{\text{Res}}$ , the axial form factor normalization  $C_A^5$ , and the isospin= $1/2$  background. In particular,  $M_A^{\text{Res}}$  and  $C_A^5$  are strongly anticorrelated due to the parameterization of the form factor

$$f(Q^2) = \frac{C_A^5}{\left(1 + \frac{Q^2}{(M_A^{\text{Res}} c^2)^2}\right)^2}. \quad (4.24)$$

Again, this model is an effective model since the uncertainties were tuned to bubble chamber data from Brookhaven National Laboratory [42] and Argonne National Laboratory [51].

Harder to measure processes like coherent pion production are discussed next.

## Coherent Pion Production

Coherent scattering refers to scattering where the wavelength of the incoming particle is larger than the target. In the case of coherent neutrino-nucleus scattering, the neutrino's wavelength given by

$$\lambda = \frac{hc}{E_\nu}$$

is larger than the size of the nucleus. In the scattering, no quantum numbers are exchanged, but the nucleus experiences a momentum boost. In coherent pion production, the in-flight virtual boson is converted into a pion with that pion exchanging a Pomeron [5] with the nucleus. The coherent scattering model is described by Rein-Sehgal [53]. Lookup tables are used to scale the cross section to external data [66] and the Berger-Sehgal model [15]. Three tunable normalization parameters are used to describe the uncertainties in coherent production: CC on  $^{12}\text{C}$ , CC on  $^{16}\text{O}$ , and NC on all nuclei.

---

## CC DIS

The CC DIS process, which also includes multiple pion production, systematic is treated as a normalization with a relatively simple uncertainty,  $\tilde{\sigma}_{\text{CCDIS}}$ , of

$$\sigma_{\text{CCDIS}}(E_\nu) = \frac{0.4}{E_\nu \text{ [GeV]}}$$

where the fractional uncertainty at 4.0 GeV is  $\sim 10\%$  [66].

## NC Other

There is one free normalization parameter for the NC processes. The NC other parameter contains the normalization uncertainties in NC DIS, single kaon production, single  $\eta$ -meson production, and elastic processes with a conservative 30% fractional uncertainty [66].

## Final State Interactions (FSI)

Final state interactions [34] are effects that alter final state pions from neutrino-nucleus events before the pion exits the nucleus. The microscopic model in NEUT is a cascade implementation of the Salcedo-Oset model [57] which describes interactions in the nucleus as probabilities of position and momentum. The systematics are parameterized as scattering probabilities for different interaction processes tuned to world data [54]. These processes are divided into four classes: inelastic (INEL) scattering, pion absorption (ABS), pion production (PROD), and charge exchange (CEX). There are a total of six FSI shape parameters in the fit. The PROD and ABS classes are each single shape parameters. For the INEL and CEX classes, they divided into low (LO) and high (HI) energy regions where the transition occurs at  $p_\pi = 500$  MeV/c.

---

## Other Fixed Parameters

As mentioned in the CC- $0\pi$  model, the BeRPA  $U$  parameter is fixed to remove correlations with the other BeRPA scale parameters. However, there are three fixed normalization parameters in the BANFF fit since they correspond to Super-K only parameters. They are included in the fit in order to maintain consistency between the ND280 constraint and oscillation analysis parameterizations. In other words, they are spectators in the BANFF fit. These parameters are the CC  $\nu_e$ - $\nu_\mu$  event rate ratio, CC  $\bar{\nu}_e$ - $\bar{\nu}_\mu$  event rate ratio, and NC  $1\gamma$  event rate.

## Fit Parameters

There are a total of 31 cross section parameters in the BANFF fit, four of which are fixed. The fit parameters are listed in Table 4.3 on page 128 with the associated covariance matrix shown in Figure 4.10 on page 126. Following the definition of the flux and bin normalization parameters, cross section parameters are defined as fractional differences either in shape, scale, or normalization. If no prefit uncertainty is shown in Table 4.3 on page 128, and emphasized using red font, then the parameter had a flat prior assigned. A model parameter with an asterisk (\*) next to it is fixed in the fit. Abbreviations used in this table are “dim.-less” for dimensionless, “norm.” for normalization, “Near” for ND280, “Far” for Super-Kamiokande, and “bkg” for background. Parameters with physical units are shown in both dimensionless and dimensional values for comparison. Prefit values are relative to the NEUT nominal value.

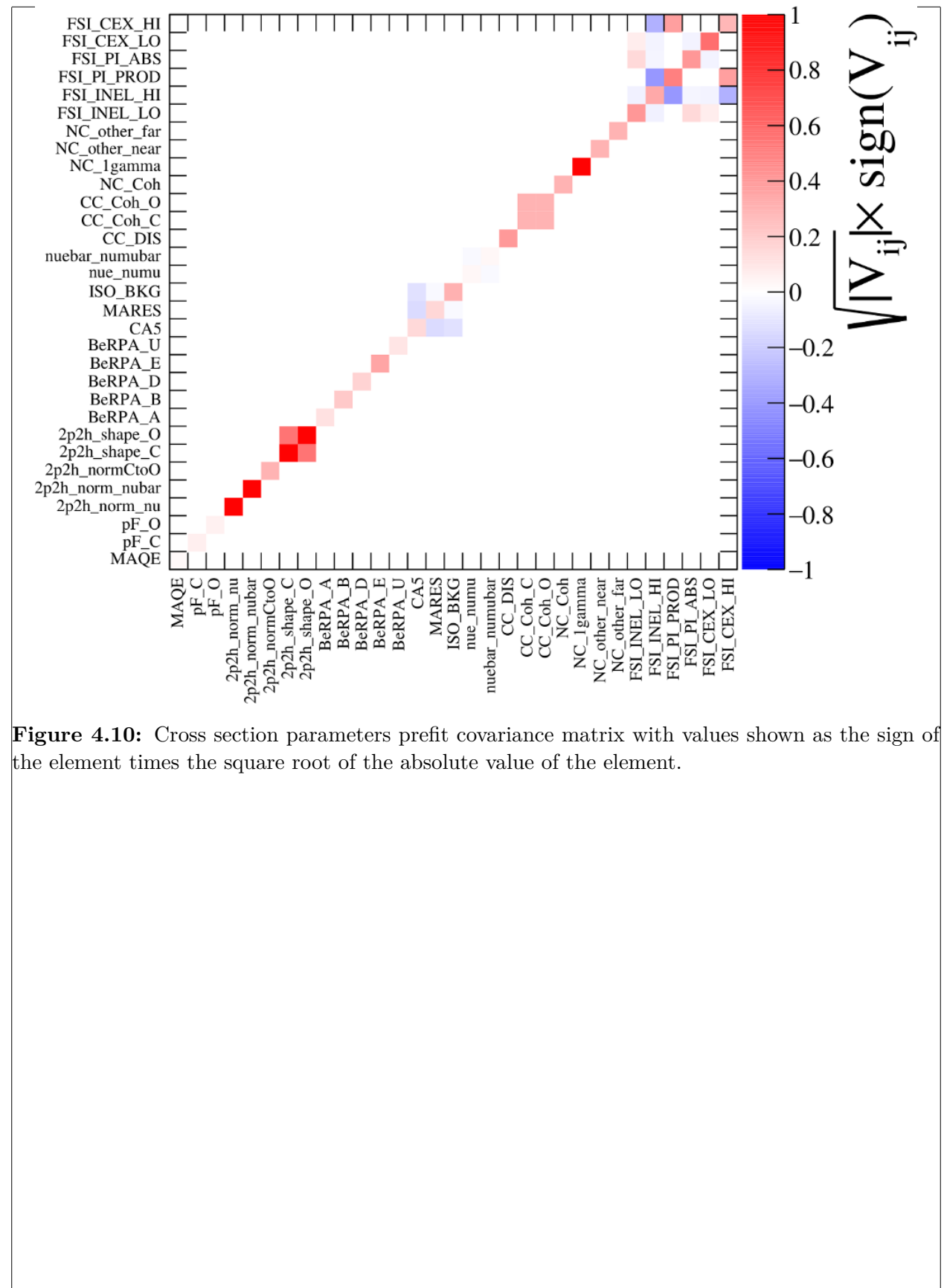


**Figure 4.10:** Cross section parameters prefit covariance matrix with values shown as the sign of the element times the square root of the absolute value of the element.

**Table 4.3:** Cross section model parameters in the fit. See the text for a full description.

Fit index	Topology	Model	Parameter	Prefit
562	FSI shape		Low energy INEL	$0 \pm 0.41$
563			High energy INEL	$0 \pm 0.34$
564			PROD	$0 \pm 0.41$
565			ABS	$0 \pm 0.5$
566			Low energy CEX	$0 \pm 0.57$
567			High energy CEX	$0 \pm 0.28$
568		Llewellyn-Smith	$M_A^{\text{QE}}$ (dim.-less) $M_A^{\text{QE}} (\text{GeV}/c^2)$	1 1.20
569	RFG		$p_F^C$ (dim.-less) $p_F^C (\text{MeV}/c)$	1 217
570			$p_F^O$ (dim.-less) $p_F^O (\text{MeV}/c)$	1 225
571		Nieves 2p2h	$\nu$ norm. on $^{12}\text{C}$	1
572			$\bar{\nu}$ norm. on $^{12}\text{C}$	1
573			$^{12}\text{C}/^{16}\text{O}$ norm.	1
574			$^{16}\text{C}$ shape location	0
575			$^{12}\text{O}$ shape location	0
576	BeRPA nuclear model (functional)		A scale	$0.59 \pm 0.118$
577			B scale	$1.05 \pm 0.21$
578			D scale	$1.13 \pm 0.1695$
579			E scale	$0.88 \pm 0.352$
580			U scale*	$1.2 \pm 0.1$

**Table 4.3:** Cross section model parameters in the fit. See the text for a full description.

Fit index	Topology	Model	Parameter	Prefit
581	CC-1 $\pi$	Rein-Seghal resonant 1 $\pi$ prodction	$C_A^5$	$0.96 \pm 0.148$
582			$M_A^{\text{Res}} \text{ (dim.-less)}$	$1.1263 \pm 0.157$
			$M_A^{\text{Res}} \text{ (GeV/c}^2\text{)}$	$1.07 \pm 0.15$
583			I= $^{1/2}$ bkg. norm.	$0.74 \pm 0.307$
584	Other	Event rate at SK	CC- $\nu_e/\nu_\mu^*$	$1 \pm 0.0282$
585			CC- $\bar{\nu}_e/\bar{\nu}_\mu^*$	$1 \pm 0.0282$
586			CC-DIS shape location	$0 \pm 0.4$
587		Coherent pion production	CC norm. on $^{12}\text{C}$	$1 \pm 0.3$
588			CC norm. on $^{16}\text{O}$	$1 \pm 0.3$
589			NC norm.	$1 \pm 0.3$
590		Event rate	NC- $1\gamma^*$	$1 \pm 1$
591			NC Other Near	$1 \pm 0.3$
592			NC Other Far*	$1 \pm 0.3$

### 4.3 BANFF Fit Parameterization Summary

This chapter has described all the fit bins and systematic parameters that go into the BANFF fit. For the fit bins, they are used in the LLR term to model the best possible fit between data and MC without any constraints. However, since there are known systematic uncertainties in the flux, detector inefficiencies, and cross sections, we have described their parameterizations to force the fit work within those constraints. The flux model is constrained by T2K primary and secondary beamline data while the cross sections are con-

---

---

strained by external data. Finally, the detector systematics are determined via an ensemble of toy experiments based on well established control samples in the ND280.

Next chapter explores the set of validation studies to examine how the BANFF fit works.

---

# Chapter 5

## Fitter Validation

This chapter will present the checks, tests and validations of the BANFF fit using the MC as input. The first such test is using the weighted MC as the data, referred to as an Asimov data fit. The next are two validation tests using two different data sets that have altered event weights compared to the MC. These are referred to as "fake data" sets. One fake data set alters the flux prediction and is referred to as the "High Energy Neutrino Flux Variation" fake data set. The other is the "Single Pion Event Rate Variation" fake data set.

### 5.1 Asimov Data Fit

Asimov data refers replacing the ensemble of simulated data sets by a single representative one [26]. In this analysis, this involves fitting the MC data set to itself for the primary purpose of checking the closure of the fitting framework. The Asimov set is produced with the same models as is implemented in the fitter and has all parameters set to their prior central values as defined in Chapter 4. Instead of statistically sampling from the MC, which can insert statistical variations in the fit, the Asimov data set is created by scaling the set down to the full T2K POT with additional finer corrections like flux and cross section weights. The prefit correlation matrix is shown in Figure 5.1 on page 131.

---

---

### Prefit Correlation Matrix

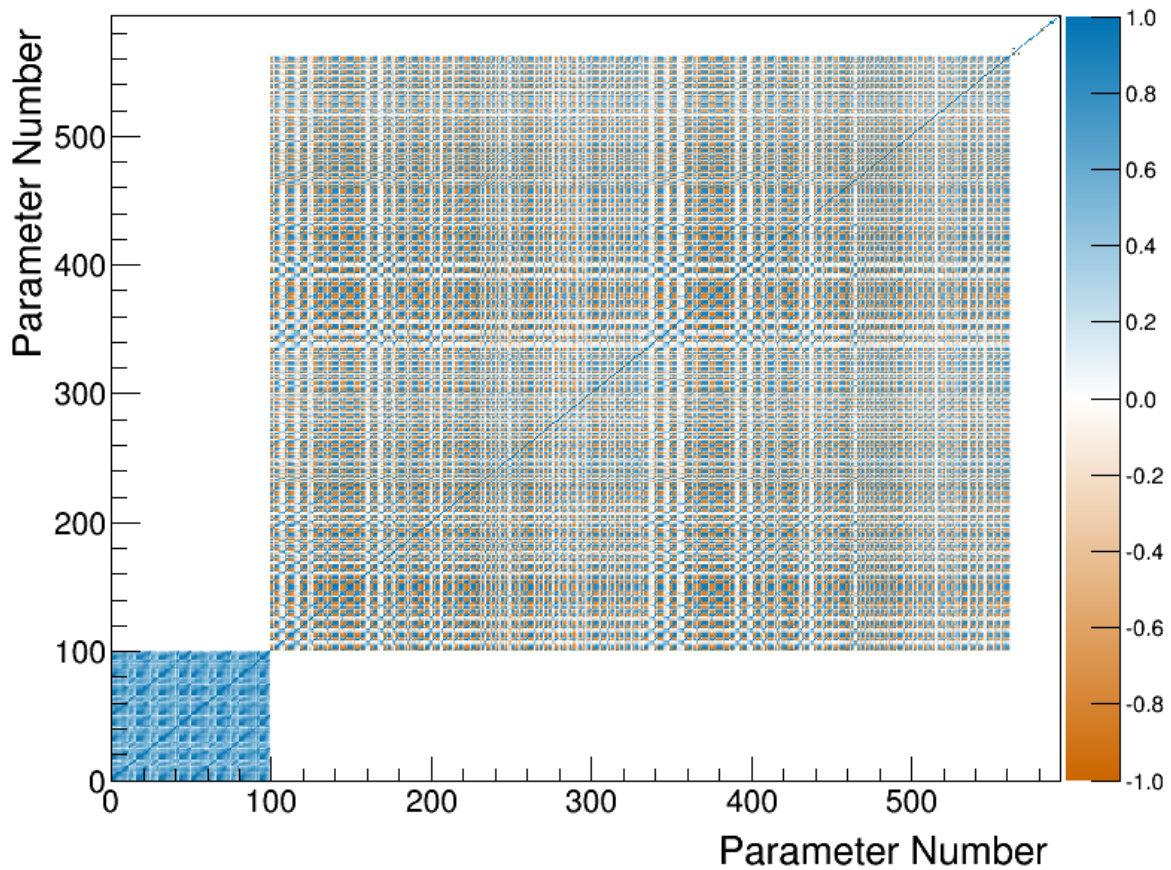


**Figure 5.1:** Complete prefit correlation matrix for the BANFF fit. The first 100 parameters are the flux bins. Between 100 and 561 are the bin normalization parameters. Finally 562 through 592 are the cross section parameters.

---

---

In addition to running an Asimov fit, other metrics were examined in the Asimov set. Shown first is a comparison of the event rates before and after applying weights to the MC. Next is an examination of the cross section weight functions. Finally is a set of scans of the test statistic space to ensure the sample and penalty terms are behaving as expected. Then the Asimov data set fit is explored.

### 5.1.1 Event Rate

Shown in Table 5.1 on page 133 is the event rates for the various samples for the Asimov fit. The data events column refers to real T2K data collected in the sample with the rest are MC events. There are a weights that correct differences between the data and MC. The POT weight normalizes the MC event rate to data rate. The other weights, which where discussed in Chapter 2, are the flux, cross section, and detector corrections. We see that applying the POT weight scales the MC event rate close to that of the data. The other weights are fine tuning corrections to the rate from known systematics like flux and cross sections. Application of all the weights is the prefit event rate and is collectively referred to as Asimov data set.

Sample name	Data events	Raw MC events	POT only	Application of weights			Prefit
				POT+Flux	POT+xsec	POT+Det	POT+flux+xsec+Det
$\nu_\mu$ 1-Trk Wtr	27151.00	526226.00	26270.98	28766.86	24222.45	26286.14	27327.94
$\nu_\mu$ N-Trks	31013.00	529538.00	26708.61	31464.27	26267.19	26708.74	31098.20
$\bar{\nu}_\mu$ RHC 1-Trk	8779.00	176007.00	9152.04	9365.78	8321.76	9161.91	8461.37
$\bar{\nu}_\mu$ RHC N-Trks	4613.00	93132.00	4876.93	5014.74	4652.01	4876.81	4802.12
$\nu_\mu$ RHC 1-Trk	3502.00	56861.00	2933.20	3182.20	2747.29	2938.29	3025.76
$\nu_\mu$ RHC N-Trks	5424.00	85599.00	4460.10	4988.89	4413.01	4464.45	4956.19
$\nu_\mu$ 1-Trk Air	23504.00	309373.00	23383.39	25319.17	21594.49	23402.63	23603.03
$\nu_\mu$ N-Trks	32736.00	371986.00	28495.10	33255.58	27822.42	28505.66	32302.08
$\bar{\nu}_\mu$ RHC 1-Trk	6681.00	75374.00	7374.13	7512.47	6732.25	7381.37	6767.79
$\bar{\nu}_\mu$ RHC N-Trks	4437.00	47951.00	4689.16	4820.43	4446.52	4690.57	4544.72
$\nu_\mu$ RHC 1-Trk	2324.00	20943.00	2049.01	2198.46	1916.33	2052.56	2067.12
$\nu_\mu$ RHC N-Trks	4801.00	42098.00	4119.63	4586.22	4050.71	4122.39	4567.72
Total	154965.00	2335088.00	144512.28	160475.06	137186.41	144591.53	153524.03

**Table 5.1:** Event rate table for Asimov set. The “Raw MC” column refers the number of events in the sample from the nominal MC prediction without any weights applied. From left to right, applications of weights are applied to understand their affect on the samples. The “POT only” column refers to applying the POT weight to all events. Columns with “POT+Flux”, “POT+xsec”, and “POT+Det” refer to applying the POT weight together with the flux, cross section, and detector weights, respectively. The “Prefit” column has the POT, flux, cross section, and detector (POT+Flux+xsec+Det) weights all multiplied together.

---

### 5.1.2 One Sigma Variation of Cross Section Parameters

To ensure the cross section spline weight functions were functioning properly, the samples were analyzed when the parameters were set to their  $\pm 1\sigma$  values. The results of the variations are shown in Appendix B, which show the samples are indeed affected by the weight functions.

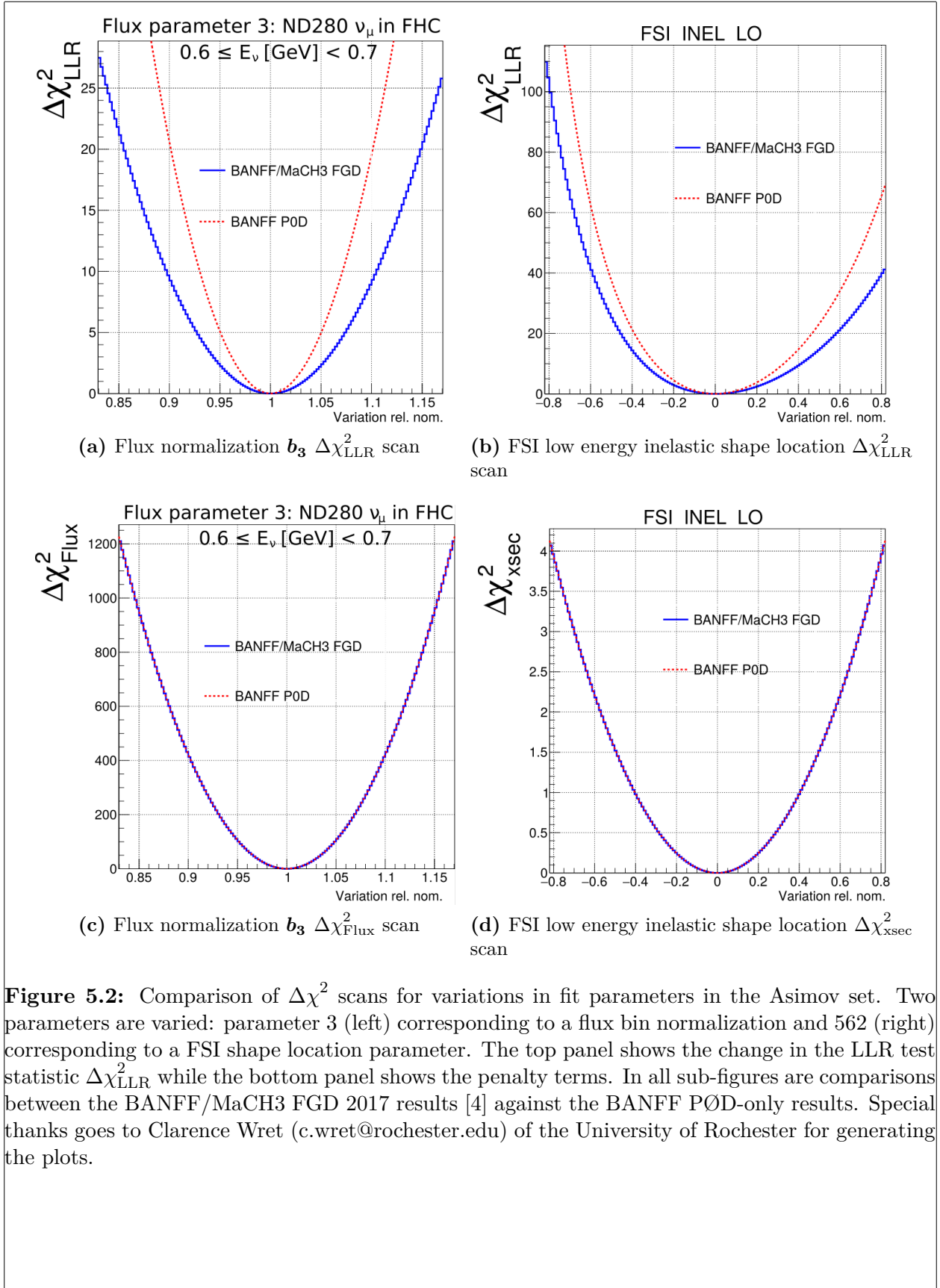
### 5.1.3 Log-Likelihood Scans

Log-likelihood scans of the sample and penalty terms were examined in the Asimov data set. The results of the scans are shown in Figure 5.2 on page 135 with comparisons between the PØD-only samples and FGD-only samples shown. It demonstrates that same penalties are applied between the PØD-only and FGD-only analyses. Also observed is that the PØD-only data has similar sensitivity and shape dependence on the flux parameters with that of the FGD-only data. The complete set of scans are shown in Appendix C and Appendix D.

### 5.1.4 Fit Results

The postfit results of the Asimov data fit are shown in Figure 5.3 on page 136 to Figure 5.6 on page 139. In order to provide a unified graphical representation for all the parameters, the prefit and postfit cross section shape parameters are adjusted to be relative to one (1).

We see that the postfit parameters have uncertainties that are different compared to their prefit values. This is expected since correlations between the sub-matrices in the covariance matrix, which were assumed uncorrelated to start, have been calculated. The complete postfit correlation matrix is shown in Figure 5.7 on page 140 and the flux and cross section only correlation matrix is shown in Figure 5.8 on page 140. We observe significant anti-correlations between each of the sub-matrices which is predicted from (2.7) since any increase in one parameter weight forces a decrease in the others.



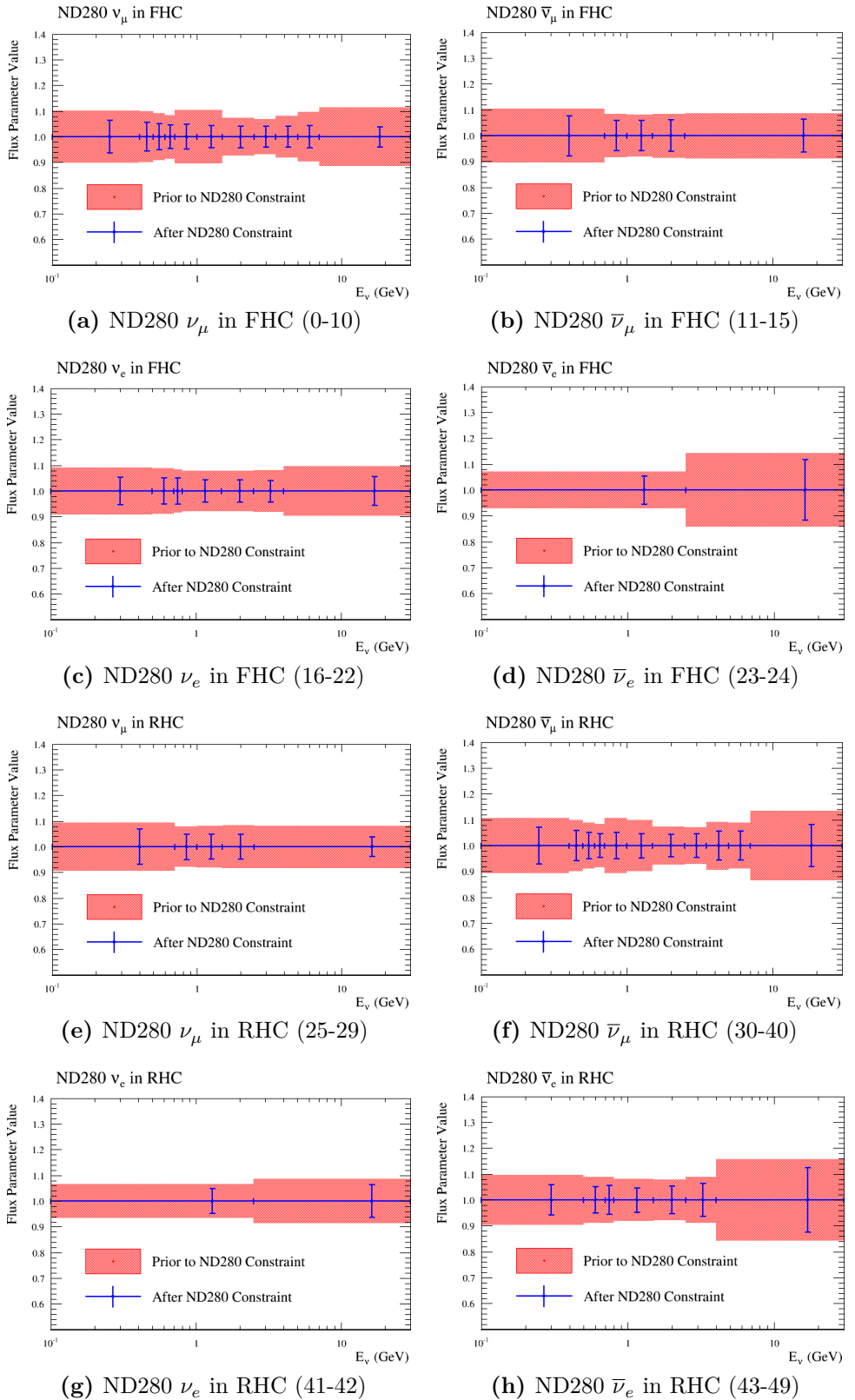


**Figure 5.3:** Asimov fit results for the Flux at ND280. The numbers in parentheses indicate the fit indices.

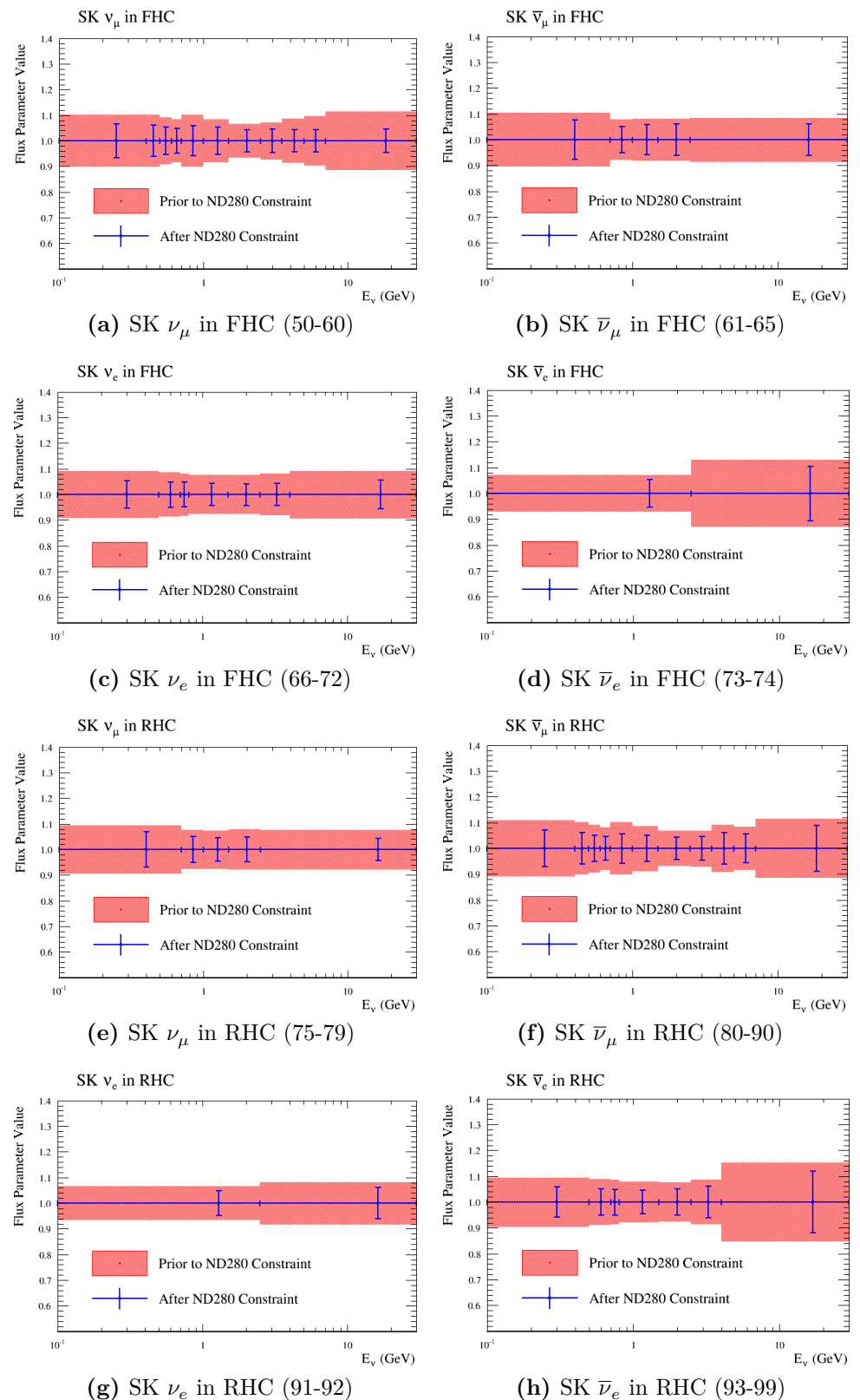


**Figure 5.4:** Asimov fit results for the Flux at Super-K. The numbers in parentheses indicate the fit indices .

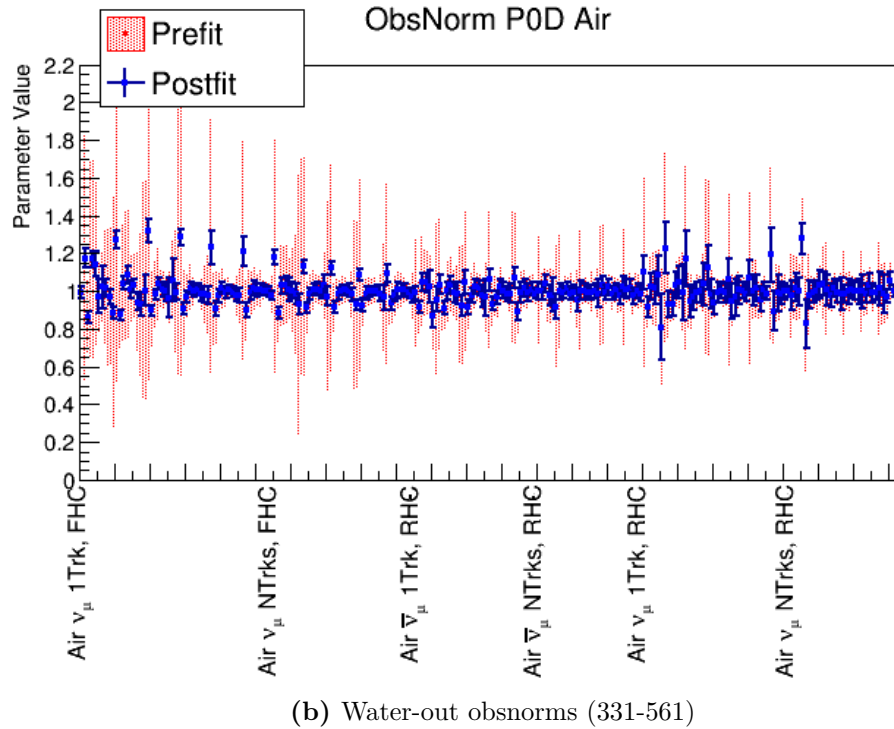
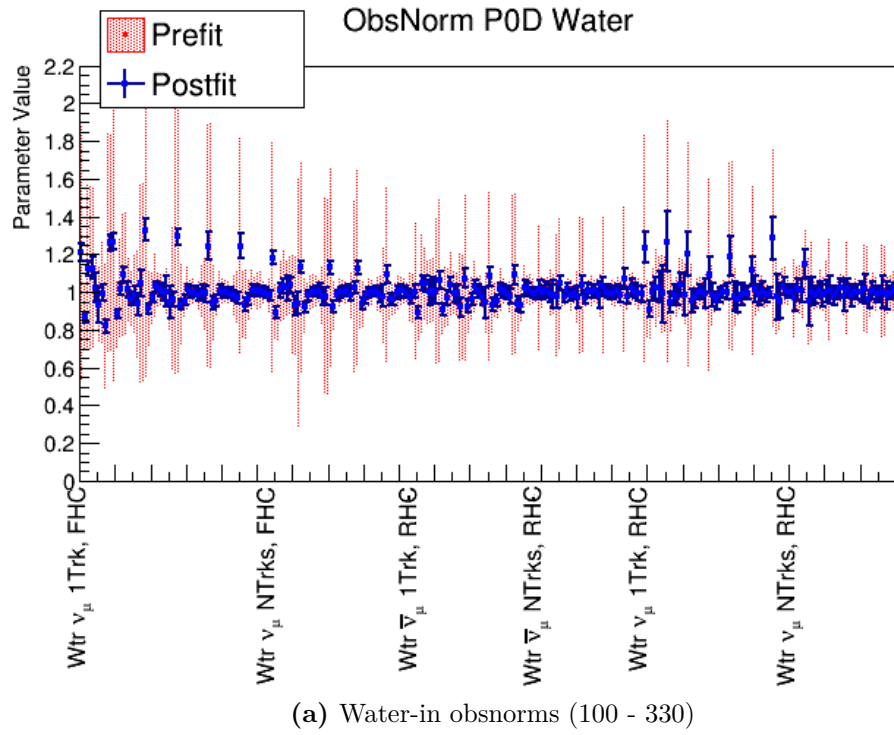
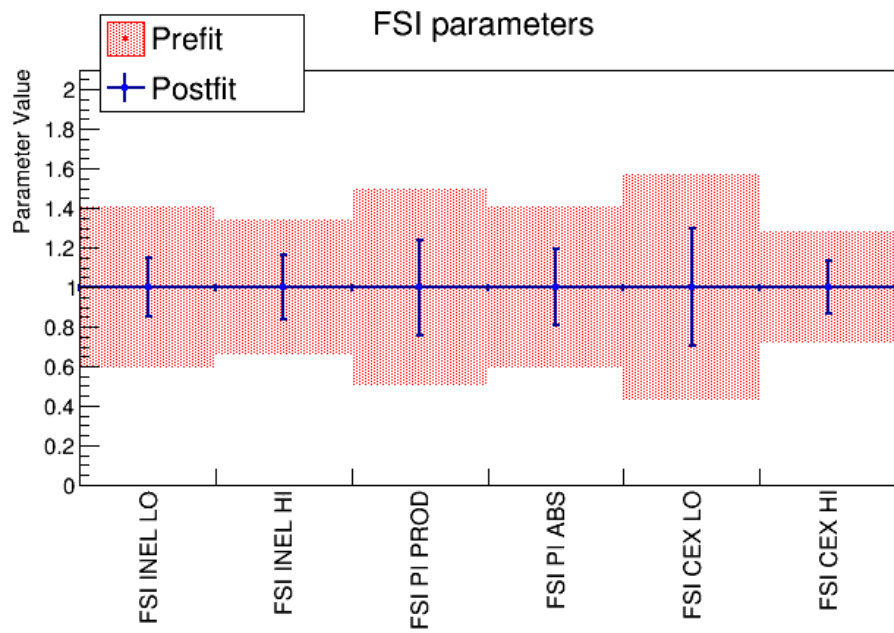
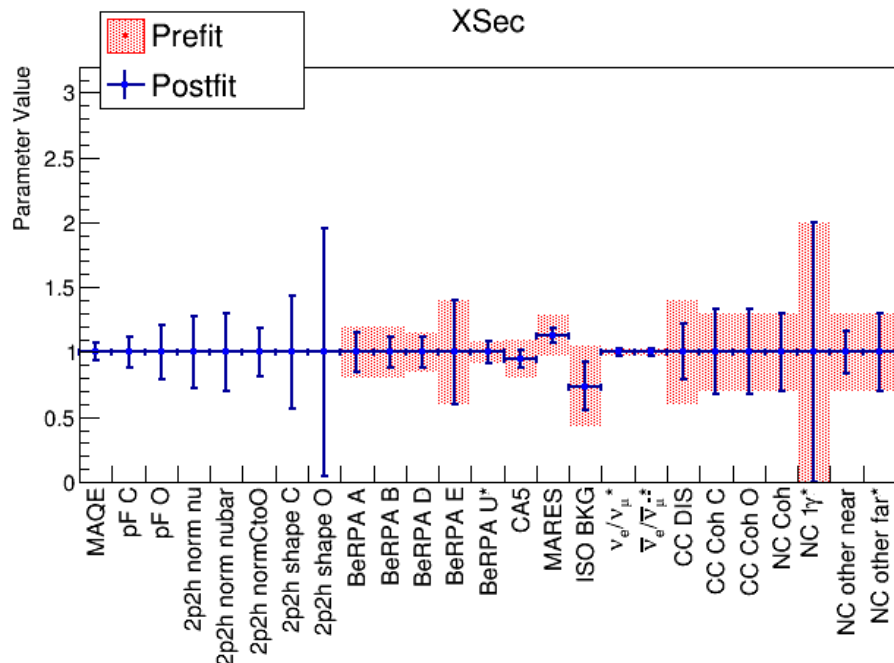


**Figure 5.5:** Asimov fit results for the obsnorm parameters. The numbers in parentheses indicate the fit indices. The large jumps in the bin normalization parameters is an artifact of the indexing choice with the indices increasing in increasing momentum in constant angular slices. Compare the changes in the bin normalizations in the  $\nu_\mu$  in FHC CC 1-Track in Figure 4.5 on page 111.



(a) FSI (562-567)



(b) Cross Section (568-592)

**Figure 5.6:** Asimov fit results for the FSI and cross section parameters. The numbers in parentheses indicate the fit indices. In order to provide a consistent presentation of parameter changes between prefit and postfit among all parameters, shape location and scale parameters are adjusted to prefits of one (1). In effect, the value and uncertainties for all parameters are fractional changes.

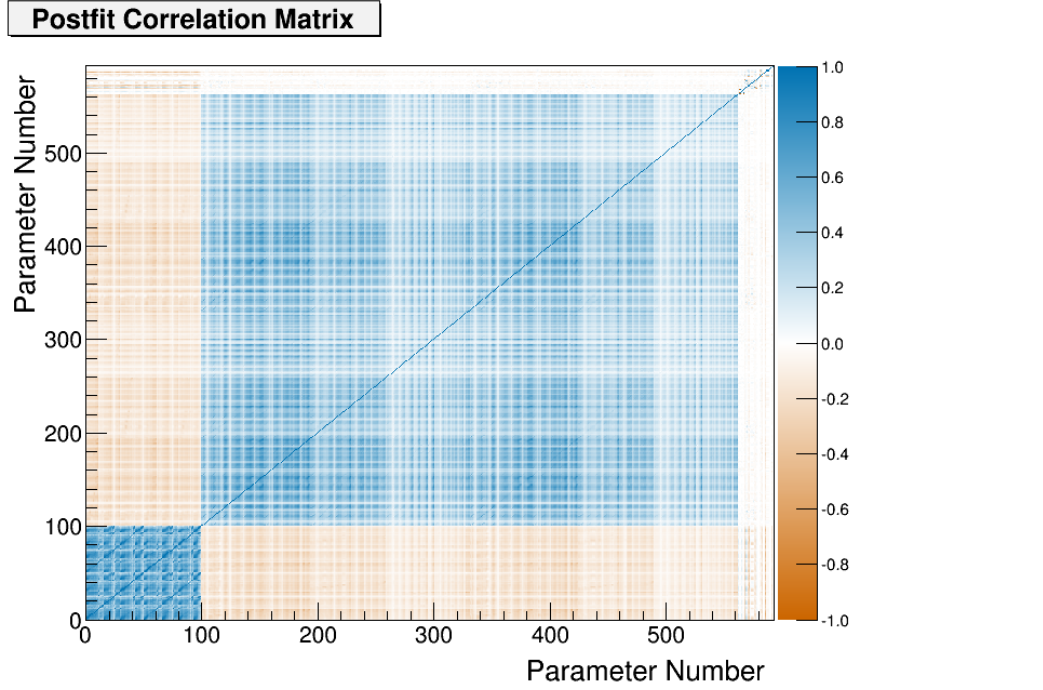


**Figure 5.7:** Complete postfit correlation matrix for the Asimov data fit.

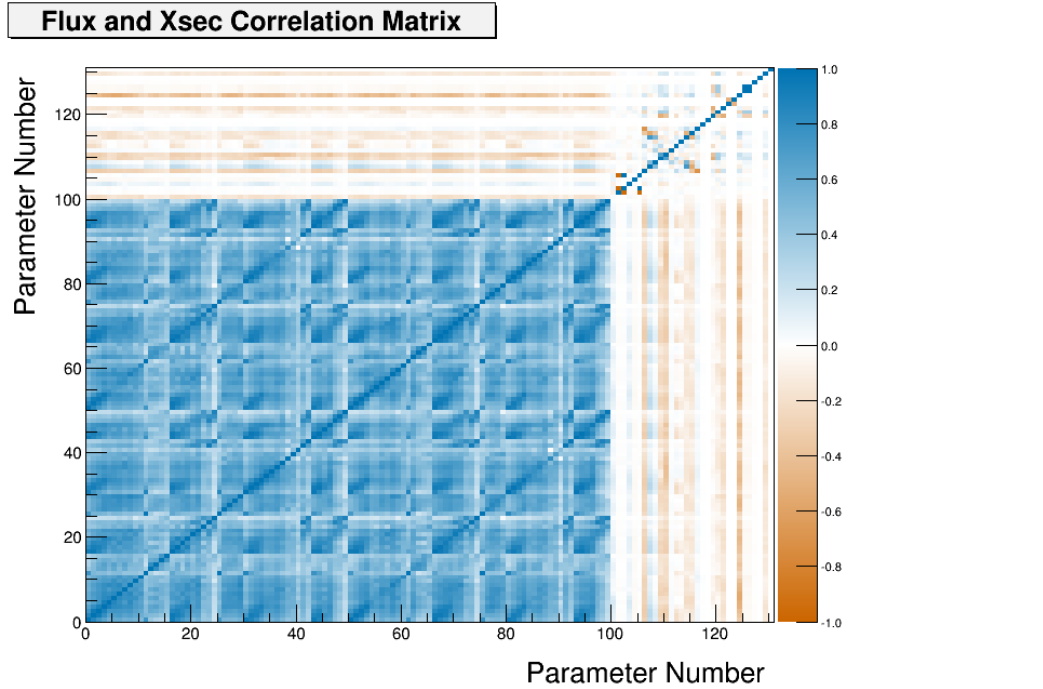


**Figure 5.8:** Flux and cross section postfit correlation matrix for the Asimov data fit. The parameters from 1-100 are the flux parameters and all parameters after are the cross section.

---

## 5.2 Fake Data

In this section, we examine the results of BANFF fits when given data sets with non-physical alterations. As stated earlier, these are called “fake data” sets since we are treating these as data in the fit, but they are in fact generated starting with the MC. These data sets initially start with the Asimov data set and have variations applied to it. Here we are only interested in the results of the flux and cross section parameters since they are the parameters that are propagated to the oscillation analysis. The first fake data set is a variation of the high energy  $\nu_\mu$  in FHC neutrino flux. The other test is a variation of the Single Pion Event Rate Variation.

While other fake data sets could be generated that are more or less similar to the Asimov data set, that is not the purpose of fitting to fake data sets. *The purpose of these tests is to show the fit can converge when provided with non-Asimov data sets and we can understand the results.* The fitting software MINUIT in the BANFF fit is known to not converge on a global minimum when using altered Asimov data. In particular, fitting FGD-only data generated from random and uncorrelated variations of all fit flux, cross section, and bin normalization parameters, 127 out of 500 fits ( $\sim 25\%$ ) reported fit convergence problems. So convergence is not assured in all situations, but is possible. The information it does provide is possible biases in the fit results for given systematic parameters. By demonstrating the BANFF fit converges with PØD-only fake data and we can sensibly understand the results, we establish that a credible PØD-only real data fit result is possible.

### 5.2.1 High Energy $\nu_\mu$ in FHC Flux Variation

This fake data set arbitrarily increases the  $\nu_\mu$  in FHC flux between 7 and 30 GeV by +25%. This variation was chosen since this energy range corresponds precisely to flux parameter  $b_{10}$  and it could affect all analysis bins. The input fake data in true neutrino energy is shown in Figure 5.9 on page 142.

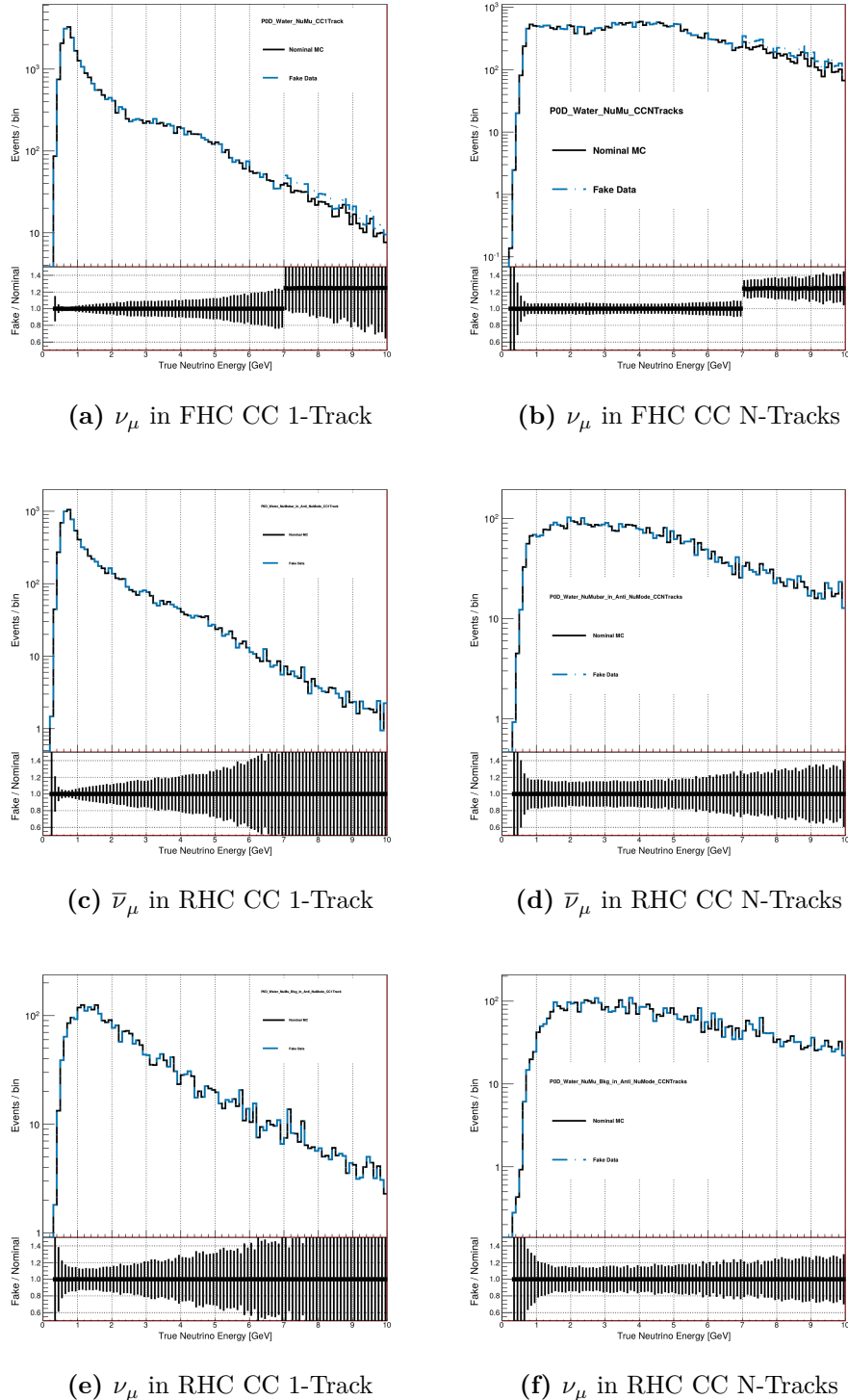


**Figure 5.9:** Neutrino flux before and after applying the +25% increase to  $\nu_\mu$  in FHC flux in the High Energy Neutrino Flux Variation data set. In the figures, “Nominal MC” refers to the Asimov prediction and “Fake Data” is the altered data set. A ratio of the fake data to nominal MC is shown below each histogram to show the variation was applied correctly. The flux of neutrinos, both  $\nu_\mu$  and  $\bar{\nu}_\mu$ , in RHC are not affected.

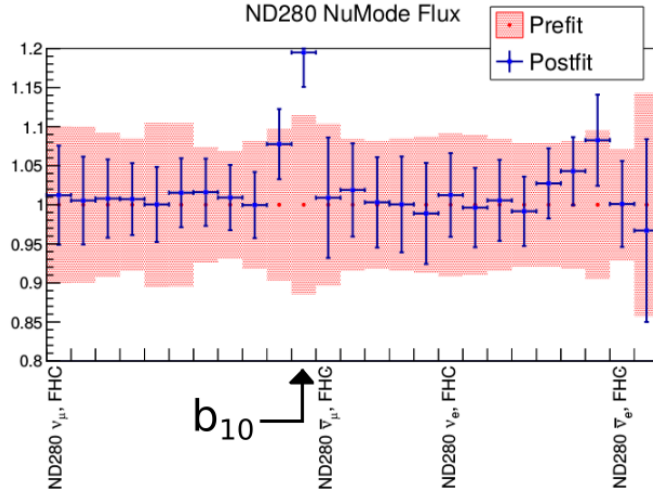
---

The postfit parameter plots are shown in Figure 5.10 on page 144. We see that the target flux parameter  $b_{10}$  has significantly increased from its prefit value by almost +20%. However, due to correlations in the flux covariance matrix, other flux parameters have changed. The BANFF fit prefers to increase the previous energy flux parameter and the high energy  $\nu_e$  flux parameters as well. While we saw that the flux and hence event rate was not changed in the RHC samples, the RHC flux parameters are also slightly affected. However, the RHC flux parameters are still well within prefit uncertainties. The statement is true for the cross section and FSI parameters. Therefore we can conclude that the fit prefers to resolve nonphysical changes large, singular changes with many correlated parameter variations.

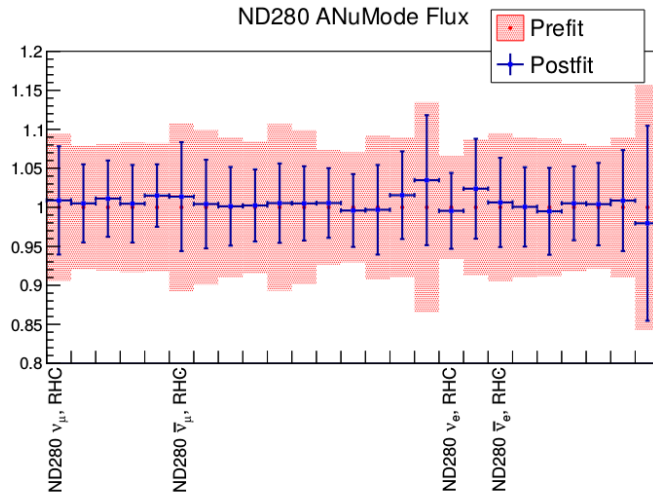
### 5.2.2 Single Pion Event Rate Variation

This fake data set arbitrarily increases the number of resonant single pion events by +25%. This was implemented by taking all true NEUT CC- $1\pi$  events, extracting the event weight, and increasing it by +25%. This is what is observed in the lepton candidate momentum distributions as shown in Figure 5.11 on page 145. According to the CC- $1\pi$  model, the event rate can be singly absorbed in  $C_A^5$ . However as seen in Appendix B, increases in any CC- $1\pi$  parameter will increase the event rate. Additionally,  $C_A^5$  and  $M_A^{\text{Res}}$  are anticorrelated with one another meaning that these parameters will be forced to shift in opposite directions together. Given the postfit results from the previous fake data fit, we should expect to see more than just the CC- $1\pi$  parameters to vary.

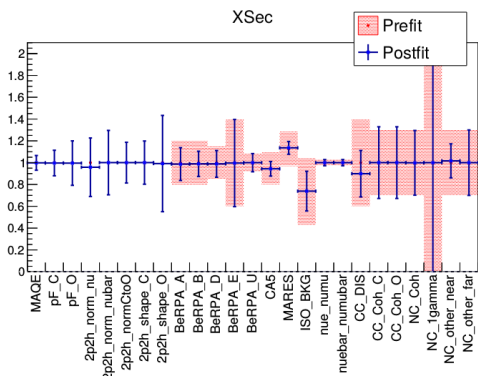
The postfit results for this fake data set are shown in Figure 5.12 on page 147. We observe that the CC- $1\pi$  parameter  $C_A^5$  increased by ~10%, but this is not enough to account for the input fake data shift. We also notice that due to anticorrelations,  $M_A^{\text{Res}}$  was decreased by about several percent. What the fit prefers is to increase the isospin= $1/2$  background, 2p2h normalization, and all the flux parameters. Like the first fake data set, we see that in the presence of nonphysical variations to the Physics, the fit prefers to spread out variations



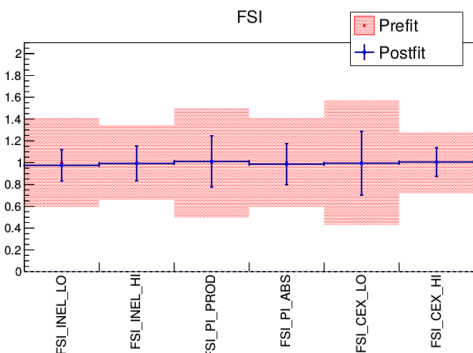
(a) ND280 FHC Flux



(b) ND280 RHC Flux



(c) Cross section parameters



(d) FSI parameters

**Figure 5.10:** Postfit parameters for the high energy  $\nu_\mu$  in FHC flux variation fake data fit. All the flux parameters in FHC are shown together and ordered sequentially from left to right. The same is true the RHC flux.

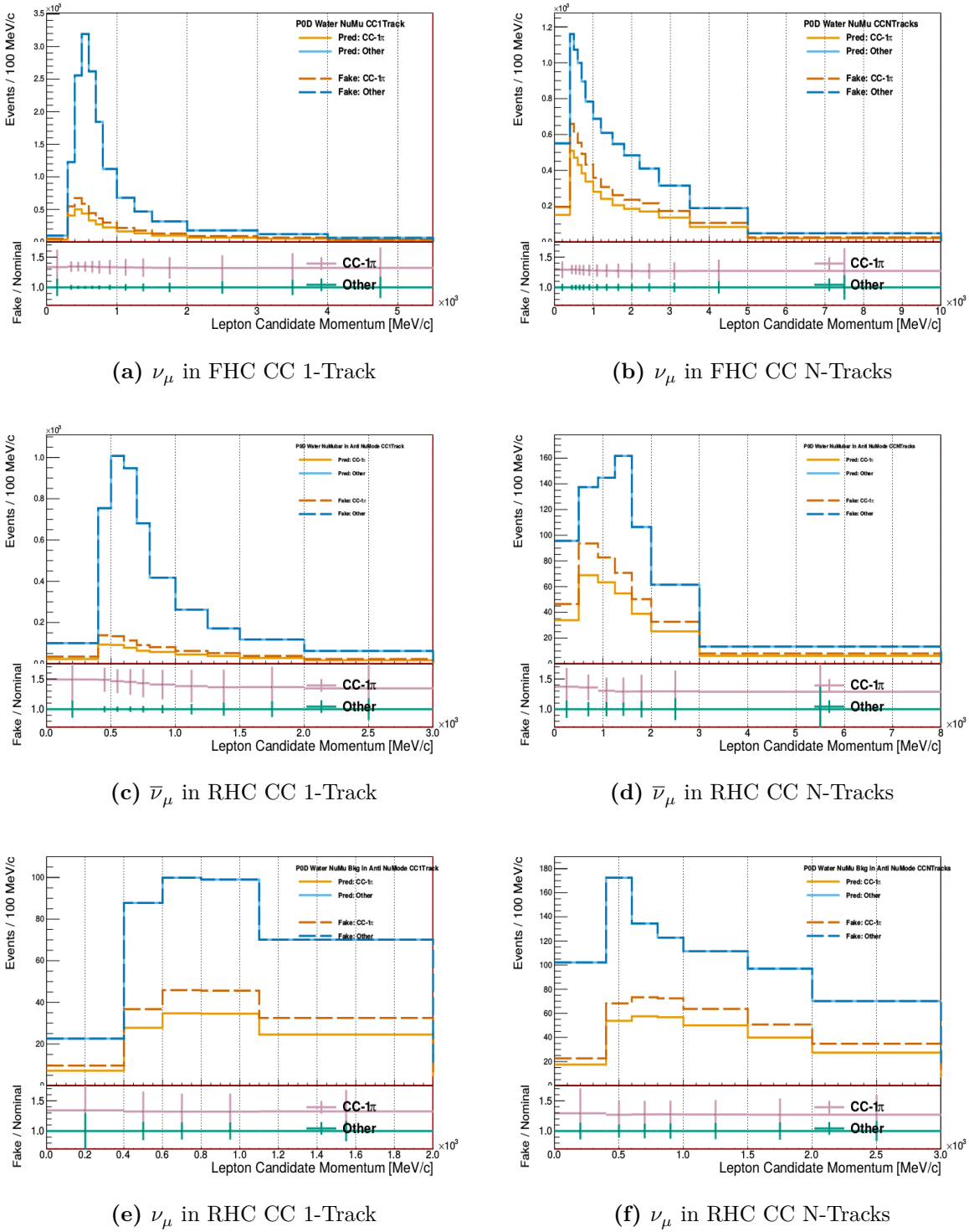


**Figure 5.11:** Lepton candidate momentum for the Single Pion Event Rate Variation fake data set. The nominal MC and fake data predictions are shown as solid and dashed lines, respectively. True CC-1 $\pi$  events are differentiated from all other interactions to illustrate the event scaling applied. A ratio plot of CC-1 $\pi$  events to all other interaction events shown beneath each main histogram.

---

among the other parameters. However, this time the variations are shared among flux and cross section parameters.

### 5.3 Validation Summary

We have validated the BANFF fit indeed works and tested its robustness in a variety of scenarios. We learned from the Asimov data set, which is the T2K nominal MC corrected to data POT with fine tuning corrections, in particular how the flux and cross section parameters affect the samples. In the fake data sets, we saw the effect of the penalty terms and how their correlations influence the fit. While more rigorous tests could establish where biases exist, these limitations are beyond the scope of this thesis. What has been established is that sensible fit results using the PØD selections are possible. We can now examine the PØD-only data and be assured the BANFF can fit can converge with PØD-only data.

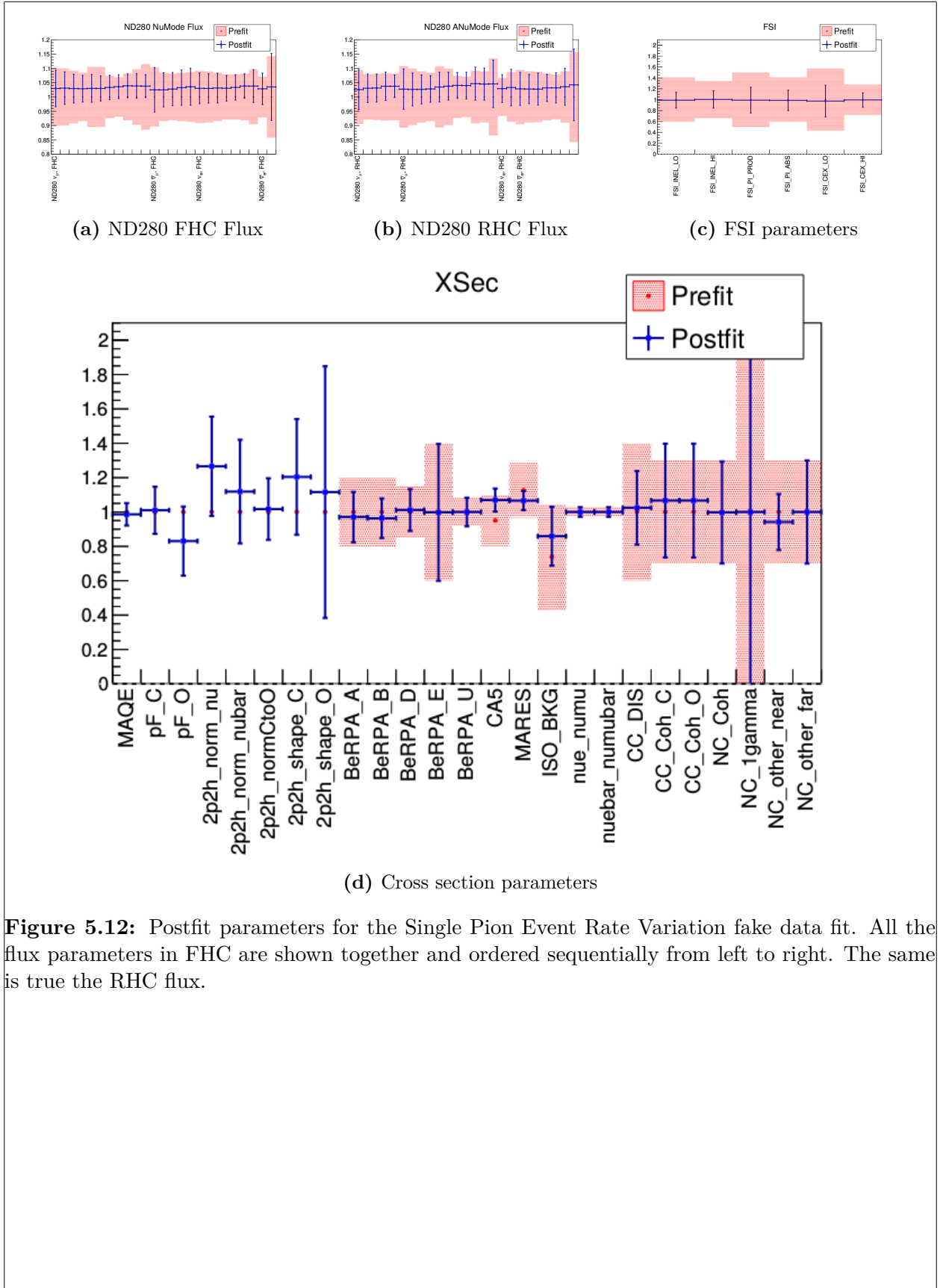


**Figure 5.12:** Postfit parameters for the Single Pion Event Rate Variation fake data fit. All the flux parameters in FHC are shown together and ordered sequentially from left to right. The same is true the RHC flux.

---

---

# Chapter 6

## Fitter Results

Fitter results

### 6.1 Prefit Sample Distributions

Prefit distributions

### 6.2 Postfit Results

#### 6.2.1 Parameter Value Comparisons

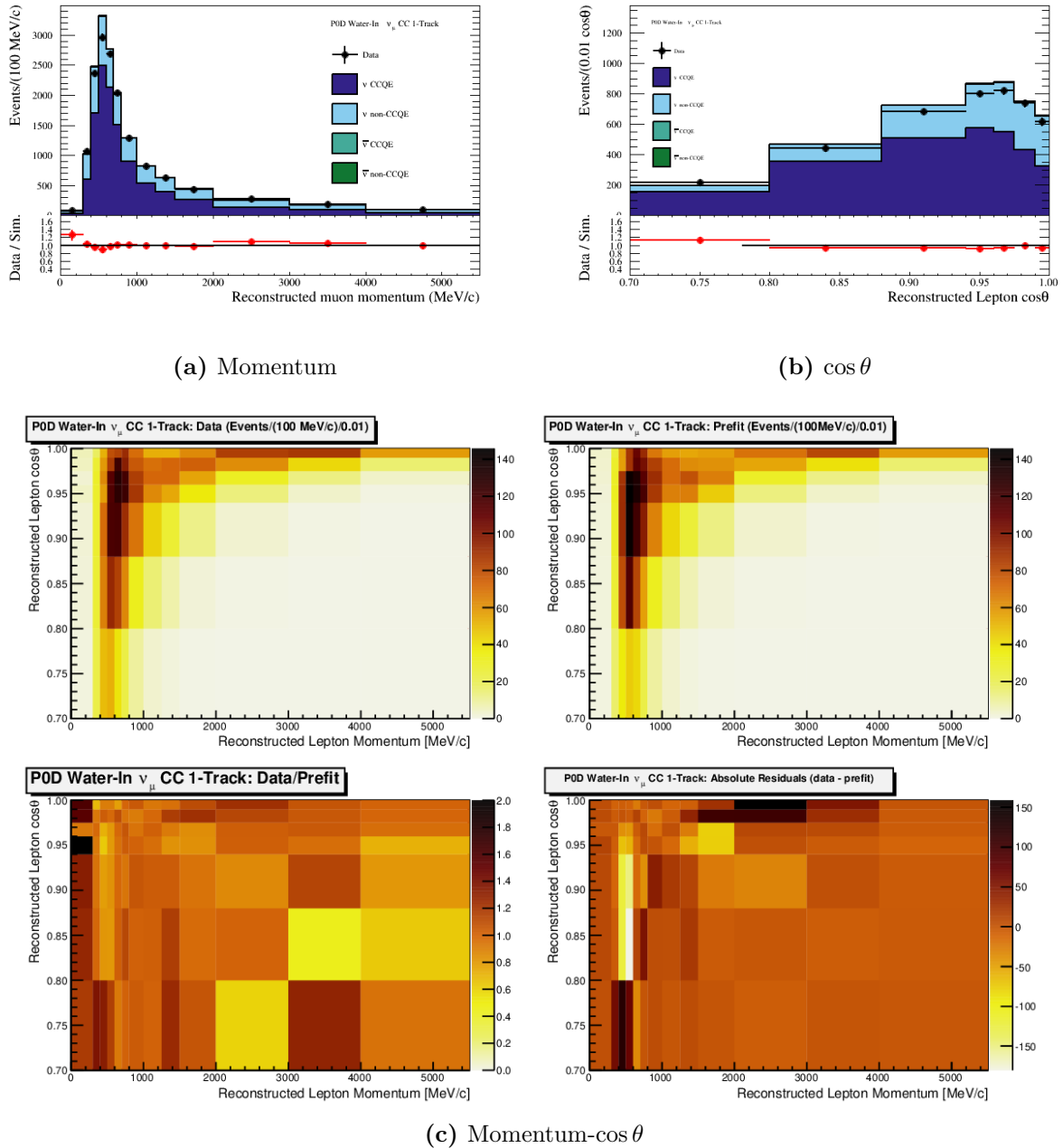
Parameter value comparisons

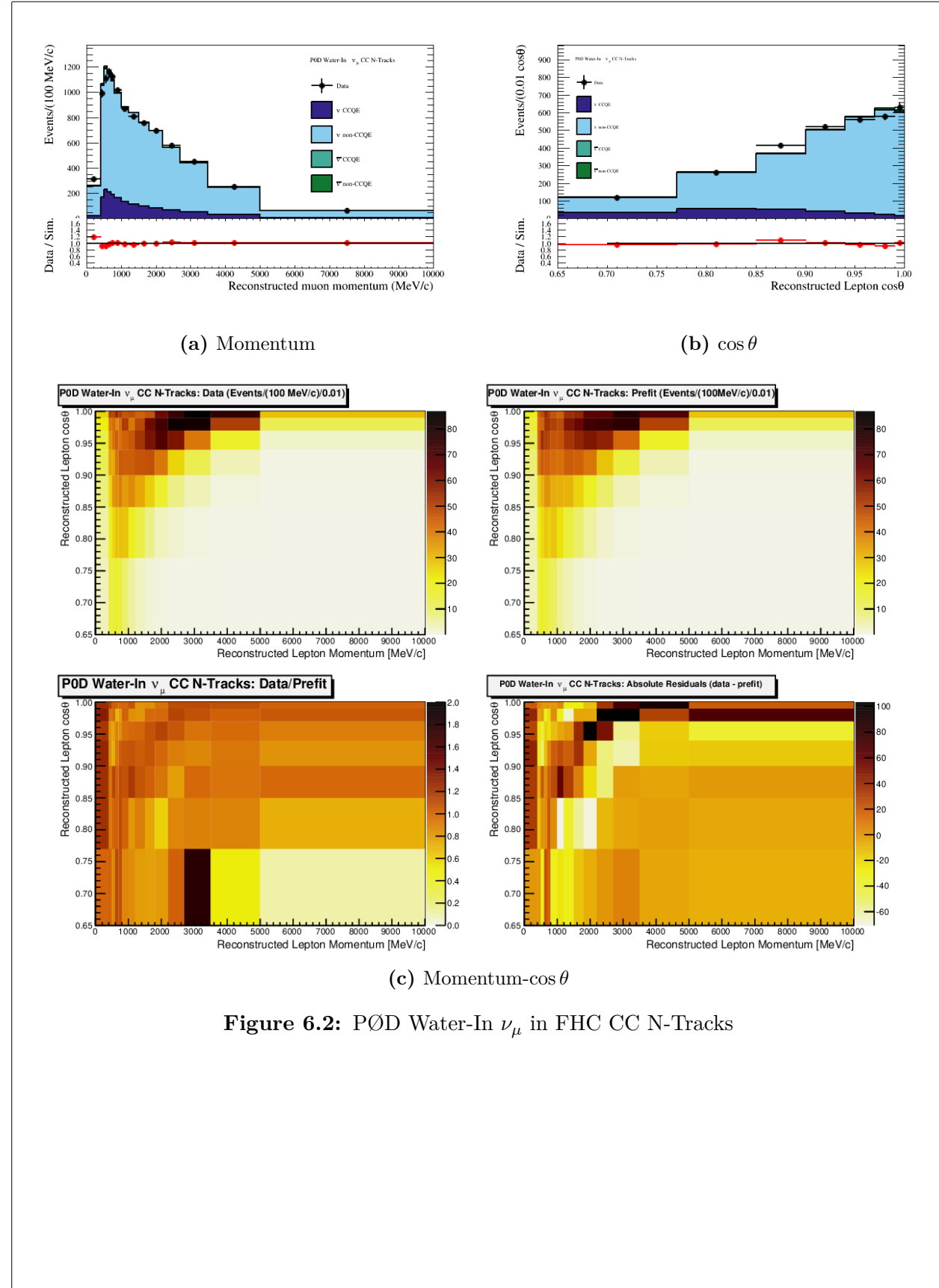
#### 6.2.2 Postfit Sample Distributions

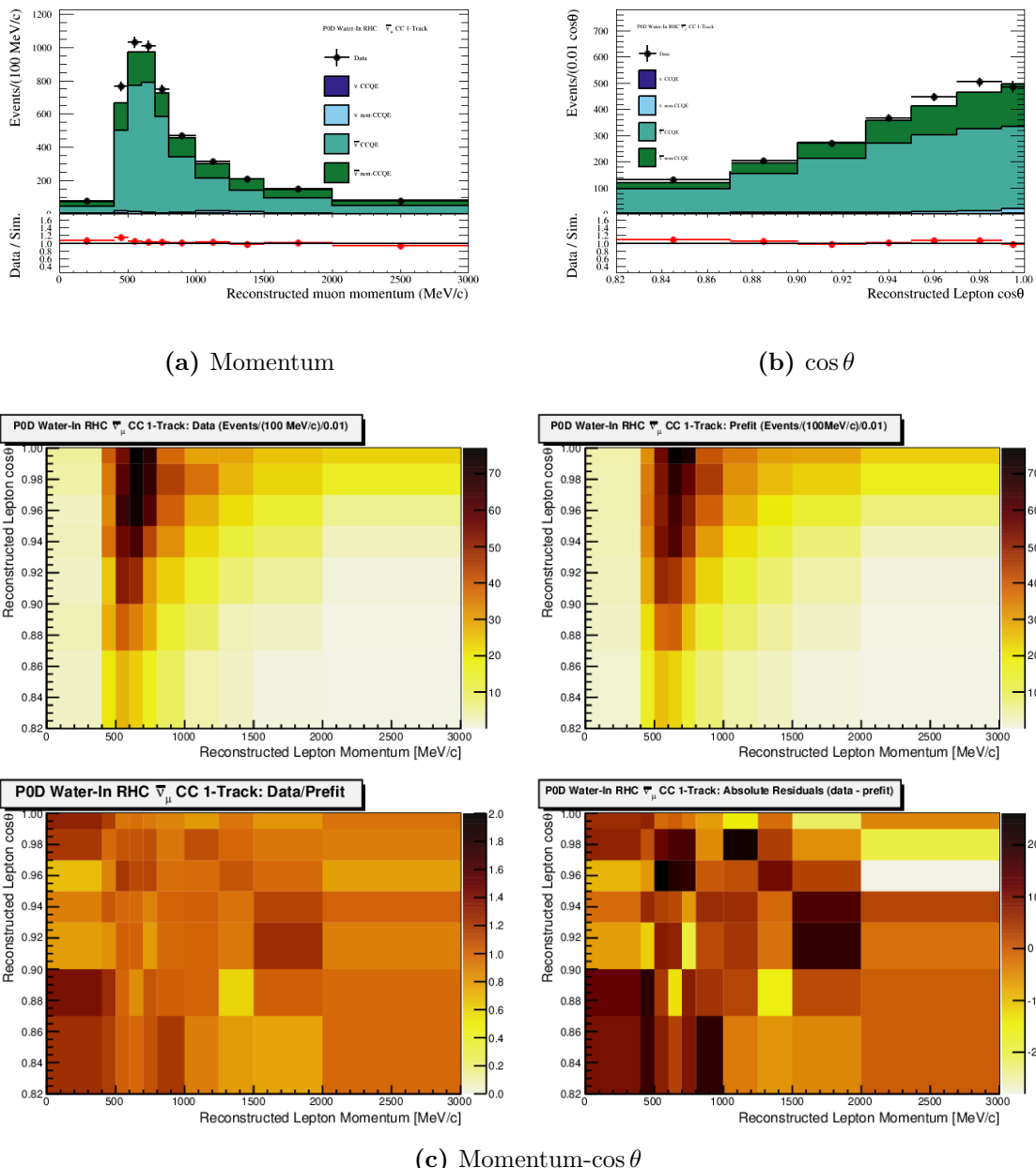
Postfit distributions

#### 6.2.3 P-Value Between PØD and FGD Fits

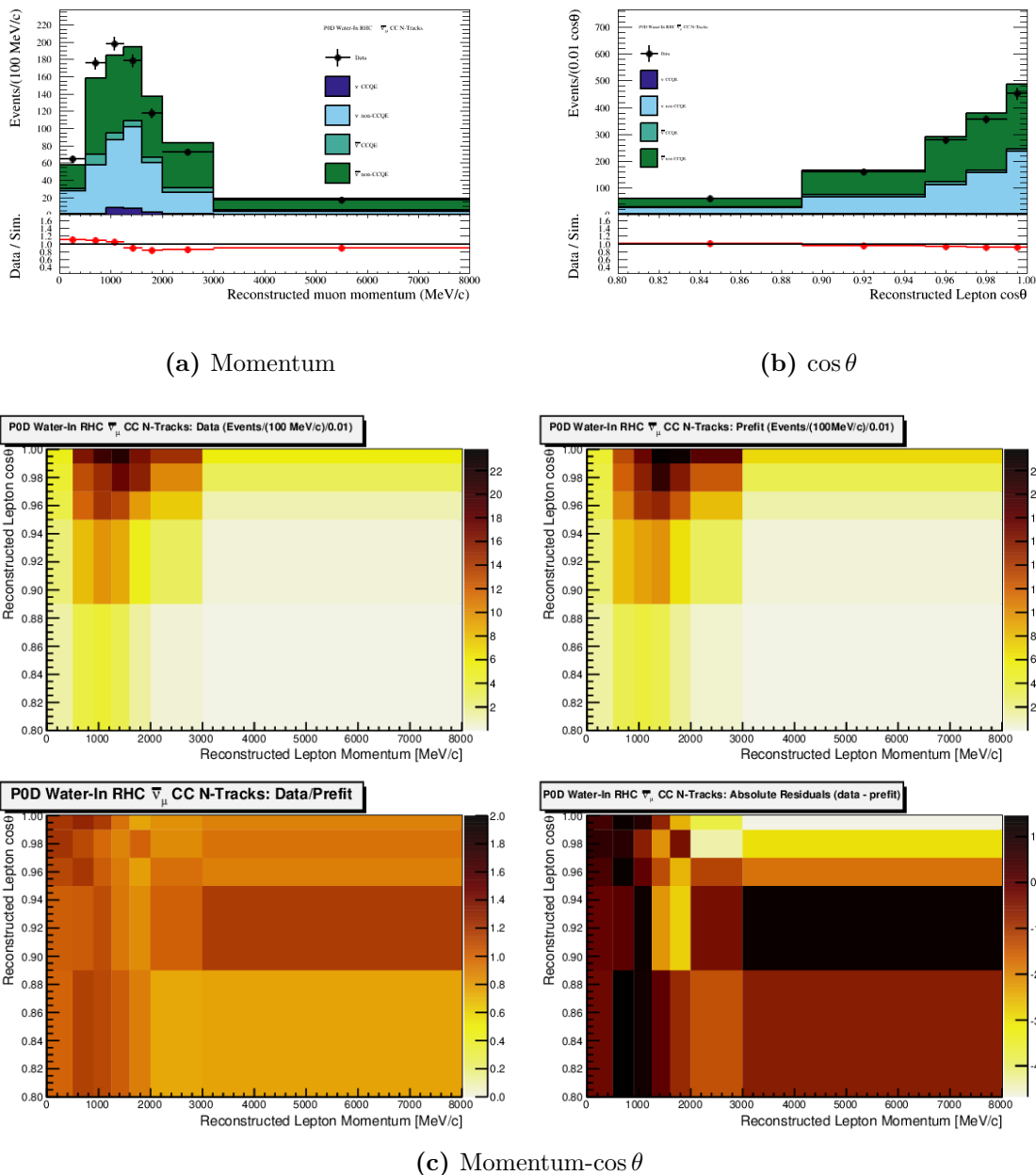
We can now provide a quantification of the agreement between the PØD-only BANFF fit and that of the FGD-only BANFF fit. As a starting assumption, let the FGD-only result



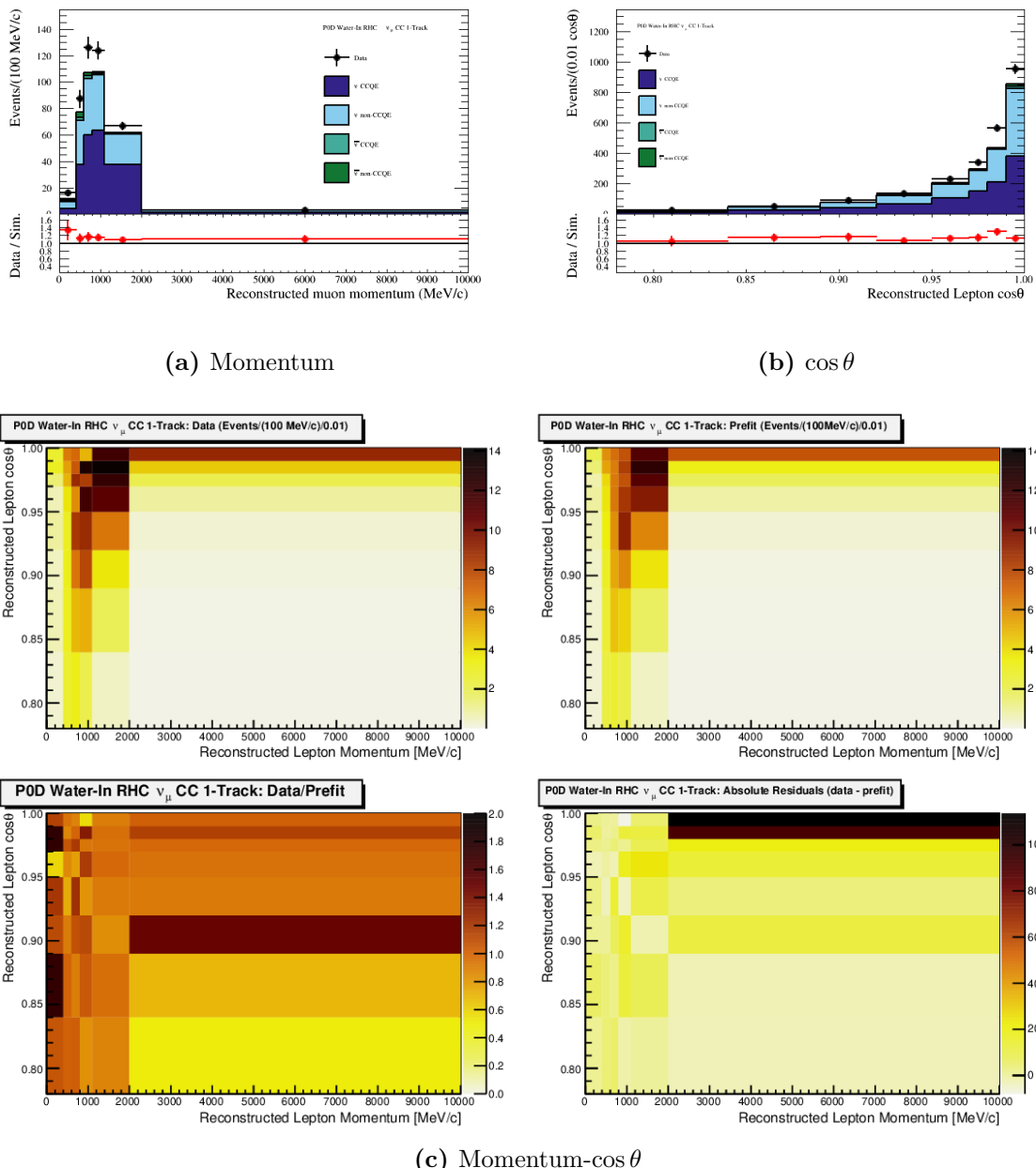




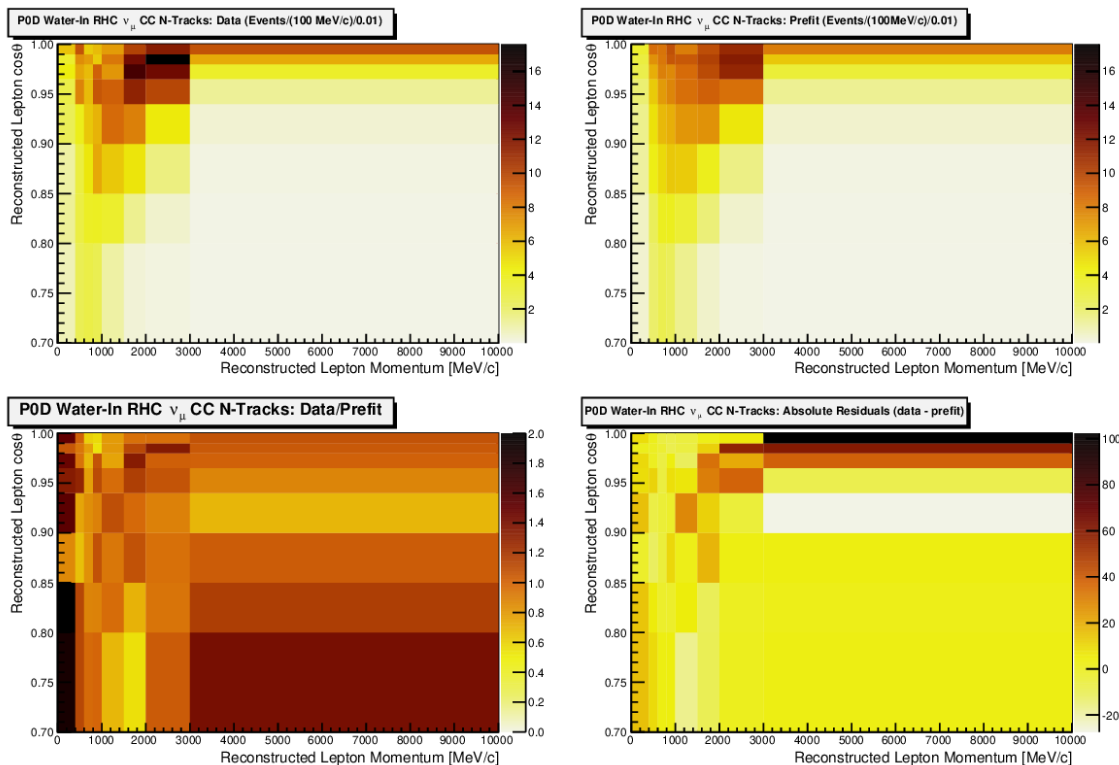
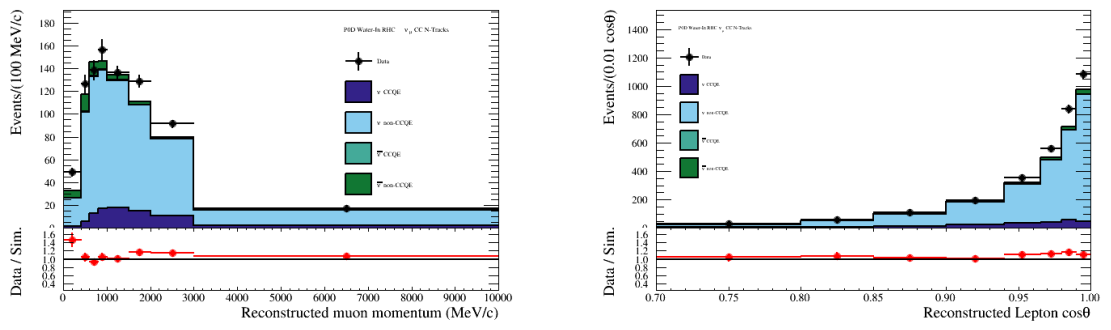
**Figure 6.3:** PØD Water-In  $\bar{\nu}_\mu$  in RHC CC 1-Track



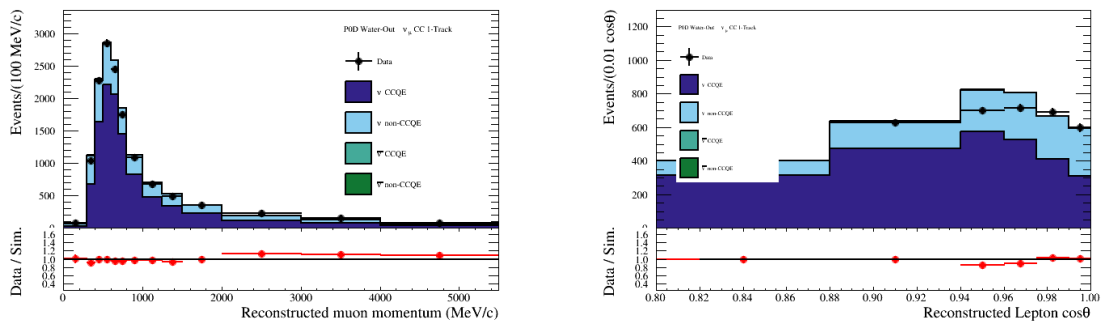
**Figure 6.4:** PØD Water-In  $\bar{\nu}_\mu$  in RHC CC N-Tracks



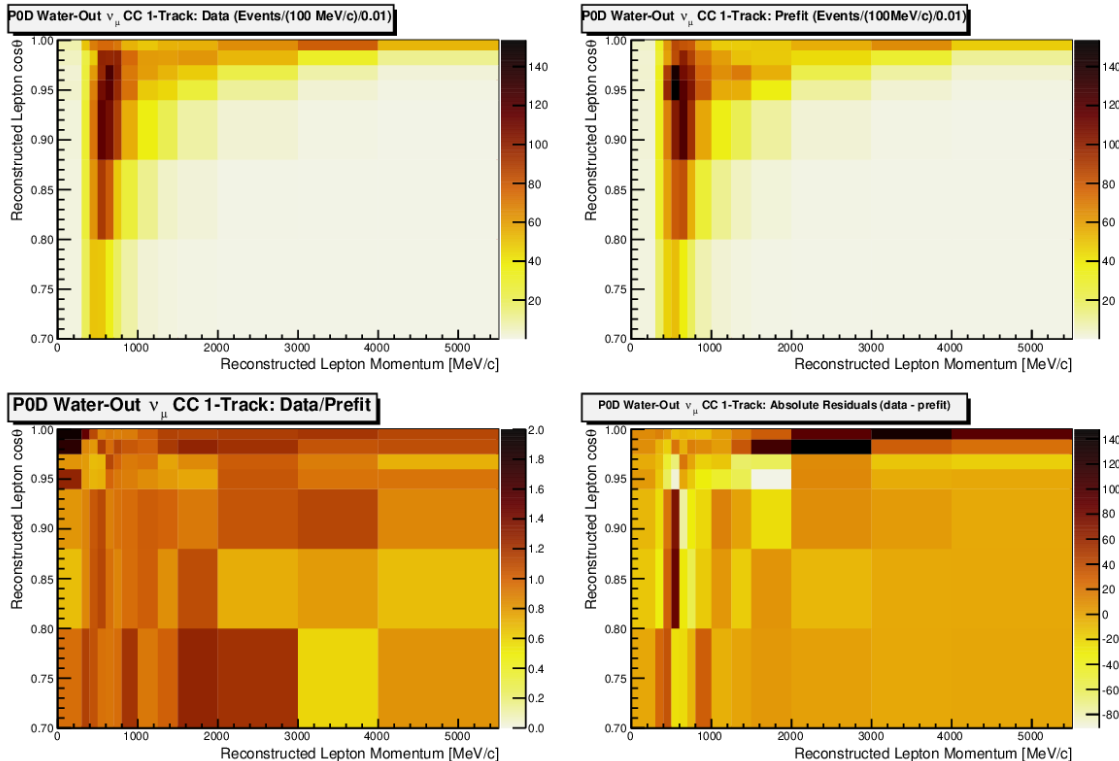
**Figure 6.5:** PØD Water-In  $\nu_\mu$  in RHC CC 1-Track

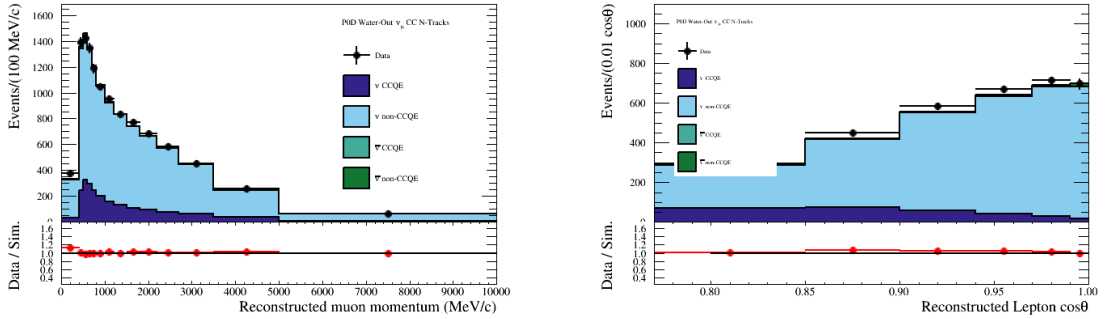


**Figure 6.6:** PØD Water-In  $\nu_\mu$  in RHC CC N-Tracks

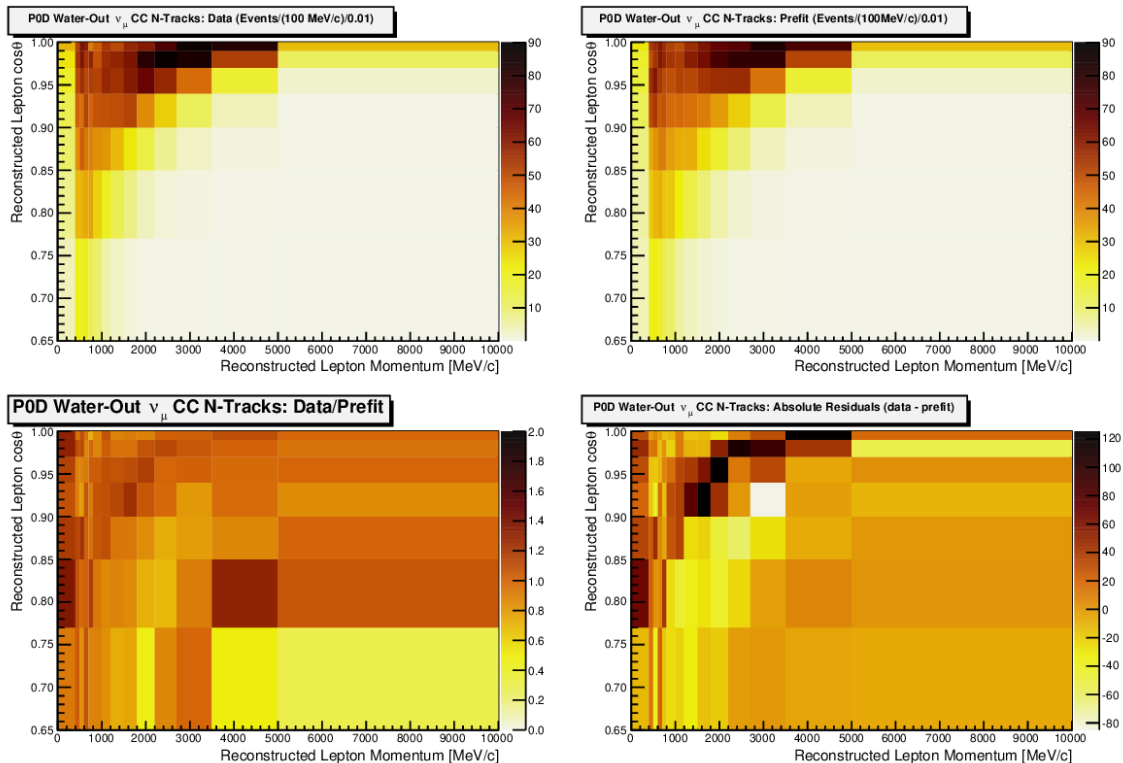


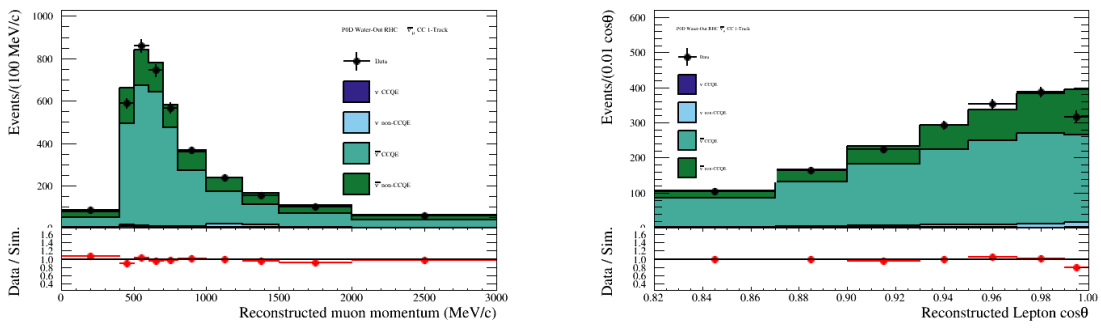
(a) Momentum

(b)  $\cos \theta$ (c) Momentum- $\cos \theta$ **Figure 6.7:** PØD Water-Out  $\nu_\mu$  in FHC CC 1-Track

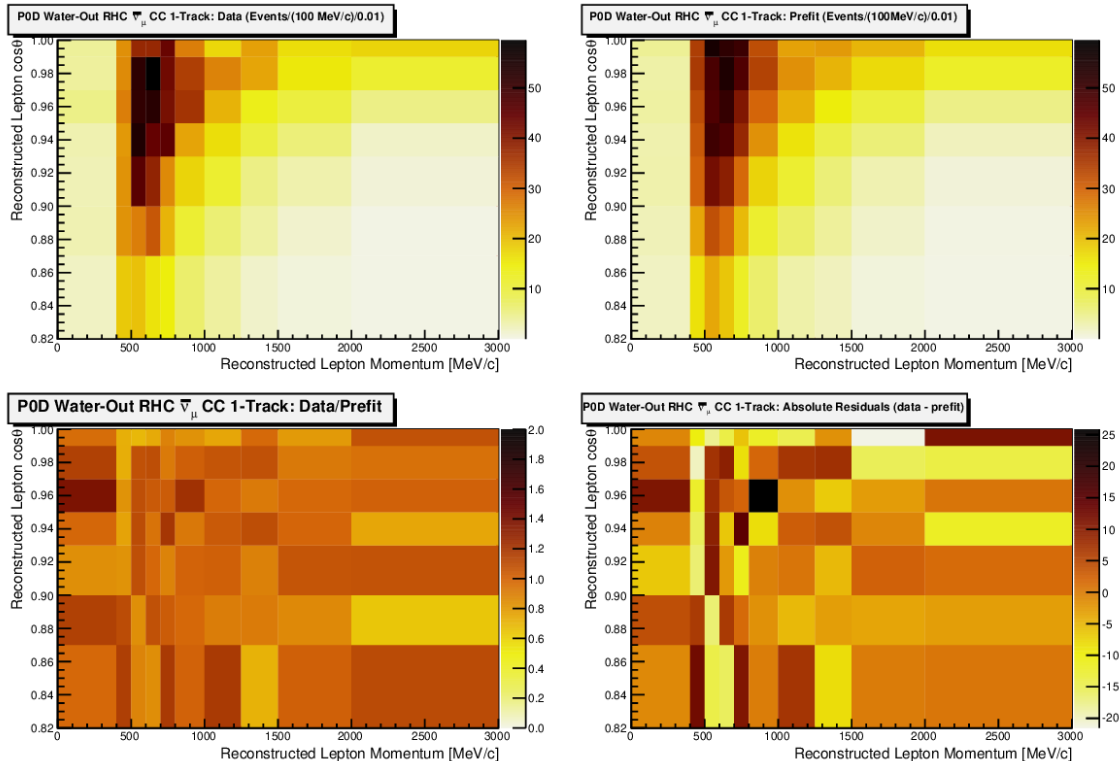


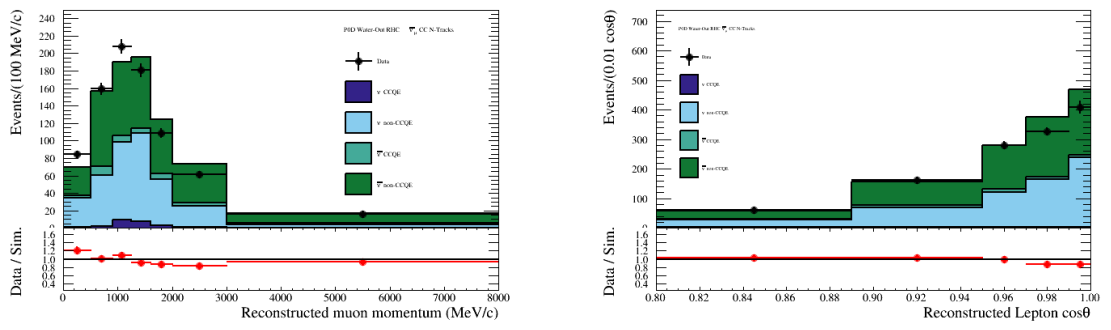
(a) Momentum

(b)  $\cos \theta$ (c) Momentum- $\cos \theta$ **Figure 6.8:** PØD Water-Out  $\nu_{\mu}$  in FHC CC N-Tracks

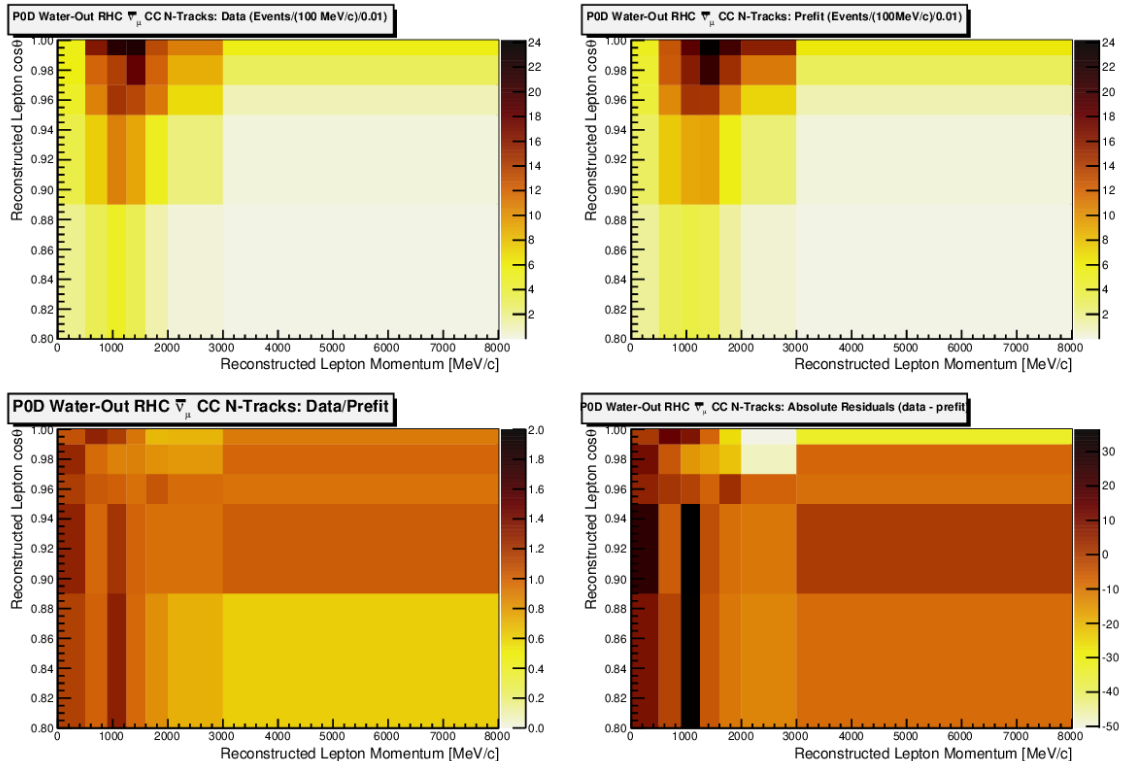


(a) Momentum

(b)  $\cos\theta$ (c) Momentum- $\cos\theta$ **Figure 6.9:** PØD Water-Out  $\bar{\nu}_\mu$  in RHC CC 1-Track



(a) Momentum

(b)  $\cos \theta$ (c) Momentum- $\cos \theta$ **Figure 6.10:** PØD Water-Out  $\bar{\nu}_\mu$  in RHC CC N-Tracks

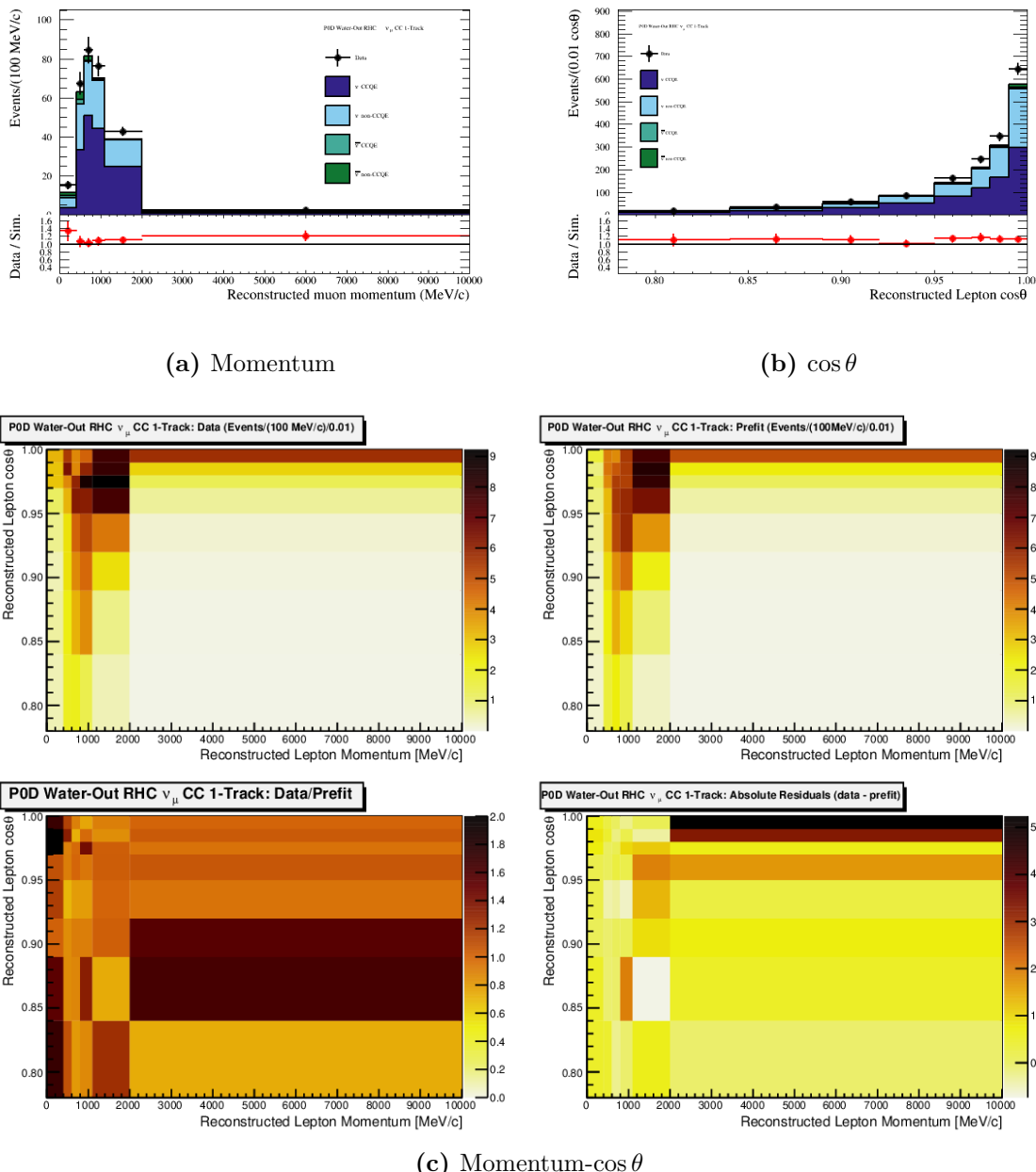


**Figure 6.11:** PØD Water-Out  $\nu_\mu$  in RHC CC 1-Track

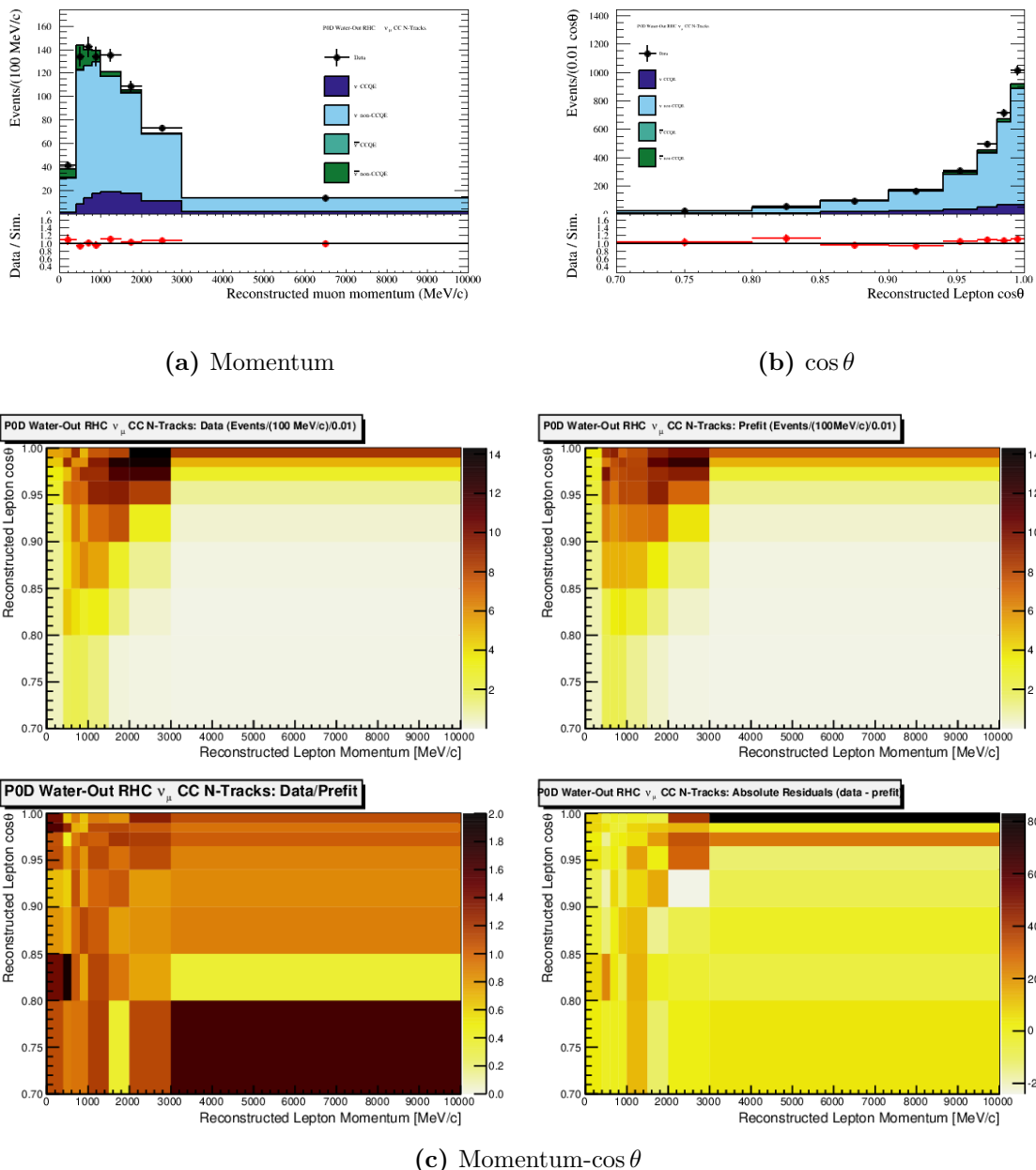


**Figure 6.12:** PØD Water-Out  $\nu_\mu$  in RHC CC N-Tracks

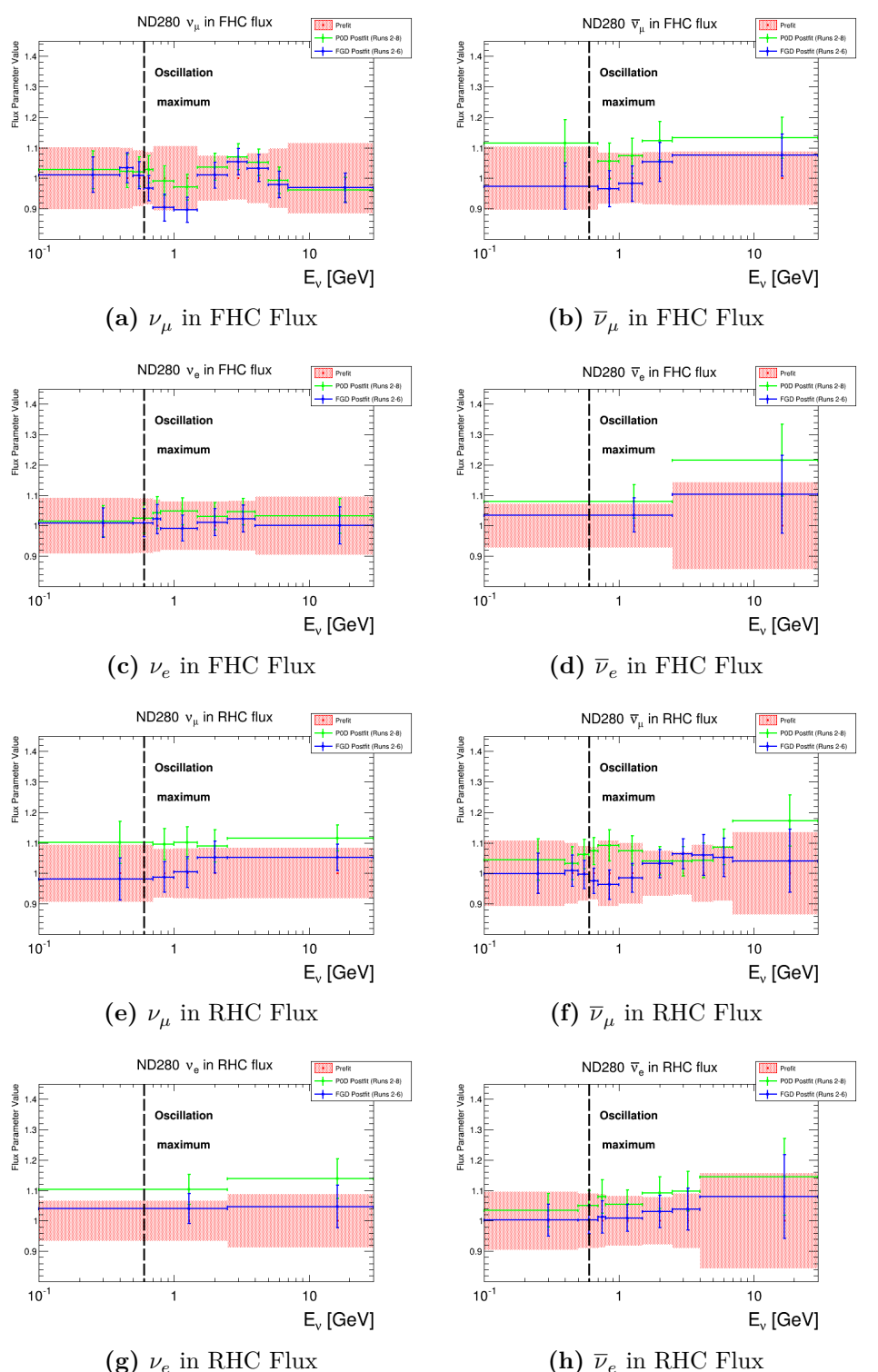


**Figure 6.13:** Prefit and postfit ND280 flux parameters for the PØD-only and FGD-only results

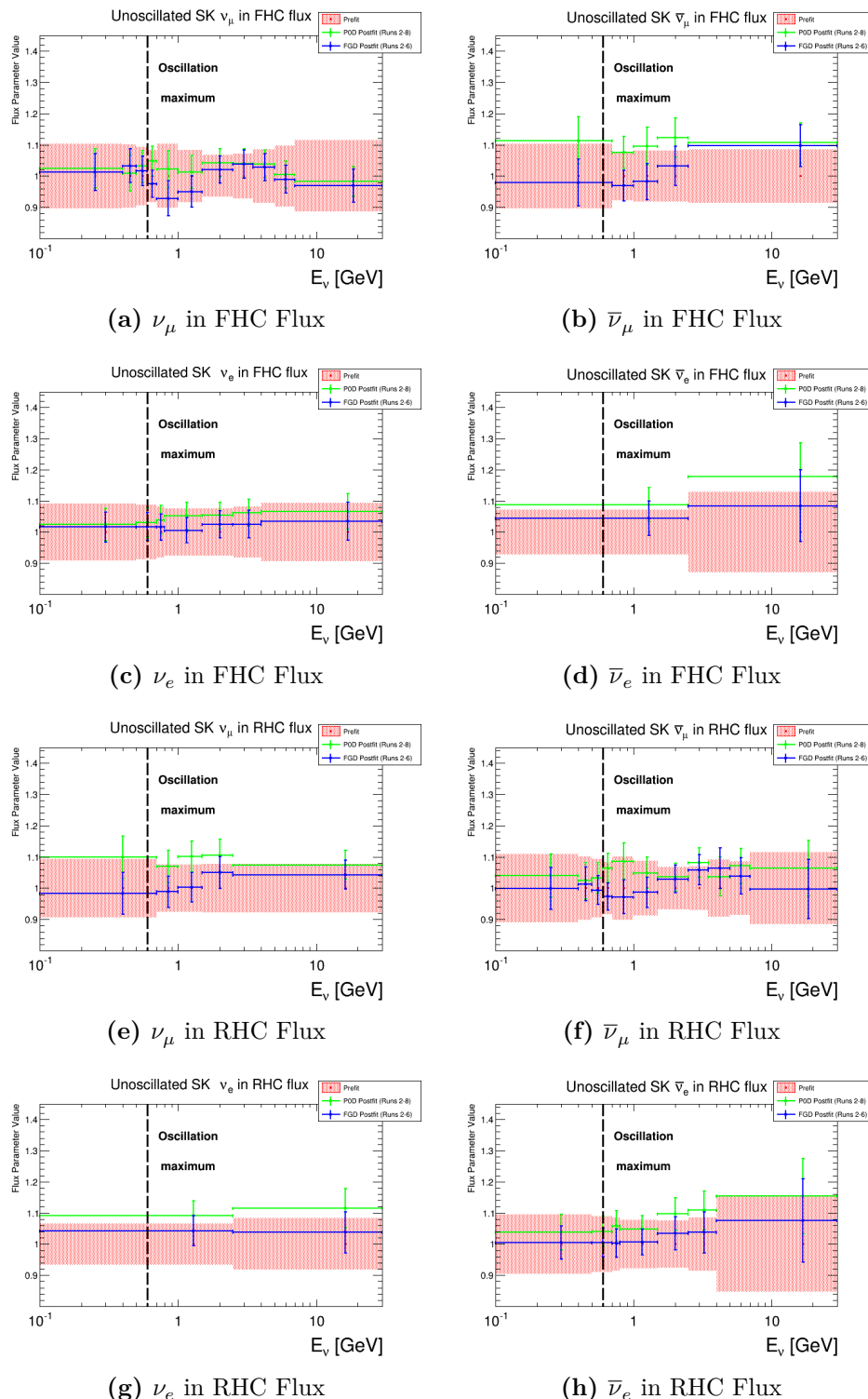


**Figure 6.14:** Prefit and postfit Super-K flux parameters for the PØD-only and FGD-only results

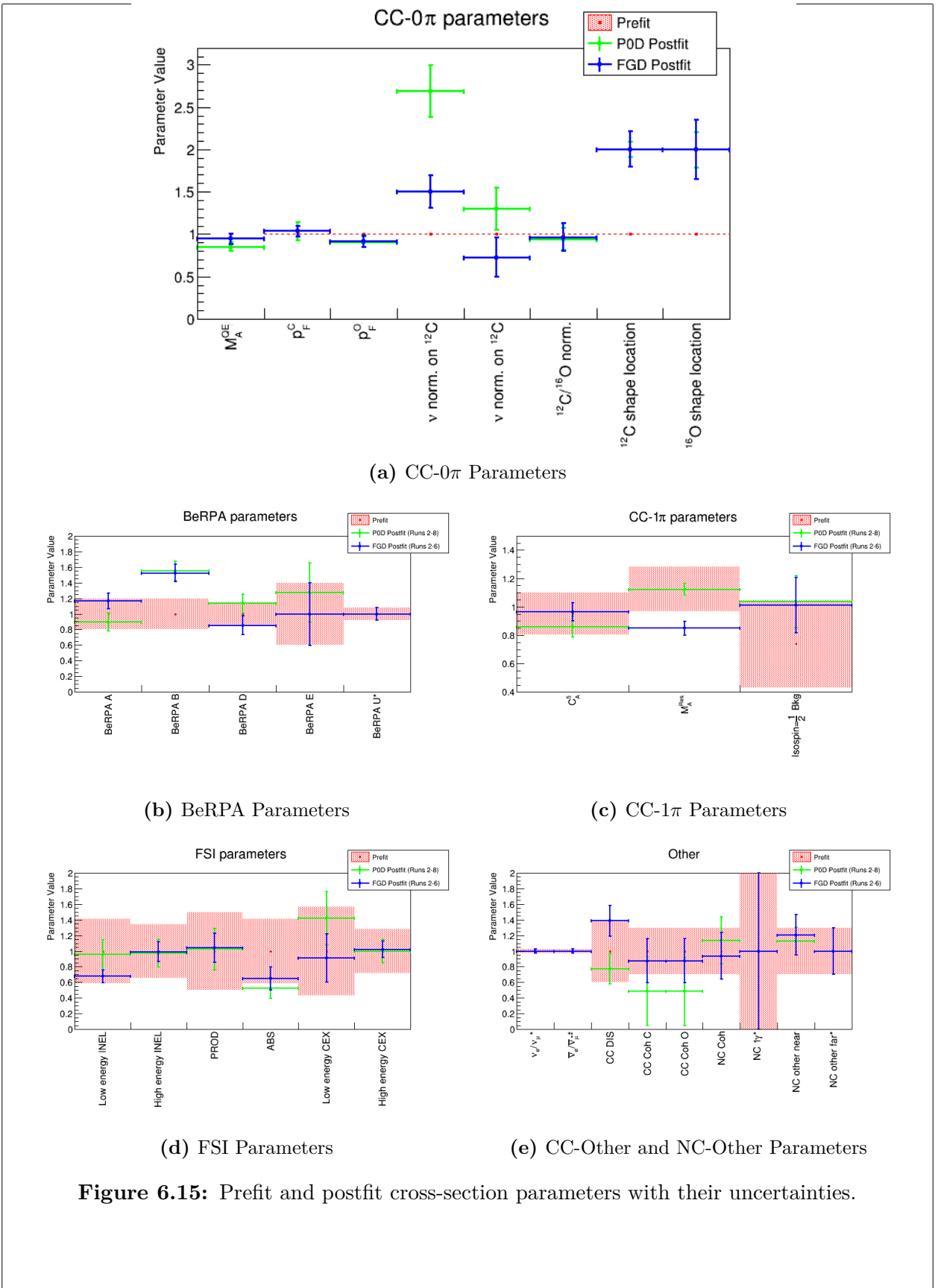
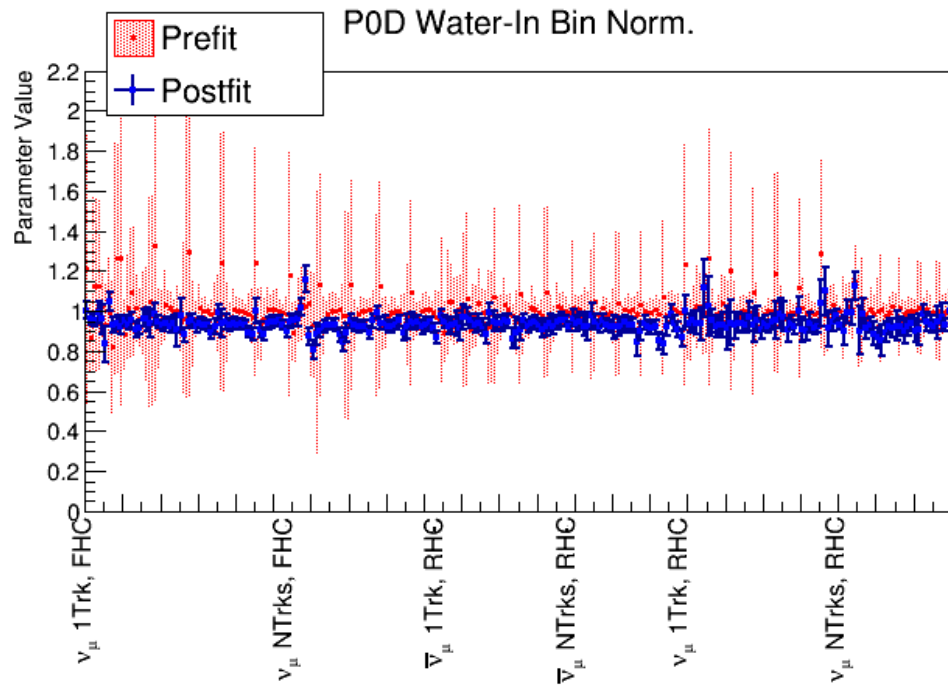
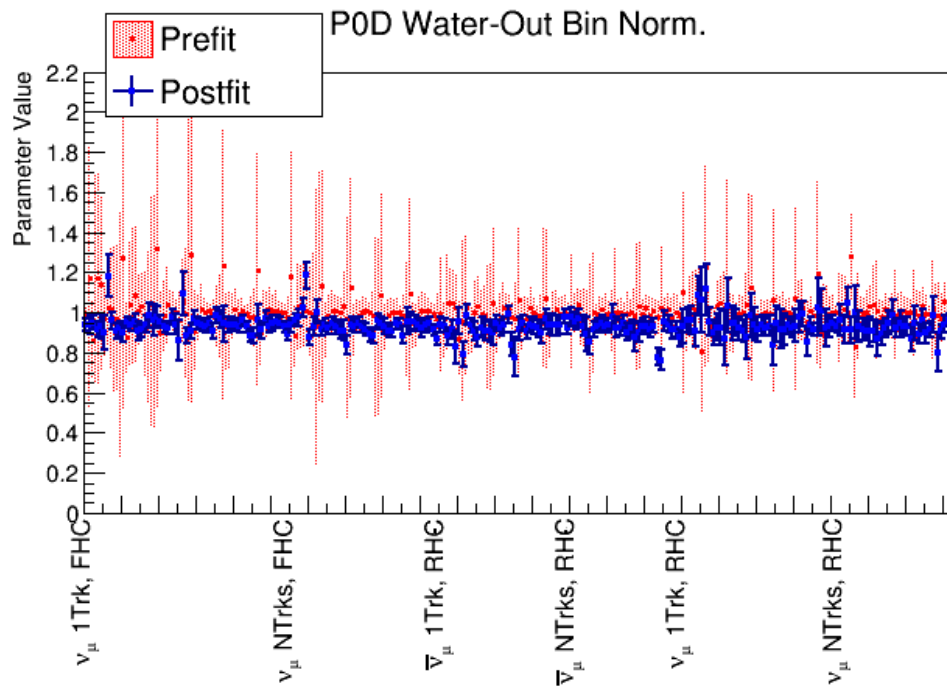


**Figure 6.15:** Prefit and postfit cross-section parameters with their uncertainties.



(a) Water-In Bin Normalizations



(b) Water-Out Bin Normalizations

**Figure 6.16:** Prefit and postfit PØD bin normalization parameters

**Postfit Correlation Matrix**

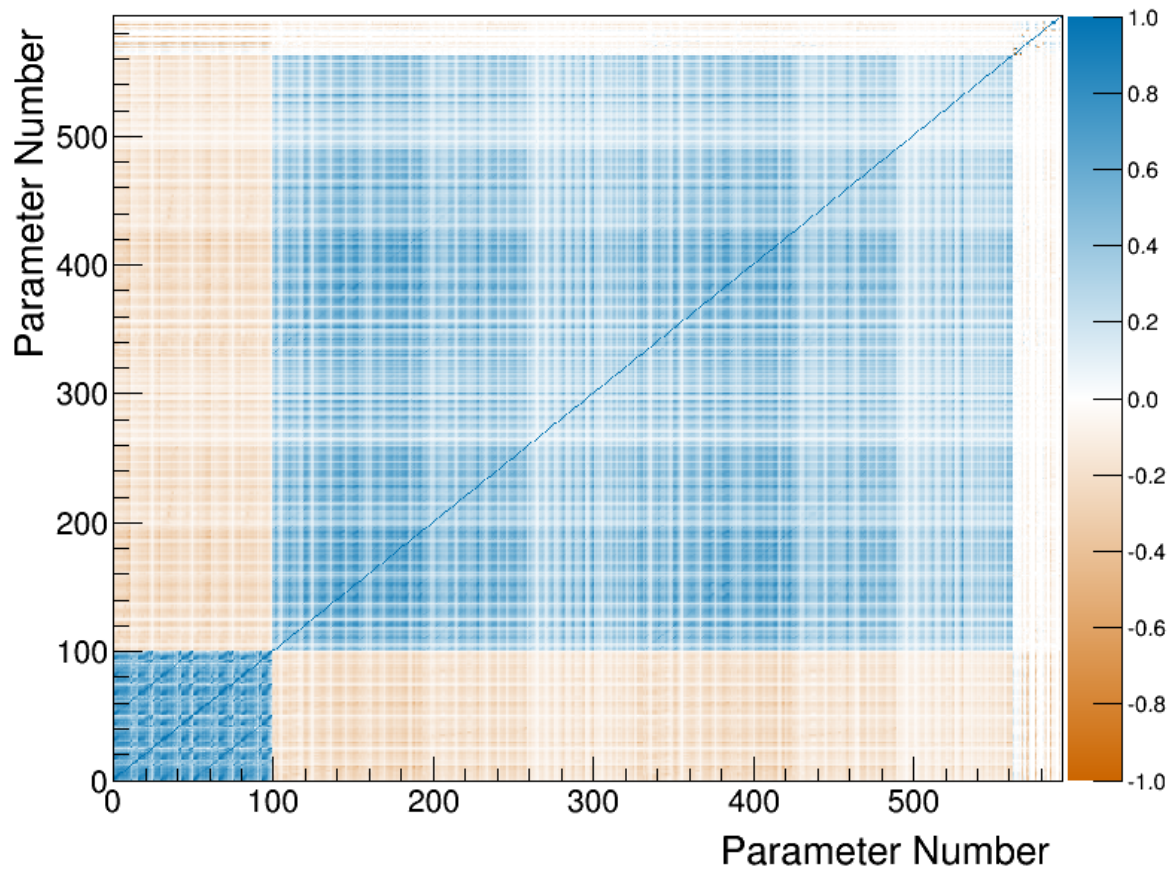
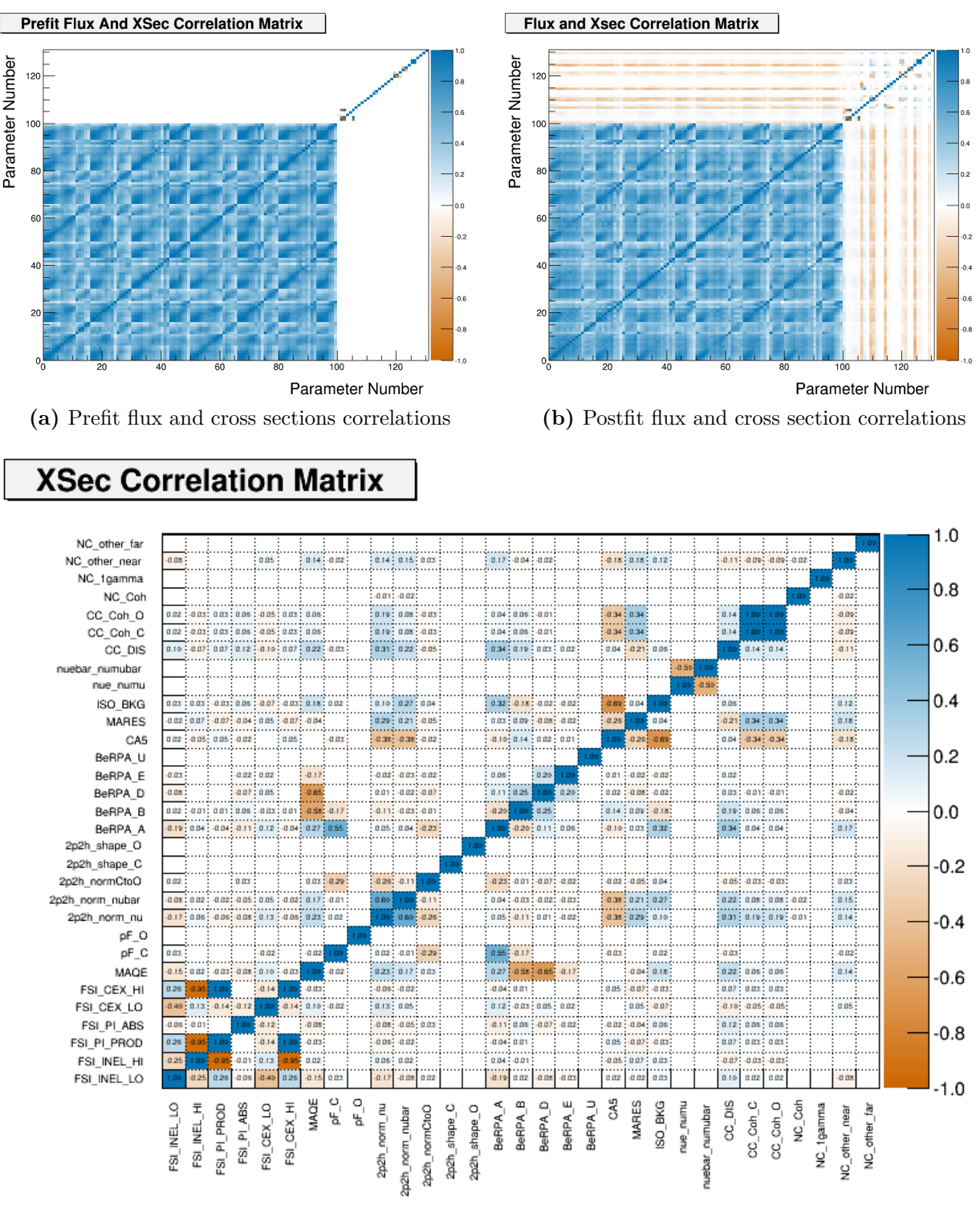
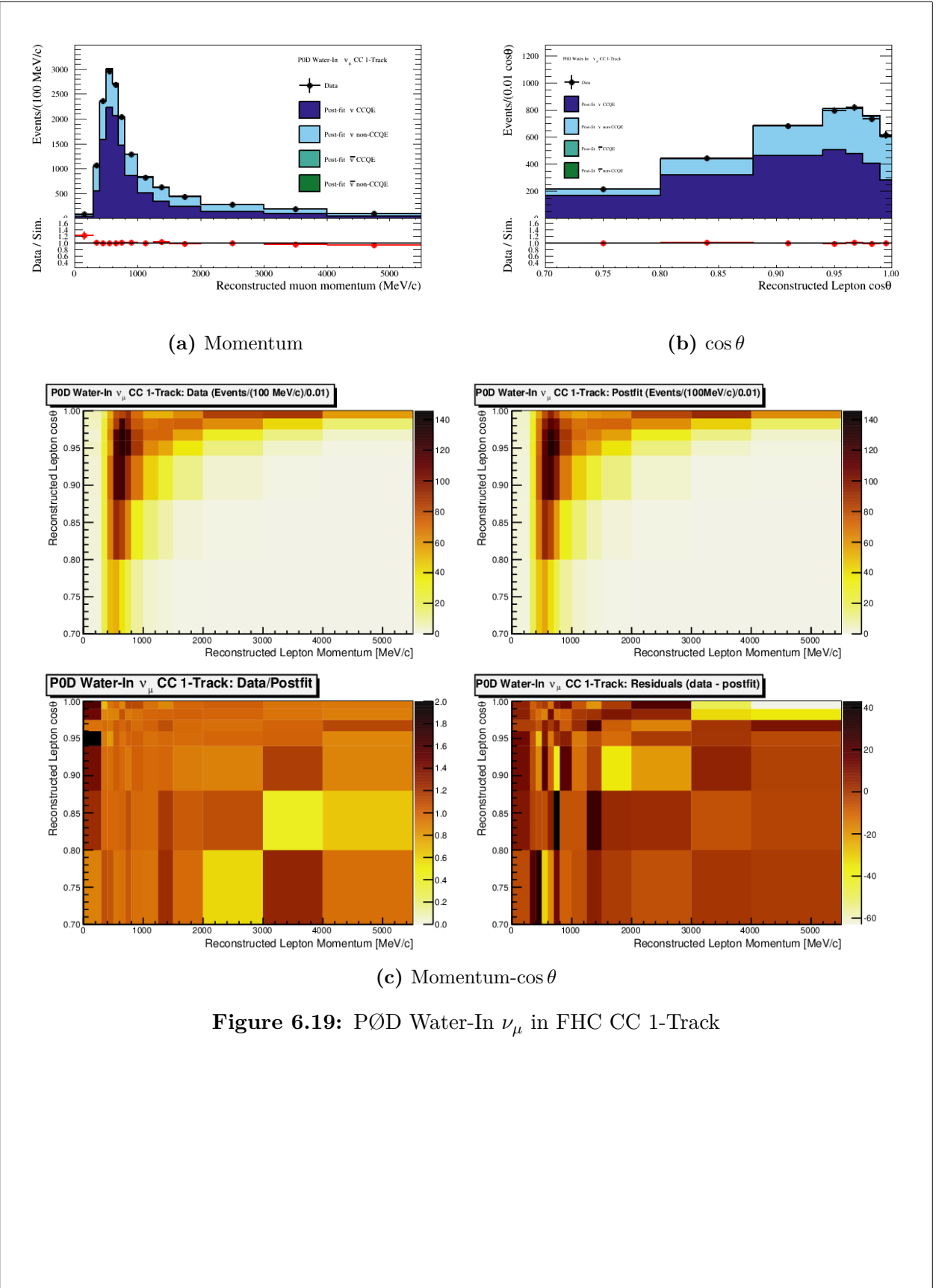
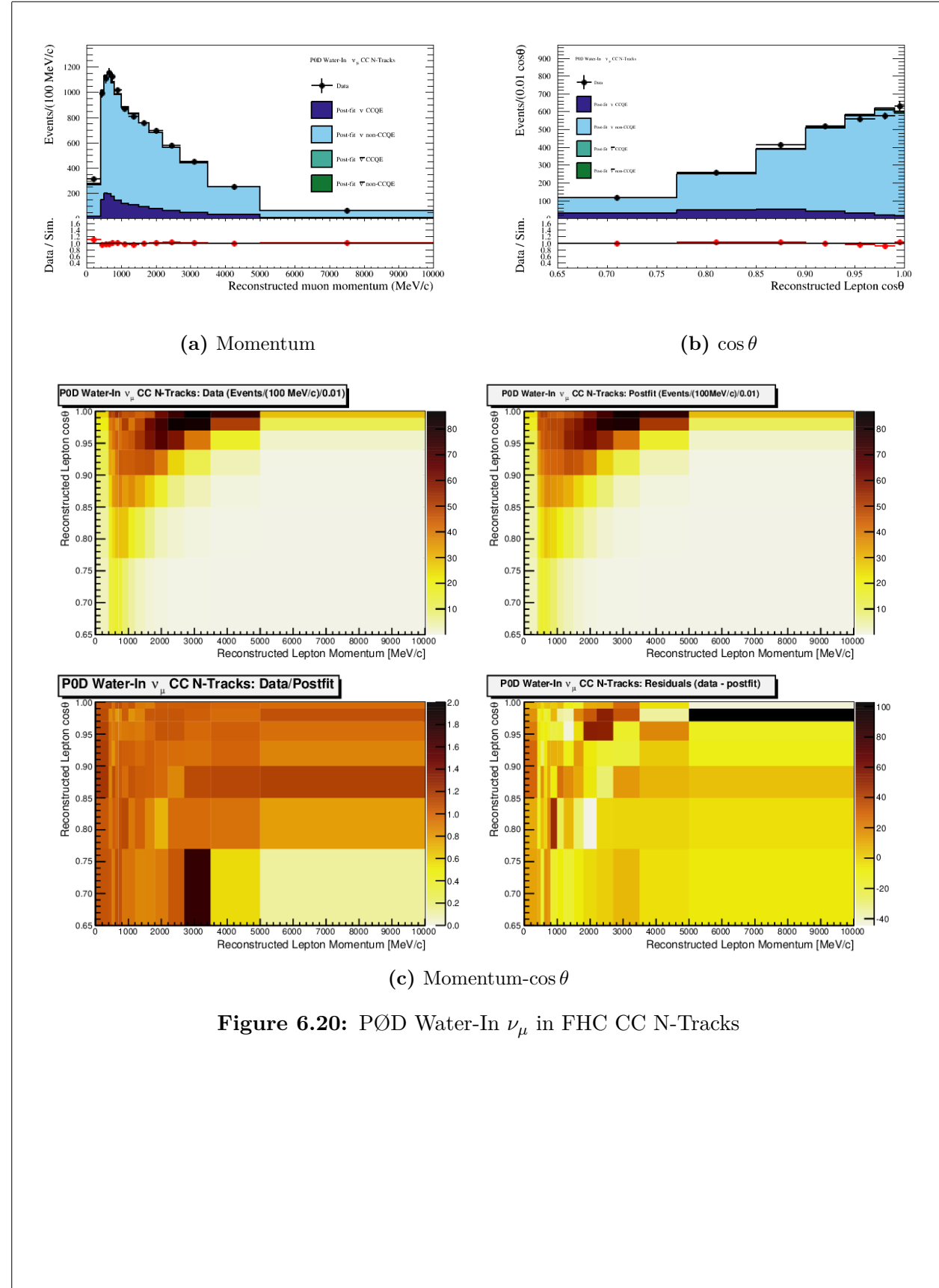


Figure 6.17

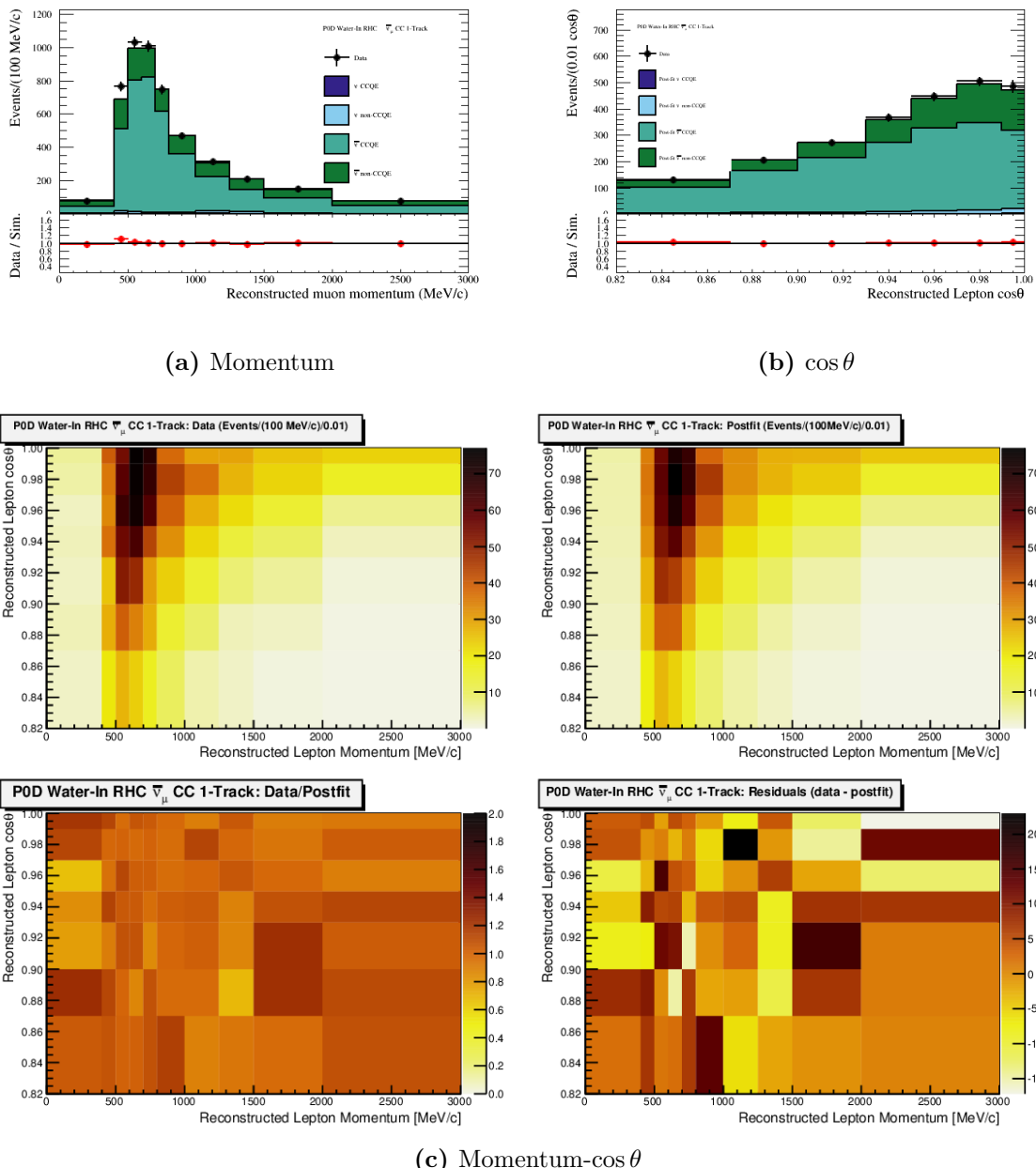


**Figure 6.18:** Prefit and post flux and cross section correlations

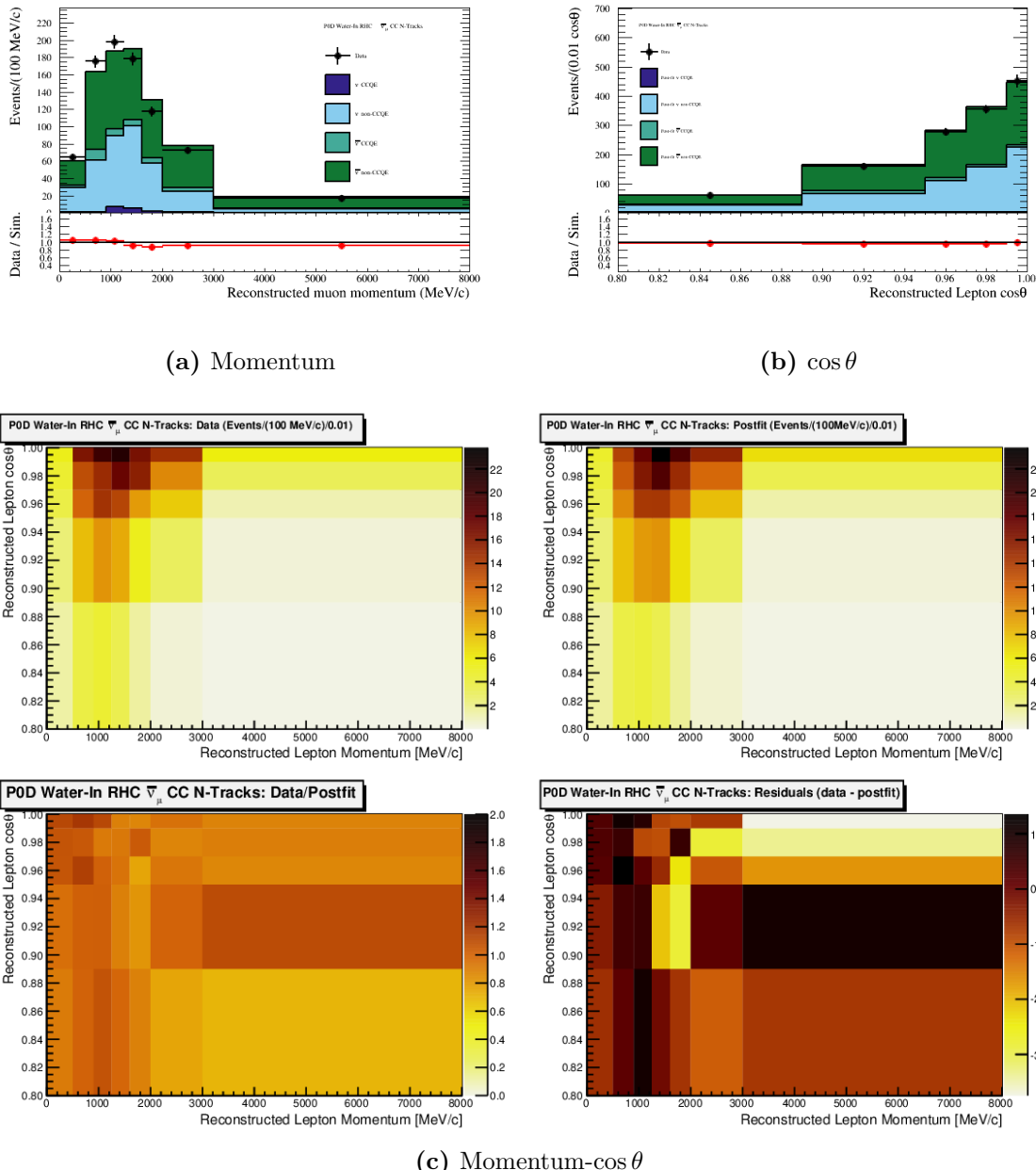




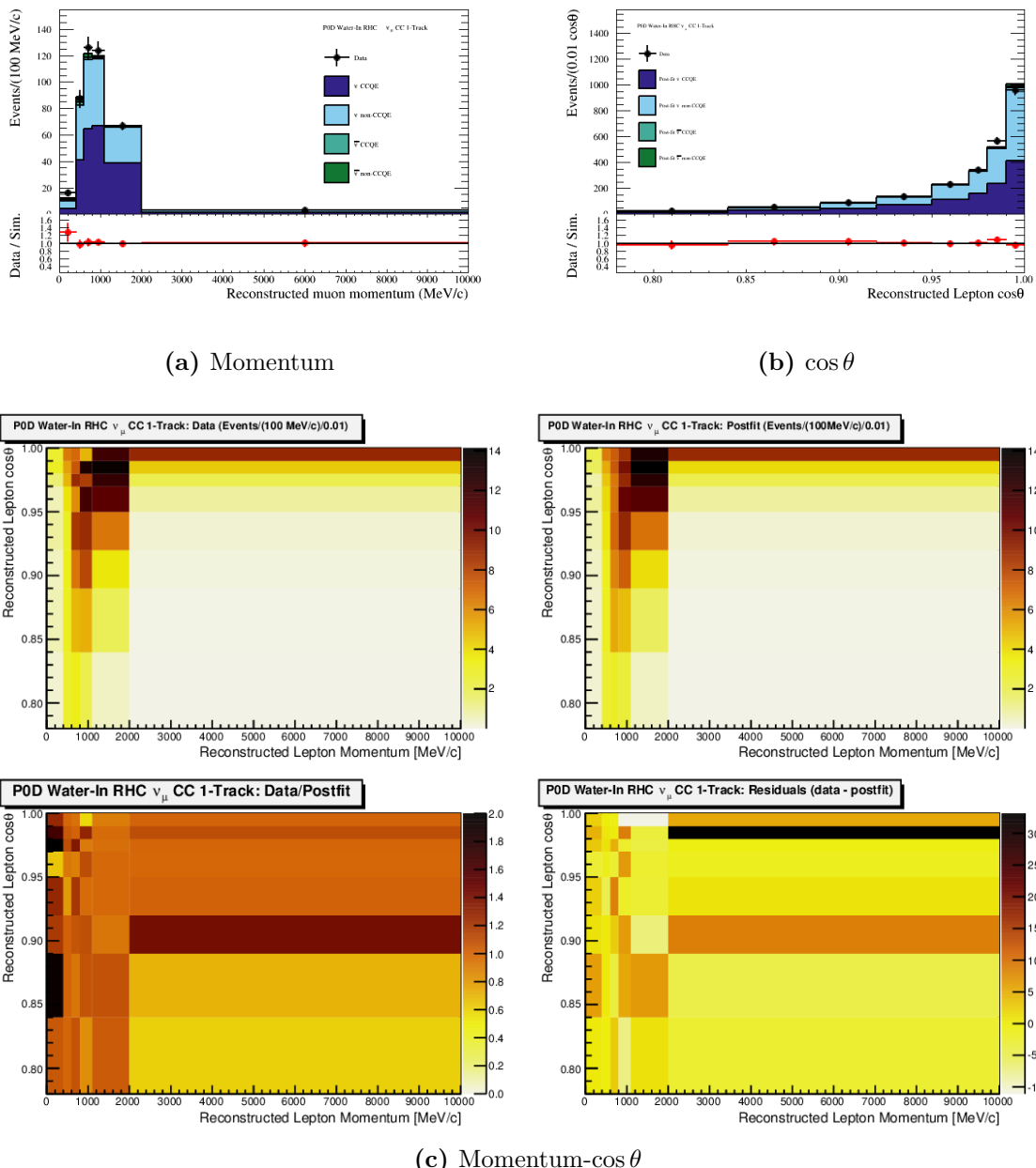
**Figure 6.20:** PØD Water-In  $\nu_\mu$  in FHC CC N-Tracks

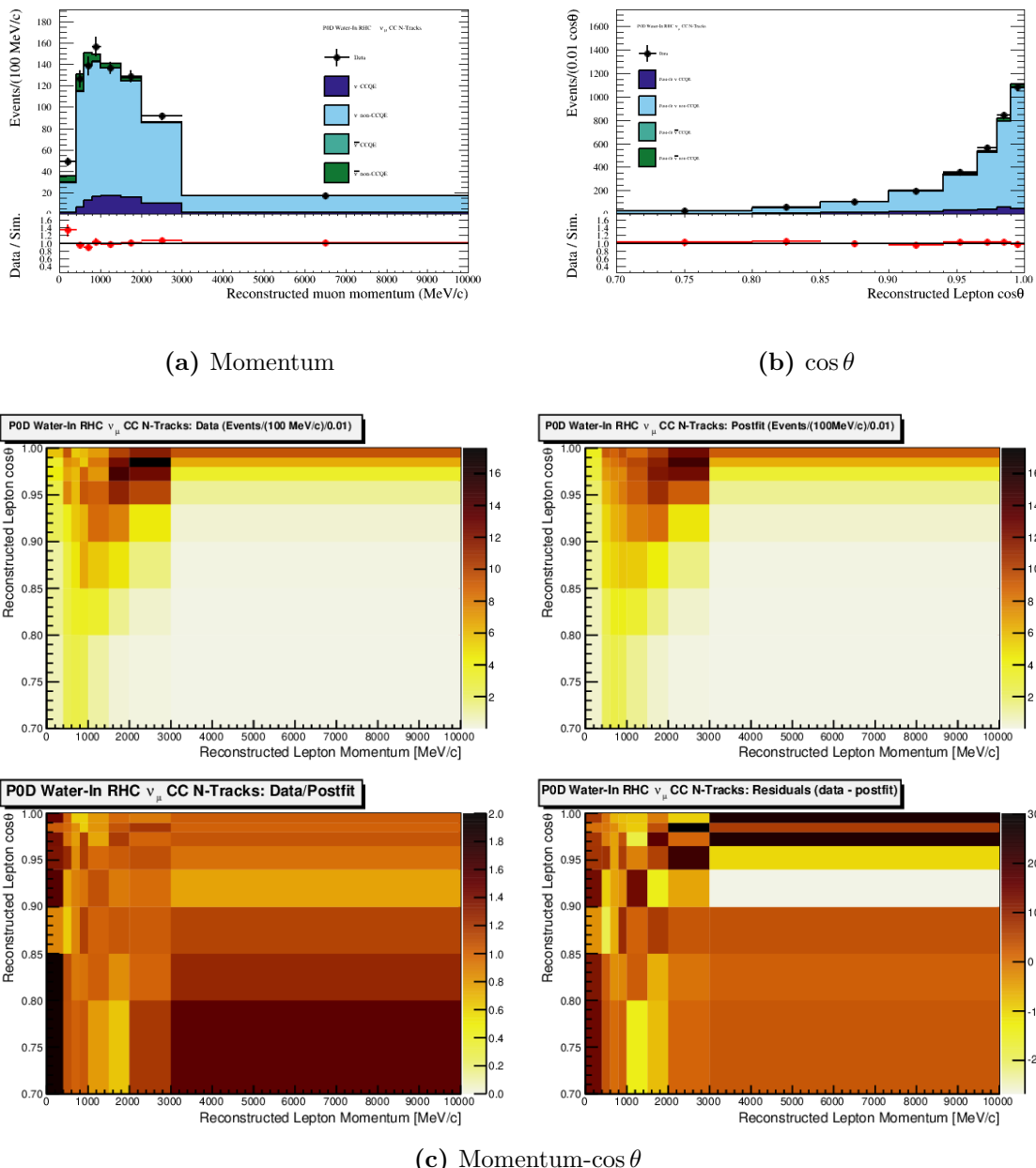


**Figure 6.21:** PØD Water-In  $\bar{\nu}_\mu$  in RHC CC 1-Track

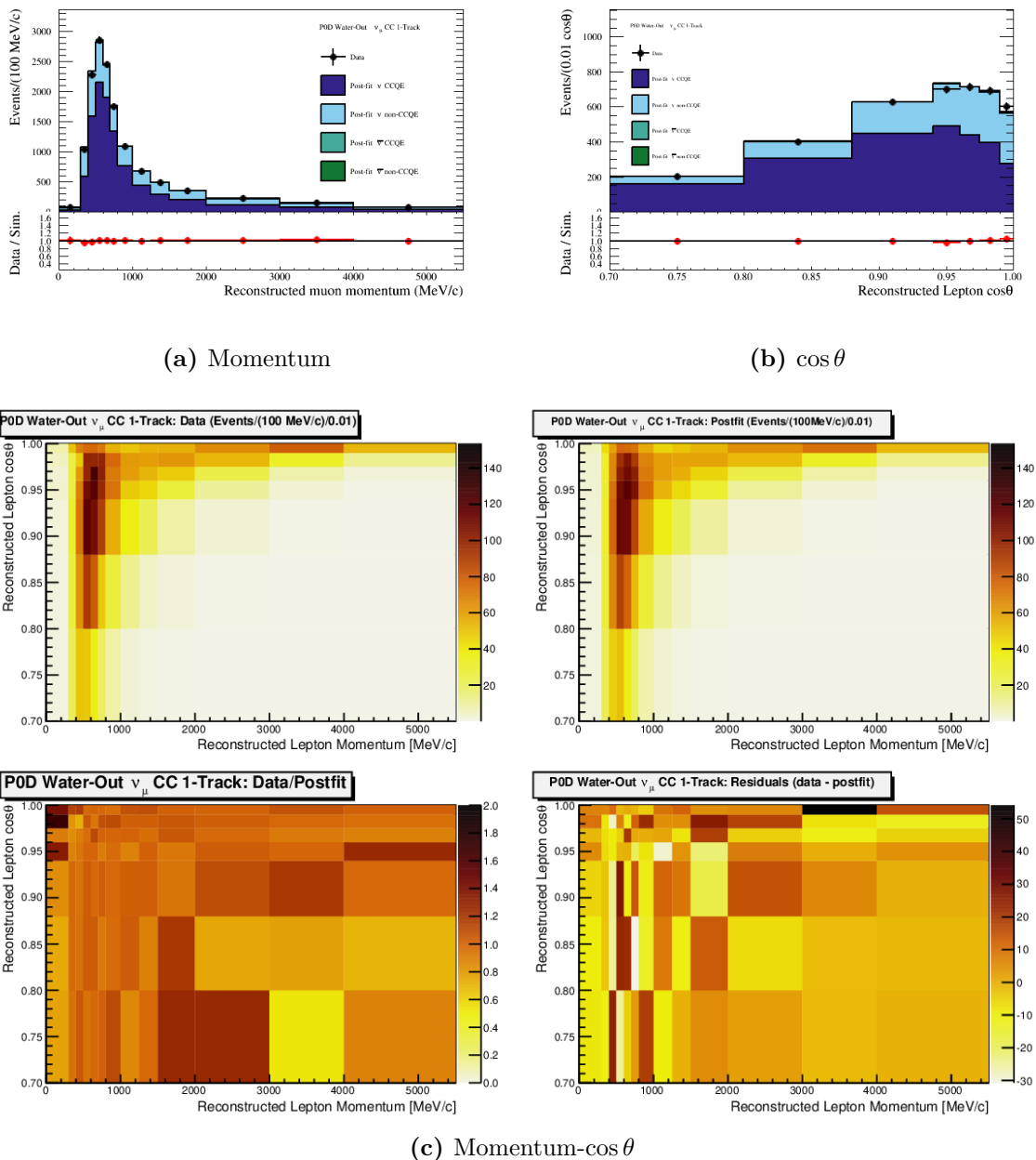


**Figure 6.22:** PØD Water-In  $\bar{\nu}_\mu$  in RHC CC N-Tracks

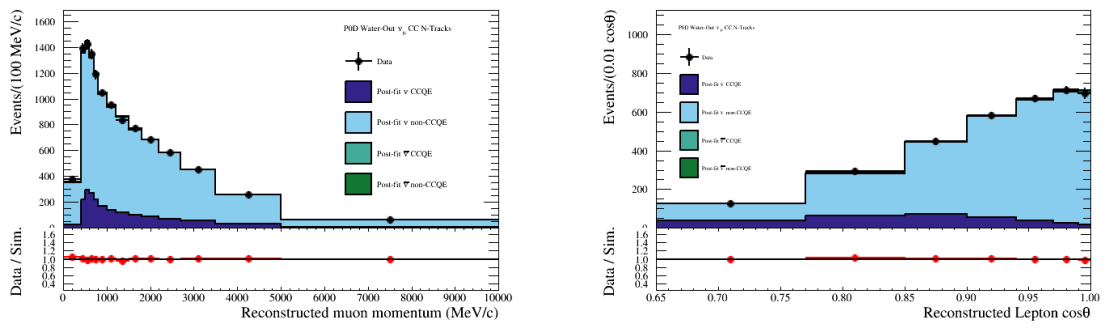




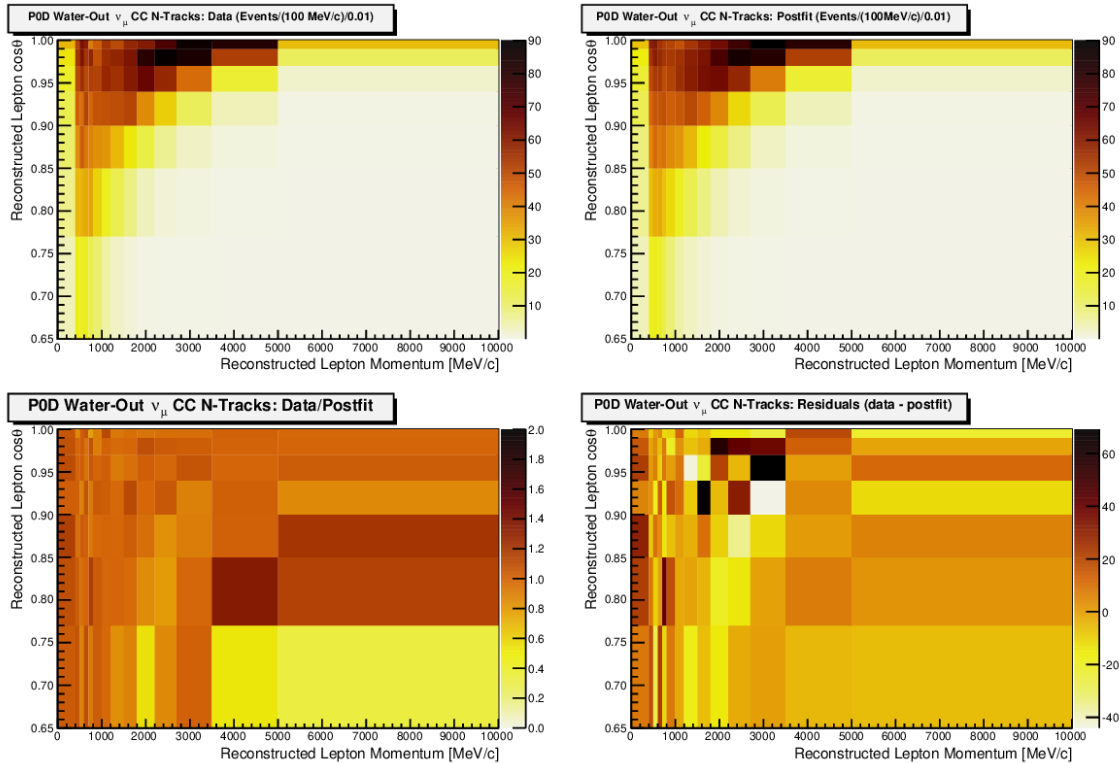
**Figure 6.24:** PØD Water-In  $\nu_\mu$  in RHC CC N-Tracks

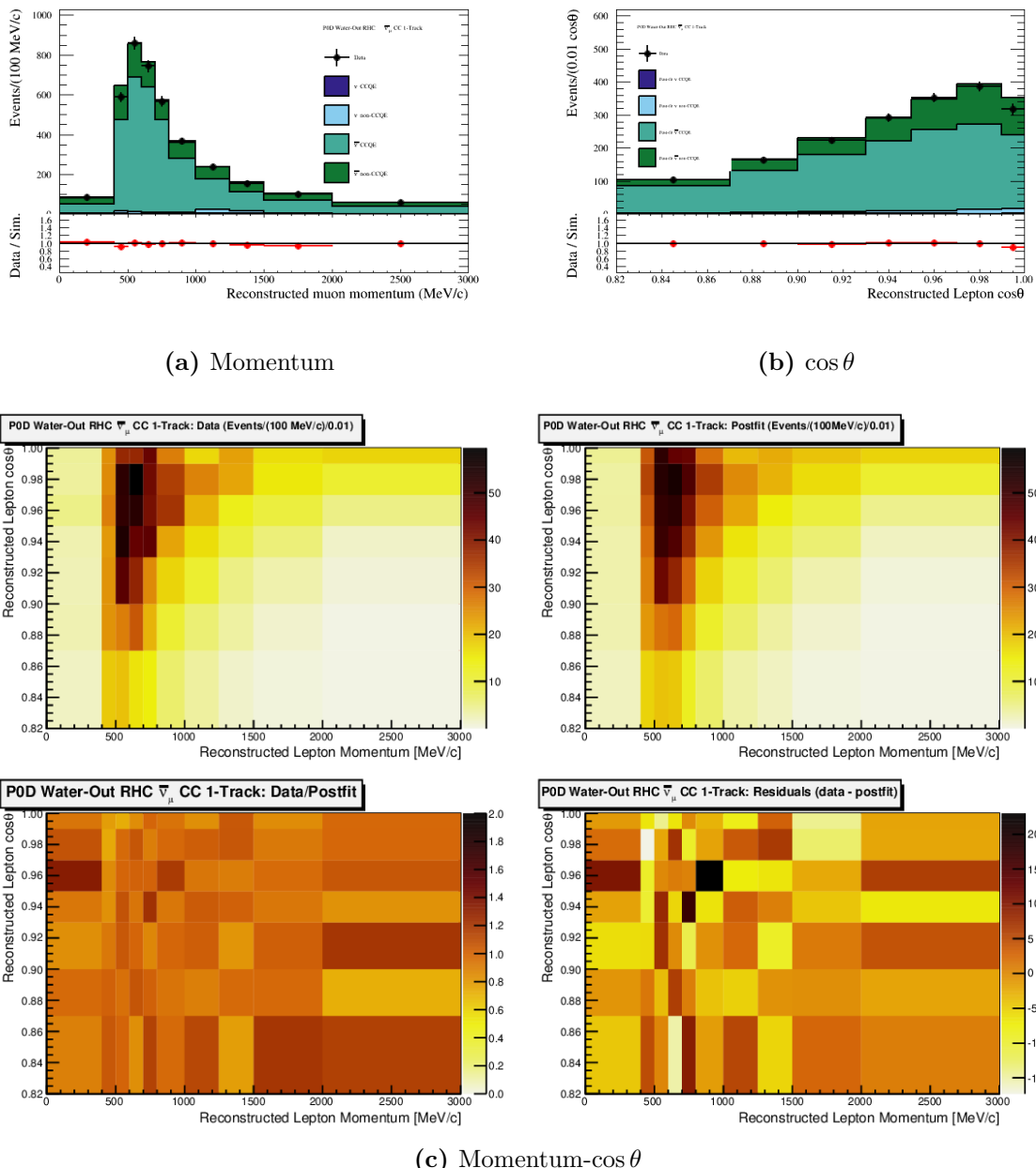


**Figure 6.25:** PØD Water-Out  $\nu_\mu$  in FHC CC 1-Track

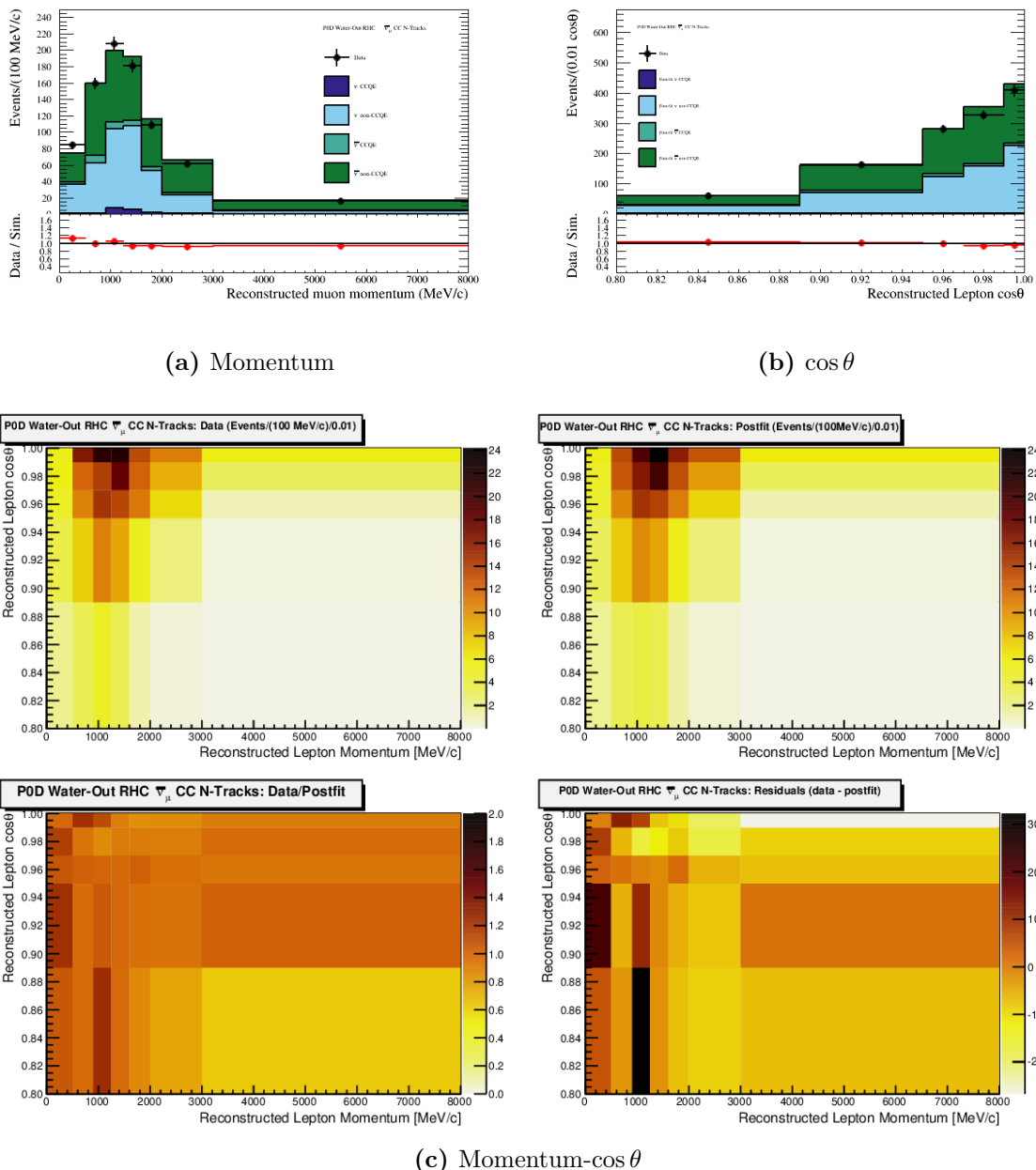


(a) Momentum

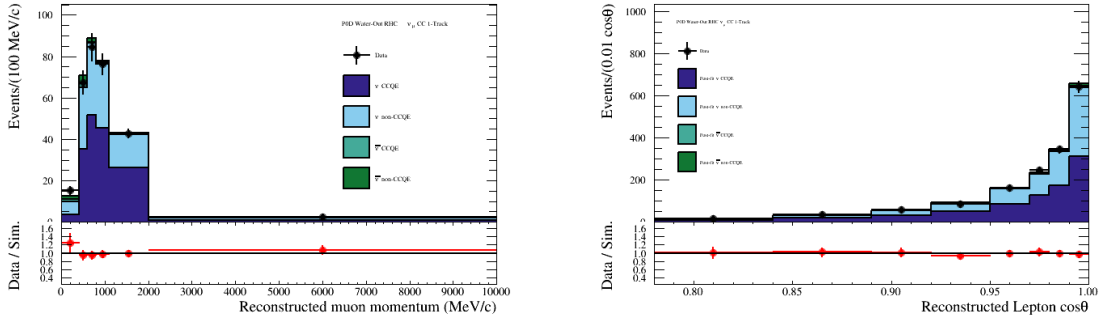
(b)  $\cos\theta$ (c) Momentum- $\cos\theta$ **Figure 6.26:** P̄D Water-Out  $\nu_\mu$  in FHC CC N-Tracks



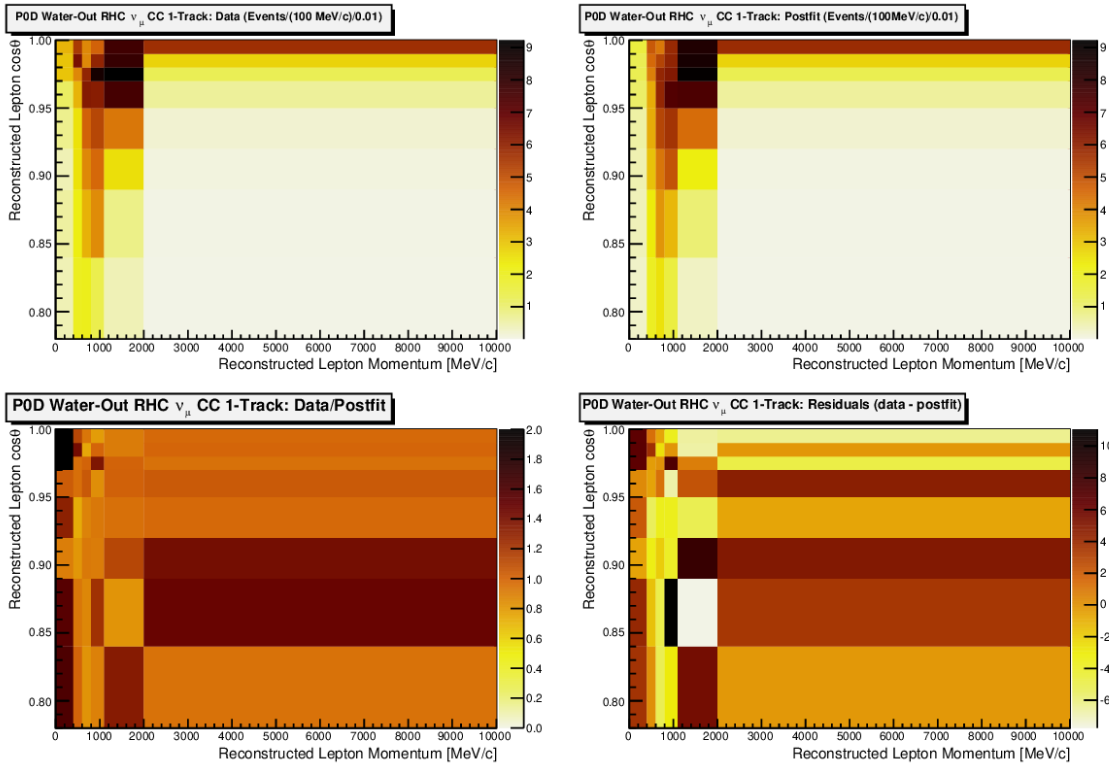
**Figure 6.27:** PØD Water-Out  $\bar{\nu}_\mu$  in RHC CC 1-Track



**Figure 6.28:** PØD Water-Out  $\bar{\nu}_\mu$  in RHC CC N-Tracks



(a) Momentum

(b)  $\cos \theta$ (c) Momentum- $\cos \theta$ **Figure 6.29:** P0D Water-Out  $\nu_\mu$  in RHC CC 1-Track

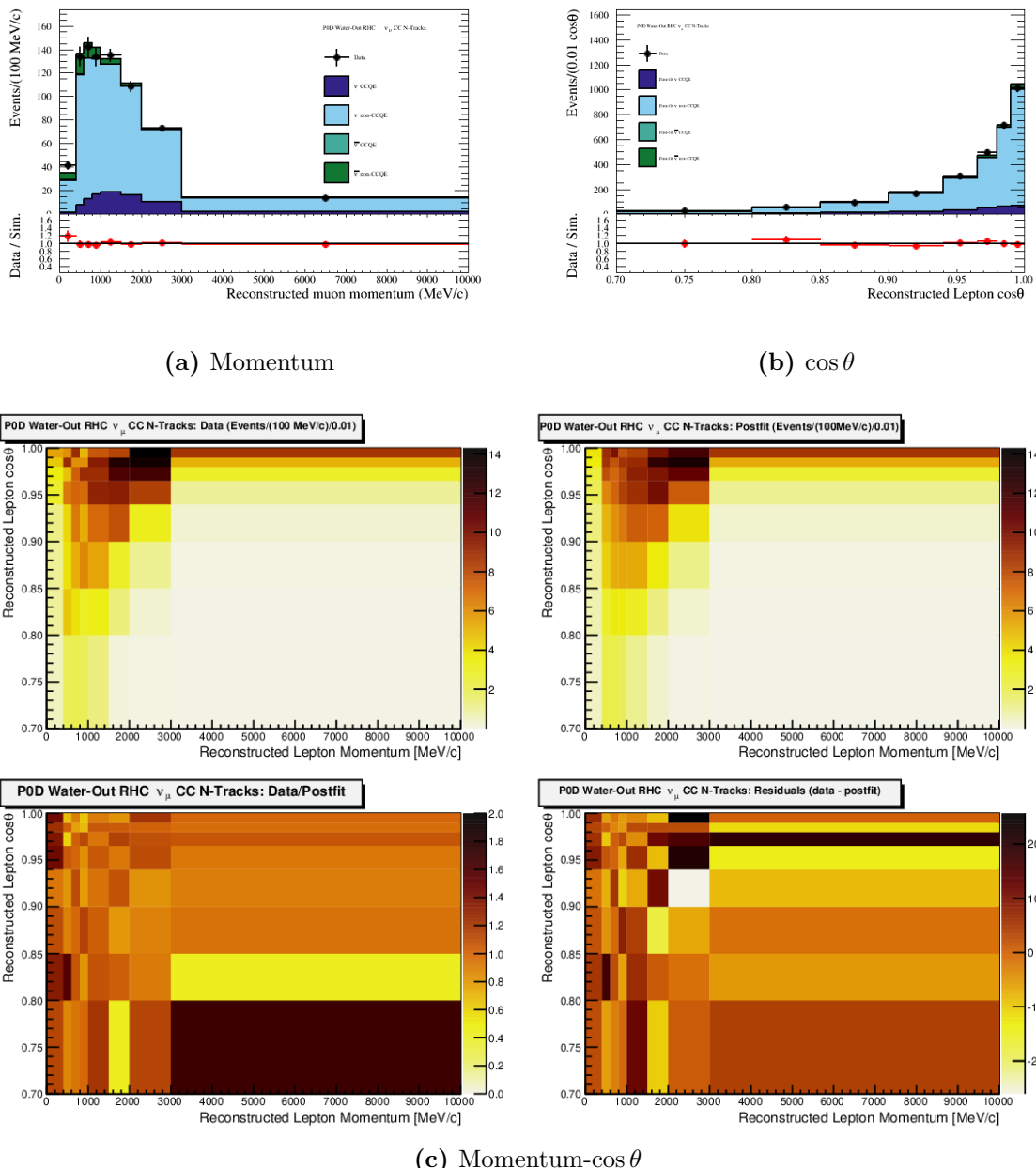


**Figure 6.30:** PØD Water-Out  $\nu_\mu$  in RHC CC N-Tracks

be the expectation of the result. We wish to test the hypothesis,  $H_1$ , that the PØD-only data fit and FGD-only data fit are sampling from two different neutrino populations. The null hypothesis,  $H_0$ , is that PØD-only and FGD-only data fits are sampled from the same population. If

$$\chi^2 = \sum_i X_i^2, \quad (6.1)$$

is distributed according to a chi-square distribution

$$F(\chi^2, r) = \frac{1}{2^{r/2} \Gamma(r/2)} (\chi^2)^{(r/2-1)} e^{(-\chi^2/2)}, \quad (6.2)$$

where  $r$  is the number of degrees of freedom (NDOF), we can calculate a p-value to reject the null hypothesis. This all assumes that each  $X_i$  is independently and identically distributed (i.d.d) from a standard normal  $\mathcal{N}(\mu = 0, \sigma^2 = 1)$ .

If we let  $p_i^{\text{PØD}} (p_i^{\text{FGD}})$  represent the measurement of the  $i$ th parameter for the PØD-only (FGD-only) BANFF fit, then our test statistic can be formally defined as

$$\chi_{\text{PØDvsFGD}}^2 = \sum_i \sum_j \frac{(p_i^{\text{PØD}} - p_i^{\text{FGD}})(p_j^{\text{PØD}} - p_j^{\text{FGD}})}{V_{i,j}^{\text{PØDvsFGD}}} \quad (6.3)$$

where  $V_{i,j}^{\text{PØDvsFGD}}$  is the covariance of measurement  $i, j$ . Since the purpose of the BANFF fit is to provide a ND constraint on the flux and cross section, we will ignore the bin normalization parameters since they are nuisance parameters. Also assume for simplicity that the PØD and FGD data are completely uncorrelated, then test statistic collapses to

$$\chi_{\text{PØDvsFGD}}^2 = \sum_i \frac{(p_i^{\text{PØD}} - p_i^{\text{FGD}})^2}{V_{i,i}^{\text{PØD}} + V_{i,i}^{\text{FGD}}}, \quad (6.4)$$

where  $V_{i,i}^{\text{PØD}} / V_{i,i}^{\text{FGD}}$  is the variance of the  $i$ th parameter from the PØD-/FGD-only measurement. We can calculate a p-value,  $p$ , of observing a test statistic at least as extreme in a chi-square distribution by integrating the right-hand tail of the chi-square distribution with

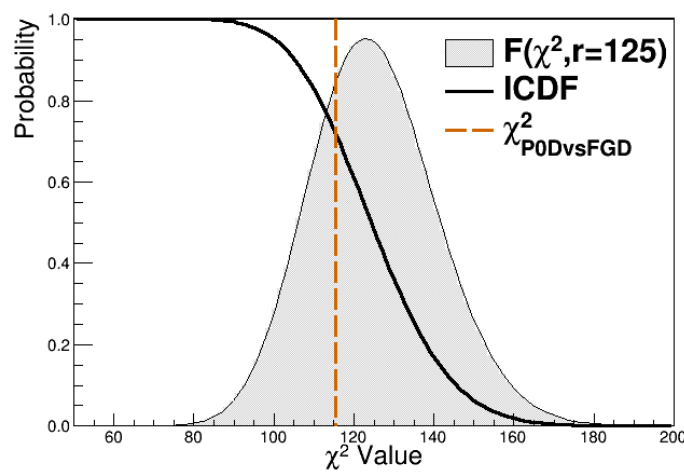


**Figure 6.31:**  $r=125$  and p-value=0.7163

the inverse cumulative distribution function (ICDF)

$$p(\chi^2, r) = \int_{\chi^2}^{\infty} F(x', r) dx', \quad (6.5)$$

where  $p$  is the p-value.

Now let us count the NDOF for p-value calculation. Since we have assumed the FGD-only result is our expectation, we have one less NDOF. There are 100 flux parameters and 31 cross section parameters. However, five of cross section fitted parameters are fixed, so we have.

$$r = \underbrace{100}_{\text{Flux}} + \underbrace{(31 - 5)}_{\text{XSec}} - 1 = 125$$

with p-value = 0.716322183192

$$r = \underbrace{50}_{\text{ND Flux}} + \underbrace{(31 - 5)}_{\text{XSec}} - 1 = 75$$

or p-value = 0.167315064026

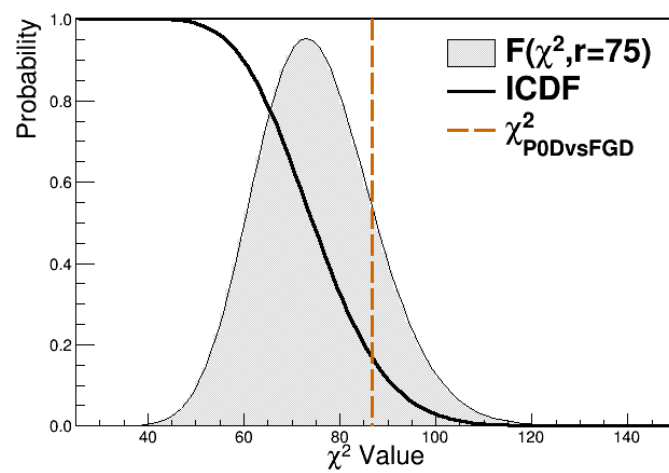


**Figure 6.32:**  $r=75$  and  $p\text{-value}=0.1673$

## Bibliography

- [1] K. Abe et al. The T2K Experiment. *Nucl. Instrum. Meth.*, A659:106–135, 2011. 26, 29, 31, 34, 36, 42, 46
- [2] K. Abe et al. Measurements of the T2K neutrino beam properties using the INGRID on-axis near detector. *Nucl. Instrum. Meth.*, A694:211–223, 2012. 37, 38
- [3] K. Abe et al. Observation of Electron Neutrino Appearance in a Muon Neutrino Beam. *Phys. Rev. Lett.*, 112:061802, 2014. 27
- [4] K. Abe et al. Measurement of neutrino and antineutrino oscillations by the T2K experiment including a new additional sample of  $\nu_e$  interactions at the far detector. *Phys. Rev. D*, 96(9), NOV 21 2017. 50, 98, 105, 106, 135
- [5] K. Abe and Others. Measurement of Coherent pi(+) Production in Low Energy Neutrino-Carbon Scattering. *Phys. Rev. Lett.*, 117(19), NOV 4 2016. 123
- [6] K. Abe and Others. Measurement of  $\nu_\mu$  and  $\bar{\nu}_\mu$  charged current inclusive cross sections and their ratio with the T2K off-axis near detector. *Phys. Rev. D*, 96(5), September 2017. 44, 45, 61, 63
- [7] K. Abe and Others. First measurement of the  $\nu_\mu$  charged-current cross section on a water target without pions in the final state. *Phys. Rev. D*, 97:012001, January 2018. 61, 62, 63, 66, 117

- [8] K. Abe and Others. Search for  $CP$  Violation in Neutrino and Antineutrino Oscillations by the T2K Experiment with  $2.2 \times 10^{21}$  Protons on Target. *Phys. Rev. Lett.*, 121:171802, October 2018. 27, 120
- [9] K. Abe and Others. First Measurement of the Anti-NuMu Charge Current Double Differential Cross Section on Water without Pions in the Final State. *Phys. Rev. D.*, Forthcoming. 61
- [10] N. Abgrall and Others. Measurements of  $\pi^\pm$ ,  $K^\pm$ ,  $K_S^0$ ,  $\Lambda$  and proton production in proton-carbon interactions at 31 GeV/c with the NA61/SHINE spectrometer at the CERN SPS. *Eur. Phys. J. C*, 76:84, 2016. 49, 98
- [11] C. Adams et al. The Long-Baseline Neutrino Experiment: Exploring Fundamental Symmetries of the Universe. 2013. arXiv:1307.7335. 4, 23, 26
- [12] S. Agostinelli et al. GEANT4: A Simulation toolkit. *Nucl. Instrum. Meth.*, A506:250–303, 2003. 69
- [13] Jiro Arafune, Masafumi Koike, and Joe Sato. CP violation and matter effect in long baseline neutrino oscillation experiments. *Phys. Rev. D*, 56:3093–3099, September 1997. 25
- [14] S. Baker and R. D. Cousins. Clarification of the use of Chi-Square and Likelihood Functions in Fits to Histograms. *Nucl. Instrum. Meth.*, A221:437–442, 1983. 56
- [15] Ch. Berger and L. M. Sehgal. Lepton mass effects in single pion production by neutrinos. *Phys. Rev. D*, 76:113004, December 2007. 123
- [16] S. Bienstock, A. Kaboth, M. Scott, and C. Wret. Constraining the Flux and Cross Section Models with Data from the ND280 Detector using FGD1 and FGD2 for the 2017 Joint Oscillation Analysis, 2017. T2K-TN-324. 234

- 
- [17] R. Bradford and Others. A new parameterization of the nucleon elastic form factors. *Nucl. Phys.*, B159(127), 2006. 121
- [18] T. Campbell. *Measurement of the muon anti-neutrino charged current double differential cross section with no pions in the final state on water using the pi-zero detector at T2K*. PhD thesis, Colorado State University, Fort Collins, Colorado, USA, 2018. 61, 62
- [19] T. Campbell and Others. Analysis of  $\nu_\mu$  Charged Current Inclusive Events in the PØD in Runs 1+2+3+4, March 2014. T2K-TN-80 v4. 64
- [20] T. Campbell, E. Reinherz-Aronis, and W. Toki. The ANuMu/NuMu Cross Sections Ratio With the P0D+TPC Samples, 2017. 64, 118
- [21] J-PARC Center. What is J-PARC?, January 2019. <https://j-parc.jp/researcher/en/about/what/index.html>, Accessed on 26 January 2019. 29
- [22] L. H. Chan, K. W. Chen, J. R. Dunning, et al. Nucleon Form Factors and Their Interpretation. *Phys. Rev.*, 141:1298–1307, January 1966. 121
- [23] A. Chulliat and Others. The US/UK World Magnetic Model for 2015-2020. Technical report, National Geophysical Data Center, NOAA, 2015. 41
- [24] B. T. Cleveland and Others. Measurement of the Solar Electron Neutrino Flux with the Homestake Chlorine Detector. *Astronomical Journal*, 496:505–526, March 1998. 14
- [25] Giampaolo Co'. Random phase approximation and neutrino-nucleus cross sections. *Acta Phys. Polon.*, B37:2235–2242, 2006. 121
- [26] Glen Cowan, Kyle Cranmer, Eilam Gross, and Ofer Vitells. Asymptotic formulae for likelihood-based tests of new physics. *Eur. Phys. J.*, C71:1554, 2011. [Erratum: Eur. Phys. J.C73,2501(2013)]. 130

- [27] R. Das. *Measurement of NuMu induced charged current inclusive cross section on water using the near detector of the T2K experiment*. PhD thesis, Colorado State University, Fort Collins, Colorado, USA, 2016. 61, 63
- [28] A. de Gouvea et al. Working Group Report: Neutrinos. In *Proceedings, 2013 Community Summer Study on the Future of U.S. Particle Physics: Snowmass on the Mississippi*, 2013. arXiv:1310.4340. 23
- [29] I. Esteban et al. Global analysis of three-flavour neutrino oscillations: synergies and tensions in the determination of  $\theta_{23}$ ,  $\delta_{\text{CP}}$ , and the mass ordering. 2018. arXiv:1811.05487. 24
- [30] Rida T. Farouki. The Bernstein polynomial basis: A centennial retrospective. *Computer Aided Geometric Design*, 29(6):379–419, 2012. 122
- [31] A. Ferrero. The ND280 Near Detector of the T2K Experiment. *AIP Conference Proceedings*, 1189(1):77–82, 2009. 26
- [32] J. A. Formaggio and G. P. Zeller. From eV to EeV: Neutrino Cross Sections Across Energy Scales. *Rev. Mod. Phys.*, 84:1307–1341, 2012. 50, 51
- [33] S. Fukuda et al. The Super-Kamiokande detector. *Nucl. Instrum. Meth. A*, 501(2):418–462, 2003. 26
- [34] Tomasz Golan, Cezary Juszczak, and Jan T. Sobczyk. Final State Interactions Effects in Neutrino-Nucleus Interactions. *Phys. Rev. C*, 86:015505, 2012. 124
- [35] K. M. Graczyk, D. Kielczewska, P. Przewlocki, and J. T. Sobczyk.  $C_A^5$  axial form factor from bubble chamber experiments. *Phys. Rev.*, D80:093001, 2009. 123
- [36] Krzysztof M. Graczyk, Jakub Źmuda, and Jan T. Sobczyk. Electroweak form factors of the  $\Delta(1232)$  resonance. *Phys. Rev. D*, 90:093001, November 2014. 123

- 
- [37] Krzysztof M. Graczyk and Jan T. Sobczyk. Form factors in the quark resonance model. *Phys. Rev. D*, 77:053001, March 2008. 123
- [38] Krzysztof M. Graczyk and Jan T. Sobczyk. Lepton mass effects in weak charged current single pion production. *Phys. Rev. D*, 77:053003, March 2008. 123
- [39] M. Hartz and Others. Constraining the Flux and Cross Section Models with Data from the ND280 Detector for the 2014/15 Oscillation Analysis. Technical report, T2K Collaboration, May 2015. T2K-TN-220 v4. 54, 57
- [40] Y. Hayato. A neutrino interaction simulation program library NEUT. *Acta Phys. Polon.*, B40:2477–2489, 2009. 49
- [41] C. Jarlskog. A Basis Independent Formulation of the Connection Between Quark Mass Matrices, CP Violation and Experiment,. *Z. Phys.*, C29:491–497, 1985. 23
- [42] T. Kitagaki and Others. Charged-current exclusive pion production in neutrino-deuterium interactions. *Phys. Rev. D*, 34:2554–2565, November 1986. 123
- [43] E. Komatsu and Others. Seven-year Wilkinson Microwave Anisotropy Probe (WMAP) Observations: Cosmological Interpretation. *Astrophys. J.*, 192:18, February 2011. 26
- [44] C. H. Llewellyn Smith. Neutrino Reactions at Accelerator Energies. *Phys. Rept.*, 3:261–379, 1972. 121
- [45] Z Maki, M. Nakagawa, and S. Sakata. Remarks on the Unified Model of Elementary Particles. *Progr. Theor. Exp. Phys.*, 28(5), 1962. 20
- [46] M. Martini, M. Ericson, G. Chanfray, and J. Marteau. A Unified approach for nucleon knock-out, coherent and incoherent pion production in neutrino interactions with nuclei. *Phys. Rev.*, C80:065501, 2009. 121
- [47] J. Nieves, I. Ruiz Simo, and M. J. Vicente Vacas. Inclusive Charged–Current Neutrino–Nucleus Reactions. *Phys. Rev.*, C83:045501, 2011. 121, 122

- 
- [48] Kajetan Niewczas and Jan T. Sobczyk. Search for nucleon-nucleon correlations in neutrino-argon scattering. *Phys. Rev.*, C93(3):035502, 2016. 121
- [49] B. Pontecorvo. Inverse Beta Processes and Nonconservation of Lepton Charge. *J. Exp. Theor. Phys.*, 28(5), 1957. 20
- [50] B. Pontecorvo. Mesonium and Anti-Mesonium. *Sov. Phys. JETP*, 6:429, 1957. 15
- [51] G. M. Radecky and Others. Study of single-pion production by weak charged currents in low-energy  $\nu d$  interactions. *Phys. Rev. D*, 25:1161–1173, March 1982. 123
- [52] Dieter Rein and Lalit M Sehgal. Neutrino-excitation of baryon resonances and single pion production. *Ann. Phys.*, 133(1):79–153, 1981. 123
- [53] Dieter Rein and Lalit M. Sehgal. Coherent  $\pi^0$  production in neutrino reactions. *Nucl. Phys. B*, 223(1):29–44, 1983. 123
- [54] Glenn Rowe, Martin Salomon, and Rubin H. Landau. Energy-dependent phase shift analysis of pion-nucleon scattering below 400 MeV. *Phys. Rev. C*, 18:584–589, July 1978. 124
- [55] P. K. Saha et al. Simulation, measurement, and mitigation of beam instability caused by the kicker impedance in the 3-GeV rapid cycling synchrotron at the Japan Proton Accelerator Research Complex. *Phys. Rev. Accel. Beams*, 21:024203, February 2018. 30
- [56] Andrei D Sakharov. Violation of CP invariance, C asymmetry, and baryon asymmetry of the universe. *Soviet Physics Uspekhi*, 34(5):392, 1991. 25
- [57] L.L. Salcedo, E. Oset, M.J. Vicente-Vacas, and C. Garcia-Recio. Computer simulation of inclusive pion nuclear reactions. *Nucl. Phys. A*, 484(3):557–592, 1988. 124
- [58] J. Schechter and J. W. F. Valle. Neutrinoless double- $\beta$  decay in  $SU(2) \times U(1)$  theories. *Phys. Rev. D*, 25:2951–2954, 1982. 21

- [59] N. Schmitz. *Neutrinophysik*. Teubner, Stuttgart, 1997. 19
- [60] T. Sekiguchi et al. Development and operational experience of magnetic horn system for T2K experiment. *Nucl. Instrum. Meth. A*, 789:57–80, 2015. 31
- [61] R.A. Smith and E.J. Moniz. Neutrino reactions on nuclear targets. *Nucl. Phys. B*, 43:605–622, 1972. 121
- [62] M. Tanabashi et al. The Review of Particle Physics. *Phys. Rev. D*, 98(030001), 2018. 20, 24
- [63] Peter von Ballmoos. Antimatter in the Universe: constraints from gamma-ray astronomy. *Hyperfine Interact.*, 228(1):91–100, October 2014. 25
- [64] G. Welch and G. Bishop. An Introduction to the Kalman Filter. Technical Report 95041, University of North Carolina at Chapel Hill, Chapel Hill, NC 27599-3175, July 2006. A description of the mathematics involved in the Kalman filer. 62
- [65] L. Wolfenstein. Neutrino oscillations in matter. *Phys. Rev. D*, 17:2369–2374, May 1978. 24
- [66] Carl Vincent Clarence Wret. *Minimising Systematic Uncertainties in the T2K Experiment Using Near-Detector and External Data*. PhD thesis, Imperial College London, 2019. 108, 120, 121, 123, 124
- [67] Y. Yamazaki. Accelerator technical design report for high-intensity proton accelerator facility project, J-PARC. Report 2002-013, KEK, 2003. 30
- [68] Kai Zuber. *Neutrino Physics*. CRC Press, Boca Raton, FL., 2nd edition, 2012. 1, 14, 19

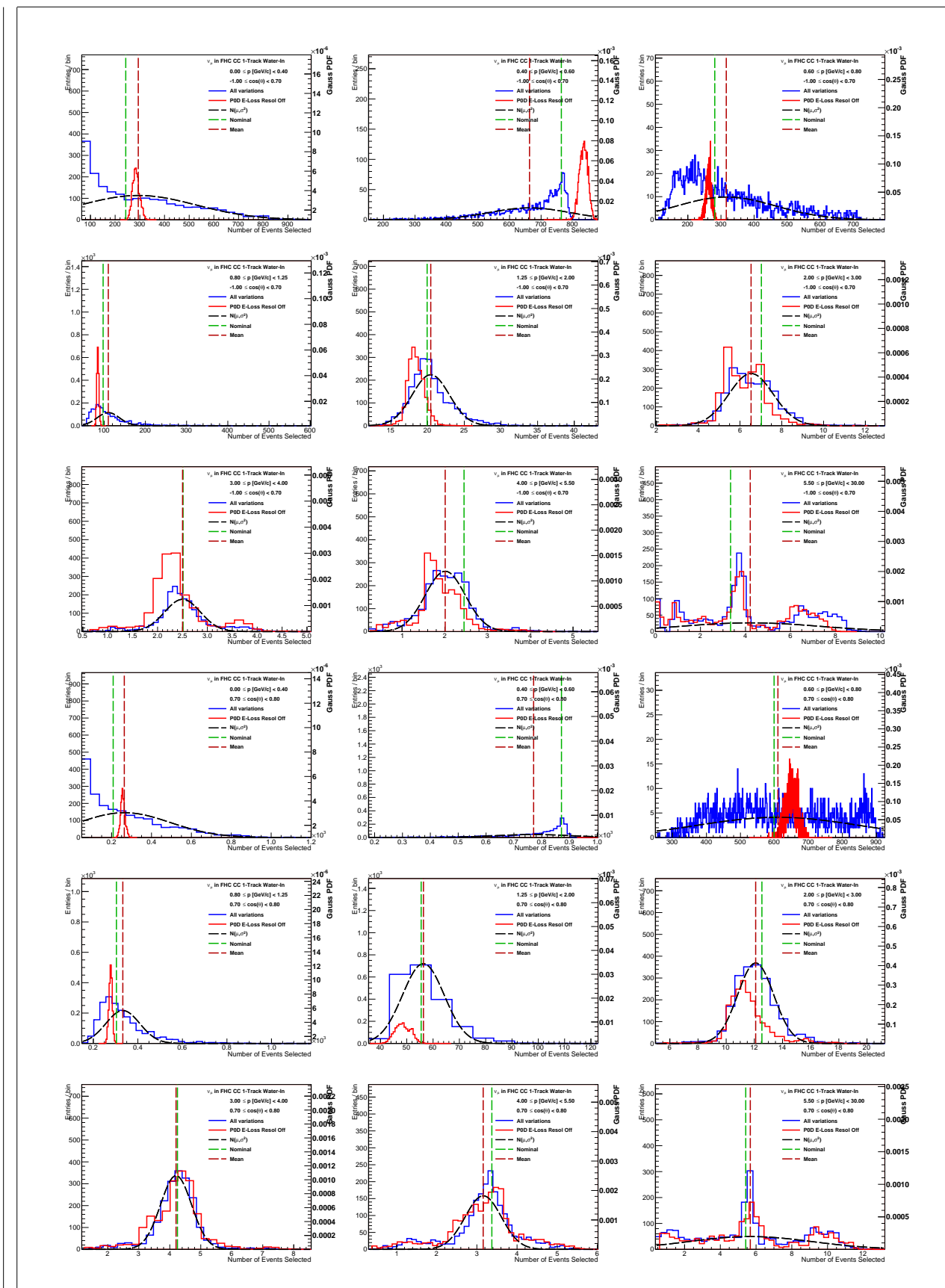
---

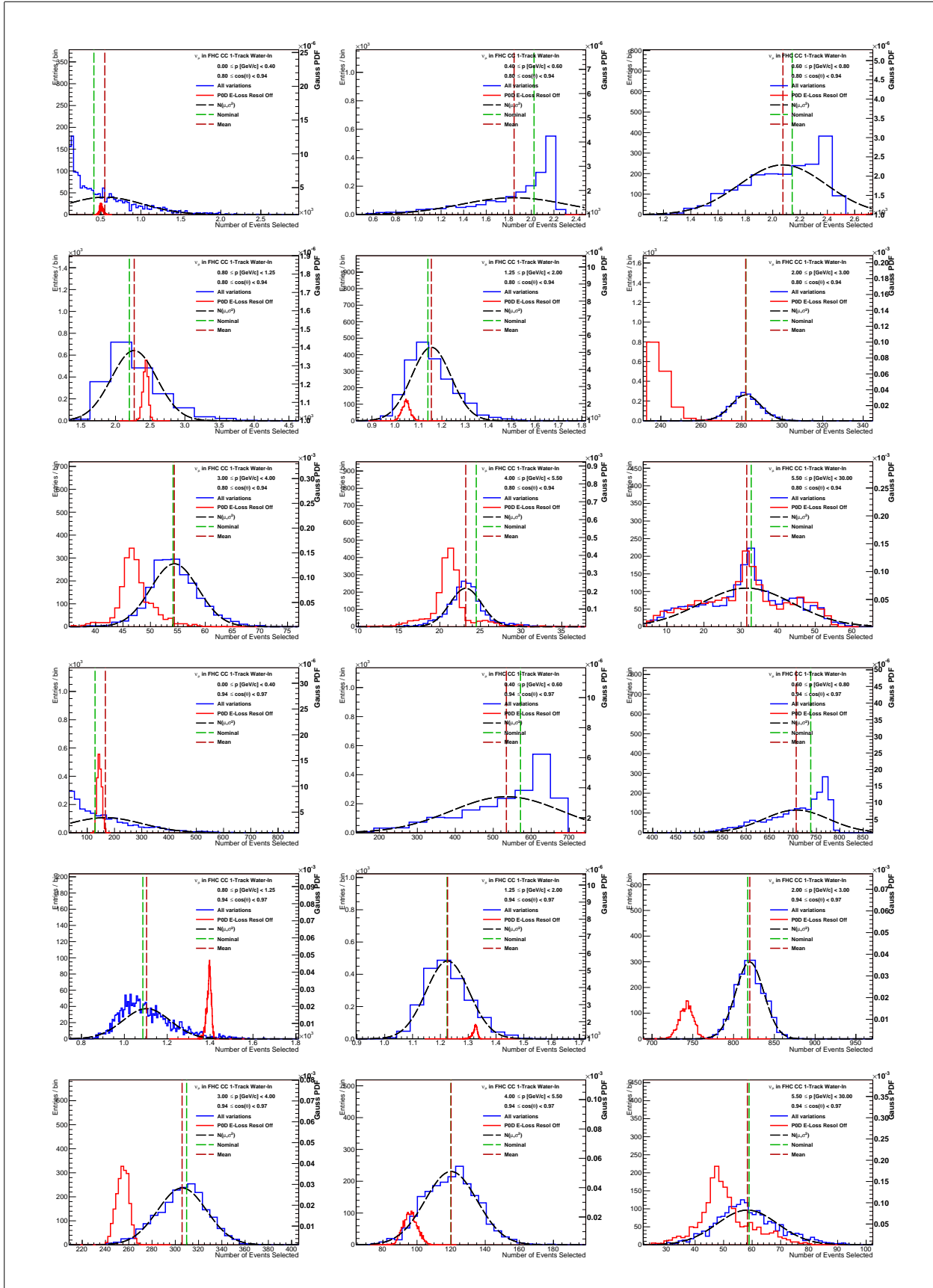
---

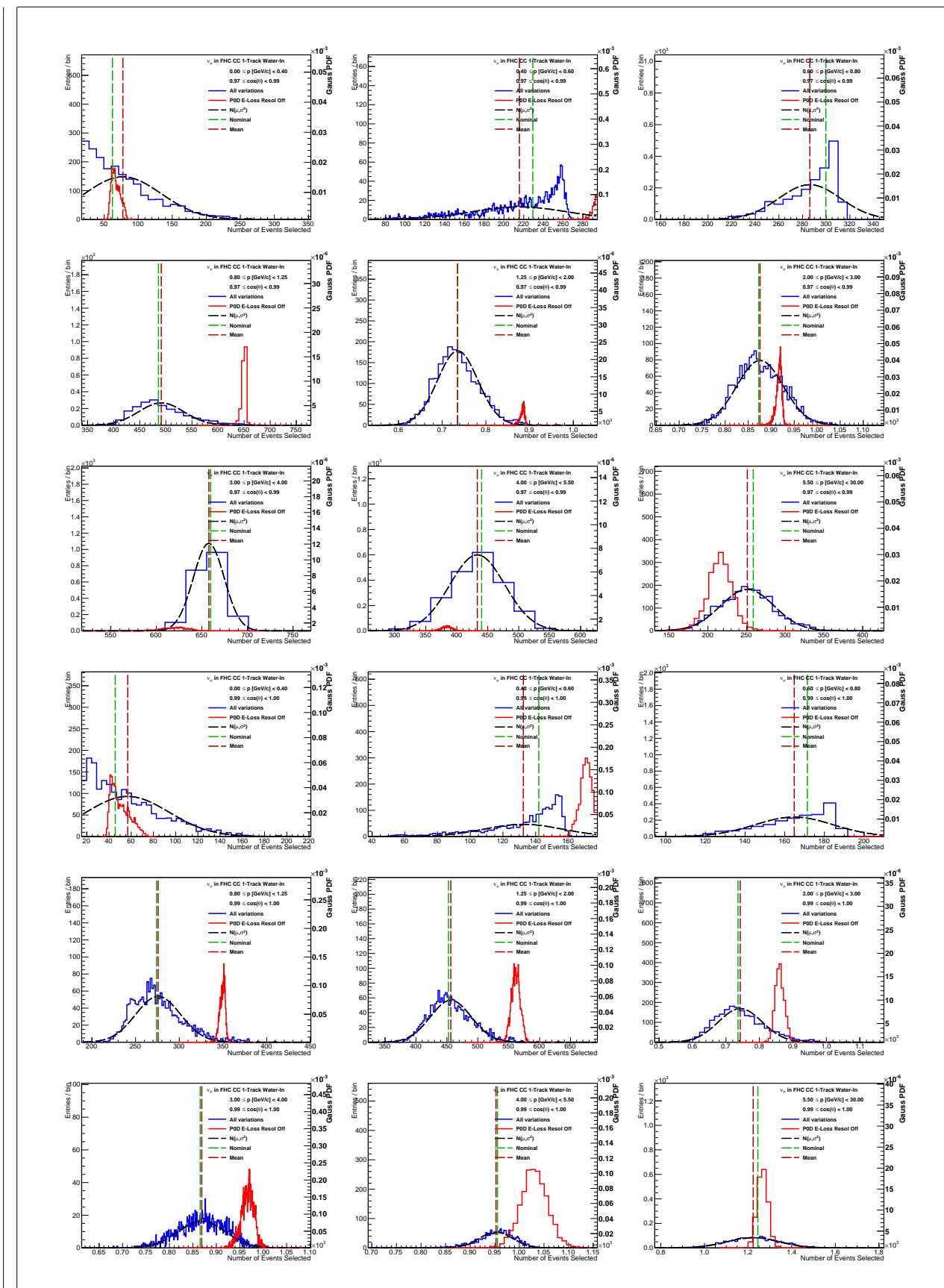
## Appendix A

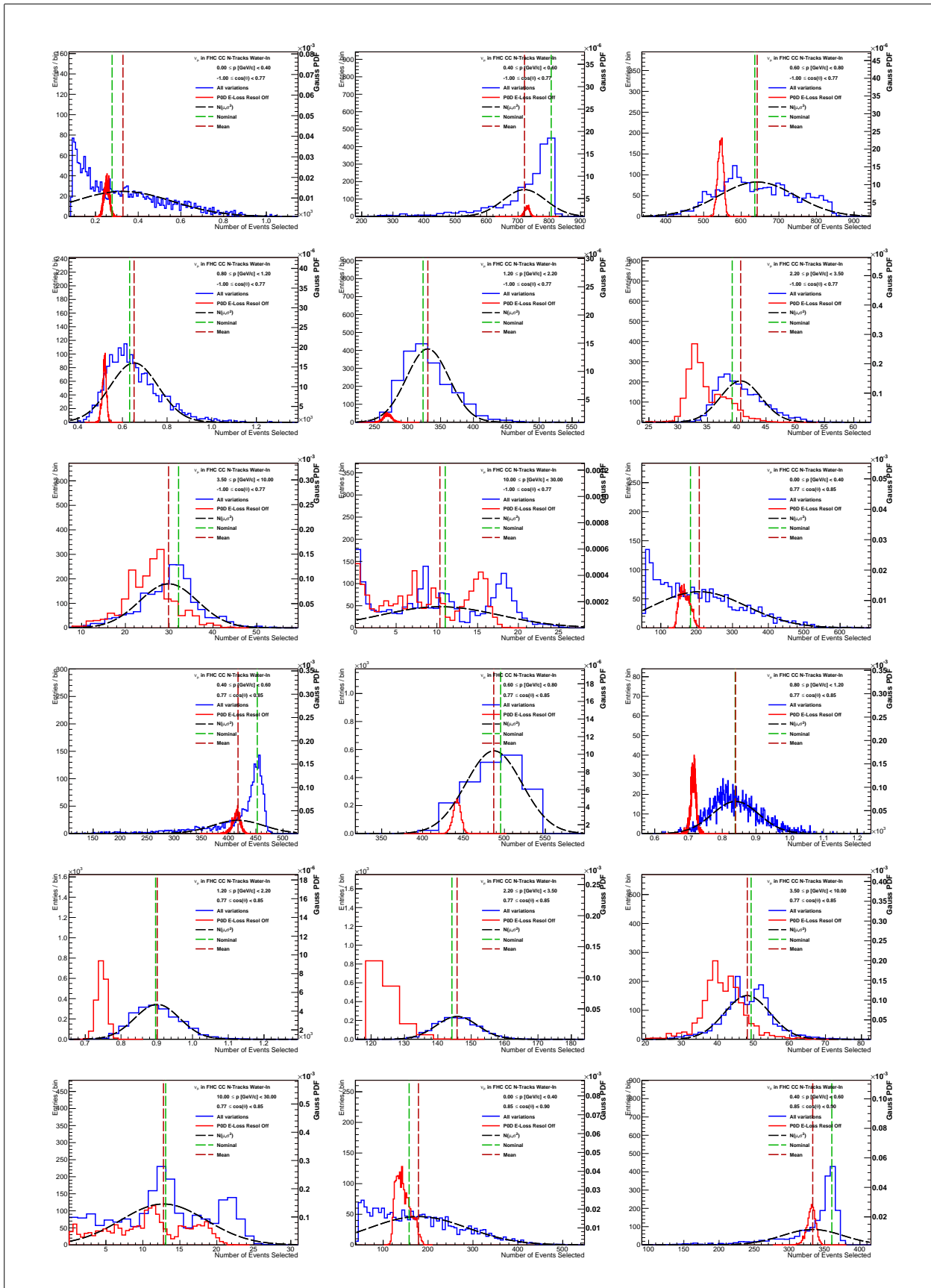
### Toy Experiment Variations

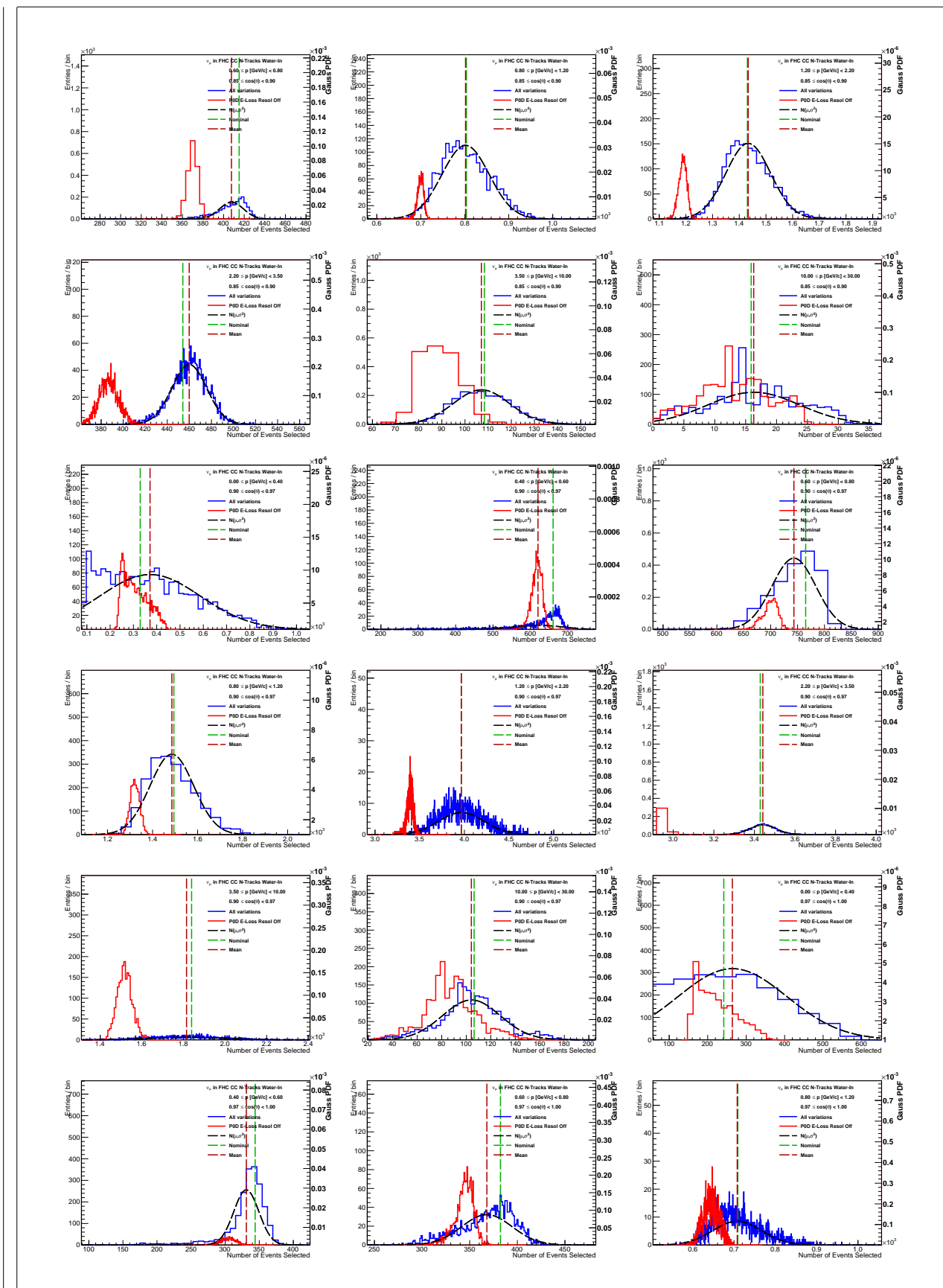
In this appendix is the collection of all toy experiments used to make observable normalization parameters and detector covariance matrix. Each of the observable bin relevant samples and  $(p, \cos \theta)$  edges are listed in the plots. The nominal MC (Nominal) predicted value and varied mean are shown as differently dashed lines. A normal curve, whose variance was extracted from the covariance matrix itself, is shown to illustrate the estimate on the bin normalization uncertainty. In addition, toy experiment variations with the PØD energy loss resolution off (E-Loss Resol Off) is shown to demonstrate the absence of the energy correction and its affect on when not varied.

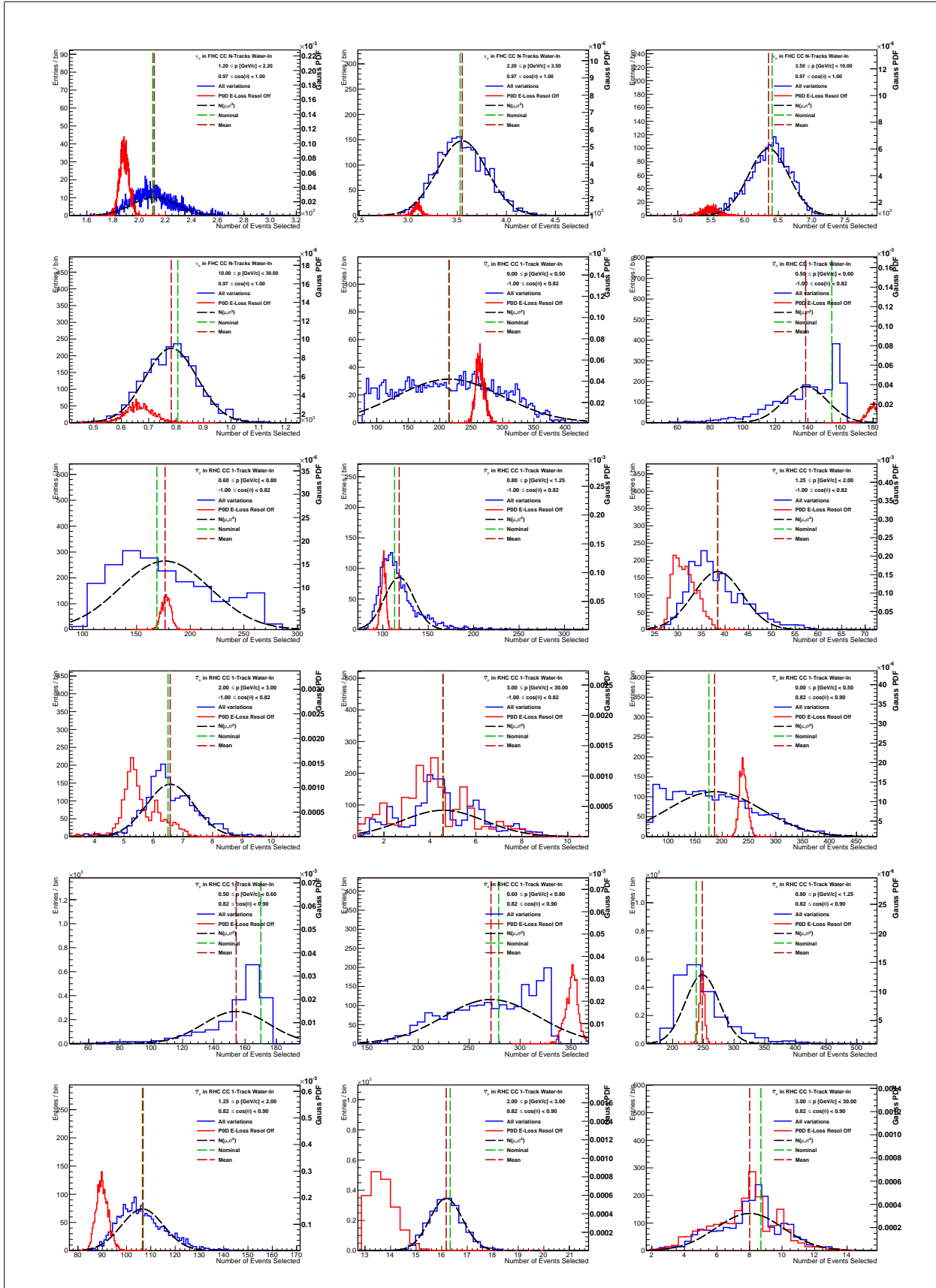


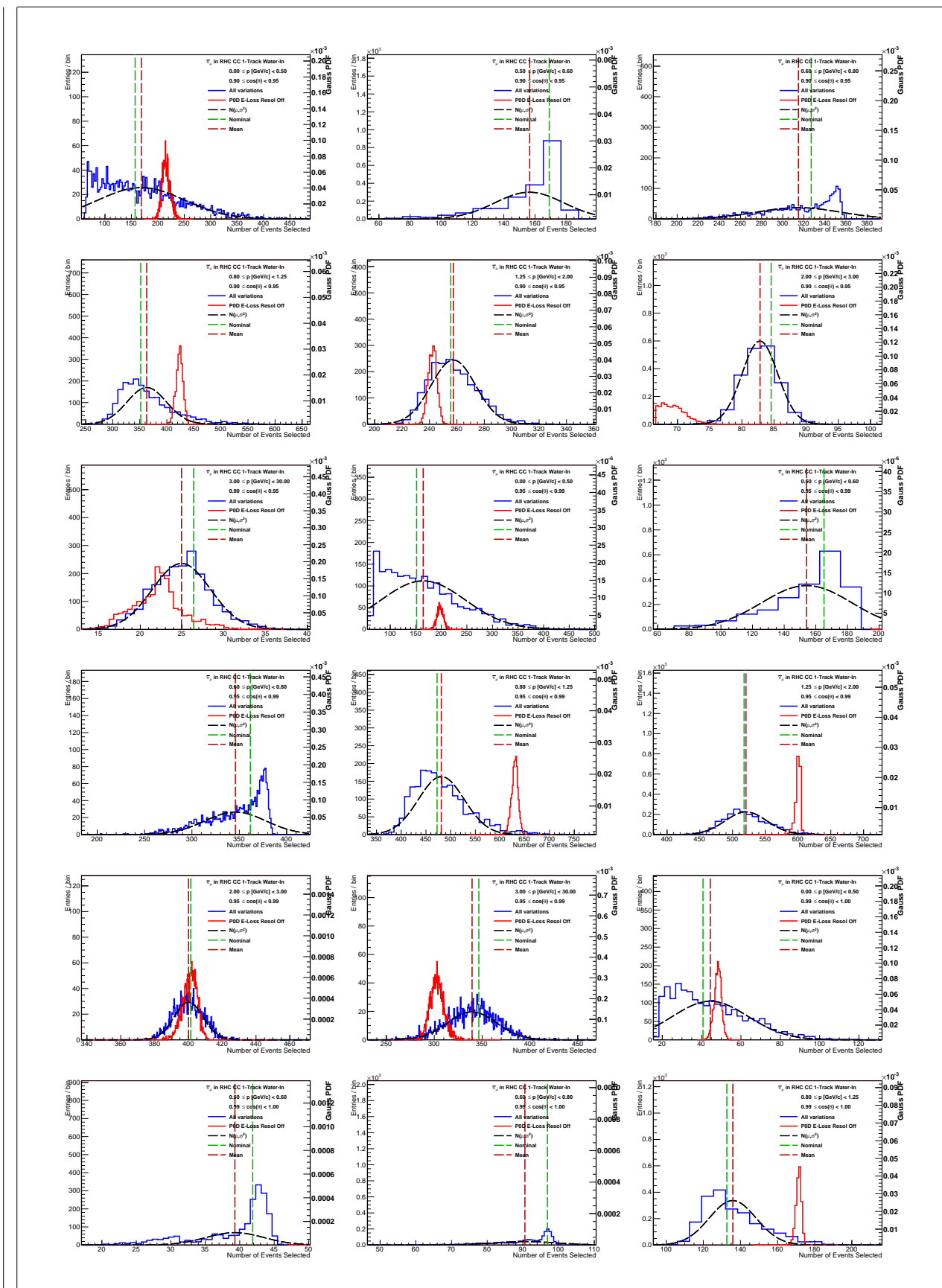


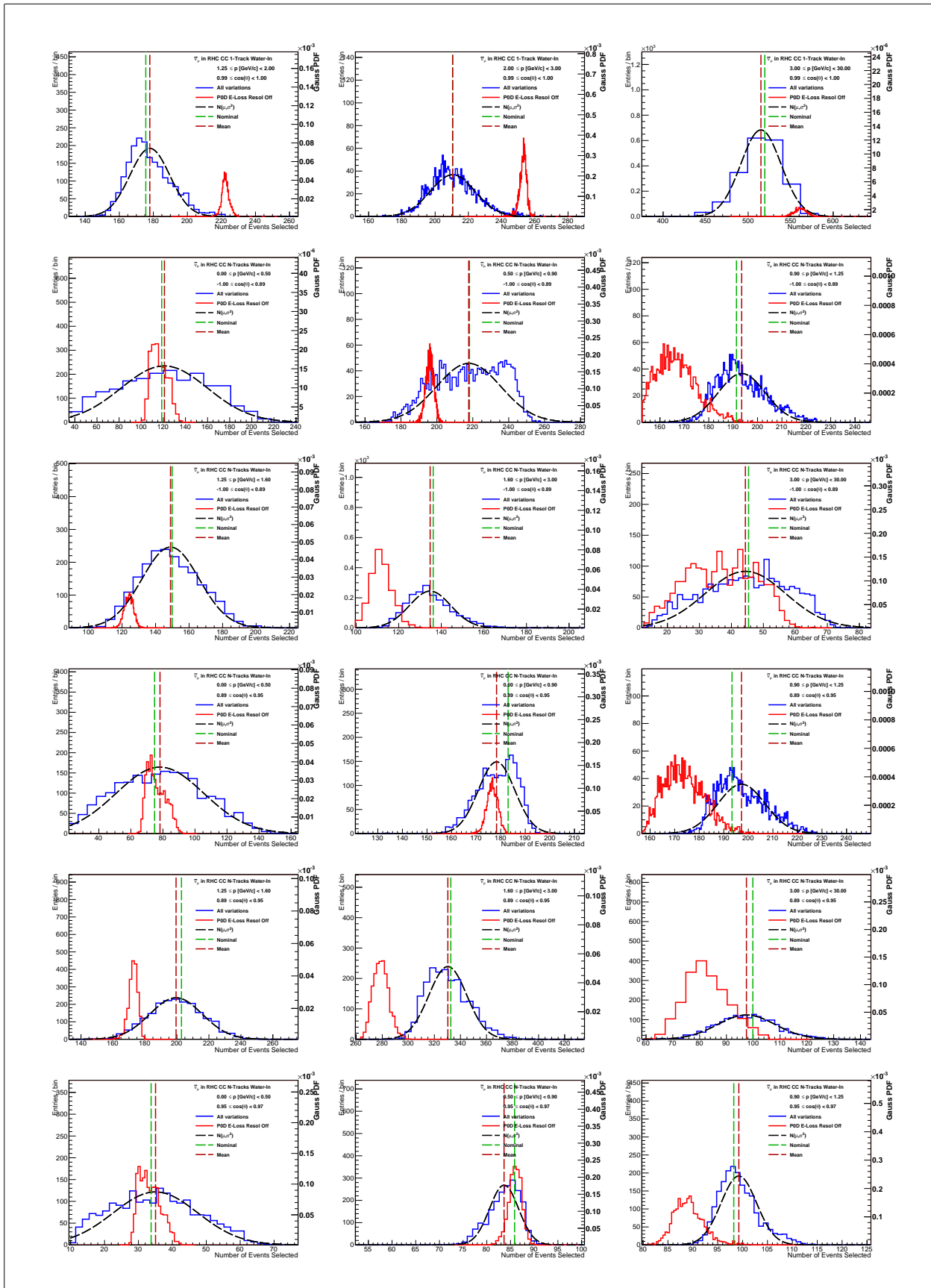


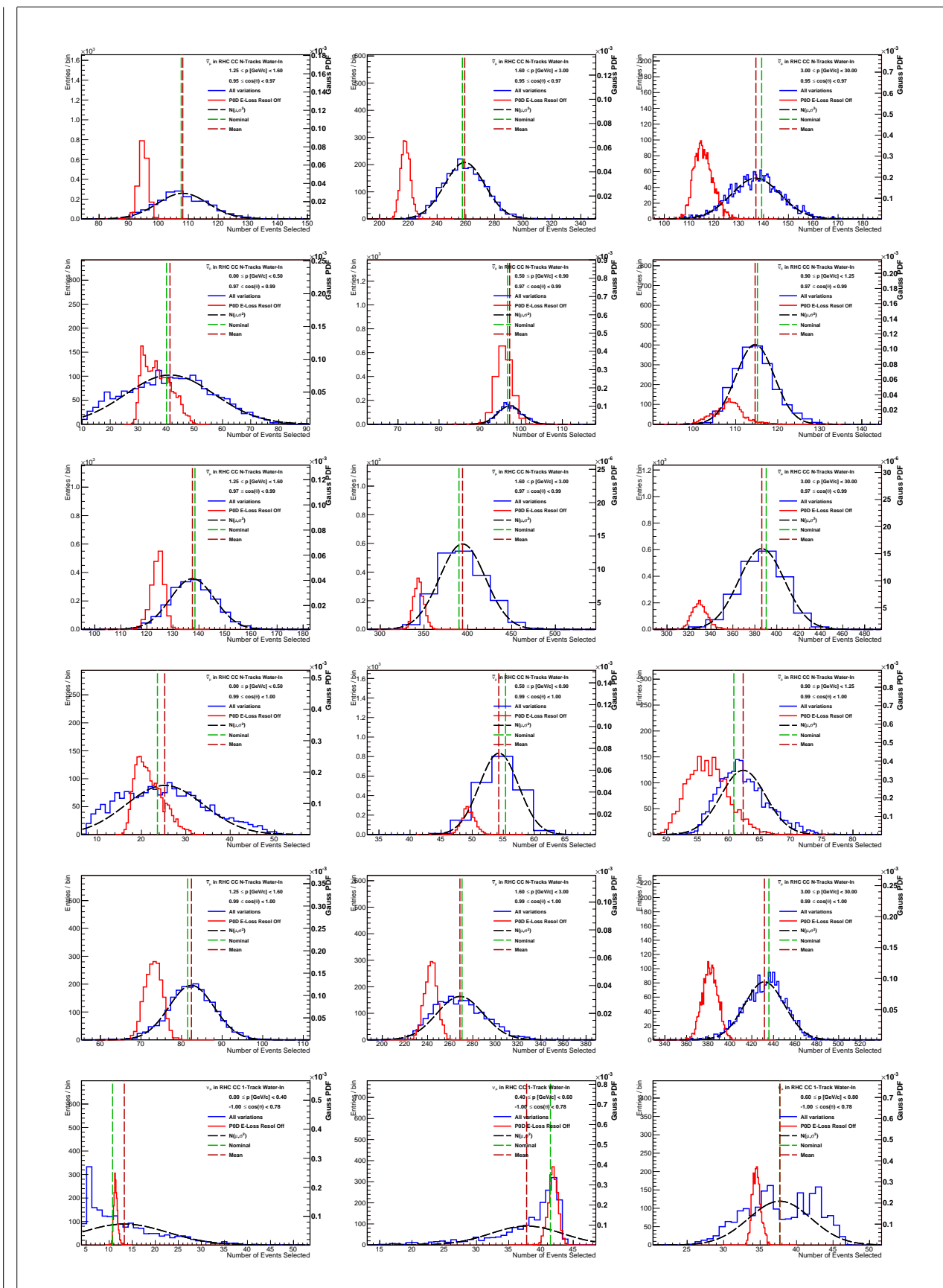


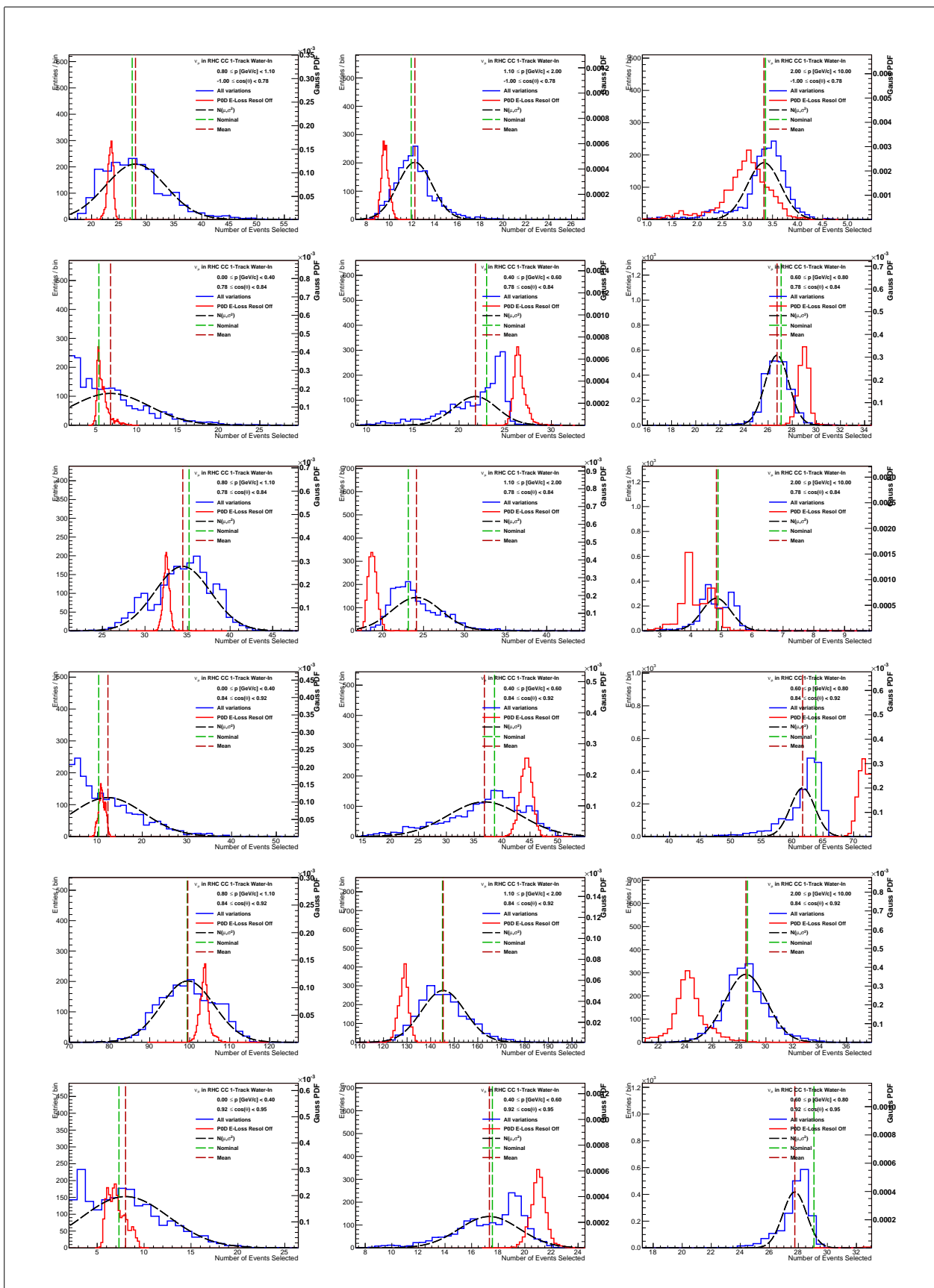


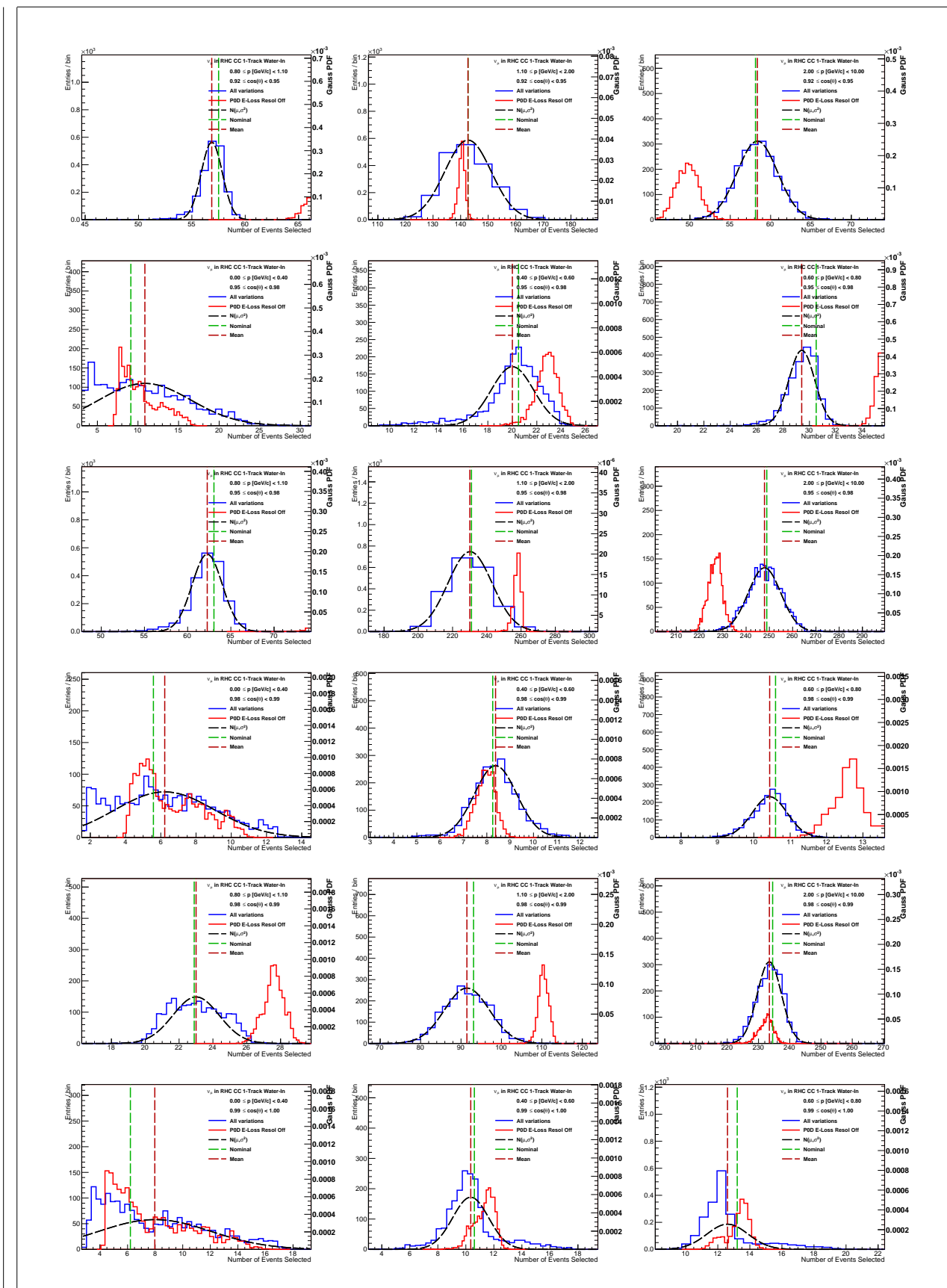


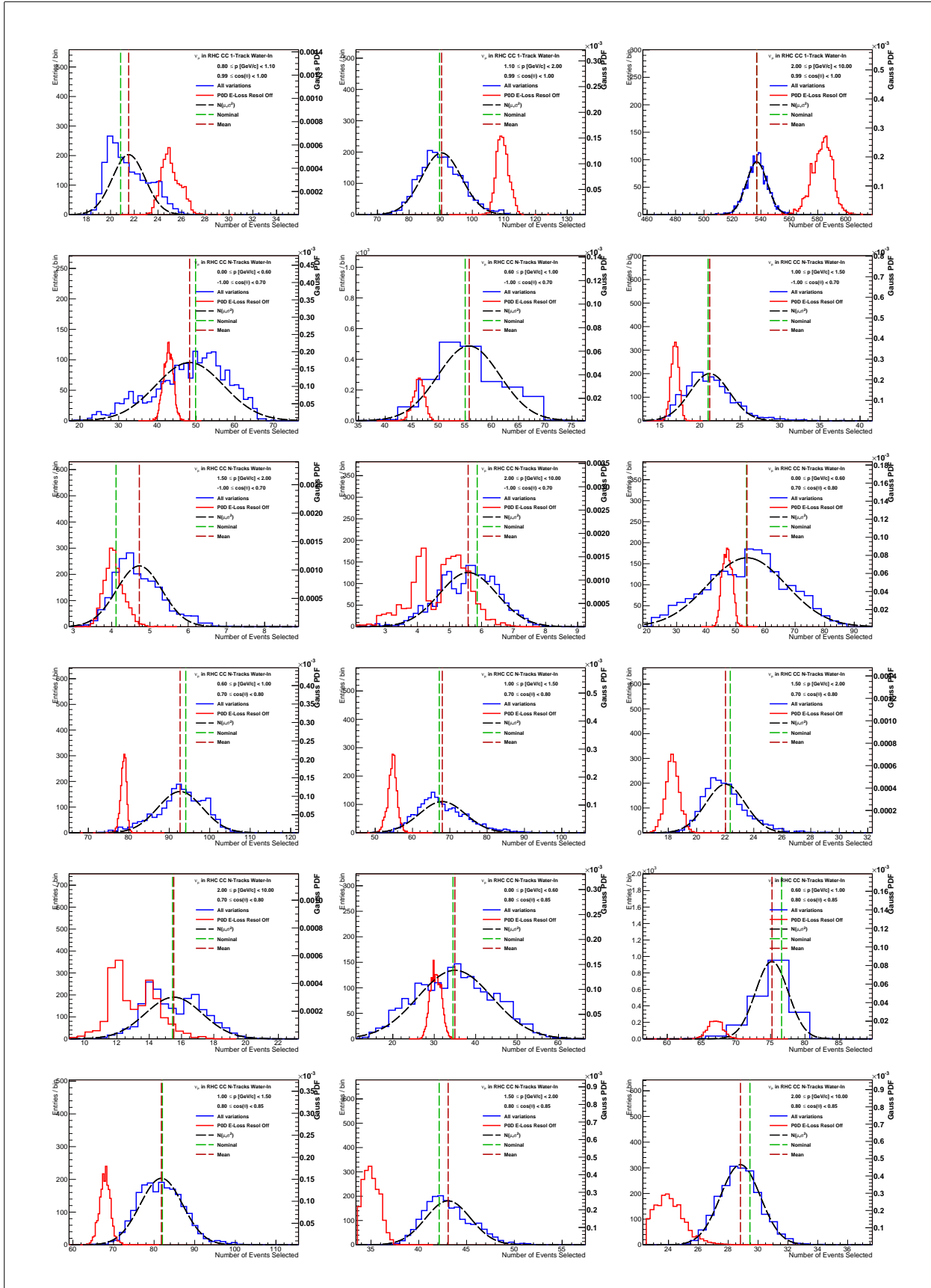


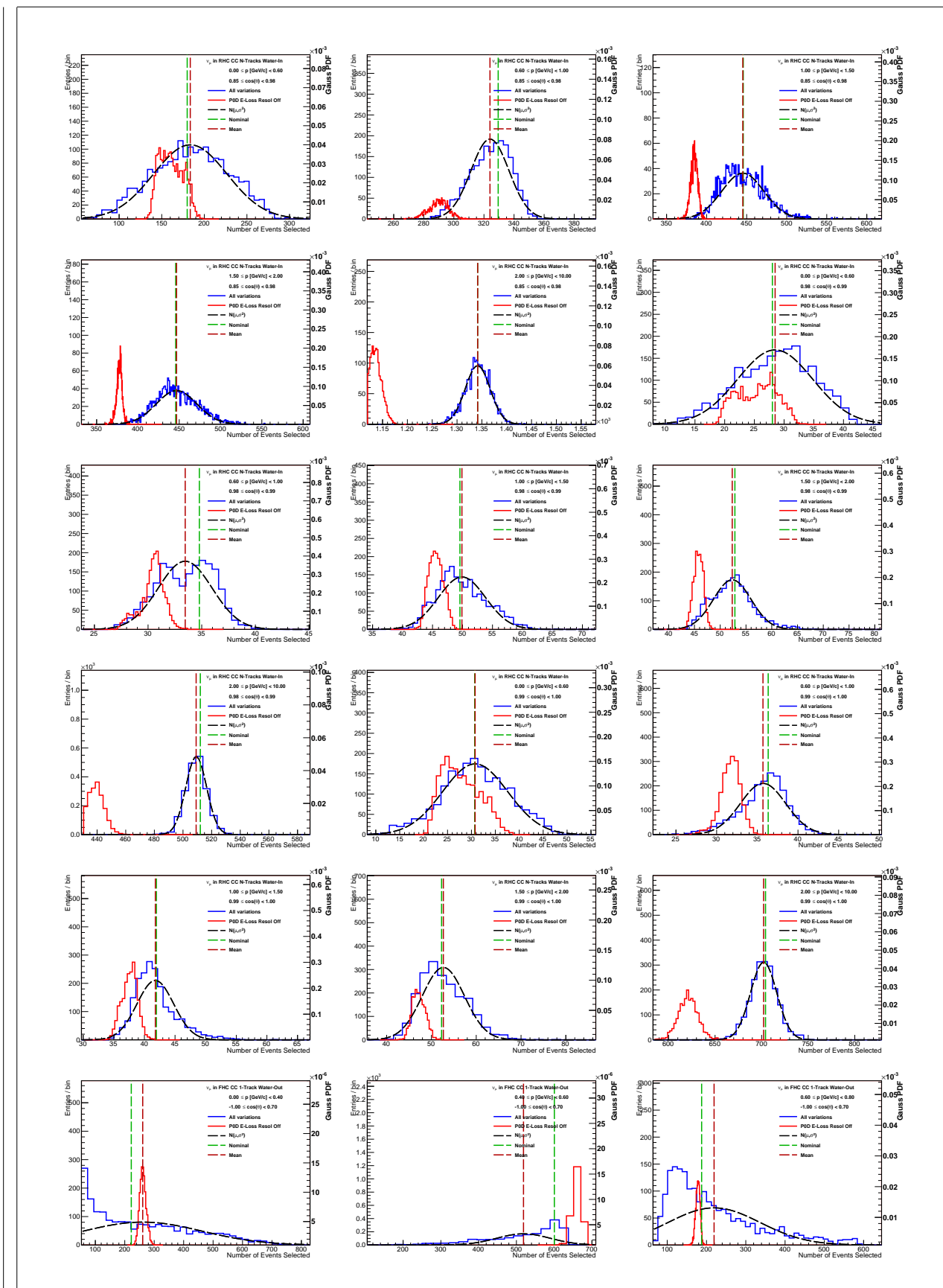


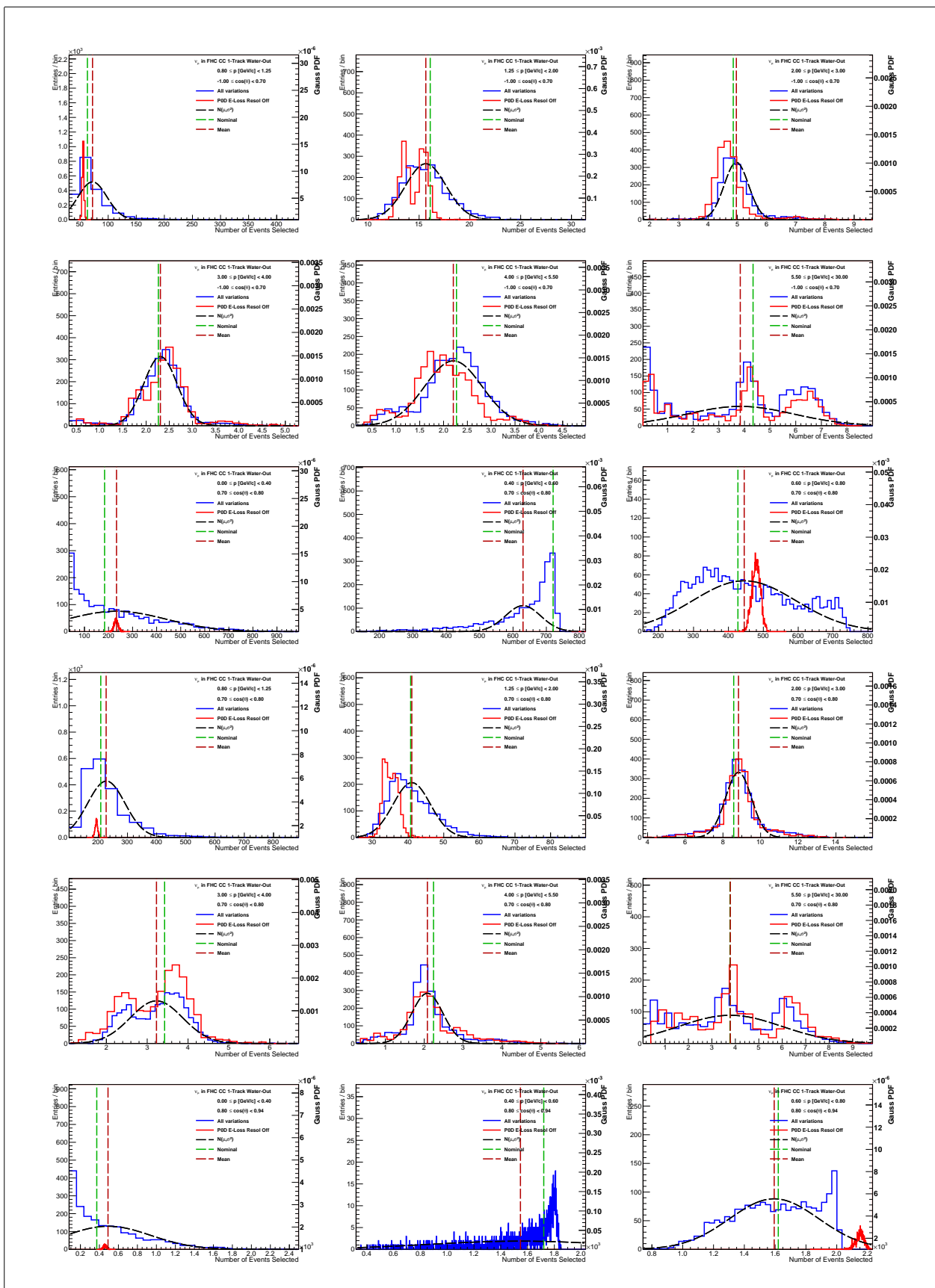


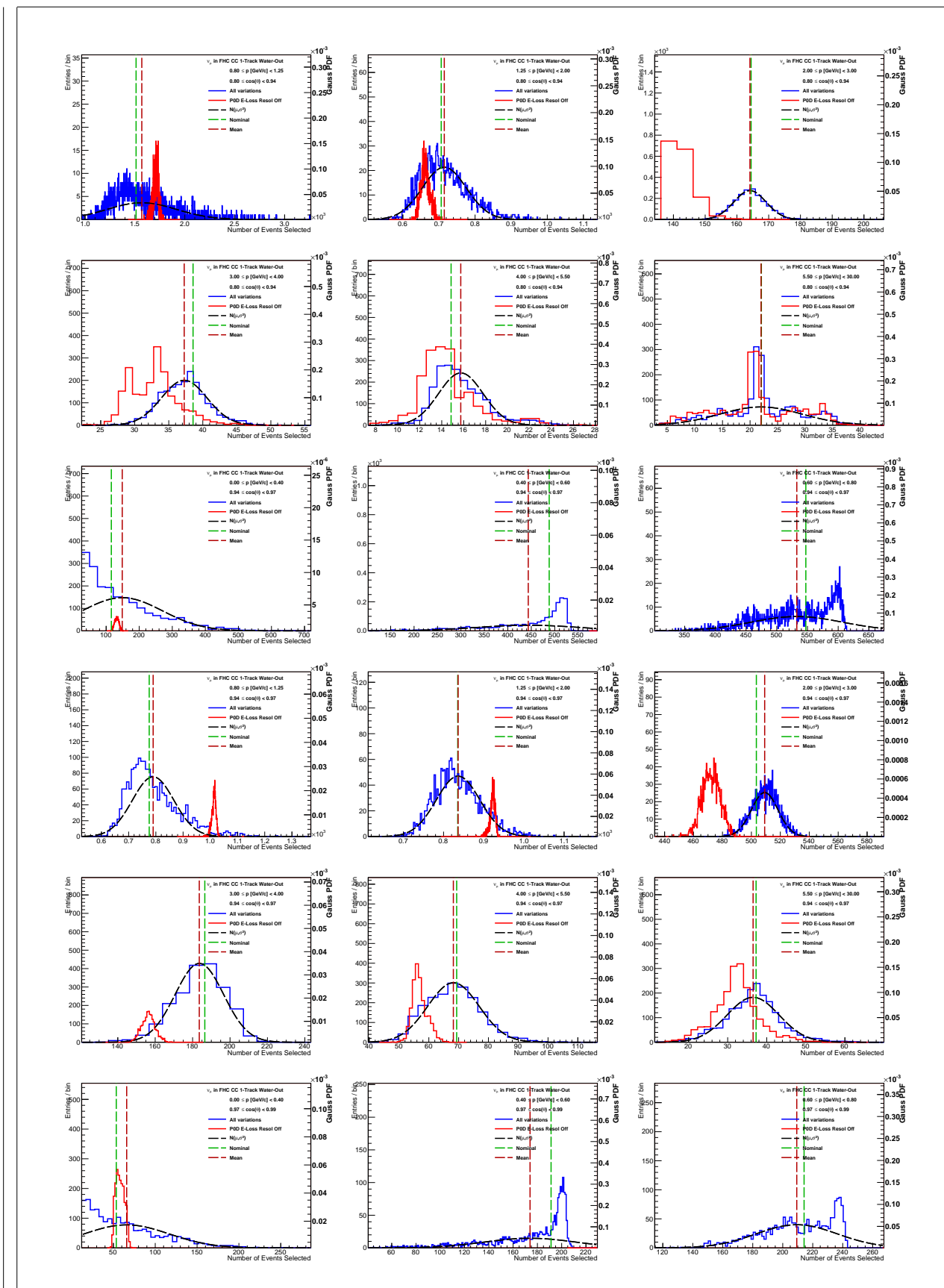


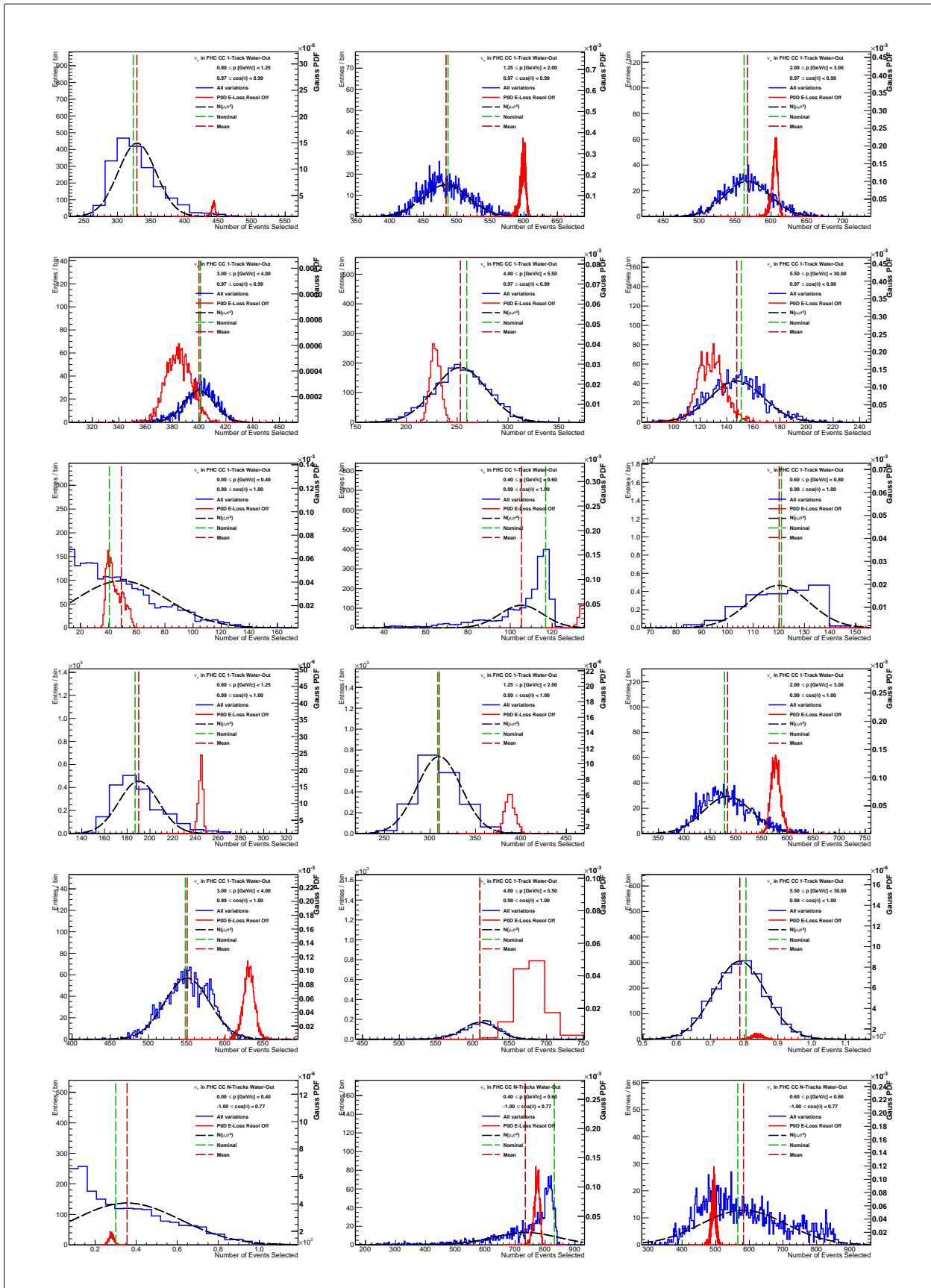


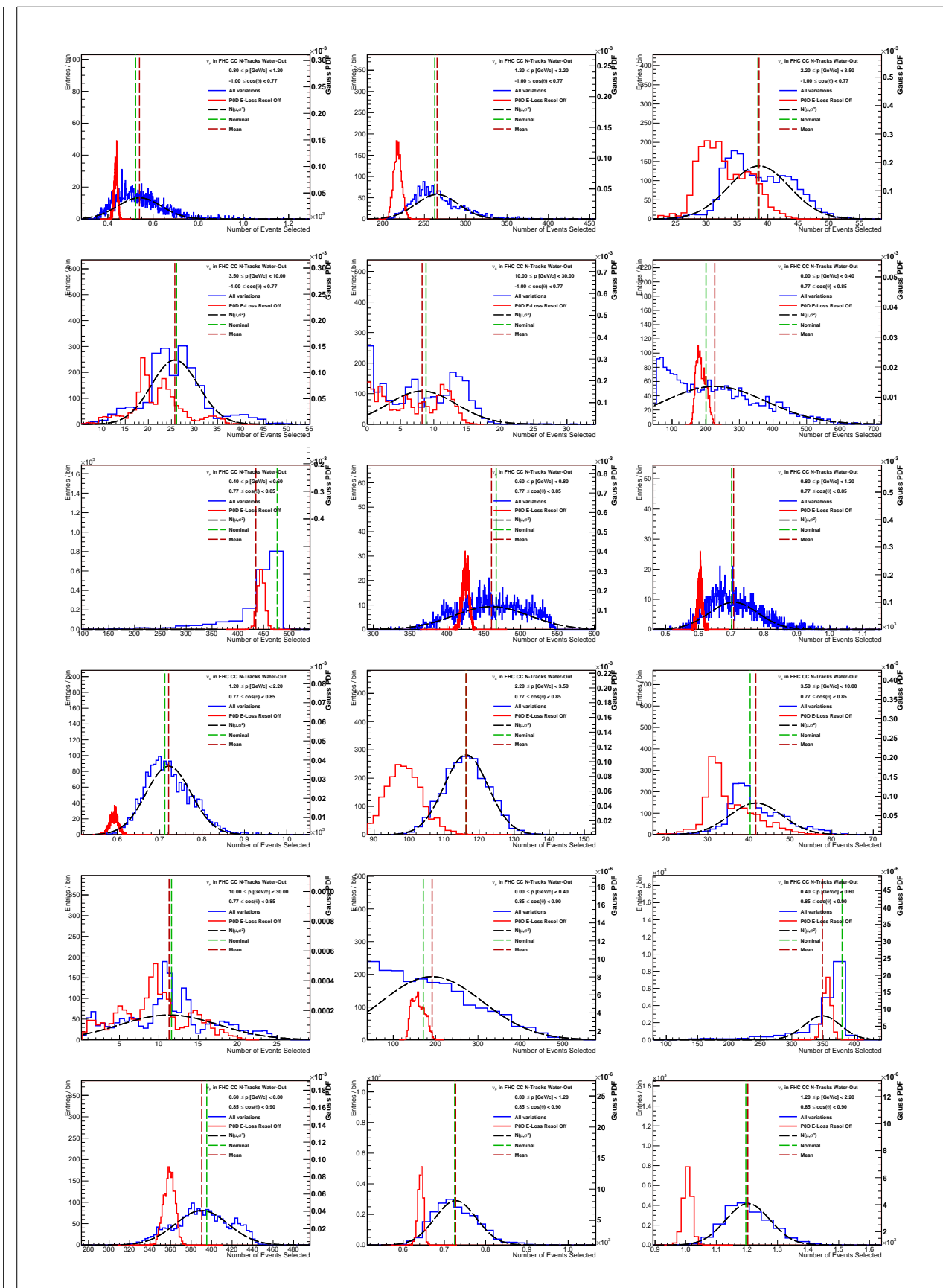


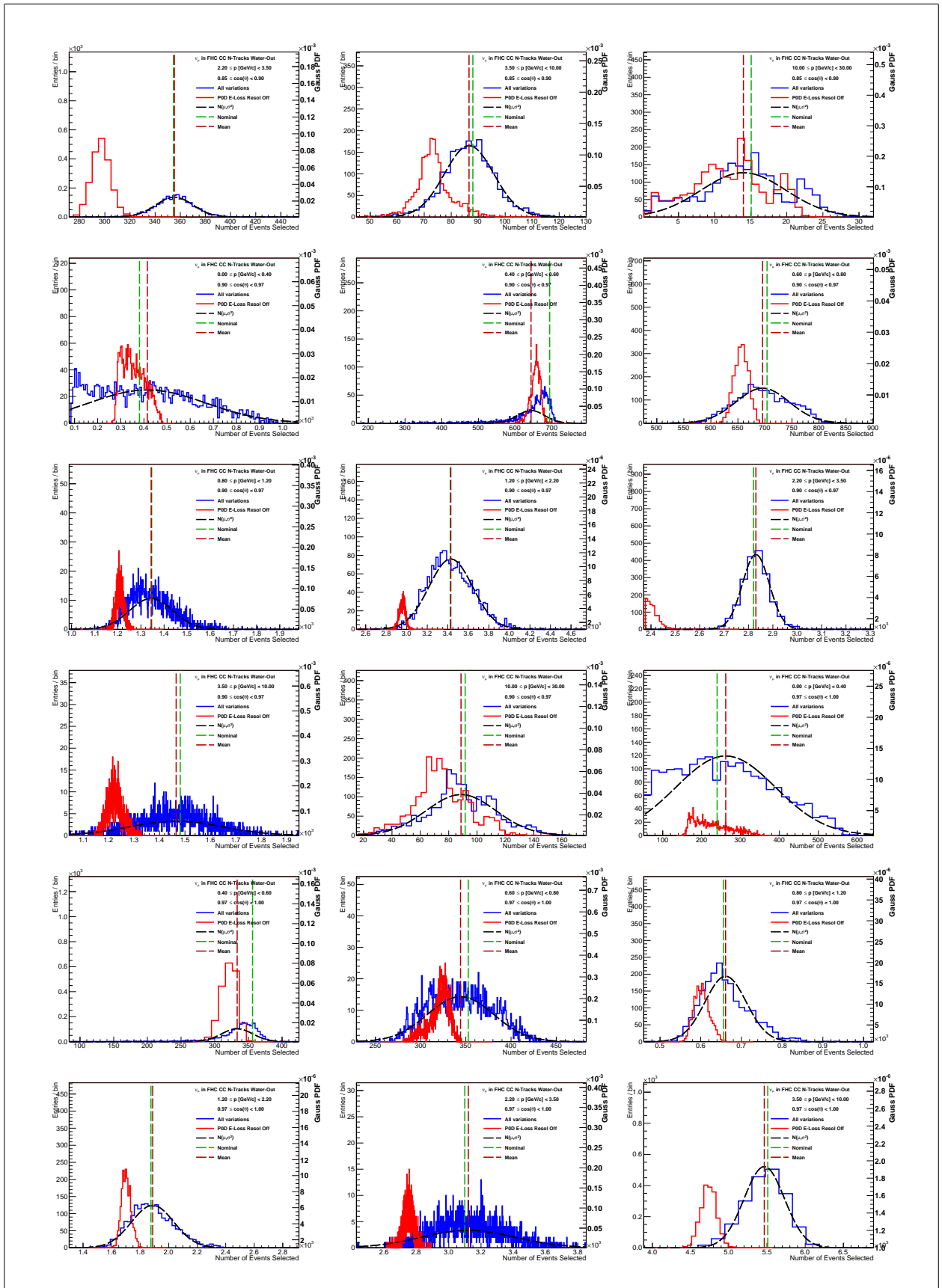


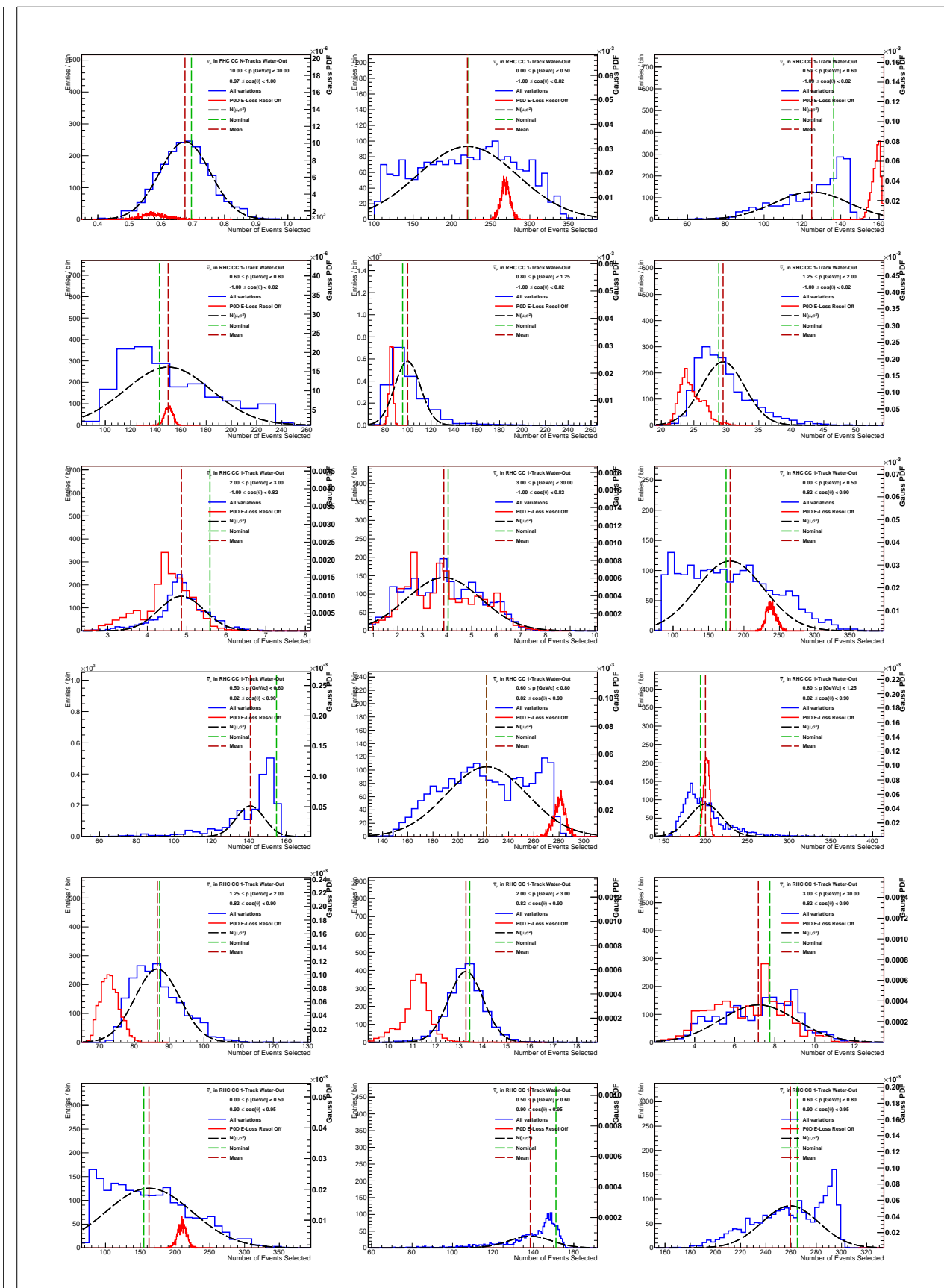


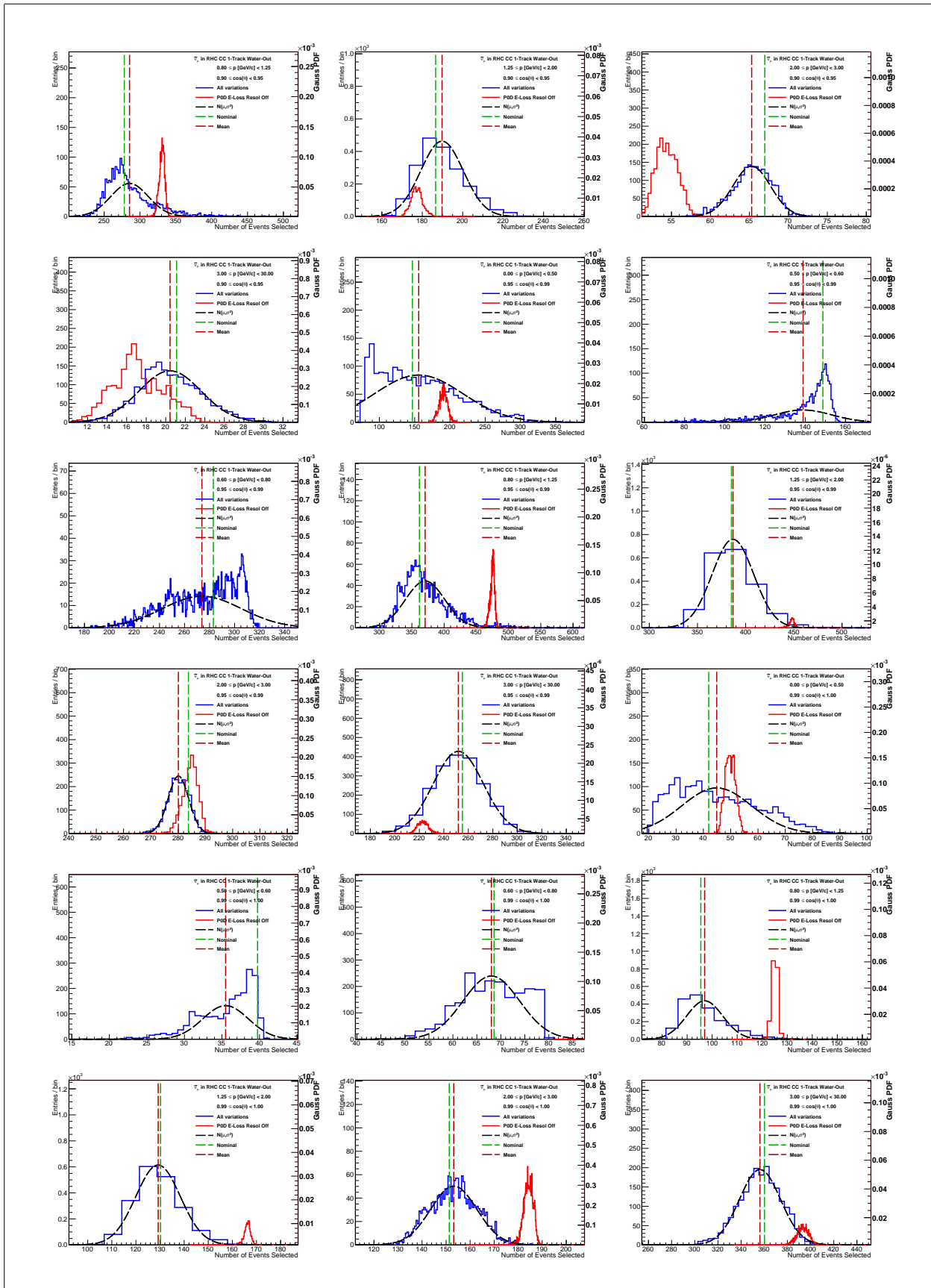


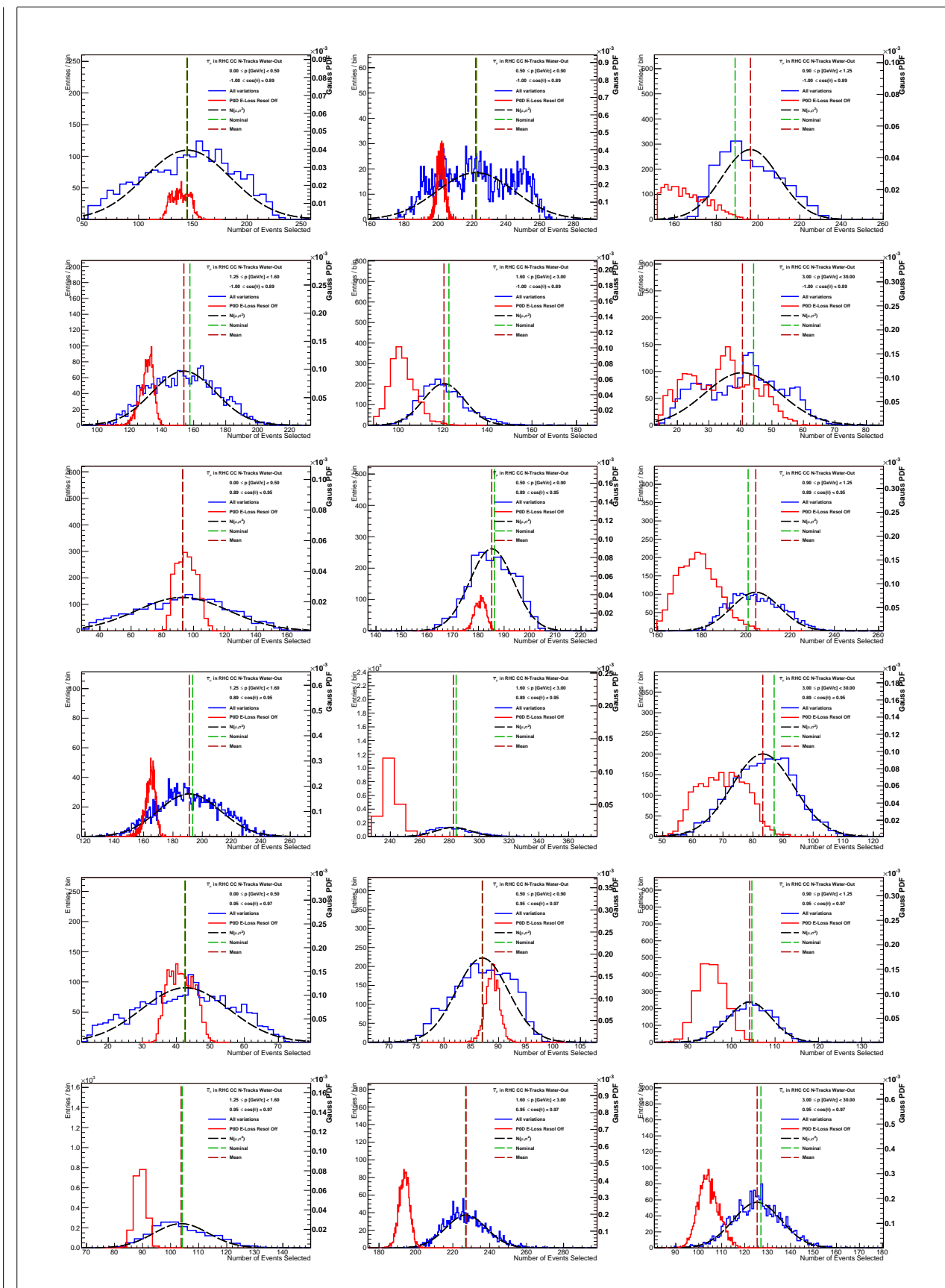


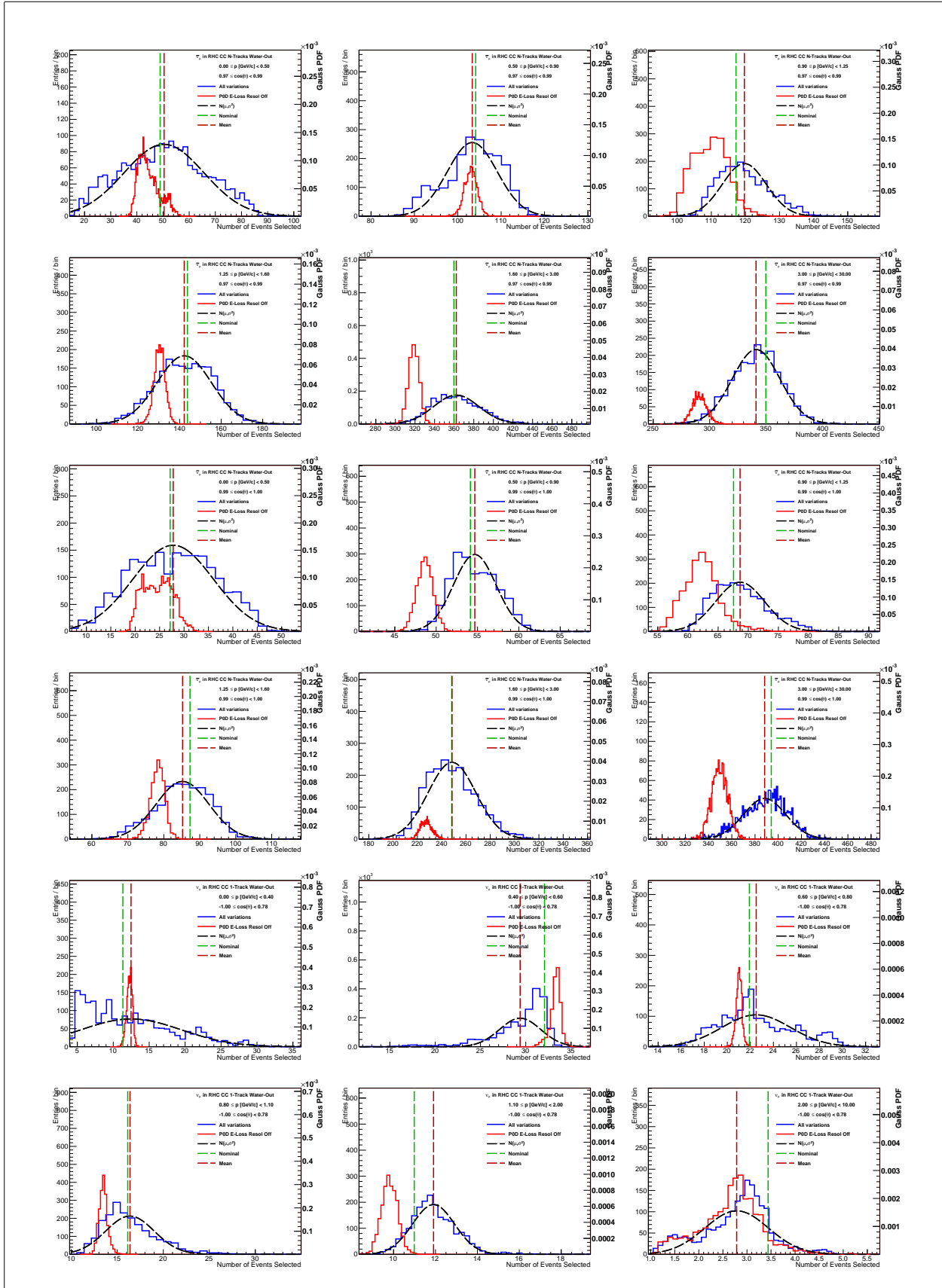


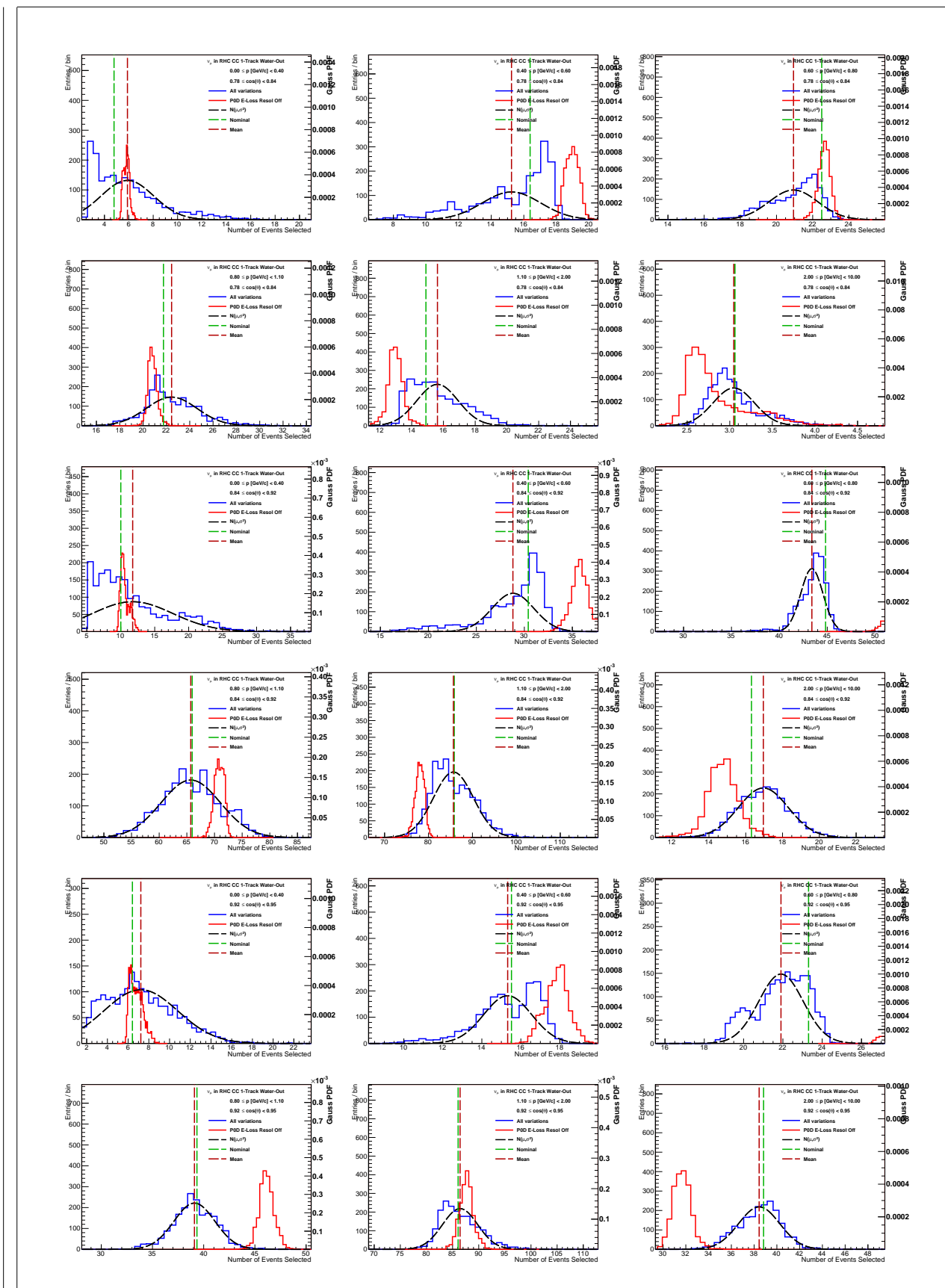


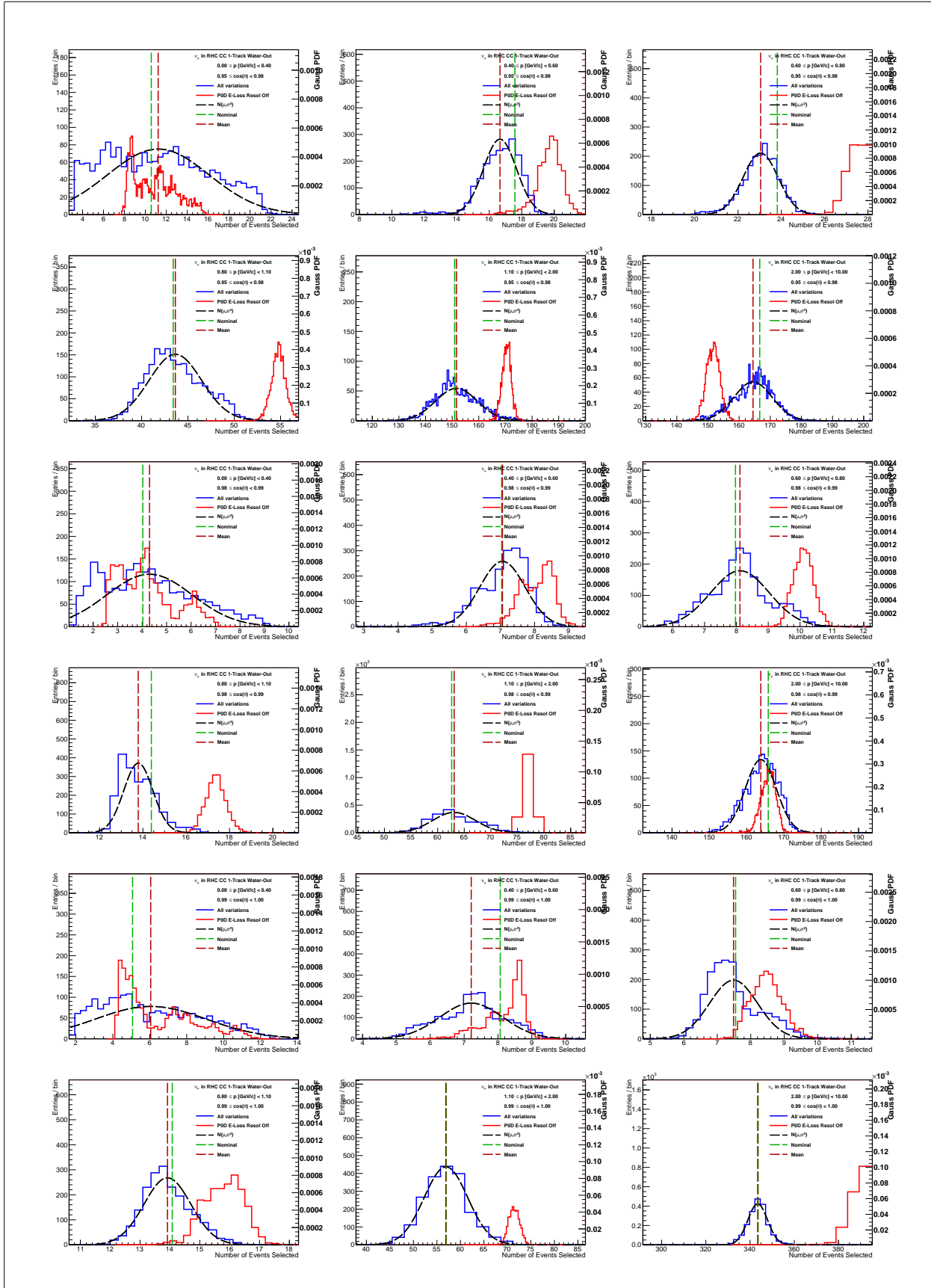


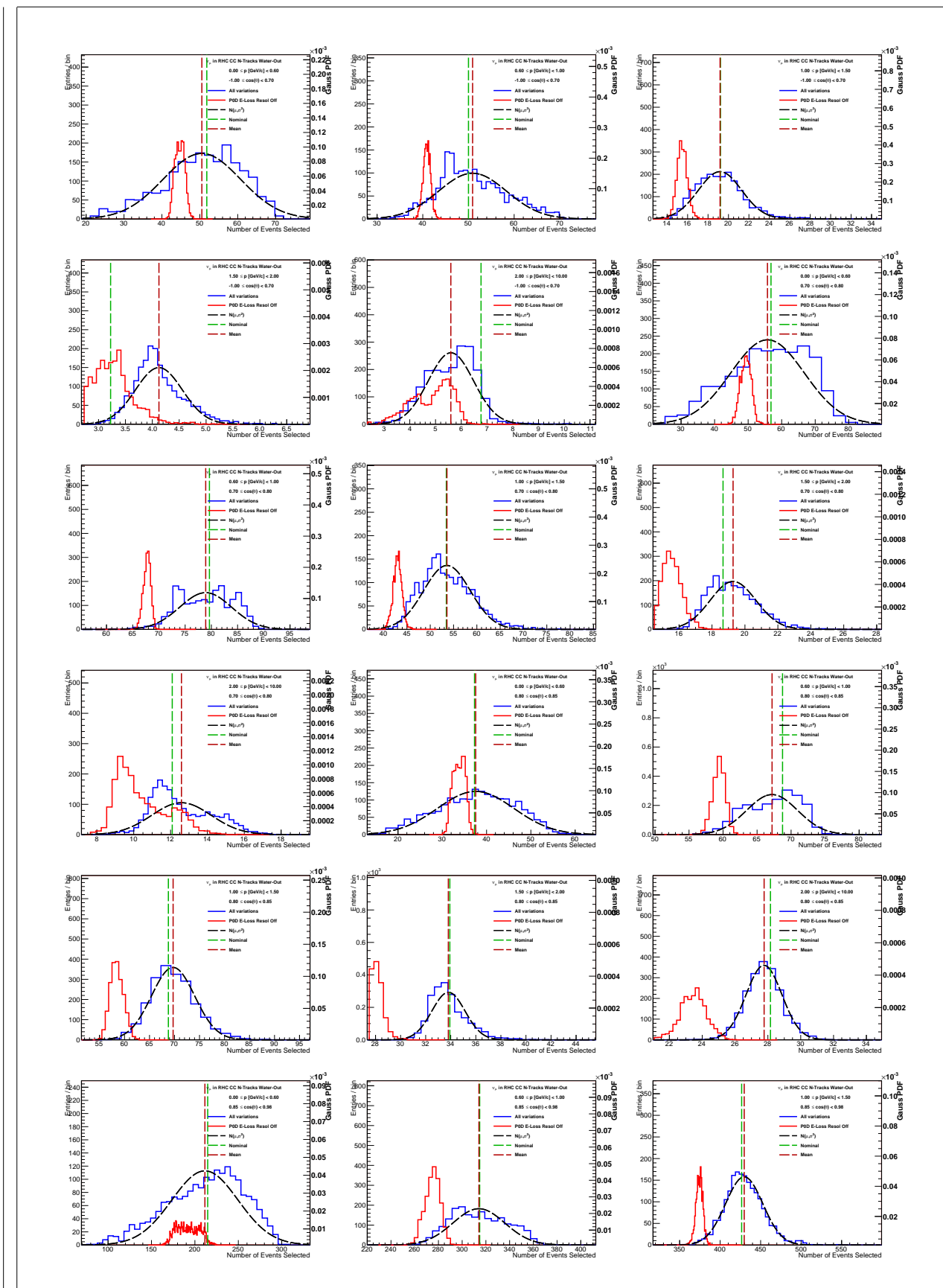


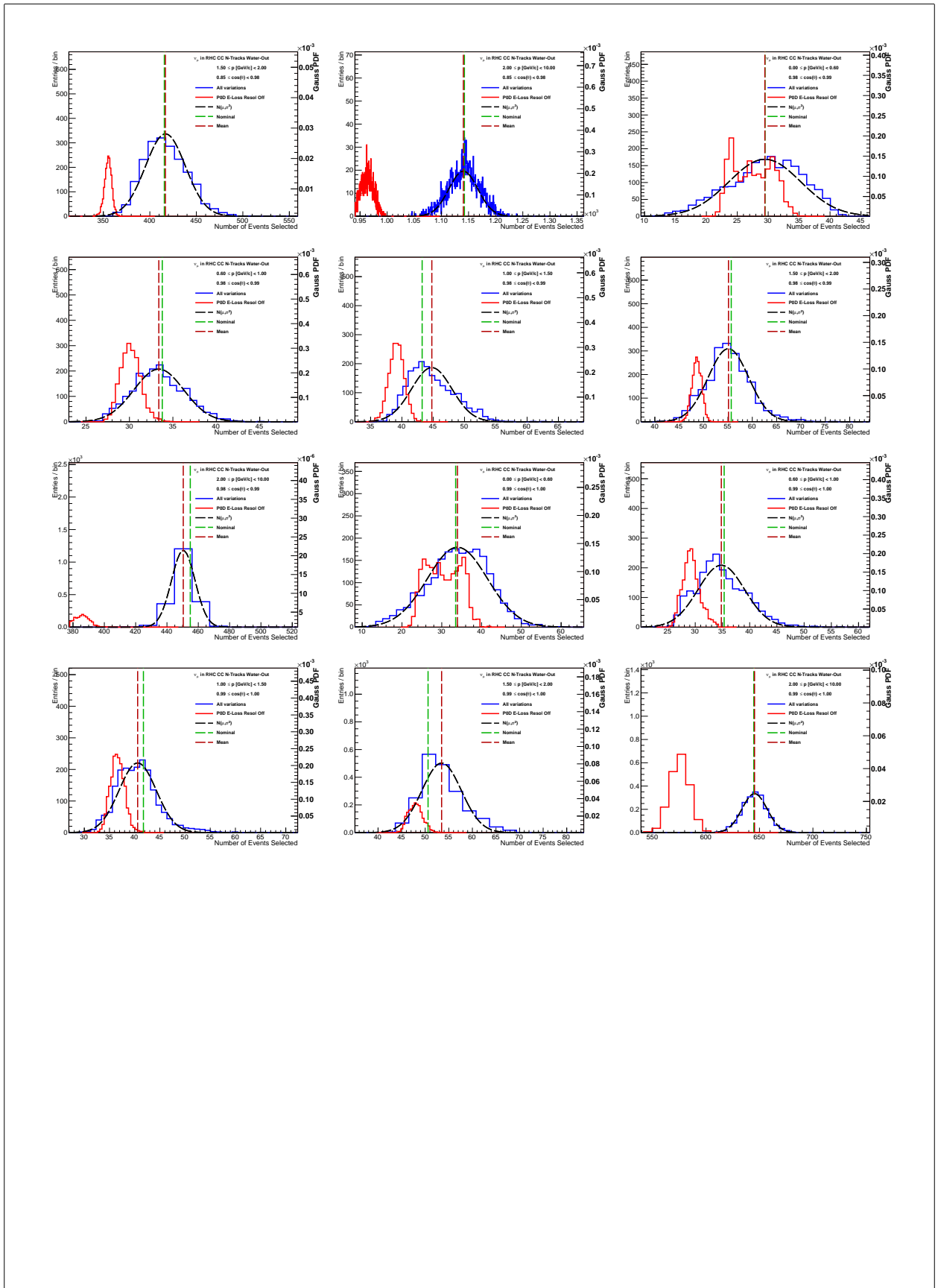












---

---

## Appendix B

### Cross Section Parameters Variations

This appendix is a tabulation of variations of the cross section parameters and their uncorrelated affect on the analysis samples. Note that the “nominal” column refers to all weighted events in the sample. When a “ $\pm 1\sigma$ ” variation is applied, the corresponding fractional change is reported.

Parameter	$1\sigma$ value	Sample	$-1\sigma$ (%)	nominal	$+1\sigma$ (%)
<b>562 : FSI Low energy INEL</b>	<b>0.41</b>	$\nu_\mu$ 1-Trk Wtr	-0.9	27316.74	0.7
		$\nu_\mu$ N-Trks	0.7	30904.32	-0.5
		$\bar{\nu}_\mu$ RHC 1-Trk	-0.5	8414.09	0.4
		$\bar{\nu}_\mu$ RHC N-Trks	1.0	4724.34	-0.7
		$\nu_\mu$ RHC 1-Trk	-1.2	3022.10	0.9
		$\nu_\mu$ RHC N-Trks	0.5	4928.38	-0.4
		$\nu_\mu$ 1-Trk Air	-0.9	23605.76	0.7
		$\nu_\mu$ N-Trks	0.5	32304.13	-0.4
		$\bar{\nu}_\mu$ RHC 1-Trk	-0.6	6767.65	0.5
		$\bar{\nu}_\mu$ RHC N-Trks	0.8	4544.65	-0.6
		$\nu_\mu$ RHC 1-Trk	-1.5	2067.37	1.4
		$\nu_\mu$ RHC N-Trks	0.6	4568.13	-0.7
<b>563 : FSI High energy INEL</b>	<b>0.34</b>	$\nu_\mu$ 1-Trk Wtr	-0.2	27316.74	0.2
		$\nu_\mu$ N-Trks	-0.1	30904.32	0.2
		$\bar{\nu}_\mu$ RHC 1-Trk	-0.1	8414.09	0.1
		$\bar{\nu}_\mu$ RHC N-Trks	-0.0	4724.34	0.1
		$\nu_\mu$ RHC 1-Trk	-0.4	3022.10	0.4
		$\nu_\mu$ RHC N-Trks	-0.1	4928.38	0.1
		$\nu_\mu$ 1-Trk Air	-0.2	23605.76	0.1
		$\nu_\mu$ N-Trks	-0.2	32304.13	0.2
		$\bar{\nu}_\mu$ RHC 1-Trk	-0.1	6767.65	0.1
		$\bar{\nu}_\mu$ RHC N-Trks	-0.1	4544.65	0.1
		$\nu_\mu$ RHC 1-Trk	-0.2	2067.37	0.2
		$\nu_\mu$ RHC N-Trks	-0.1	4568.13	0.2

**Table B.1:** Event rate broken by sample for one  $\sigma$  variation of each parameter.

Parameter	$1\sigma$ value	Sample	$-1\sigma$ (%)	nominal	$+1\sigma$ (%)
564 : FSI PROD	0.50	$\nu_\mu$ 1-Trk Wtr	-0.1	27316.74	0.1
		$\nu_\mu$ N-Trks	-0.0	30904.32	0.1
		$\bar{\nu}_\mu$ RHC 1-Trk	-0.0	8414.09	0.0
		$\bar{\nu}_\mu$ RHC N-Trks	0.1	4724.34	-0.0
		$\nu_\mu$ RHC 1-Trk	-0.1	3022.10	0.1
		$\nu_\mu$ RHC N-Trks	-0.1	4928.38	0.1
		$\nu_\mu$ 1-Trk Air	-0.0	23605.76	0.1
		$\nu_\mu$ N-Trks	-0.1	32304.13	0.1
		$\bar{\nu}_\mu$ RHC 1-Trk	-0.0	6767.65	0.0
		$\bar{\nu}_\mu$ RHC N-Trks	0.2	4544.65	-0.1
565 : FSI ABS	0.41	$\nu_\mu$ RHC 1-Trk	-0.1	2067.37	0.1
		$\nu_\mu$ RHC N-Trks	-0.1	4568.13	0.1
		$\nu_\mu$ 1-Trk Wtr	-0.7	27316.74	0.5
		$\nu_\mu$ N-Trks	0.6	30904.32	-0.5
		$\bar{\nu}_\mu$ RHC 1-Trk	-0.6	8414.09	0.5
		$\bar{\nu}_\mu$ RHC N-Trks	1.0	4724.34	-0.8
		$\nu_\mu$ RHC 1-Trk	-1.0	3022.10	0.8
		$\nu_\mu$ RHC N-Trks	0.5	4928.38	-0.4
		$\nu_\mu$ 1-Trk Air	-0.7	23605.76	0.6
		$\nu_\mu$ N-Trks	0.6	32304.13	-0.4
<b>Table B.1:</b> Event rate broken by sample for one $\sigma$ variation of each parameter.					

Parameter	$1\sigma$ value	Sample	$-1\sigma$ (%)	nominal	$+1\sigma$ (%)
<b>566 : FSI Low energy CEX</b>	<b>0.57</b>	$\nu_\mu$ 1-Trk Wtr	0.3	27316.74	-0.2
		$\nu_\mu$ N-Trks	-0.3	30904.32	0.2
		$\bar{\nu}_\mu$ RHC 1-Trk	0.2	8414.09	-0.1
		$\bar{\nu}_\mu$ RHC N-Trks	-0.2	4724.34	0.2
		$\nu_\mu$ RHC 1-Trk	0.4	3022.10	-0.3
		$\nu_\mu$ RHC N-Trks	-0.3	4928.38	0.2
		$\nu_\mu$ 1-Trk Air	0.3	23605.76	-0.2
		$\nu_\mu$ N-Trks	-0.3	32304.13	0.2
		$\bar{\nu}_\mu$ RHC 1-Trk	0.2	6767.65	-0.1
		$\bar{\nu}_\mu$ RHC N-Trks	-0.3	4544.65	0.3
		$\nu_\mu$ RHC 1-Trk	0.2	2067.37	-0.2
		$\nu_\mu$ RHC N-Trks	-0.1	4568.13	0.1
<b>567 : FSI High energy CEX</b>	<b>0.28</b>	$\nu_\mu$ 1-Trk Wtr	-0.0	27316.74	0.0
		$\nu_\mu$ N-Trks	-0.0	30904.32	0.0
		$\bar{\nu}_\mu$ RHC 1-Trk	-0.0	8414.09	0.0
		$\bar{\nu}_\mu$ RHC N-Trks	0.0	4724.34	-0.0
		$\nu_\mu$ RHC 1-Trk	-0.1	3022.10	0.1
		$\nu_\mu$ RHC N-Trks	-0.0	4928.38	0.0
		$\nu_\mu$ 1-Trk Air	-0.0	23605.76	0.0
		$\nu_\mu$ N-Trks	-0.1	32304.13	0.1
		$\bar{\nu}_\mu$ RHC 1-Trk	-0.0	6767.65	0.0
		$\bar{\nu}_\mu$ RHC N-Trks	0.0	4544.65	-0.0
		$\nu_\mu$ RHC 1-Trk	-0.0	2067.37	0.0
		$\nu_\mu$ RHC N-Trks	-0.0	4568.13	0.0

**Table B.1:** Event rate broken by sample for one  $\sigma$  variation of each parameter.

Parameter	$1\sigma$ value	Sample	$-1\sigma$ (%)	nominal	$+1\sigma$ (%)
568 : $M_A^{QE}$	0.03	$\nu_\mu$ 1-Trk Wtr	-0.8	27316.74	0.8
		$\nu_\mu$ N-Trks	-0.4	30904.32	0.4
		$\bar{\nu}_\mu$ RHC 1-Trk	-0.7	8414.09	0.7
		$\bar{\nu}_\mu$ RHC N-Trks	-0.2	4724.34	0.3
		$\nu_\mu$ RHC 1-Trk	-0.9	3022.10	0.9
		$\nu_\mu$ RHC N-Trks	-0.4	4928.38	0.4
		$\nu_\mu$ 1-Trk Air	-0.8	23605.76	0.8
		$\nu_\mu$ N-Trks	-0.5	32304.13	0.5
		$\bar{\nu}_\mu$ RHC 1-Trk	-0.7	6767.65	0.7
		$\bar{\nu}_\mu$ RHC N-Trks	-0.2	4544.65	0.3
		$\nu_\mu$ RHC 1-Trk	-0.9	2067.37	0.9
		$\nu_\mu$ RHC N-Trks	-0.4	4568.13	0.4
569 : $p_F^C$	0.06	$\nu_\mu$ 1-Trk Wtr	0.8	27316.74	-0.7
		$\nu_\mu$ N-Trks	0.0	30904.32	-0.0
		$\bar{\nu}_\mu$ RHC 1-Trk	0.7	8414.09	-0.7
		$\bar{\nu}_\mu$ RHC N-Trks	0.0	4724.34	-0.0
		$\nu_\mu$ RHC 1-Trk	0.4	3022.10	-0.4
		$\nu_\mu$ RHC N-Trks	0.0	4928.38	-0.0
		$\nu_\mu$ 1-Trk Air	1.1	23605.76	-1.0
		$\nu_\mu$ N-Trks	0.0	32304.13	-0.0
		$\bar{\nu}_\mu$ RHC 1-Trk	1.2	6767.65	-1.1
		$\bar{\nu}_\mu$ RHC N-Trks	0.0	4544.65	-0.0
		$\nu_\mu$ RHC 1-Trk	0.7	2067.37	-0.7
		$\nu_\mu$ RHC N-Trks	0.0	4568.13	-0.0

**Table B.1:** Event rate broken by sample for one  $\sigma$  variation of each parameter.

Parameter	$1\sigma$ value	Sample	$-1\sigma$ (%)	nominal	$+1\sigma$ (%)
<b>570 : <math>p_F^O</math></b>	<b>0.06</b>	$\nu_\mu$ 1-Trk Wtr	0.4	27316.74	-0.4
		$\nu_\mu$ N-Trks	0.0	30904.32	-0.0
		$\bar{\nu}_\mu$ RHC 1-Trk	0.5	8414.09	-0.5
		$\bar{\nu}_\mu$ RHC N-Trks	0.0	4724.34	-0.0
		$\nu_\mu$ RHC 1-Trk	0.3	3022.10	-0.3
		$\nu_\mu$ RHC N-Trks	0.0	4928.38	-0.0
		$\nu_\mu$ 1-Trk Air	0.0	23605.76	-0.0
		$\nu_\mu$ N-Trks	0.0	32304.13	-0.0
		$\bar{\nu}_\mu$ RHC 1-Trk	0.0	6767.65	-0.0
		$\bar{\nu}_\mu$ RHC N-Trks	-0.0	4544.65	-0.0
		$\nu_\mu$ RHC 1-Trk	-0.0	2067.37	0.0
		$\nu_\mu$ RHC N-Trks	0.0	4568.13	-0.0
<b>571 : 2p2h <math>\nu</math> norm. on <math>^{12}\text{C}</math></b>	<b>1.00</b>	$\nu_\mu$ 1-Trk Wtr	-8.9	27316.74	8.9
		$\nu_\mu$ N-Trks	-3.0	30904.32	3.0
		$\bar{\nu}_\mu$ RHC 1-Trk	-0.1	8414.09	0.1
		$\bar{\nu}_\mu$ RHC N-Trks	-0.2	4724.34	0.2
		$\nu_\mu$ RHC 1-Trk	-9.0	3022.10	9.0
		$\nu_\mu$ RHC N-Trks	-2.6	4928.38	2.6
		$\nu_\mu$ 1-Trk Air	-8.1	23605.76	8.1
		$\nu_\mu$ N-Trks	-3.3	32304.13	3.3
		$\bar{\nu}_\mu$ RHC 1-Trk	-0.1	6767.65	0.1
		$\bar{\nu}_\mu$ RHC N-Trks	-0.2	4544.65	0.2
		$\nu_\mu$ RHC 1-Trk	-8.6	2067.37	8.6
		$\nu_\mu$ RHC N-Trks	-2.8	4568.13	2.8

**Table B.1:** Event rate broken by sample for one  $\sigma$  variation of each parameter.

Parameter	$1\sigma$ value	Sample	$-1\sigma$ (%)	nominal	$+1\sigma$ (%)
<b>572 : 2p2h <math>\bar{\nu}</math> norm. on <math>^{12}\text{C}</math></b>	<b>1.00</b>	$\nu_\mu$ 1-Trk Wtr	-0.0	27316.74	0.0
		$\nu_\mu$ N-Trks	-0.0	30904.32	0.0
		$\bar{\nu}_\mu$ RHC 1-Trk	-9.3	8414.09	9.3
		$\bar{\nu}_\mu$ RHC N-Trks	-2.1	4724.34	2.1
		$\nu_\mu$ RHC 1-Trk	-0.2	3022.10	0.2
		$\nu_\mu$ RHC N-Trks	-0.0	4928.38	0.0
		$\nu_\mu$ 1-Trk Air	-0.0	23605.76	0.0
		$\nu_\mu$ N-Trks	-0.0	32304.13	0.0
		$\bar{\nu}_\mu$ RHC 1-Trk	-8.9	6767.65	8.9
		$\bar{\nu}_\mu$ RHC N-Trks	-2.2	4544.65	2.2
		$\nu_\mu$ RHC 1-Trk	-0.3	2067.37	0.3
		$\nu_\mu$ RHC N-Trks	-0.0	4568.13	0.0
<b>573 : 2p2h <math>^{12}\text{C}/^{16}\text{O}</math> norm.</b>	<b>0.20</b>	$\nu_\mu$ 1-Trk Wtr	-0.6	27316.74	0.6
		$\nu_\mu$ N-Trks	-0.2	30904.32	0.2
		$\bar{\nu}_\mu$ RHC 1-Trk	-0.8	8414.09	0.8
		$\bar{\nu}_\mu$ RHC N-Trks	-0.2	4724.34	0.2
		$\nu_\mu$ RHC 1-Trk	-0.8	3022.10	0.8
		$\nu_\mu$ RHC N-Trks	-0.2	4928.38	0.2
		$\nu_\mu$ 1-Trk Air	-0.0	23605.76	0.0
		$\nu_\mu$ N-Trks	-0.0	32304.13	0.0
		$\bar{\nu}_\mu$ RHC 1-Trk	-0.0	6767.65	0.0
		$\bar{\nu}_\mu$ RHC N-Trks	-0.0	4544.65	0.0
		$\nu_\mu$ RHC 1-Trk	-0.0	2067.37	0.0
		$\nu_\mu$ RHC N-Trks	-0.0	4568.13	0.0

**Table B.1:** Event rate broken by sample for one  $\sigma$  variation of each parameter.

Parameter	$1\sigma$ value	Sample	$-1\sigma$ (%)	nominal	$+1\sigma$ (%)
<b>574 : 2p2h <math>^{12}\text{C}</math> shape location</b>	<b>2.00</b>	$\nu_\mu$ 1-Trk Wtr	3.8	27316.74	0.0
		$\nu_\mu$ N-Trks	-1.1	30904.32	0.0
		$\bar{\nu}_\mu$ RHC 1-Trk	0.2	8414.09	0.0
		$\bar{\nu}_\mu$ RHC N-Trks	-0.8	4724.34	0.0
		$\nu_\mu$ RHC 1-Trk	4.3	3022.10	0.0
		$\nu_\mu$ RHC N-Trks	-0.8	4928.38	0.0
		$\nu_\mu$ 1-Trk Air	5.7	23605.76	0.0
		$\nu_\mu$ N-Trks	-1.5	32304.13	0.0
		$\bar{\nu}_\mu$ RHC 1-Trk	0.2	6767.65	0.0
		$\bar{\nu}_\mu$ RHC N-Trks	-1.1	4544.65	0.0
		$\nu_\mu$ RHC 1-Trk	8.1	2067.37	0.0
		$\nu_\mu$ RHC N-Trks	-1.4	4568.13	0.0
<b>575 : 2p2h <math>^{16}\text{O}</math> shape location</b>	<b>2.00</b>	$\nu_\mu$ 1-Trk Wtr	2.1	27316.74	0.0
		$\nu_\mu$ N-Trks	-0.5	30904.32	0.0
		$\bar{\nu}_\mu$ RHC 1-Trk	0.1	8414.09	0.0
		$\bar{\nu}_\mu$ RHC N-Trks	-0.5	4724.34	0.0
		$\nu_\mu$ RHC 1-Trk	3.2	3022.10	0.0
		$\nu_\mu$ RHC N-Trks	-0.6	4928.38	0.0
		$\nu_\mu$ 1-Trk Air	0.0	23605.76	0.0
		$\nu_\mu$ N-Trks	-0.0	32304.13	0.0
		$\bar{\nu}_\mu$ RHC 1-Trk	0.0	6767.65	0.0
		$\bar{\nu}_\mu$ RHC N-Trks	0.0	4544.65	0.0
		$\nu_\mu$ RHC 1-Trk	0.0	2067.37	0.0
		$\nu_\mu$ RHC N-Trks	-0.0	4568.13	0.0

**Table B.1:** Event rate broken by sample for one  $\sigma$  variation of each parameter.

Parameter	$1\sigma$ value	Sample	$-1\sigma$ (%)	nominal	$+1\sigma$ (%)
<b>576 : BeRPA A scale</b>	<b>0.12</b>	$\nu_\mu$ 1-Trk Wtr	-5.1	27316.74	5.1
		$\nu_\mu$ N-Trks	-0.3	30904.32	0.3
		$\bar{\nu}_\mu$ RHC 1-Trk	-4.7	8414.09	4.7
		$\bar{\nu}_\mu$ RHC N-Trks	-0.2	4724.34	0.2
		$\nu_\mu$ RHC 1-Trk	-3.5	3022.10	3.5
		$\nu_\mu$ RHC N-Trks	-0.1	4928.38	0.1
		$\nu_\mu$ 1-Trk Air	-5.1	23605.76	5.1
		$\nu_\mu$ N-Trks	-0.3	32304.13	0.3
		$\bar{\nu}_\mu$ RHC 1-Trk	-4.6	6767.65	4.6
		$\bar{\nu}_\mu$ RHC N-Trks	-0.1	4544.65	0.1
		$\nu_\mu$ RHC 1-Trk	-3.7	2067.37	3.7
		$\nu_\mu$ RHC N-Trks	-0.2	4568.13	0.2
<b>577 : BeRPA B scale</b>	<b>0.21</b>	$\nu_\mu$ 1-Trk Wtr	-3.4	27316.74	3.4
		$\nu_\mu$ N-Trks	-0.6	30904.32	0.6
		$\bar{\nu}_\mu$ RHC 1-Trk	-2.6	8414.09	2.6
		$\bar{\nu}_\mu$ RHC N-Trks	-0.2	4724.34	0.2
		$\nu_\mu$ RHC 1-Trk	-3.1	3022.10	3.1
		$\nu_\mu$ RHC N-Trks	-0.4	4928.38	0.4
		$\nu_\mu$ 1-Trk Air	-3.3	23605.76	3.3
		$\nu_\mu$ N-Trks	-0.6	32304.13	0.6
		$\bar{\nu}_\mu$ RHC 1-Trk	-2.5	6767.65	2.5
		$\bar{\nu}_\mu$ RHC N-Trks	-0.2	4544.65	0.2
		$\nu_\mu$ RHC 1-Trk	-3.0	2067.37	3.0
		$\nu_\mu$ RHC N-Trks	-0.5	4568.13	0.5

**Table B.1:** Event rate broken by sample for one  $\sigma$  variation of each parameter.

Parameter	$1\sigma$ value	Sample	$-1\sigma$ (%)	nominal	$+1\sigma$ (%)
<b>578 : BeRPA D scale</b>	<b>0.17</b>	$\nu_\mu$ 1-Trk Wtr	-1.3	27316.74	1.3
		$\nu_\mu$ N-Trks	-1.0	30904.32	1.0
		$\bar{\nu}_\mu$ RHC 1-Trk	-1.0	8414.09	1.0
		$\bar{\nu}_\mu$ RHC N-Trks	-0.5	4724.34	0.5
		$\nu_\mu$ RHC 1-Trk	-1.7	3022.10	1.7
		$\nu_\mu$ RHC N-Trks	-0.9	4928.38	0.9
		$\nu_\mu$ 1-Trk Air	-1.1	23605.76	1.1
		$\nu_\mu$ N-Trks	-0.9	32304.13	0.9
		$\bar{\nu}_\mu$ RHC 1-Trk	-0.9	6767.65	0.9
		$\bar{\nu}_\mu$ RHC N-Trks	-0.4	4544.65	0.4
		$\nu_\mu$ RHC 1-Trk	-1.4	2067.37	1.4
		$\nu_\mu$ RHC N-Trks	-0.9	4568.13	0.9
<b>579 : BeRPA E scale</b>	<b>0.35</b>	$\nu_\mu$ 1-Trk Wtr	-0.1	27316.74	0.1
		$\nu_\mu$ N-Trks	-0.0	30904.32	0.0
		$\bar{\nu}_\mu$ RHC 1-Trk	-0.1	8414.09	0.1
		$\bar{\nu}_\mu$ RHC N-Trks	0.0	4724.34	-0.0
		$\nu_\mu$ RHC 1-Trk	-0.1	3022.10	0.1
		$\nu_\mu$ RHC N-Trks	-0.0	4928.38	0.0
		$\nu_\mu$ 1-Trk Air	-0.1	23605.76	0.1
		$\nu_\mu$ N-Trks	-0.0	32304.13	0.0
		$\bar{\nu}_\mu$ RHC 1-Trk	-0.1	6767.65	0.1
		$\bar{\nu}_\mu$ RHC N-Trks	0.0	4544.65	0.0
		$\nu_\mu$ RHC 1-Trk	-0.1	2067.37	0.1
		$\nu_\mu$ RHC N-Trks	-0.0	4568.13	0.0

**Table B.1:** Event rate broken by sample for one  $\sigma$  variation of each parameter.

Parameter	$1\sigma$ value	Sample	$-1\sigma$ (%)	nominal	$+1\sigma$ (%)
<b>580 : BeRPA_U</b>	<b>scale*</b> <b>0.10</b>	$\nu_\mu$ 1-Trk Wtr	0.7	27316.74	-0.7
		$\nu_\mu$ N-Trks	0.1	30904.32	-0.1
		$\bar{\nu}_\mu$ RHC 1-Trk	0.6	8414.09	-0.5
		$\bar{\nu}_\mu$ RHC N-Trks	0.0	4724.34	-0.0
		$\nu_\mu$ RHC 1-Trk	0.7	3022.10	-0.6
		$\nu_\mu$ RHC N-Trks	0.1	4928.38	-0.1
		$\nu_\mu$ 1-Trk Air	0.7	23605.76	-0.6
		$\nu_\mu$ N-Trks	0.1	32304.13	-0.1
		$\bar{\nu}_\mu$ RHC 1-Trk	0.5	6767.65	-0.5
		$\bar{\nu}_\mu$ RHC N-Trks	0.0	4544.65	-0.0
		$\nu_\mu$ RHC 1-Trk	0.7	2067.37	-0.6
		$\nu_\mu$ RHC N-Trks	0.1	4568.13	-0.1
<b>581 : <math>C_A^5</math></b>	<b>0.15</b>	$\nu_\mu$ 1-Trk Wtr	-3.4	27316.74	3.9
		$\nu_\mu$ N-Trks	-4.4	30904.32	5.0
		$\bar{\nu}_\mu$ RHC 1-Trk	-2.7	8414.09	3.4
		$\bar{\nu}_\mu$ RHC N-Trks	-4.7	4724.34	5.8
		$\nu_\mu$ RHC 1-Trk	-4.5	3022.10	5.2
		$\nu_\mu$ RHC N-Trks	-4.1	4928.38	4.7
		$\nu_\mu$ 1-Trk Air	-2.9	23605.76	3.3
		$\nu_\mu$ N-Trks	-4.6	32304.13	5.2
		$\bar{\nu}_\mu$ RHC 1-Trk	-2.5	6767.65	3.1
		$\bar{\nu}_\mu$ RHC N-Trks	-4.9	4544.65	6.1
		$\nu_\mu$ RHC 1-Trk	-3.8	2067.37	4.4
		$\nu_\mu$ RHC N-Trks	-4.3	4568.13	5.0

**Table B.1:** Event rate broken by sample for one  $\sigma$  variation of each parameter.

Parameter	$1\sigma$ value	Sample	$-1\sigma$ (%)	nominal	$+1\sigma$ (%)
582 : $M_A^{\text{RES}}$	<b>0.16</b>	$\nu_\mu$ 1-Trk Wtr	-2.1	27316.74	1.9
		$\nu_\mu$ N-Trks	-4.8	30904.32	5.1
		$\bar{\nu}_\mu$ RHC 1-Trk	-1.6	8414.09	1.6
		$\bar{\nu}_\mu$ RHC N-Trks	-4.8	4724.34	5.8
		$\nu_\mu$ RHC 1-Trk	-3.1	3022.10	2.9
		$\nu_\mu$ RHC N-Trks	-4.8	4928.38	5.3
		$\nu_\mu$ 1-Trk Air	-1.7	23605.76	1.5
		$\nu_\mu$ N-Trks	-4.6	32304.13	4.9
		$\bar{\nu}_\mu$ RHC 1-Trk	-1.4	6767.65	1.5
		$\bar{\nu}_\mu$ RHC N-Trks	-4.8	4544.65	5.9
		$\nu_\mu$ RHC 1-Trk	-2.5	2067.37	2.3
		$\nu_\mu$ RHC N-Trks	-4.7	4568.13	5.2
583 : $I=^{1/2}$ bkg. norm.	<b>0.31</b>	$\nu_\mu$ 1-Trk Wtr	-1.1	27316.74	1.8
		$\nu_\mu$ N-Trks	-2.4	30904.32	3.7
		$\bar{\nu}_\mu$ RHC 1-Trk	-0.8	8414.09	1.3
		$\bar{\nu}_\mu$ RHC N-Trks	-3.1	4724.34	4.8
		$\nu_\mu$ RHC 1-Trk	-1.7	3022.10	2.5
		$\nu_\mu$ RHC N-Trks	-2.5	4928.38	3.8
		$\nu_\mu$ 1-Trk Air	-1.1	23605.76	1.6
		$\nu_\mu$ N-Trks	-2.4	32304.13	3.6
		$\bar{\nu}_\mu$ RHC 1-Trk	-0.7	6767.65	1.1
		$\bar{\nu}_\mu$ RHC N-Trks	-3.0	4544.65	4.5
		$\nu_\mu$ RHC 1-Trk	-1.6	2067.37	2.4
		$\nu_\mu$ RHC N-Trks	-2.4	4568.13	3.7

**Table B.1:** Event rate broken by sample for one  $\sigma$  variation of each parameter.

Parameter	$1\sigma$ value	Sample	$-1\sigma$ (%)	nominal	$+1\sigma$ (%)
584 : CC- $\nu_e/\nu_\mu^*$	0.03	$\nu_\mu$ 1-Trk Wtr	0.0	27316.74	0.0
		$\nu_\mu$ N-Trks	0.0	30904.32	0.0
		$\bar{\nu}_\mu$ RHC 1-Trk	0.0	8414.09	0.0
		$\bar{\nu}_\mu$ RHC N-Trks	0.0	4724.34	0.0
		$\nu_\mu$ RHC 1-Trk	0.0	3022.10	0.0
		$\nu_\mu$ RHC N-Trks	0.0	4928.38	0.0
		$\nu_\mu$ 1-Trk Air	0.0	23605.76	0.0
		$\nu_\mu$ N-Trks	0.0	32304.13	0.0
		$\bar{\nu}_\mu$ RHC 1-Trk	0.0	6767.65	0.0
		$\bar{\nu}_\mu$ RHC N-Trks	0.0	4544.65	0.0
585 : CC- $\bar{\nu}_e/\bar{\nu}_\mu^*$	0.03	$\nu_\mu$ RHC 1-Trk	0.0	2067.37	0.0
		$\nu_\mu$ RHC N-Trks	0.0	4568.13	0.0
		$\nu_\mu$ 1-Trk Wtr	0.0	27316.74	0.0
		$\nu_\mu$ N-Trks	0.0	30904.32	0.0
		$\bar{\nu}_\mu$ RHC 1-Trk	0.0	8414.09	0.0
		$\bar{\nu}_\mu$ RHC N-Trks	0.0	4724.34	0.0
		$\nu_\mu$ RHC 1-Trk	0.0	3022.10	0.0
		$\nu_\mu$ RHC N-Trks	0.0	4928.38	0.0
		$\nu_\mu$ 1-Trk Air	0.0	23605.76	0.0
		$\nu_\mu$ N-Trks	0.0	32304.13	0.0

**Table B.1:** Event rate broken by sample for one  $\sigma$  variation of each parameter.

Parameter	$1\sigma$ value	Sample	$-1\sigma$ (%)	nominal	$+1\sigma$ (%)
586 : CC-DIS shape location	0.40	$\nu_\mu$ 1-Trk Wtr	-0.4	27316.74	0.4
		$\nu_\mu$ N-Trks	-4.2	30904.32	4.2
		$\bar{\nu}_\mu$ RHC 1-Trk	-0.3	8414.09	0.3
		$\bar{\nu}_\mu$ RHC N-Trks	-4.3	4724.34	4.3
		$\nu_\mu$ RHC 1-Trk	-0.7	3022.10	0.7
		$\nu_\mu$ RHC N-Trks	-4.4	4928.38	4.4
		$\nu_\mu$ 1-Trk Air	-0.3	23605.76	0.3
		$\nu_\mu$ N-Trks	-3.9	32304.13	3.9
		$\bar{\nu}_\mu$ RHC 1-Trk	-0.2	6767.65	0.2
		$\bar{\nu}_\mu$ RHC N-Trks	-4.2	4544.65	4.2
		$\nu_\mu$ RHC 1-Trk	-0.6	2067.37	0.6
		$\nu_\mu$ RHC N-Trks	-4.1	4568.13	4.1
587 : CC Coherent on $^{12}\text{C}$ norm.	0.30	$\nu_\mu$ 1-Trk Wtr	-0.1	27316.74	0.1
		$\nu_\mu$ N-Trks	-0.2	30904.32	0.2
		$\bar{\nu}_\mu$ RHC 1-Trk	-0.1	8414.09	0.1
		$\bar{\nu}_\mu$ RHC N-Trks	-0.4	4724.34	0.4
		$\nu_\mu$ RHC 1-Trk	-0.1	3022.10	0.1
		$\nu_\mu$ RHC N-Trks	-0.2	4928.38	0.2
		$\nu_\mu$ 1-Trk Air	-0.1	23605.76	0.1
		$\nu_\mu$ N-Trks	-0.3	32304.13	0.3
		$\bar{\nu}_\mu$ RHC 1-Trk	-0.2	6767.65	0.2
		$\bar{\nu}_\mu$ RHC N-Trks	-0.6	4544.65	0.6
		$\nu_\mu$ RHC 1-Trk	-0.2	2067.37	0.2
		$\nu_\mu$ RHC N-Trks	-0.3	4568.13	0.3

**Table B.1:** Event rate broken by sample for one  $\sigma$  variation of each parameter.

Parameter	$1\sigma$ value	Sample	$-1\sigma$ (%)	nominal	$+1\sigma$ (%)
588 : CC Coherent on $^{16}\text{O}$ norm.	0.30	$\nu_\mu$ 1-Trk Wtr	-0.0	27316.74	0.0
		$\nu_\mu$ N-Trks	-0.1	30904.32	0.1
		$\bar{\nu}_\mu$ RHC 1-Trk	-0.1	8414.09	0.1
		$\bar{\nu}_\mu$ RHC N-Trks	-0.2	4724.34	0.2
		$\nu_\mu$ RHC 1-Trk	-0.1	3022.10	0.1
		$\nu_\mu$ RHC N-Trks	-0.1	4928.38	0.1
		$\nu_\mu$ 1-Trk Air	-0.0	23605.76	0.0
		$\nu_\mu$ N-Trks	-0.0	32304.13	0.0
		$\bar{\nu}_\mu$ RHC 1-Trk	-0.0	6767.65	0.0
		$\bar{\nu}_\mu$ RHC N-Trks	-0.0	4544.65	0.0
		$\nu_\mu$ RHC 1-Trk	-0.0	2067.37	0.0
		$\nu_\mu$ RHC N-Trks	-0.0	4568.13	0.0
589 : NC Coherent norm.	0.30	$\nu_\mu$ 1-Trk Wtr	-0.0	27316.74	0.0
		$\nu_\mu$ N-Trks	-0.0	30904.32	0.0
		$\bar{\nu}_\mu$ RHC 1-Trk	-0.0	8414.09	0.0
		$\bar{\nu}_\mu$ RHC N-Trks	-0.0	4724.34	0.0
		$\nu_\mu$ RHC 1-Trk	-0.0	3022.10	0.0
		$\nu_\mu$ RHC N-Trks	-0.0	4928.38	0.0
		$\nu_\mu$ 1-Trk Air	-0.0	23605.76	0.0
		$\nu_\mu$ N-Trks	-0.0	32304.13	0.0
		$\bar{\nu}_\mu$ RHC 1-Trk	-0.0	6767.65	0.0
		$\bar{\nu}_\mu$ RHC N-Trks	-0.0	4544.65	0.0
		$\nu_\mu$ RHC 1-Trk	-0.0	2067.37	0.0
		$\nu_\mu$ RHC N-Trks	-0.0	4568.13	0.0

**Table B.1:** Event rate broken by sample for one  $\sigma$  variation of each parameter.

Parameter	$1\sigma$ value	Sample	$-1\sigma$ (%)	nominal	$+1\sigma$ (%)
590 : NC-1 $\gamma^*$	1.00	$\nu_\mu$ 1-Trk Wtr	-0.0	27316.74	0.0
		$\nu_\mu$ N-Trks	-0.0	30904.32	0.0
		$\bar{\nu}_\mu$ RHC 1-Trk	0.0	8414.09	0.0
		$\bar{\nu}_\mu$ RHC N-Trks	-0.0	4724.34	0.0
		$\nu_\mu$ RHC 1-Trk	0.0	3022.10	0.0
		$\nu_\mu$ RHC N-Trks	0.0	4928.38	0.0
		$\nu_\mu$ 1-Trk Air	-0.0	23605.76	0.0
		$\nu_\mu$ N-Trks	0.0	32304.13	0.0
		$\bar{\nu}_\mu$ RHC 1-Trk	0.0	6767.65	0.0
		$\bar{\nu}_\mu$ RHC N-Trks	-0.0	4544.65	0.0
		$\nu_\mu$ RHC 1-Trk	0.0	2067.37	0.0
		$\nu_\mu$ RHC N-Trks	0.0	4568.13	0.0
591 : NC Other Near	0.30	$\nu_\mu$ 1-Trk Wtr	-0.1	27316.74	0.1
		$\nu_\mu$ N-Trks	-0.6	30904.32	0.6
		$\bar{\nu}_\mu$ RHC 1-Trk	-0.2	8414.09	0.2
		$\bar{\nu}_\mu$ RHC N-Trks	-1.9	4724.34	1.9
		$\nu_\mu$ RHC 1-Trk	-0.2	3022.10	0.2
		$\nu_\mu$ RHC N-Trks	-0.8	4928.38	0.8
		$\nu_\mu$ 1-Trk Air	-0.1	23605.76	0.1
		$\nu_\mu$ N-Trks	-0.6	32304.13	0.6
		$\bar{\nu}_\mu$ RHC 1-Trk	-0.3	6767.65	0.3
		$\bar{\nu}_\mu$ RHC N-Trks	-1.8	4544.65	1.8
		$\nu_\mu$ RHC 1-Trk	-0.2	2067.37	0.2
		$\nu_\mu$ RHC N-Trks	-0.8	4568.13	0.8

**Table B.1:** Event rate broken by sample for one  $\sigma$  variation of each parameter.

Parameter	$1\sigma$ value	Sample	$-1\sigma$ (%)	nominal	$+1\sigma$ (%)
591 : NC Other Far*	0.30	$\nu_\mu$ 1-Trk Wtr	-0.1	27316.74	0.1
		$\nu_\mu$ N-Trks	-0.4	30904.32	0.4
		$\bar{\nu}_\mu$ RHC 1-Trk	-0.1	8414.09	0.1
		$\bar{\nu}_\mu$ RHC N-Trks	-1.2	4724.34	1.2
		$\nu_\mu$ RHC 1-Trk	-0.1	3022.10	0.1
		$\nu_\mu$ RHC N-Trks	-0.5	4928.38	0.5
		$\nu_\mu$ 1-Trk Air	-0.1	23605.76	0.1
		$\nu_\mu$ N-Trks	-0.6	32304.13	0.6
		$\bar{\nu}_\mu$ RHC 1-Trk	-0.3	6767.65	0.3
		$\bar{\nu}_\mu$ RHC N-Trks	-1.8	4544.65	1.8
		$\nu_\mu$ RHC 1-Trk	-0.2	2067.37	0.2
		$\nu_\mu$ RHC N-Trks	-0.8	4568.13	0.8

**Table B.1:** Event rate broken by sample for one  $\sigma$  variation of each parameter.

---

## Appendix C

### Log-Likelihood Sample Scans

This appendix examines the PØD-only BANFF fit likelihood term  $\Delta\chi^2_{\text{LLR}} = \chi^2_{\text{sample}}$  response (scans) to variations in flux and cross section parameters. For the cross section terms, the scans shapes correspond to the shape of the spline weight. In addition, comparison scans are provided for the FGD MaCH3 2017 analysis. Extensive comparisons were made to ensure that the FGD MaCh3 and FGD BANFF analyses have identical splines. So it is an equal comparison with the FGD BANFF as shown in Chapter 4. In some cases, the PØD-only scans indicate higher sensitivity to parameters than the FGD.

These were generously produced by Clarence Wret ([c.wret@rochester.edu](mailto:c.wret@rochester.edu)) of the University of Rochester. Due to a bug in plotting script, the PØD scans 2p2h shape location for  $^{12}\text{C}$  and  $^{16}\text{O}$  were empty. The MaCH3 inputs were as faithfully reproduced as possible using quadratic functions and drawn with the correct PØD scans as shown in Figure C.1 on page 242.

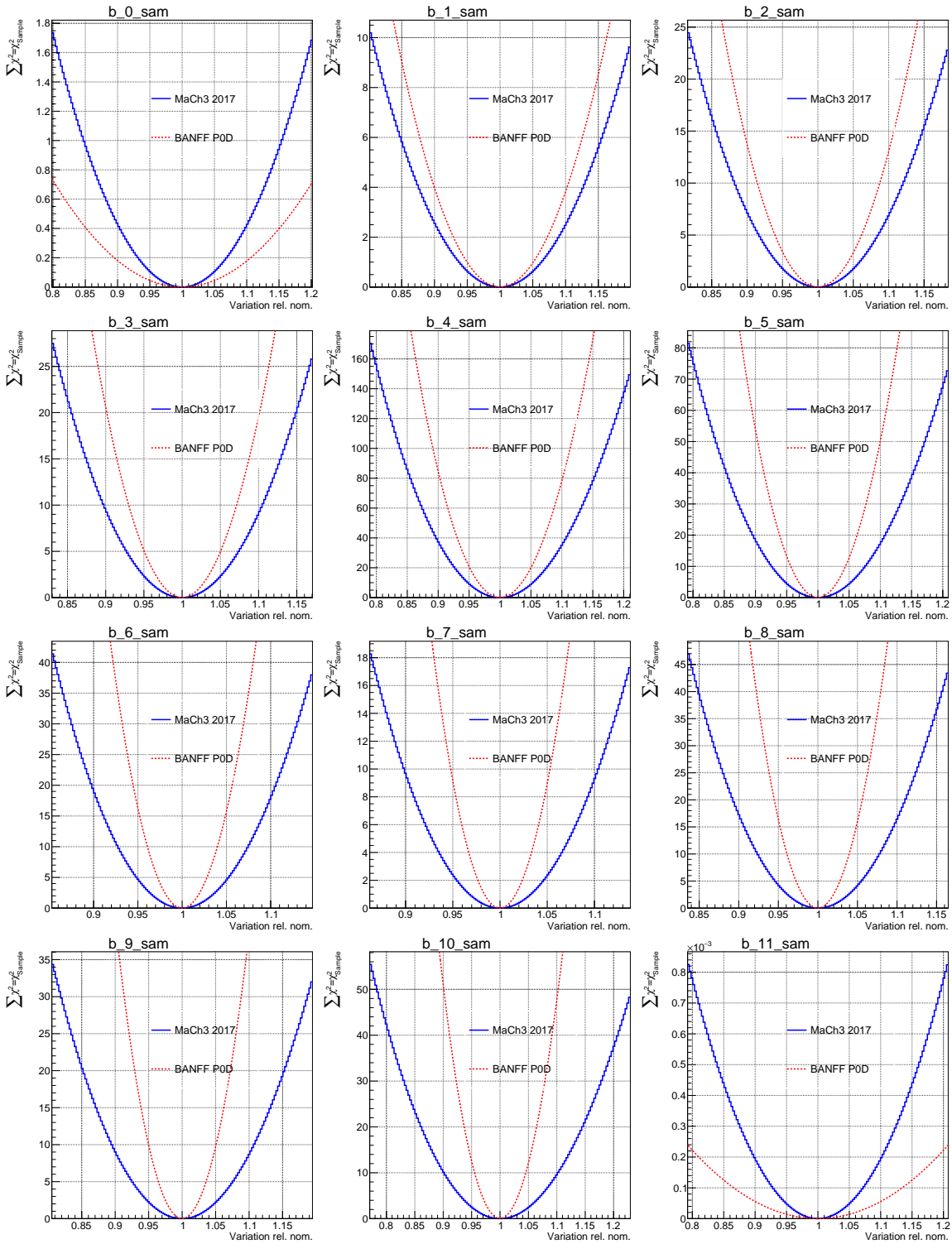
For the flux scan terms, only the ND280 (fit indices 0 - 49) terms are shown since they have data to constrain them. In other words, the log-likelihood scans are flat with respect to SK flux term variations.

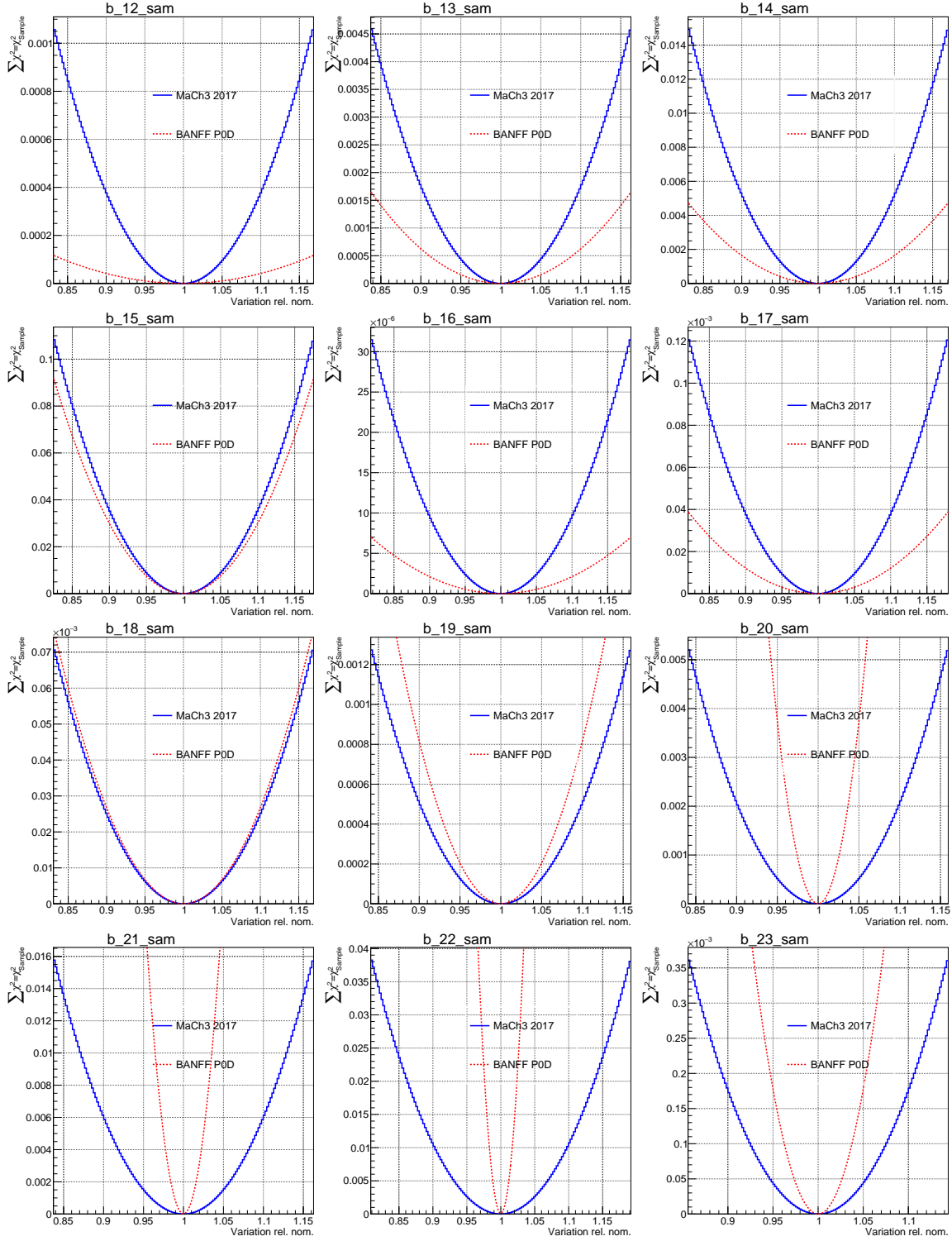
Some of cross section parameter splines are reflected about a point in order to properly calculate correlations between parameters. In previous fits to data, the 2p2h  $^{12}\text{C}$  and  $^{16}\text{O}$

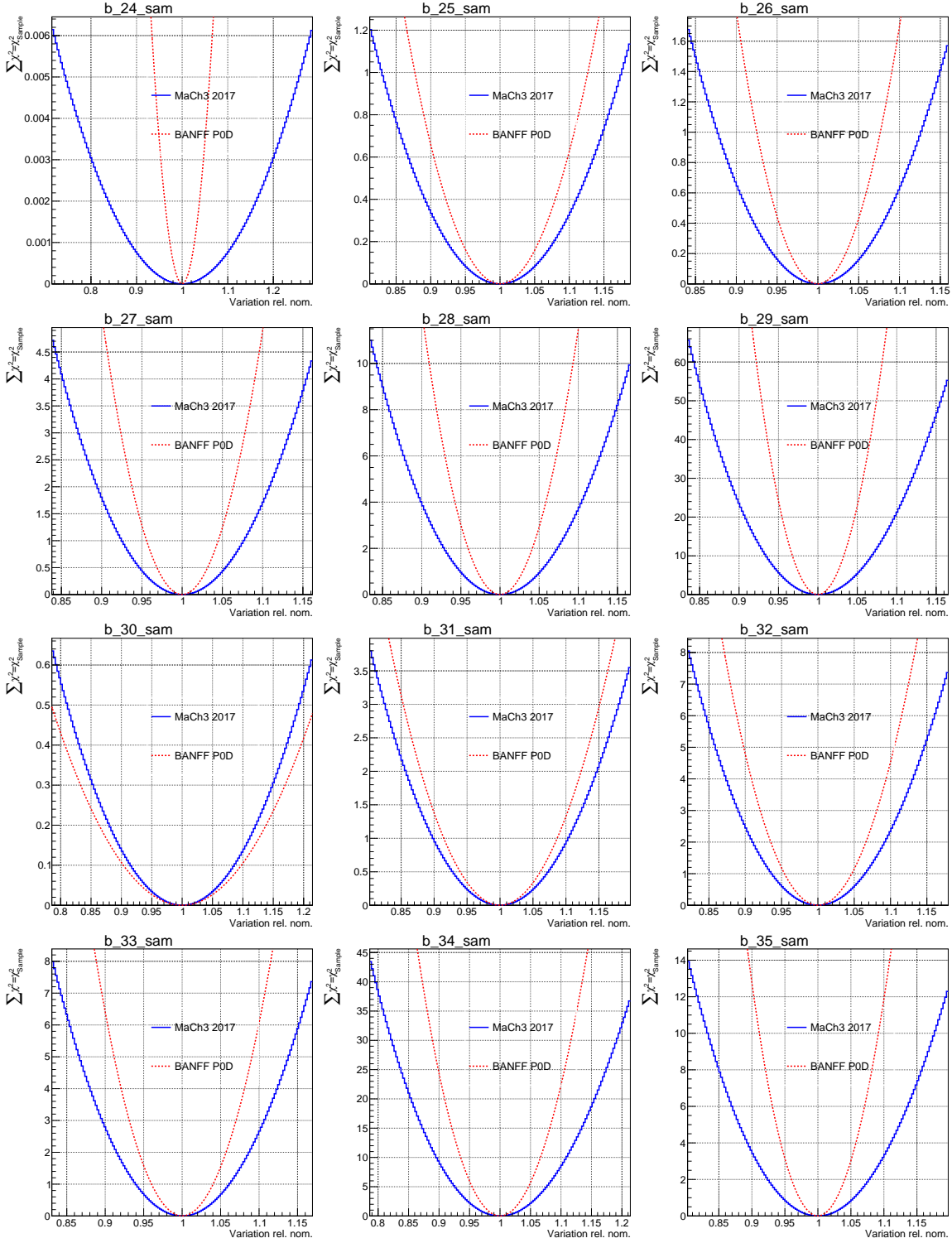
---

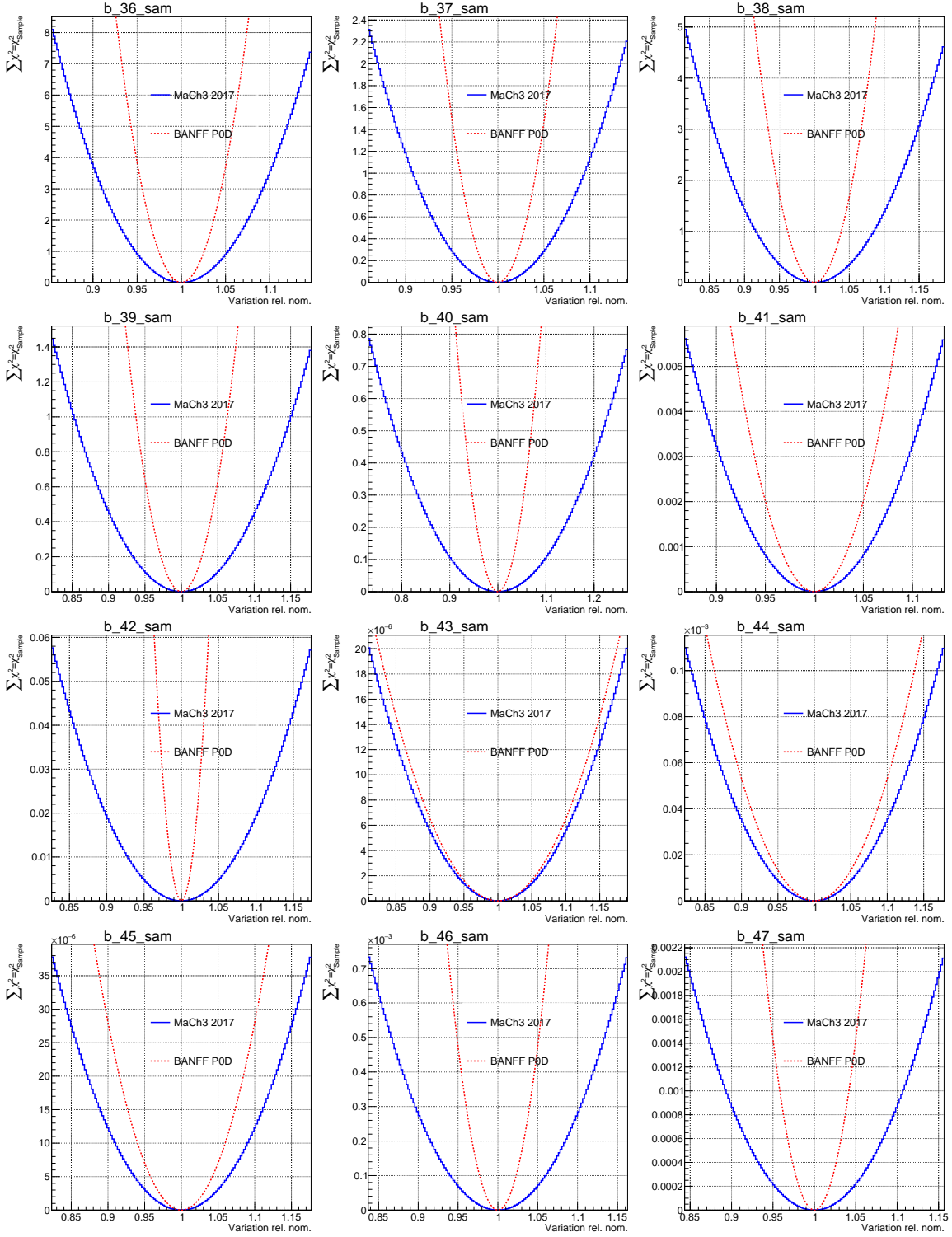
---

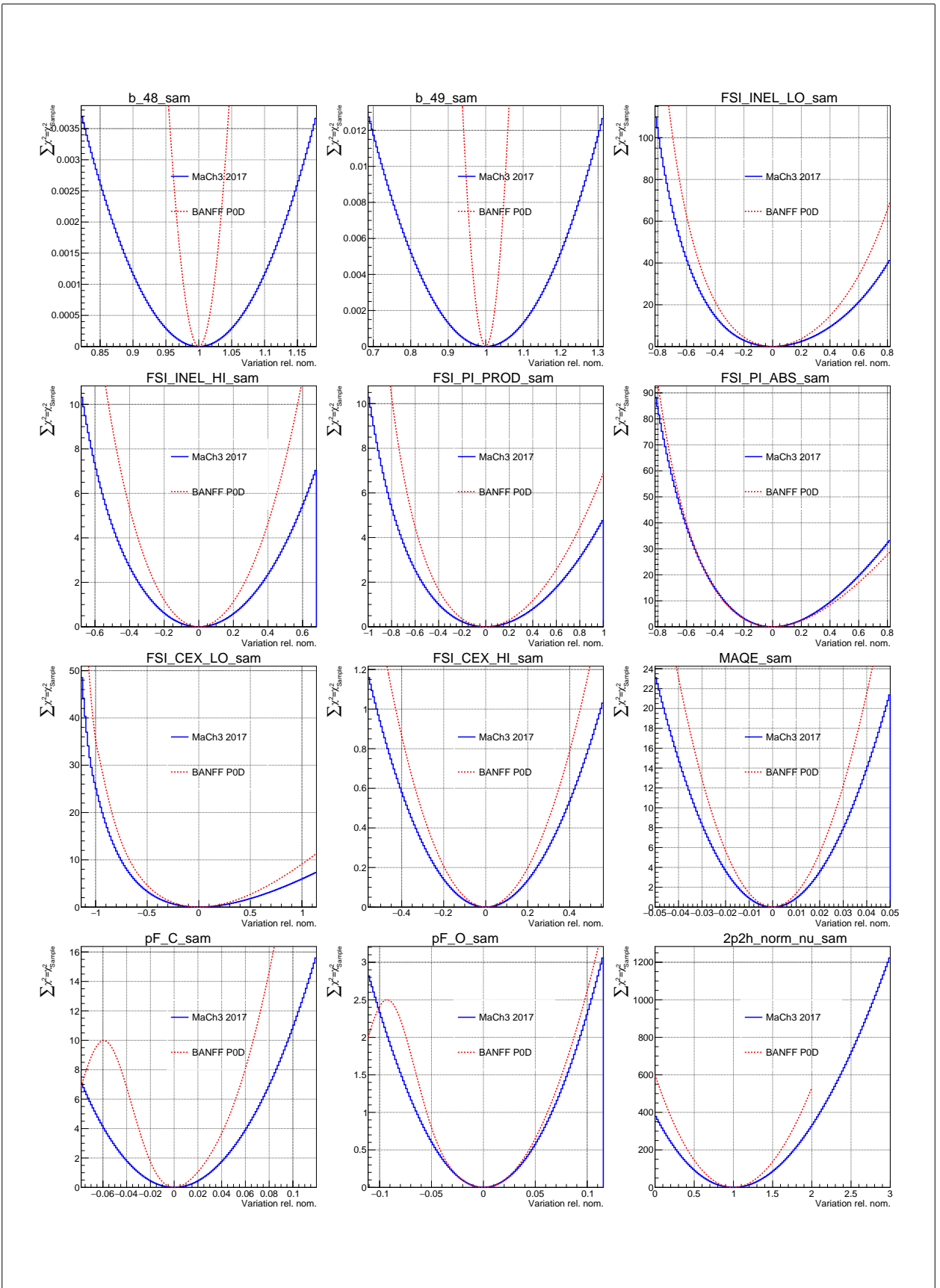
shape location terms hit their physical boundaries at +1. The result was that the fitter MINUIT inaccurately calculated the Hess matrix. The decision was made to reflect, also called “mirroring”, the splines about a certain point to expand the limit. Tests showed that this did not affect the postfit results for any parameters, but the correlations between all other parameters was calculated to less than 1% [16].

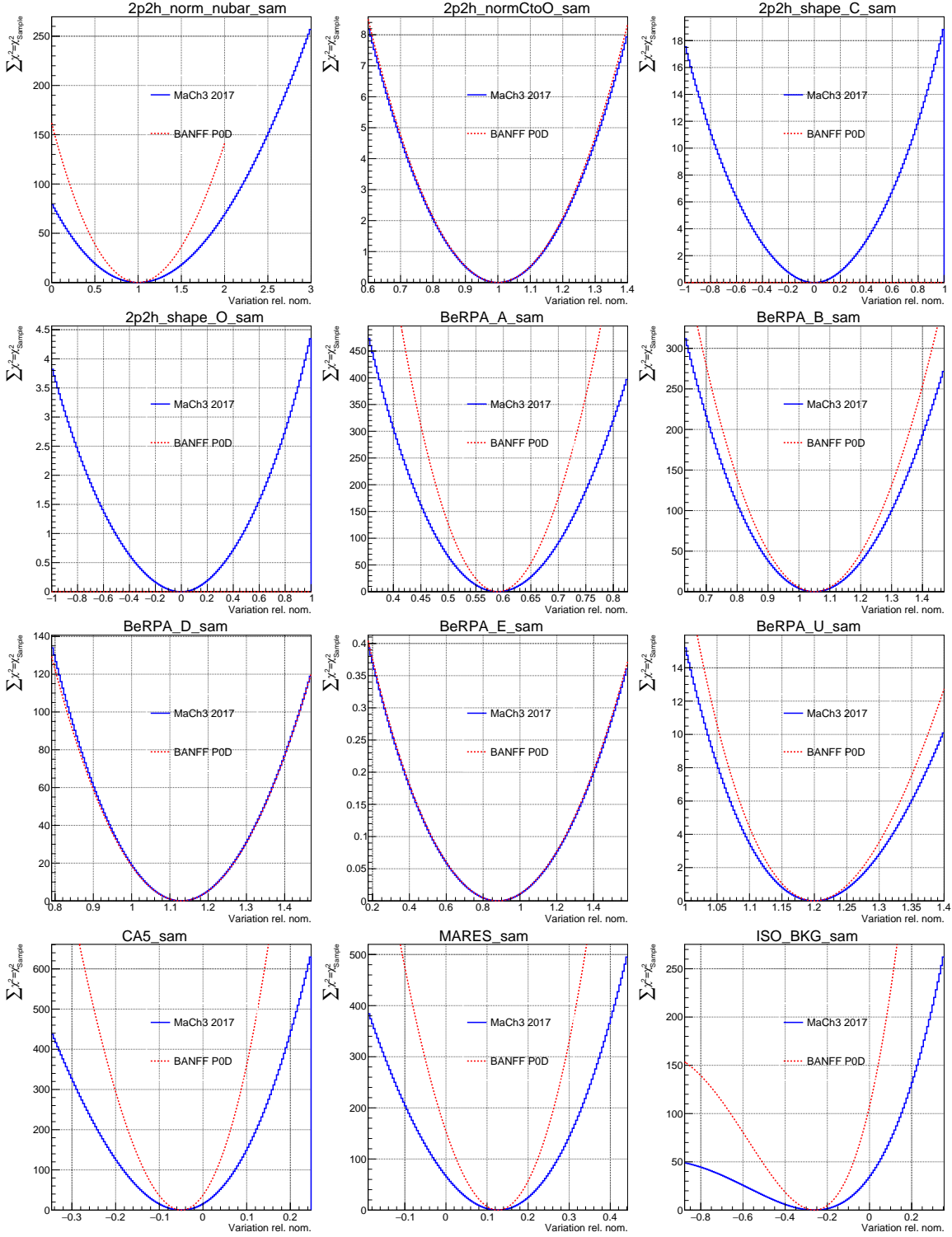


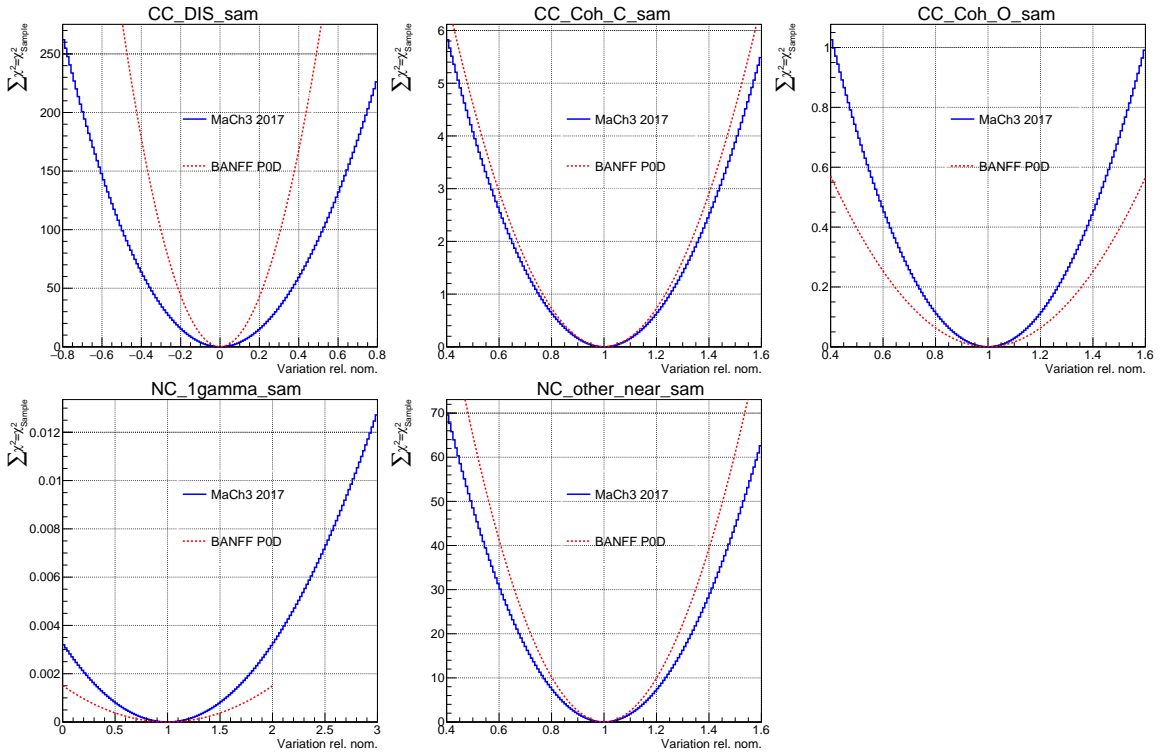












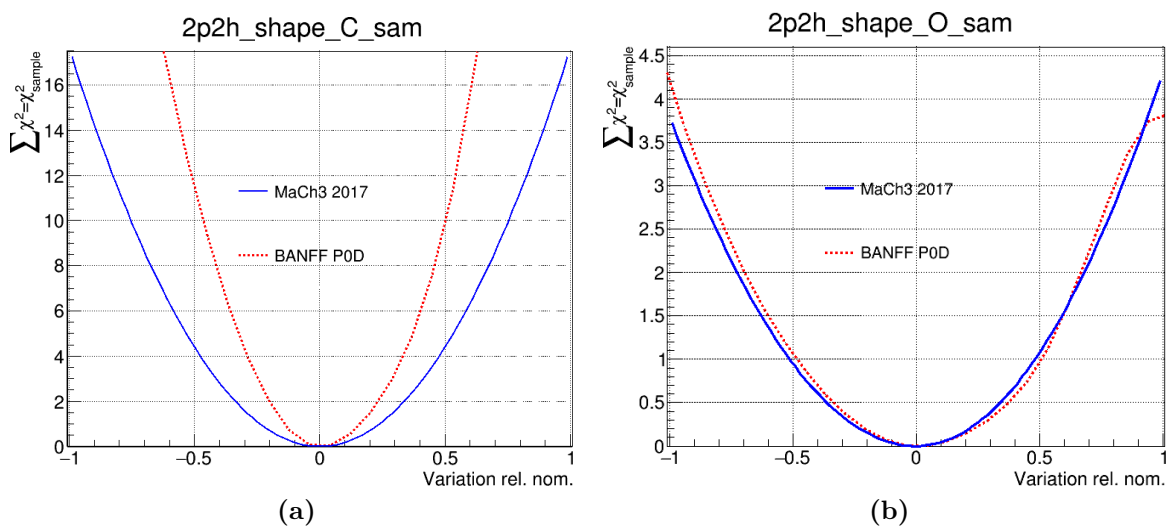


**Figure C.1:** Correct PØD scans with faithful reproductions of the MaCh3 scans for the 2p2h shape location cross section parameters.

---

---

## Appendix D

### Log-Likelihood Penalty Scans

This appendix examines the PØD-only BANFF fit penalty terms  $\Delta\chi^2_{\text{Flux}} + \Delta\chi^2_{\text{xsec}} + \Delta\chi^2_{\text{Det}}$  response (scans) to variations in flux and cross section parameters. In addition, comparison scans are provided for the FGD MaCH3/BANFF 2017 analysis. In all cases, the penalty terms overlap indicating the parameters have the same prior constraints between analyses.

